Contributors to This Volume ·

Matthias Burkardt
James J. Kelly

ADVANCES IN NUCLEAR PHYSICS

Edited by
J.W. Negele
and Erich Vogt

VOLUME 23

ADVANCES IN NUCLEAR PHYSICS

VOLUME 23

CONTRIBUTORS TO THIS VOLUME

Matthias Burkardt
Institute for Nuclear Theory
University of Washington
Seattle, Washington

Permanent Address: Department of Physics
New Mexico State University
Las Cruces, New Mexico

James J. Kelly
Department of Physics
University of Maryland
College Park, Maryland

ADVANCES IN NUCLEAR PHYSICS

Edited by

J.W. Negele

Center for Theoretical Physics
Massachusetts Institute of Technology
Cambridge, Massachusetts

Erich Vogt

Department of Physics
University of British Columbia
Vancouver, B.C., Canada

VOLUME 23

Created in the United States of America

ARTICLES PUBLISHED IN EARLIER VOLUMES

Volume 1

The Reorientation Effect • *J. de Boer and J. Eichler*
The Nuclear SU_3 Model • *M. Harvey*
The Hartree-Fock Theory of Deformed Light Nuclei • *G. Ripka*
The Statistical Theory of Nuclear Reactions • *E. Vogt*
Three-Particle Scattering—A Review of Recent Work on the Nonrelativistic Theory • *I. Duck*

Volume 2

The Giant Dipole Resonance • *B. M. Spicer*
Polarization Phenomena in Nuclear Reactions • *C. Glashausser and J. Thirion*
The Pairing-Plus-Quadrupole Model • *D. R. Bes and R. A. Sorensen*
The Nuclear Potential • *P. Signell*
Muonic Atoms • *S. Devons and I. Duerdoth*

Volume 3

The Nuclear Three-Body Problem • *A. N. Mitra*
The Interactions of Pions with Nuclei • *D. S. Koltun*
Complex Spectroscopy • *J. B. French, E. C. Halbert, J. B. McGrory, and S. S. M. Wong*
Single Nucleon Transfer in Deformed Nuclei • *B. Elbeck and P. O. **Tjøm***
Isocalar Transition Rates in Nuclei from the (α, α') Reaction • *A. M. Bernstein*

Volume 4

The Investigation of Hole States in Nuclei by Means of Knockout and Other Reactions •
 Daphne F. Jackson
High-Energy Scattering from Nuclei • *Wieslaw Czyz*
Nucleosynthesis and Neutron-Capture Cross Sections • *B. J. Allen, J. H. Gibbons, and
 R. L. Macklin*
Nuclear Structure Studies in the $Z = 50$ Region • *Elizabeth Urey Baranger*
An s-d Shell-Model Study for $A = 18 - 22$ • *E. C. Halbert, J. B. McGrory, B. H. Wildenthal,
 and S. P. Pandya*

Volume 5

Variational Techniques in the Nuclear Three-Body Problem • *L. M. Delves*
Nuclear Matter Calculations • *Donald W. L. Sprung*
Clustering in Light Nuclei • *Akito Arima, Hisashi Horiuchi, Kuniharu Kubodera, and
 Noboru Takigawa*

ARTICLES PLANNED FOR FUTURE VOLUMES

PREFACE

This volume of *Advances in Nuclear Physics* addresses two very different frontiers of contemporary nuclear physics — one highly theoretical and the other solidly phenomenological.

The first article by Matthias Burkardt provides a pedagogical overview of the timely topic of light front quantization. Although introduced decades ago by Dirac, light front quantization has been a central focus in theoretical nuclear and particle physics in recent years for two major reasons. The first, as discussed in detail by Burkardt, is that light-cone coordinates are the natural coordinates for describing high-energy scattering. The wealth of data in recent years on nucleon and nucleus structure functions from high-energy lepton and hadron scattering thus provides a strong impetus for understanding QCD on the light cone. Second, as theorists have explored light front quantization, a host of deep and intriguing theoretical questions have arisen associated with the triviality of the vacuum, the role of zero modes, rotational invariance, and renormalization. These issues are so compelling that they are now intensively investigated on their own merit, independent of the particular application to high-energy scattering. This article provides an excellent introduction and overview of the motivation from high-energy scattering, an accessible description of the basic ideas, an insightful discussion of the open problems, and a helpful guide to the specialized literature. It is an ideal opportunity for those with a spectator's acquaintance to develop a deeper understanding of this important field.

The second article provides a comprehensive review by James Kelly of major advances in the field of electron-induced nucleon knockout reactions. In principle, knockout of a nucleon by the known electromagnetic current provides a powerful tool to explore the energy and momentum distribution of protons and neutrons in finite nuclei. The advent of high duty-factor accelerators, polarized beams, out-of-plane detectors, and increased kinematic range and resolution has dramatically expanded our experimental horizons, and brings us far closer to exploiting the full potential of this probe. Kelly's

article provides a thorough review of the basic framework for extracting nuclear structure information from knockout reactions and surveys major new experimental results. It is also extremely useful in highlighting the limitations in our understanding of these reactions arising from theoretical uncertainties in the optical potential, off-shell nucleon currents, and the reaction mechanism. The combination of the recent experiments reviewed here and those about to begin at new facilities represents a major advance in nuclear physics, and this article provides both an excellent introduction for nonspecialists and a comprehensive overview for those in the field.

J. W. NEGELE
E. W. VOGT

CONTENTS

Chapter 1

LIGHT FRONT QUANTIZATION

Matthias Burkardt

Chapter 2

NUCLEON KNOCKOUT BY INTERMEDIATE ENERGY ELECTRONS

James J. Kelly

ADVANCES IN
NUCLEAR PHYSICS

VOLUME 23

Chapter 1

LIGHT FRONT QUANTIZATION

Matthias Burkardt

Institute for Nuclear Theory
University of Washington
Seattle, Washington 98195-1550

1. INTRODUCTION

1.1. Deep Inelastic Scattering

More than twenty years after quantum chromodynamics (QCD) was introduced as a microscopic theory of strong interactions, very little is known about its solutions. At least in principle, it should be possible to describe the interaction of nucleons with external probes using quark and gluon degrees

Permanent address: Department of Physics, New Mexico State University, Las Cruces, New Mexico 88003-0001.
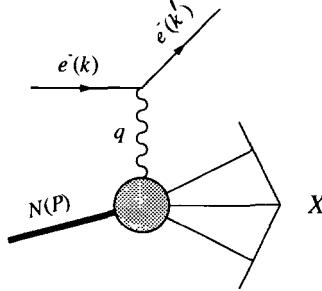
Fig. 1.1. Inclusive process $e^- + N \rightarrow e^{-\prime} + X$, where X is an unidentified hadronic state.

of freedom on the basis of QCD. So far, however, the extreme complexity of this theory has slowed any progress in this direction considerably.

Deep inelastic lepton–nucleon scattering (DIS) provides access to quark and gluon degrees of freedom in nucleons and nuclei. In these experiments one shoots high energy leptons (e.g., electrons) at a hadronic target (usually protons or nuclei) and measures the energy and momentum transfer to the target by detecting the final state lepton (Fig. 1.1). The hadronic final state X is not measured (usually the nucleon is destroyed in these reactions and the hadronic final state consists of many particles). Because of the extremely large momentum transfer to the target (typical momentum transfers in DIS experiments are several GeV/c or more), the inclusive cross sections are dominated by single particle response functions along the light cone. To illustrate this let us use the optical theorem which relates the differential lepton nucleon cross section to the imaginary part of the forward Compton amplitude[1] (Fig. 1.2). One finds

$$\frac{d^2\sigma}{d\Omega dE'} = \frac{\alpha^2}{q^4}\left(\frac{E'}{E}\right)l^{\mu\nu}\frac{\mathrm{Im}\,T_{\mu\nu}}{2\pi} \tag{1.1}$$

where E and E' are the energies of the initial and final lepton, $q = k - k'$ is the four momentum transfer of the lepton on the target and $l_{\mu\nu} = 2k_\mu k'_\nu + 2k_\nu k'_\mu + q^2 g_{\mu\nu}$ is the leptonic tensor. The hadronic tensor

$$T_{\mu\nu}(P,q) = \frac{i}{2M_N}\sum_S \int \frac{d^4x}{2\pi}e^{iq\cdot x}\langle P,S|T\left(J_\mu(x)J_\nu(0)\right)|P,S\rangle \tag{1.2}$$

(S is the spin of the target proton) contains all the information about the parton substructure of the target proton.

In the Bjorken limit ($Q^2 \equiv -q^2 \rightarrow \infty$, $P \cdot q \rightarrow \infty$, $x_{Bj} = Q^2/2P \cdot q$ fixed), deep inelastic structure functions exhibit Bjorken scaling: up to kinemat-
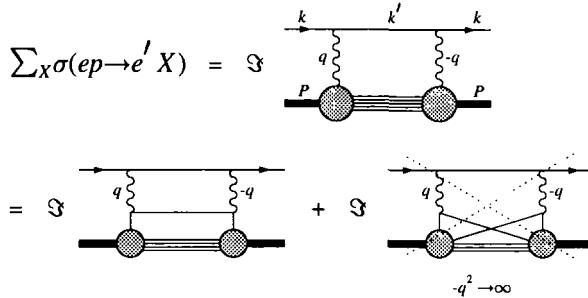
Fig. 1.2. Inclusive lepton nucleon cross section expressed in terms of the imaginary part of the forward Compton amplitude. For $Q^2 = -q^2 \to \infty$ only the "handbag diagram" (both photons couple to the same quark) survives. The "crossed diagram" (the two photons couple to different quarks) is suppressed because of wave function effects.

ical coefficients, the hadronic tensor (1.2) depends only on x_{Bj} but no longer on Q^2 (within perturbatively calculable logarithmic corrections). In order to understand this result, it is convenient to introduce *light-front* variables $a_{\mp} = a^{\pm} = \left(a^0 \pm a^3\right)/\sqrt{2}$ so that the scalar product reads $a \cdot b = a_+ b^+ + a_- b^- - \vec{a}_\perp \vec{b}_\perp = a_+ b_- + a_- b_+ - \vec{a}_\perp \vec{b}_\perp$. Furthermore let us choose a frame where $\vec{q}_\perp = 0$. The Bjorken limit corresponds to p^μ and q_- fixed, while $q_+ \to \infty$. Bjorken scaling is equivalent to the statement that the structure functions become independent of q_+ in this limit (again up to trivial kinematic coefficients). In this limit, the integrand in Eq. (1.2) contains the rapidly oscillating factor $\exp(iq_+ x^+)$, which kills all contributions to the integral except those where the integrand is singular.[2] Due to causality, the integrand must vanish for $x^2 = 2x^+ x^- - \vec{x}_\perp^2 < 0$ and the current product is singular at $x^+ = 0$, $\vec{x}_\perp = 0$. The leading singularity can be obtained from the operator product expansion by contracting two fermion operators in the product $T\left(J_\mu(x) J_\nu(0)\right) \equiv T\left(\bar{\psi}(x)\gamma_\mu \psi(x)\bar{\psi}(0)\gamma_\nu \psi(0)\right)$, yielding a nonlocal term bilinear in the fermion field multiplying a free (asymptotic freedom!) fermion propagator from 0 to x which gives rise to the above-mentioned singularity structure.[3] The $x^+ = \vec{x}_\perp = 0$ dominance in the integral has two consequences. First it explains Bjorken scaling, because q_+ enters the hadronic tensor only via the term $x^+ q_+$ in the exponent and for $x^+ = 0$ the q_+ dependence drops out. Second, and this is very important for practical calculations, the parton distributions, i.e., the Bjorken scaled structure functions, can be expressed in terms of correlation functions along the *light-front* space direction x^-. For example, for the spin averaged parton distribution one obtains

$$2P_- f(x_{Bj}) = \int \frac{dx^-}{2\pi} \langle P|\bar{\psi}(0)\gamma_- \psi(x^-)|P\rangle \exp(iP_- x^- x_{Bj}) \quad (1.3)$$

The physical origin of this result can be understood as follows. Consider again the virtual forward Compton amplitude (Fig. 1.2). In principle, the photons in the first and second interaction in Fig. 1.2 can couple to the same as well as to different quarks in the target. However, the hadronic wave function can only absorb momenta which are of the order of the QCD-scale ($\Lambda_{QCD} \approx 200$ MeV). Therefore, in the limit of large momentum transfer, only such diagrams survive where the two photons in Fig. 1.2 couple to the same quark. All other diagrams have large momenta flowing through the wave function or they involve extra hard gluon exchanges which results in their suppression at large Q^2. The large momentum transfer is also important because of asymptotic freedom. Since $\alpha_S(Q^2) \sim 1/\log\left(Q^2/\Lambda_{QCD}^2\right)$, the running coupling constant of QCD goes to zero for large Q^2, all interactions of the struck quark can be neglected and it propagates essentially without interaction between the two photon-vertices. Furthermore, since the momentum transfer is much larger than the masses of the quarks in the target, the struck quarks propagation between becomes ultrarelativistic, i.e., it moves exceedingly close to the light cone $x^2 = 0$. Due to the high-energy nature of the scattering, the relativistic structure function is a LF correlation.[4,5] Already at this point it should be clear that LF coordinates play a distinguished role in the analysis of DIS experiments—a point which will become much more obvious after we have introduced some of the formal ideas of LF quantization.

1.2. Advantages of Light-Front Coordinates

LF quantization is very similar to canonical equal time (ET) quantization[6] (here we closely follow Ref. 7). Both are hamiltonian formulations of field theory, where one specifies the fields on a particular initial surface. The evolution of the fields off the initial surface is determined by the Lagrangian equations of motion. The main difference is the choice of the initial surface, $x^0 = 0$ for ET and $x^+ = 0$ for the LF, respectively. In both frameworks states are expanded in terms of fields (and their derivatives) on this surface. Therefore, the same physical state may have very different wave functions* in the ET and LF approaches because fields at $x^0 = 0$ provide a different basis for expanding a state than fields at $x^+ = 0$. The reason is that the microscopic degrees of freedom—field amplitudes at $x^0 = 0$ versus field amplitudes at $x^+ = 0$—are in general quite different from each other in the two formalisms.

This has important consequences for the practical calculation of parton distributions (1.3) which are real time response functions in the equal time formalism.† In order to evaluate Eq. (1.3) one needs to know not only the ground state

---

*By "wave function" we mean here the collection of all Fock space amplitudes.
†The arguments of $\bar{\psi}$ and ψ in Eq. (1.3) have different time components!

wave function of the target, but also matrix elements to excited states. In contrast, in the framework of LF quantization, parton distributions are correlation functions at equal LF time x^+, i.e., *within* the initial surface $x^+ = 0$, and can thus be expressed directly in terms of ground state wave functions. (As a reminder: ET wave functions and LF wave functions are in general different objects.) In the LF framework, parton distributions $f(x_{Bj})$ can be easily calculated and have a very simple physical interpretation as single particle momentum densities, where x_{Bj} measures the fraction of momentum carried by the hadron*

$$x_{Bj} = \frac{p_-^{\text{parton}}}{P_-^{\text{hadron}}} \tag{1.4}$$

Although DIS is probably the most prominent example for practical applications of LF coordinates, they prove useful in many other places as well. For example, LF coordinates have been used in the context current algebra sum rules in particle physics.[8] Another prominent example is form factors, where moments of the wave function along the LF determine the asymptotic falloff at large momentum transfer.[9] More recently, LF quantization found applications in inclusive decays of heavy quarks.[10–12]

From the purely theoretical point of view, various advantages of LF quantization derive from properties of the ten generators of the Poincaré group (translations P^μ, rotations $\vec{L}$, and boosts $\vec{K}$).[6,7] Those generators which leave the initial surface invariant ($\vec{P}$ and $\vec{L}$ for ET, and P_-, $\vec{P}_\perp$, L_3 and $\vec{K}$ for LF) are "simple" in the sense that they have very simple representations in terms of the fields (typically just sums of single particle operators). The other generators, which include the "hamiltonians" (P_0, which is conjugate to x^0 in ET and P_+, which is conjugate to the LF time x^+ in LF quantization) contain interactions among the fields and are typically very complicated. Generators which leave the initial surface invariant are also called *kinematic* generators, while the others are called *dynamic* generators. Obviously it is advantageous to have as many of the ten generators kinematic as possible. There are seven kinematic generators on the LF but only six in ET quantization.

The fact that P_-, the generator of x^- translations, is kinematic (obviously it leaves $x^+ = 0$ invariant!) and positive has striking consequences for the LF vacuum.[7] For free fields $p^2 = m^2$ implies for the LF energy $p_+ = (m^2 + \vec{p}_\perp)/2p_-$. Hence positive energy excitations have positive p_-. After the usual reinterpretation of the negative energy states this implies that p_-

---

*In DIS with nonrelativistic kinematics (e.g., thermal neutron scattering off liquid ^{4}He) one also observes scaling and the structure functions can be expressed in terms of single particle response functions. However, due to the different kinematics, nonrelativistic structure functions at large momentum transfer are dominated by Fourier transforms of equal time response functions, i.e., ordinary momentum distributions.

for a single particle is positive [which makes sense, considering that $p_- = (p_0 - p_3)/\sqrt{2}$]; P_- being kinematic means that it is given by the sum of single particle p_-. Combined with the positivity of p_- this implies that the Fock vacuum (no particle excitations) is the unique state with $P_- = 0$. All other states have positive P_-. Hence, even in the presence of interactions, the LF Fock vacuum does not mix with any other state and is therefore an exact eigenstate of the LF hamiltonian P_+ (which commutes with P_-). If one further assumes parity invariance of the ground state, this implies that the Fock vacuum must be the exact ground state of the fully interacting LF quantum field theory.* In sharp contrast to other formulations of field theory, the LF vacuum is trivial! This implies a tremendous technical advantage but also raises the question whether nonperturbative LF-field theory is equivalent to conventional field theory, where nonperturbative effects usually result in a highly nontrivial vacuum structure. This very deep issue will be discussed in more detail in Section 3.

Dirac was the first who had the idea to formulate field theory in LF coordinates[6](see also Ref. 13).† In this remarkable work (almost 20 years before scaling was discovered in deep inelastic lepton nucleon scattering!) he has shown that it should in principle be possible to formulate a consistent quantum theory on the LF. This work laid the basis for all further developments, but left many details open. The main issues are the structure of the vacuum, renormalization, and practical algorithms for solution.

1.3. Outline

There are many similarities between the formal steps in ET quantization and LF quantization. In Section 2 we will explain the basic steps in constructing LF hamiltonians and give examples for scalar fields, fermions, and gauge fields. The vacuum on the LF is very controversial. On the one hand simple kinematical arguments seem to show that in LF field theory the vacuum of interacting field theories is the same as the free field theory vacuum (all interactions turned off). In QCD we know that chiral symmetry is spontaneously broken. It is up to now unclear whether a LF hamiltonian, with its trivial vacuum, is capable of describing this physics. We will elaborate on this point in Section 3. Renormalization is an issue because the LF approach to field theory is not manifestly covariant. Thus UV divergences (which occur on the LF as they do everywhere in quantum field theory) are not necessarily

---

*Practical calculations show that typical LF hamiltonians are either unbounded from below or their ground state is indeed the Fock vacuum.

†Later, a similar framework was developed independently on the basis of a Lorentz frame ("the infinite momentum frame") that moves with $v \to c$.[8,14-18]

the same for all Lorentz components of a particular operator under consideration. Clearly this requires a more complex counterterm structure to render the theory finite and to restore Lorentz invariance for physical observables (see Section 4). Despite certain technical simplifications, field theory on the LF is *a priori* still an enormously complex many body problem. In particular, in QCD one knows from DIS experiments that the nucleon consists not only of the three valence quarks, but that sea quark pairs and gluons are a significant, if not dominant, component of the nucleon's LF wave function, i.e., one should not expect that the LF wave functions of ground state hadrons in QCD are simple. Recent attempts to cast LF bound state problems into a form that can be solved on a computer will be described in Section 5.

2. CANONICAL QUANTIZATION

2.1. Quantization in Light-Front Coordinates

In this chapter, the formal steps for quantization on the light front are presented. For pedagogical reasons this will be done by comparing with conventional quantization (with x^0 as "time"). On the one hand this shows that the basic steps in the quantization procedure in LF and in ET formalism are in fact very similar. More importantly, however, we will thus be able to highlight the essential differences between these two approaches to quantum field theory more easily.

In the context of canonical quantization one usually starts from the action

$$S = \int d^4 x \mathcal{L} \tag{2.1}$$

where $\mathcal{L} = \mathcal{L}(\phi, \partial_\mu \phi)$. After selecting a time direction τ,[*] one forms the momenta which are canonically conjugate to ϕ

$$\Pi(x) = \frac{\delta \mathcal{L}}{\delta \partial_\tau \phi} \tag{2.2}$$

and postulates canonical commutation relations between fields and corresponding momenta at equal "time" τ (Table 2.1).[†]

In the next step one constructs the Hamilton operator and the other components of the momentum vector. Thus one has completely specified the

---

[*] Here τ may stand for ordinary time x^0 as well as for LF time $x^+ = (x^0 + x^3)/\sqrt{2}$ or any other (not space-like) direction.

[†] The canonical quantization procedure in the ET formulation can, for example, be found in Ref. 19. The rules for canonical LF quantization have been taken from Refs. 20 and 21.

TABLE 2.1
Canonical Quantization in Ordinary Coordinates and on the Light Front

Normal coordinates	Light front

Coordinates

x^0	time	$x^+ = \dfrac{x^0 + x^3}{\sqrt{2}}$	time
x^1, x^2, x^3	space	$x^- = \dfrac{x^0 - x^3}{\sqrt{2}}, x^1, x^2$	space

Scalar product

$$a \cdot b = \qquad\qquad\qquad a \cdot b =$$
$$a^0 b^0 - a^1 b^1 - a^2 b^2 - a^3 b^3 \qquad a^+ b^- + a^- b^+ - a^1 b^1 - a^2 b^2$$
$$= a^0 b^0 - \vec{a}\vec{b} \qquad\qquad = a^+ b^- + a^- b^+ - \vec{a}_\perp \vec{b}_\perp$$

Lagrangian density

$$\mathcal{L} = \tfrac{1}{2}(\partial_0 \phi)^2 - \tfrac{1}{2}\left(\vec{\nabla}\phi\right)^2 - V(\phi) \qquad \mathcal{L} = \partial_+ \phi \partial_- \phi - \tfrac{1}{2}\left(\vec{\nabla}_\perp \phi\right)^2 - V(\phi)$$

Conjugate momenta

$$\pi = \frac{\delta \mathcal{L}}{\delta \partial_0 \varphi} = \partial_0 \varphi \qquad\qquad \pi = \frac{\delta \mathcal{L}}{\delta \partial_+ \varphi} = \partial_- \varphi$$

Canonical commutation relations

$$[\pi(\vec{x}, t), \varphi(\vec{y}, t)] \qquad\qquad [\pi(x^-, x_\perp, x^+), \varphi(y^-, y_\perp, x^+)]$$
$$= -i\delta^3(\vec{x} - \vec{y}) \qquad\qquad = -\tfrac{i}{2}\delta(x^- - y^-)\delta^2(\vec{x}_\perp - \vec{y}_\perp)$$

Hamilton operator

$$P^0 = \int d^3 x\, \mathcal{H}(\varphi, \pi) \qquad\qquad P_+ = \int dx^- \int d^2 x_\perp\, \mathcal{H}(\varphi, \pi)$$
$$\mathcal{H} = \pi \partial_0 \varphi - \mathcal{L} \qquad\qquad \mathcal{H} = \pi \partial_+ \varphi - \mathcal{L}$$

Momentum operator

$$\vec{P} = \int d^3 x\, \pi \vec{\nabla} \varphi \qquad\qquad P_- = \int dx^- d^2 x_\perp\, \pi \partial_- \varphi$$
$$\vec{P}_\perp = \int dx^- d^2 x_\perp\, \pi \vec{\partial}_\perp \varphi$$

Eigenvalue equation

$$P^0 |\psi_n\rangle = E_n |\psi_n\rangle \qquad\qquad P_+ |\psi_n\rangle = P_{+n} |\psi_n\rangle$$
$$\vec{P} \text{ fixed} \qquad\qquad P_-, \vec{P}_\perp \text{ fixed}$$

Hadron masses

$$M_n^2 = E_n^2 - \vec{P}^2 \qquad\qquad M_n^2 = 2 P_{+n} P_- - \vec{P}_\perp^2$$

dynamics and can start solving the equations of motion. Typically, one either makes some variational ansatz or a Fock space expansion. In the latter approach one writes the hadron wave function as a sum over components with a fixed number of elementary quanta (for example, in QCD: $q\bar{q}$, $q\bar{q}q\bar{q}$, $q\bar{q}g$, etc.). The expansion coefficients, i.e., the wave functions for the corresponding Fock space sector, are used as variational parameters. They are determined by making the expectation value of the energy stationary with respect to variations in the wave function. Typically the variation is done for fixed momentum.* This whole procedure results in coupled integral equations for the Fock space components. In general they have to be solved numerically. In practical calculations, since one cannot include infinitely many Fock components, one has to introduce some *ad hoc* cutoff in the Fock space. Thus it is very important to demonstrate that physical observables do not depend on how many Fock components are included.

Until one selects the canonically conjugate momenta and postulates equal τ commutation relations, i.e., at the level of the classical Lagrangian, the transition from ET to the LF consists of a mere rewriting. After quantization, the independent degrees of freedom consist of the fields and their conjugate momenta on the initial surface ($x^0 = 0$ for ET and $x^+ = 0$ for LF). Thus different degrees of freedom are employed to expand physical states in the ET and in the LF approach. Of course, after solving the equations of motion, physical observables must not depend on the choice of quantization plane. However, it may turn out that one approach is more efficient (e.g., faster numerical convergence) than the other, or more elegant and more easy to interpret physically. In general, this will of course depend on the details of the interaction. An extreme example is $QCD_{1+1}(N_C \to \infty)$. In the ET approach[22–24] one first has to solve coupled, nonlinear integral equations with a singular kernel to obtain the Hartree–Fock solution for the vacuum. Then, in order to calculate meson masses, one has to solve the two-body equation in this background, which amounts to solving another set of coupled (linear) integral equations with singular kernel. In the LF approach[25,26] all one has to do is solve one linear integral equation with singular kernel. The numerical results for the meson spectrum are in extremely good agreement between the two approaches, but numerically the LF calculation is more than one order of magnitude faster! In this case the simplification arises because the LF vacuum is trivial — a point which will be elaborated in more detail below as well as in Section 3.

Which approach is preferable may, however, also depend on the observ-

_____

*On the LF this is very important because $P_+ \propto 1/P_-$, i.e., unrestricted variation (P_- allowed to vary) results in $P_- \to \infty$.

ables in which one is interested. The most prominent example is deep inelastic scattering. As discussed in the introduction, parton distributions are much more easily accessible on the LF than in usual coordinates.

2.2. ε-Coordinates on Finite Light-Front Intervals

One issue that one may be worried about is the question of equivalence between the LF approach to field theories and other approaches. On the LF one imposes commutation relations at equal LF time, i.e., between two space–time points that are connected by a light-like distance. Thus it is *a priori* not clear whether the initial value problem with initial conditions on a null plane is well defined[27,28]) and whether there arise any conflicts with causality on the LF. The situation becomes particularly worrisome when one introduces a "box" in the longitudinal x^- direction (to keep IR singularities under control) and imposes periodic or quasiperiodic boundary conditions at the ends of the box — i.e., one imposes boundary conditions between points that may be causally related. One way to address this issue in a well defined way is to define the LF via a limiting procedure by starting from a space-like quantization surface and carefully rotating this surface until one has "reached" the LF (note: although there are some similarities, this should not be confused with a Lorentz boost to infinite momentum[15,18]).

In order to be able to control infrared singularities, let us formulate the dynamics on a finite LF interval with extension L in the x^- direction.* On a finite interval, boundary conditions have to be specified, e.g., $\phi(x^- + L, x^+) = \phi(x^-, x^+)$. However, if one is working on the LF, imposing boundary conditions means relating fields at points that are separated by a light-like distance — obviously one may run into trouble with causality at this point. To avoid this dilemma, Lenz *et al.*[29] have introduced ε-coordinates which are defined as follows,†

$$x_\varepsilon^- = x^- \qquad x_\varepsilon^+ = x^+ + \frac{\varepsilon}{L} x^- \tag{2.3}$$

Now points at opposite ends of the interval with coordinates $(x_\varepsilon^- + L, x_\varepsilon^+)$ and $(x_\varepsilon^-, x_\varepsilon^+)$ are separated by a space-like distance $ds^2 = -2\varepsilon L$ and no conflict with causality arises from imposing boundary conditions. In ε-coordinates the scalar product is given by

$$A \cdot B = A_+ B_- + A_- B_+ + 2\frac{\varepsilon}{L} A_+ B_+ \tag{2.4}$$

---

*To simplify the notation, only 1 + 1 dimensional examples will be discussed in this section.
†See also Ref. 30. A slightly different approach, where both x^+ and x^- are rotated away from the light-cone, has been studied in Ref. 31.

and thus the Lagrangian density (for the rest of this section, the subscript ε will be dropped to simplify the notation) for ϕ^4_{1+1} reads

$$\mathcal{L} = \partial_+\phi\left(\partial_-\phi + \frac{\varepsilon}{L}\partial_+\phi\right) - \frac{m^2}{2}\phi^2 - \frac{\lambda}{4!}\phi^4 \tag{2.5}$$

Since $\mathcal{L}$ is quadratic in $\partial_+\phi$, quantization in ε-coordinates is straightforward (as in usual coordinates). One finds[29]

$$\Pi = \frac{\delta\mathcal{L}}{\delta\partial_+\phi} = \partial_-\phi + \frac{2\varepsilon}{L}\partial_+\phi \tag{2.6}$$

$$\left[\Pi(x^-,x^+), \phi(y^-,x^+)\right] = -i\delta(x^- - y^-) \tag{2.7}$$

and

$$H = \int dx^- \frac{L}{4\varepsilon}(\Pi - \partial_-\phi)^2 + \frac{m^2}{2}\phi^2 + \frac{\lambda}{4!}\phi^4 \tag{2.8}$$

In these coordinates, the free dispersion relation $(\lambda = 0)$ is given by

$$p_+(n) = \frac{L}{2\varepsilon}\left(-p_-(n) \pm \sqrt{p_-(n)^2 + \frac{2\varepsilon}{L}m^2}\right) \tag{2.9}$$

where $p_-(n) = 2\pi/nL$ as usual in a box with periodic boundary conditions. Later, we will also need the normal mode expansion of the fields with periodic boundary conditions

$$\phi(x^-) = \sum_n \frac{1}{2\sqrt{\omega_n}}\left[a_n e^{-ip_-(n)x^-} + a_n^\dagger e^{ip_-(n)x^-}\right]$$

$$\Pi(x^-) = \sum_n \frac{-i\sqrt{\omega_n}}{L}\left[a_n e^{-ip_-(n)x^-} - a_n^\dagger e^{ip_-(n)x^-}\right] \tag{2.10}$$

where $\omega_n = L\sqrt{p_-(n)^2 + \frac{2\varepsilon}{L}m^2}$ and the a, $a^\dagger$ satisfy the usual commutation relations, e.g.,

$$\left[a_m, a_n^\dagger\right] = \delta_{m,n} \tag{2.11}$$

The most significant difference between the dispersion relation in ε-coordinates (2.9) and the dispersion relation on the LF $(p_+ = m^2/2p_-)$ is the appearance of two solutions of p_+ for each p_- in ε-coordinates, while the dispersion relation on the LF yields just one solution for each p_- (Fig.
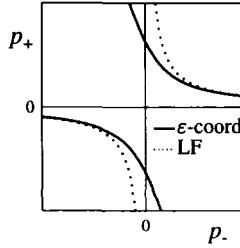
Fig. 2.1. Free dispersion relation in ε-coordinates versus the dispersion relation in the LF limit.

2.1). For positive energy $(p_+ > 0)$ modes, the LF momentum p_- is positive whereas the momentum p_- in ε-coordinates can be both positive and negative. This has importance consequences for the vacuum structure which will be discussed in Section 3.

In the limit $\frac{\varepsilon}{L} \to 0$ (*L* fixed) the LF is recovered:

$$\Pi \overset{\varepsilon/L \to 0}{\longrightarrow} \partial_- \phi \tag{2.12}$$

$$H \overset{\varepsilon/L \to 0}{\longrightarrow} \int dx^- \frac{m^2}{2} \phi^2 + \frac{\lambda}{4!} \phi^4 \tag{2.13}$$

For all nonzero ε, the relation between the momenta and the fields (2.6) contains the time derivative of the fields and the fields are quantized as usual (2.7). However, for $\varepsilon = 0$, Eq. (2.6) becomes a constraint equation, and the Dirac–Bergmann algorithm (see Appendix 7) yields $[\partial_-\phi(x^-, x^+), \phi(y^-, x^+)] = \frac{i}{2}\delta(x^- - y^-)$.

It should be noted that the order of limits does matter, i.e., it is important whether one takes the LF limit $(\frac{\varepsilon}{L} \to 0)$ first or the continuum limit $(L \to \infty)$. This will be discussed in detail in Section 3.

2.3. Examples for Canonical Light-Front Hamiltonians

2.3.1. Scalar Fields

Self-interacting scalar fields in the LF framework have been discussed in Refs. 20 and 21. In order to keep the discussion as general as possible, we will work in $D_\perp$ transverse dimensions, where $D_\perp = 0, 1, 2$. For a

polynomial interaction,*

$$\mathcal{L} = \frac{1}{2}\partial_\mu\phi\partial^\mu\phi - \frac{m^2}{2}\phi^2 - \mathcal{L}^{\text{int}} \tag{2.14}$$

where $\mathcal{L}^{\text{int}}$ is a polynomial in ϕ, the momenta conjugate to ϕ are

$$\Pi = \partial_-\phi \tag{2.15}$$

with commutation relations

$$\left[\Pi(x^-,\vec{x}_\perp,x^+),\phi(y^-,\vec{y}_\perp,x^+)\right] = -\frac{i}{2}\delta(x^- - y^-)\delta(\vec{x}_\perp - \vec{y}_\perp) \tag{2.16}$$

Note that this implies nonlocal commutation relations for the field ϕ, e.g.,

$$\left[\phi(x^-,\vec{x}_\perp,x^+),\phi(y^-,\vec{y}_\perp,x^+)\right] = -\frac{i}{4}\varepsilon(x^- - y^-)\delta(\vec{x}_\perp - \vec{y}_\perp) \tag{2.17}$$

where $\varepsilon(x) = 1$ for $x > 0$ and $\varepsilon(x) = -1$ for $x < 0$. The hamiltonian density $(P_+ = \int dx^- d^{D\perp}x_\perp \mathcal{H})$ is obtained from Eq. (2.14) via a Legendre transformation

$$\mathcal{H} = \Pi\partial_+\phi - \mathcal{L}$$
$$= \frac{1}{2}\left(\vec{\nabla}_\perp\phi\right)^2 + \frac{m^2}{2}\phi^2 + \mathcal{L}^{\text{int}} \tag{2.18}$$

The commutation relations (2.16) are easily satisfied if we make a mode expansion

$$\phi(x) = \int_0^\infty \frac{dk_-}{\sqrt{4\pi k_-}} \int \frac{d^{D\perp}k_\perp}{(2\pi)^{D\perp/2}} \left[a_{k_-\vec{k}_\perp} e^{-ikx} + a^\dagger_{k_-\vec{k}_\perp} e^{ikx}\right] \tag{2.19}$$

where $a_{k_-\vec{k}_\perp}$, $a^\dagger_{k_-\vec{k}_\perp}$ satisfy the usual boson commutation relations, e.g.,

$$\left[a_{k_-\vec{k}_\perp}, a^\dagger_{q_-\vec{q}_\perp}\right] = \delta(k_- - q_-)\delta(\vec{k}_\perp - \vec{q}_\perp) \tag{2.20}$$

Longitudinal and transverse momentum operators contain no interaction terms

$$P_- = \int dx^- d^{D\perp}x_\perp \Pi\partial_-\phi = \int_0^\infty dk_- \int d^{D\perp}k_\perp k_- a^\dagger_{k_-\vec{k}_\perp} a_{k_-\vec{k}_\perp}$$

$$\vec{P}_\perp = \int dx^- d^{D\perp}x_\perp \Pi\vec{\nabla}_\perp\phi = \int_0^\infty dk_- \int d^{D\perp}k_\perp \vec{k}_\perp a^\dagger_{k_-\vec{k}_\perp} a_{k_-\vec{k}_\perp} \tag{2.21}$$

---

*In $3 + 1$ dimensions, renormalizability restricts the interaction to 4th order polynomials, but in $2 + 1$ or $1 + 1$ dimensions higher order polynomials are conceivable (6th order and ∞ order, respectively).

where normal ordering terms have been dropped. Most of the numerical studies of self-interacting scalar fields have been done in $1 + 1$ dimensions[32,33] using discrete light-cone quantization (Section 5.1). A more recent work employs Monte Carlo techniques to solve ϕ^4-theory in $2 + 1$ dimensions.[34]

Complex scalar fields can always be reduced to real scalar fields by working in a Cartesian basis $\Phi = \frac{1}{\sqrt{2}} (\phi_1 + i\phi_2)$ and thus need not be discussed here.

2.3.2. Fermions with Yukawa Interactions

To keep the discussion as general as possible we assume an interaction of the form $\bar\psi\Gamma\psi\phi$, where ϕ is either scalar or pseudo-scalar and Γ is either 1 or $i\gamma_5$,

$$\mathcal{L} = \bar\psi \left(i\ \not\partial - M - g\Gamma\phi\right)\psi + \frac{1}{2}\left(\partial_\mu\phi\partial^\mu\phi - m^2\phi^2\right) \qquad (2.22)$$

One novel feature compared to normal coordinates and compared to self-interacting scalar fields on the LF is the fact that not all components of ψ are independent dynamical degrees of freedom. To see this, let us introduce projection matrices $\mathcal{P}^{(\pm)} = \frac{1}{2}\gamma^\mp\gamma^\pm$ where $\gamma^\pm = \left(\gamma^0 \pm \gamma^3\right)/\sqrt{2}$. Note that $\gamma^+\gamma^+ = \gamma^-\gamma^- = 0$ implies $\mathcal{P}^{(+)}\mathcal{P}^{(-)} = \mathcal{P}^{(-)}\mathcal{P}^{(+)} = 0$. These projection matrices can be used to decompose the fermion spinors into dynamical and nondynamical components $\psi = \psi_{(+)} + \psi_{(-)}$, where $\psi_{(\pm)} \equiv \mathcal{P}^{(\pm)}\psi$. The Lagrangian does not contain a LF-time derivative (∂_+) of $\psi_{(-)}$

$$\mathcal{L} = \sqrt{2}\psi_{(+)}^\dagger i\partial_+\psi_{(+)} + \sqrt{2}\psi_{(-)}^\dagger i\partial_-\psi_{(-)} - \psi_{(+)}^\dagger \left(i\vec\alpha_\perp\vec\partial_\perp + \gamma^0\mathcal{M}\right)\psi_{(-)}$$

$$-\psi_{(-)}^\dagger \left(i\vec\alpha_\perp\vec\partial_\perp + \gamma^0\mathcal{M}\right)\psi_{(+)} + \frac{1}{2}\left(\partial_\mu\phi\partial^\mu\phi - m^2\phi^2\right) \qquad (2.23)$$

where $\vec\alpha_\perp = \gamma^0\vec\gamma_\perp$ and $\mathcal{M}(x) = M + g\Gamma\phi(x)$. Thus the Euler-Lagrange equation for $\psi_{(-)}$ is a constraint equation

$$\sqrt{2}i\partial_-\psi_{(-)} = \left(i\vec\alpha_\perp\vec\partial_\perp + \gamma^0\mathcal{M}\right)\psi_{(+)} \qquad (2.24)$$

It is therefore necessary to eliminate the dependent degrees of freedom ($\psi_{(-)}$) before quantizing the theory. Here we proceed by solving Eq. (2.24) and

inserting the solution back in the Lagrangian (2.23), yielding[21]*

$$
\mathcal{L}_{(+)} = \sqrt{2}\psi^{\dagger}_{(+)}\partial_+\psi_{(+)} + \frac{1}{2}\left(\partial_\mu\phi\partial^\mu\phi - m^2\phi^2\right)
$$
$$
- \frac{1}{\sqrt{2}}\psi^{\dagger}_{(+)}\left(i\vec{\alpha}_\perp\vec{\partial}_\perp + \gamma^0\mathcal{M}\right)\frac{1}{i\partial_-}\left(i\vec{\alpha}_\perp\vec{\partial}_\perp + \gamma^0\mathcal{M}\right)\psi_{(+)} \quad (2.25)
$$

The ambiguities associated with the inversion of the differential operator will be discussed in Section 3.2.2. Here we just define

$$
\left(\frac{1}{\partial_-}f\right)(x^-,\vec{x}_\perp) = \frac{1}{2}\int_{-\infty}^{\infty}dy^-\,\epsilon(x^- - y^-)f(y^-,\vec{x}_\perp) \quad (2.26)
$$

The rest of the quantization procedure is now straightforward. The hamiltonian is given by

$$
P^- = \int dx^- d^{D_\perp}x_\perp \mathcal{H} \quad (2.27)
$$

where

$$
\mathcal{H} = \frac{1}{\sqrt{2}}\psi^{\dagger}_{(+)}\left(i\vec{\alpha}_\perp\vec{\partial}_\perp + \gamma^0\mathcal{M}\right)\frac{1}{i\partial_-}\left(i\vec{\alpha}_\perp\vec{\partial}_\perp + \gamma^0\mathcal{M}\right)\psi_{(+)}
$$
$$
+ \frac{1}{2}\left[\left(\vec{\nabla}_\perp\phi\right)^2 + m^2\phi^2\right] \quad (2.28)
$$

Note that Eq. (2.28) contains four-point interactions of the form

$$
\psi^{\dagger}_{(+)}\phi\,(i\partial_-)^{-1}\,\phi\psi_{(+)}
$$

which were not present in the original Lagrangian (2.22). Note also that the fermion mass M enters the hamiltonian density (2.28) in two different places: in the kinetic term for the dynamical fermion field, $\mathcal{H}_{\text{kin}} \propto M^2\psi^{\dagger}_{(+)}(i\partial_-)^{-1}\psi_{(+)}$, as well as in the three-point vertex, $Mg\psi^{\dagger}_{(+)}(i\partial_-)^{-1}\Gamma\phi\psi_{(+)} + h.c.$ In Section 4 we will find that, in general, these two masses are renormalized differently.

The scalar field ϕ is quantized as in Section (2.3.1). For the fermions, one imposes anti-commutation relations only for the independent component $\psi_{(+)}$[21]

$$
\left\{\psi_{(+)}(x),\psi^{\dagger}_{(+)}(y)\right\}_{x^+=y^+} = \frac{1}{\sqrt{2}}\mathcal{P}^{(+)}\delta(x^- - y^-)\delta(\vec{x}_\perp - \vec{y}_\perp) \quad (2.29)
$$

---

*Another option would be to use Dirac–Bergmann quantization (Appendix 7). Up to possible differences in the zero-mode sector, the result is the same.

with $\left\{ \psi^{\dagger}_{(+)}(x), \psi^{\dagger}_{(+)}(y) \right\}_{x^+=y^+}$ and $\left\{ \psi_{(+)}(x), \psi_{(+)}(y) \right\}_{x^+=y^+}$ both vanishing.

For practical calculations it is very useful to make a mode expansion. Let $u(p,s)$ and $v(p,s)$ be the usual particle and antiparticle spinors, satisfying $(\not{p} - M) u(p,s) = 0$ and $(\not{p} + M) v(p,s) = 0$, where s labels the spin. The normalization is fixed such that

$$\sqrt{2} u^{\dagger}_{(+)}(p,s') u_{(+)}(p,s) = \bar{u}(p,s') \gamma_- u(p,s) = 2p_- \delta_{ss'}$$
$$\sqrt{2} v^{\dagger}_{(+)}(p,s') v_{(+)}(p,s) = \bar{v}(p,s') \gamma_- v(p,s) = 2p_- \delta_{ss'} \qquad (2.30)$$

For $\psi_{(+)}$ we make a plane wave ansatz

$$\psi_{(+)}(x) = \int \frac{d^{D_\perp} p_\perp}{(2\pi)^{D_\perp/2}} \int_0^\infty \frac{dp_-}{\sqrt{4\pi p_-}} \qquad (2.31)$$
$$\times \sum_s \left[b_{p_- \vec{p}_\perp s} u_{(+)}(p,s) e^{-ipx} + d^{\dagger}_{p_- \vec{p}_\perp s} v_{(+)}(p,s) e^{ipx} \right]$$

One can easily verify that $\psi_{(+)}$ in Eq. (2.32) satisfies the anti-commutation relations above (2.29), provided

$$\left\{ b^{\dagger}_{p_- \vec{p}_\perp r}, b_{q_- \vec{q}_\perp s} \right\} = \delta(p_- - q_-)\delta(\vec{p}_\perp - \vec{q}_\perp)\delta_{rs}$$
$$\left\{ d^{\dagger}_{p_- \vec{p}_\perp r}, d_{q_- \vec{q}_\perp s} \right\} = \delta(p_- - q_-)\delta(\vec{p}_\perp - \vec{q}_\perp)\delta_{rs} \qquad (2.32)$$

with all other anti-commutators vanishing.

Nonperturbative numerical works on the LF hamiltonian with Yukawa interactions (2.28) have been restricted to DLCQ calculations in $1 + 1$ dimensions[35] as well as to $1 + 1$ dimensional,[36] $3 + 1$ dimensional[37] calculations which use Tamm–Dancoff truncations to fermion and at most two bosons or fermion, antifermion and at most one boson.

2.3.3.   QED and QCD

Before one can canonically quantize a gauge field theory, one must fix the gauge — otherwise one has to deal with the infinite degeneracy associated with the gauge symmetry.

In the context of LF quantization one usually picks the LF gauge $A^+ = A_- = 0$. There are several (related) reasons for this choice. In QED, the constraint equation for the "bad" spinor component reads

$$\sqrt{2} i D_- \psi_{(-)} \equiv \sqrt{2} \left(i\partial_- - eA_- \right) \psi_{(-)} = \left(i\vec{\alpha}_\perp \vec{D}_\perp + \gamma^0 M \right) \psi_{(+)} \qquad (2.33)$$

The solution to this constraint equation,

$$\psi_{(-)} = \frac{1}{\sqrt{2}} \left(i\partial_- - eA_- \right)^{-1} \left(i\vec{\alpha}_\perp \vec{D}_\perp + \gamma^0 M \right) \psi_{(+)} \qquad (2.34)$$

contains A_- in the denominator and, unless one chooses $A_- = 0$ gauge, one thus obtains terms which have A_- in the denominator in the LF hamiltonian. In other words, in any gauge other than the LF gauge the canonical LF hamiltonian always contains all powers of A_- (after expanding the geometric series) appearing in the interactions.

In QCD one faces the additional problem that $\vec{\Pi}_\perp$, the momentum conjugate to $\vec{A}_\perp$, satisfies a nonlinear constraint equation if $A_- \neq 0$ (Section 3.2.3). Another reason to pick LF gauge is that $A_- = 0$ is invariant under the kinematic Lorentz symmetries of the LF, i.e., under all transformations that leave the plane $x^+ = 0$ invariant. It is for these reasons that the LF gauge has been commonly used for canonical LF quantization of gauge field theories, and will also be used here — despite all the difficulties which are inherent to the LF and axial gauges.[38–43]

Even after fixing the gauge, not all degrees of freedom are dynamical (similar to $\psi_{(-)}$, their time derivative does not enter the Lagrangian). Before we can proceed with the canonical quantization we first have to eliminate these dependent variables by solving those equations of motion which are constraint equations. For $\psi_{(-)}$ we use Eq. (2.34) (note: $A_- = 0$) and proceed similar to the example of the Yukawa theory. Since the time derivative of A_+ does not enter the Lagrangian, A_+ has to be eliminated as well, by solving its constraint equation (obtained by varying the Lagrangian density with respect to A_+)

$$\partial_-^2 A_+ = \partial_- \vec{\nabla}_\perp \vec{A}_\perp - j^+ \qquad (2.35)$$

where $j^+ = \sqrt{2} e \psi_{(+)}^\dagger \psi_{(+)}$, in QED and

$$\partial_-^2 A_{+a} = \partial_- \vec{\nabla}_\perp \vec{A}_{\perp a} + g f^{abc} \vec{A}_{\perp b} \partial_- \vec{A}_{\perp c} - j_a^+ \qquad (2.36)$$

where $j_a^+ = \sqrt{2} g \psi_{(+)\alpha}^\dagger \psi_{(+)\beta} \frac{\lambda_a^{\alpha\beta}}{2}$, in QCD. After inserting A_+ back into the Lagrangian one can proceed with the quantization as usual. One finds

$$\mathcal{H}_{\text{QED}} = \frac{1}{\sqrt{2}} \psi_{(+)}^\dagger \left(i\vec{\alpha}_\perp \vec{D}_\perp + \gamma^0 M \right) \frac{1}{i\partial_-} \left(i\vec{\alpha}_\perp \vec{D}_\perp + \gamma^0 M \right) \psi_{(+)}$$
$$- \frac{1}{2} \left(\partial_- \vec{\nabla}_\perp \vec{A}_\perp - j^+ \right) \frac{1}{\partial_-^2} \left(\partial_- \vec{\nabla}_\perp \vec{A}_\perp - j^+ \right) \qquad (2.37)$$

and

$$\mathcal{H}_{\mathrm{QCD}} = \frac{1}{\sqrt{2}} \psi^{\dagger}_{(+)} \left(i \vec{\alpha}_{\perp} \vec{D}_{\perp} + \gamma^0 M \right) \frac{1}{i \partial_-} \left(i \vec{\alpha}_{\perp} \vec{D}_{\perp} + \gamma^0 M \right) \psi_{(+)}$$

$$- \frac{1}{2} \left(\vec{D}_{\perp} \partial_- \vec{A}_{\perp a} - j_a^+ \right) \frac{1}{\partial_-^2} \left(\vec{D}_{\perp} \partial_- \vec{A}_{\perp a} - j_a^+ \right) \qquad (2.38)$$

where $\vec{D}_{\perp} \partial_- \vec{A}_{\perp a} = \vec{\nabla}_{\perp} \partial_- \vec{A}_{\perp a} + g f^{abc} \vec{A}_{\perp b} \partial_- \vec{A}_{\perp c}$. The commutation relations are similar to the ones in Yukawa theory

$$\mathrm{QED:} \left\{ \psi_{(+)}(x), \psi^{\dagger}_{(+)}(y) \right\}_{x^+ = y^+} = \frac{1}{\sqrt{2}} \mathcal{P}^{(+)} \delta(x^- - y^-) \delta(\vec{x}_{\perp} - \vec{y}_{\perp})$$

$$[\partial_- A_{\perp i}(x), A_{\perp j}(y)]_{x^+ = y^+} = -\frac{i}{2} \delta(x^- - y^-) \delta(\vec{x}_{\perp} - \vec{y}_{\perp}) \delta_{ij}$$

$$\mathrm{QCD:} \left\{ \psi_{(+)\alpha}(x), \psi^{\dagger}_{(+)\beta}(y) \right\}_{x^+ = y^+} = \frac{1}{\sqrt{2}} \mathcal{P}^{(+)} \delta(x^- - y^-) \delta(\vec{x}_{\perp} - \vec{y}_{\perp}) \delta_{\alpha\beta}$$

$$[\partial_- A_{\perp ai}(x), A_{\perp bj}(y)]_{x^+ = y^+} = -\frac{i}{2} \delta(x^- - y^-) \delta(\vec{x}_{\perp} - \vec{y}_{\perp}) \delta_{ij} \delta_{ab}$$

Similar to the approach to scalar field theories and Yukawa theories, one may now attempt to solve the above hamiltonians by making a mode expansion and using matrix diagonalization. In $1 + 1$ dimension this method was very successful.[44–49] In $3 + 1$ dimensions, this approach suffers from a fundamental problem*: charged particles are subject to a linear, confining interaction — which is present even in $\mathcal{H}_{\mathrm{QED}}$. For gauge invariant amplitudes (all intermediate states included, which contribute to a given order of the coupling) this linear potential is canceled by infrared singular couplings of charges to the ⊥-components of the gauge field. However, in most practical calculations, drastic truncations of the Fock space are used to keep the dimension of the hamiltonian matrix within practical limits.[50,51] This approximation results in incomplete cancellations of IR singularities and IR divergences result. Partly responsible for this disaster is an improper treatment of zero modes and incomplete gauge fixing. If one integrates the Maxwell equation for $F^{\mu+}$ over x^- one finds[52]

$$-\vec{\partial}_{\perp}^2 \int dx^- A_-(x^+, x^-, x_{\perp}) = \int dx^- j^+(x^+, x^-, x_{\perp}) \qquad (2.39)$$

i.e., in general, when $\int dx^- j^+(x^+, x^-, x_{\perp}) \neq 0$, the "gauge" $A_- = 0$ is inconsistent with the equations of motion. On a finite interval, with periodic boundary condition, this becomes clearer because then a Wilson loop

---

*Besides numerical difficulties which will be discussed in Section 5.1.

"around the torus," $\exp\left(ie \oint dx^- A_-(x^+, x^-, x_\perp)\right)$, is a gauge invariant quantity. The closest one can get to the LF gauge is $\partial_- A_- = 0$. In this gauge one can now investigate the problem of incomplete gauge fixing. The gauge $\partial_- A_- = 0$ still leaves the freedom of x^--independent gauge transformations $A_\mu \to A'_\mu = A_\mu + \partial_\mu \chi$ where $\partial_-^2 \chi = 0$ (or $\partial_- \chi = 0$ if we restrict ourselves to periodic χ).[52] In such an incompletely gauge fixed situation, not all degrees of freedom are physical and approximations may result in inconsistencies. A typical example is the residual or transverse Gauss' law (2.39), which is a constraint on the physical Hilbert space. Such constraints must either be imposed on the states or one can also use them to eliminate "unphysical" degrees of freedom (here $\partial_\perp^2 \int dx^- A^+$). The above-mentioned, incomplete cancellation of IR singularities in the Tamm–Dancoff approximation occurs because the transverse Gauss' law (2.39) is violated. A more thorough discussion on this subject and possible caveats can be found in Refs. 41 and 52.
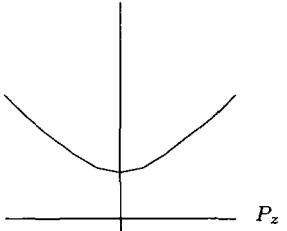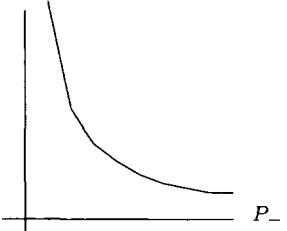
3. THE LIGHT-FRONT VACUUM

3.1. The Physical Picture

In the Fock space expansion one starts from the vacuum as the ground state and constructs physical hadrons by successive application of creation operators. In an interacting theory the vacuum is in general an extremely complicated state and not known *a priori*. Thus, in general, a Fock space expansion is not practical because one does not know the physical vacuum (i.e., the ground state of the hamiltonian). In normal coordinates, particularly in the hamiltonian formulation, this is a serious obstacle for numerical calculations. As is illustrated in Table 3.1, the LF formulation provides a dramatic simplification at this point.

While all components of the momentum in normal coordinates can be positive as well as negative, the longitudinal LF momentum P_- is always positive. In free field theory (in normal coordinates as well as on the LF) the vacuum is the state which is annihilated by all annihilation operators a_k. In general, in an interacting theory, excited states (excited with respect to the free hamiltonian) mix with the trivial vacuum (i.e., the free field theory vacuum) state resulting in a complicated physical vacuum. Of course, there are certain selection rules and only states with the same quantum numbers as the trivial vacuum can mix with this state; for example, states with the same momentum as the free vacuum ($\vec{P} = 0$ in normal coordinates, $P_- = 0$, $\vec{P}_\perp = 0$ on the LF). In normal coordinates this has no deep consequences

TABLE 3.1

Zero Modes and the Vacuum

Normal coordinates	Light front

Free theory

$$P^0 = \sqrt{m^2 + \vec{P}^2}$$
$$P_+ = \frac{m^2 + \vec{P}_\perp^2}{2P_-}$$

$$P^0 = \sum_{\vec{k}} a_{\vec{k}}^\dagger a_{\vec{k}} \sqrt{m^2 + \vec{k}^2}$$
$$P_+ = \sum_{k_-, \vec{k}_\perp} a_{k_-, \vec{k}_\perp}^\dagger a_{k_-, \vec{k}_\perp} \frac{m^2 + \vec{k}_\perp^2}{2k_-}$$

Vacuum (free theory)

$$a_{\vec{k}}|0\rangle = 0$$
$$a_{k_-, k_\perp}|0\rangle = 0$$

Vacuum (interacting theory)

many states with $\vec{P} = 0$	$k_- \geq 0$
(e. g. $a_{\vec{k}}^\dagger a_{-\vec{k}}^\dagger |0\rangle$)	$\hookrightarrow$ only pure zero-mode excitations have $P_- = 0$
$\hookrightarrow |\tilde{0}\rangle$ very complex	$\hookrightarrow |\tilde{0}\rangle$ can only contain zero-mode excitations

because there are many excited states which have zero momentum. On the LF the situation is completely different. Except for pure zero-mode excitations, i.e., states where only the zero mode (the mode with $k_- = 0$) is excited, all excited states have positive longitudinal momentum P_-. Thus only these pure zero-mode excitations can mix with the trivial LF vacuum. Thus with the exception of the zero modes the physical LF vacuum (i.e., the ground state) of an interacting field theory must be trivial.*

Of course, this cannot mean that the vacuum is entirely trivial. Otherwise it seems impossible to describe many interesting problems which are related to spontaneous symmetry breaking within the LF formalism. For example, one knows that chiral symmetry is spontaneously broken in QCD and that this is responsible for the relatively small mass of the pions — which play

---

*Cases where the LF hamiltonian has no ground state will be discussed below.

an important role in strong interaction phenomena at low energies. What it means is that one has reduced the problem of finding the LF vacuum to the problem of understanding the dynamics of these zero modes.

First this sounds just like merely shifting the problem about the structure of the vacuum from nonzero modes to zero modes. However, as the free dispersion relation on the LF,

$$k_+ = \frac{m^2 + \vec{k}_\perp^2}{2k_-} \tag{3.1}$$

indicates, zero modes are high energy modes! Hence it should, at least in principle, be possible to eliminate these zero modes systematically giving rise to an effective LF field theory.[29]

Before we embark on theoretically analyzing zero modes, it should be emphasized that zero modes may have experimentally measurable implications. This is discussed in Refs. 53 and 54.

3.2. Examples for Zero Modes

Usually, in the context of LF quantization, fields that do not depend on x^- are called zero modes (regardless of whether they depend on $\vec{x}_\perp$ or not). However, for practical purposes, the following classification scheme seems to be particularly useful[52]: If one denotes

$$\langle f \rangle_o \equiv \frac{1}{2L} \int_{-L}^{L} dx^- f(x^-, \vec{x}_\perp) \tag{3.2}$$

then

$$\langle f \rangle \equiv \frac{1}{(2L_\perp)^2} \int d^2 x_\perp \langle f \rangle_o = \frac{1}{2L(2L_\perp)^2} \int d^2 x_\perp \int_{-L}^{L} dx^- f(x^-, \vec{x}_\perp) \tag{3.3}$$

is called the *global zero mode,* while

$$\overset{o}{f} \equiv \langle f \rangle_o - \langle f \rangle \tag{3.4}$$

is called the *proper zero mode.* The "rest," i.e.,

$$\overset{n}{f} \equiv f - \langle f \rangle_0 \tag{3.5}$$

is called the *normal mode* part of f. The motivation for this distinction arises primarily from the fact that usually only the global zero mode can develop a

vacuum expectation value, but also since proper and global zero modes have very different dynamics.

Zero modes occur in various contexts and it is not yet entirely clear to what extent the various zero-mode effects, which will be discussed below, are connected.

3.2.1. Constant Scalar Fields

In ϕ^4 theory

$$\mathcal{L} = \frac{1}{2}\partial_\mu\phi\partial^\mu\phi - \frac{m^2}{2}\phi^2 - \frac{\lambda}{4!}\phi^4 \tag{3.6}$$

if one chooses the "wrong" sign for the mass $(m^2 < 0, \lambda > 0)$, spontaneous symmetry breaking occurs already at the classical level. The field ϕ develops a vacuum expectation value and the symmetry $\phi \to -\phi$ is spontaneously broken. At least in $1 + 1$ and $2 + 1$ dimensions, with appropriate values for the renormalized mass, a similar behavior is observed in the quantum version. Clearly, such a scenario requires a zero mode. In the case of ϕ^4 theory, one may imagine that a redefinition

$$\phi \to \tilde{\phi} + \langle 0|\phi|0\rangle \tag{3.7}$$

eliminates the VEV of the global zero mode.[32] However, this does not mean that one has eliminated the zero modes. In fact, by integrating the equations of motion over x^-, one finds

$$0 = m^2\langle\phi\rangle + \frac{\lambda}{3!}\frac{1}{2L}\int_{-L}^{L}dx^-\phi^3 \tag{3.8}$$

which relates the zero-mode part of the field to the normal-mode part. Clearly, this nonlinear operator identity implies that (for finite L) a mere shift of the scalar field is not sufficient to completely eliminate the zero mode. Instead, two main classes of approaches are being used to get the zero modes under control. In DLCQ one attempts to solve the zero-mode constraint equation [Eq. (3.8)] using various approximation or expansion schemes.[55–57] Due to nonlinear effects and operator ordering ambiguities, solving Eq. (3.8) becomes a nontrivial endeavor.[55–59] In the other approach (the effective LF hamiltonian approach, which will be discussed in detail in Section 3.3) one makes use of the fact that zero modes freeze out for $L \to \infty$. Instead of keeping zero modes explicitly, one allows for an effective hamiltonian, which should account for their effects on normal modes in the large volume limit.[33]

So far it is not known whether either one of these approaches to LF quantization (explicit zero modes and effective LF hamiltonian) leads to a consistent formulation of ϕ^4 theory in the broken phase. It is also not known to what extent the particle spectrum in the equal time formulation agrees with the spectrum on the LF. Since the broken phase of ϕ^4 in $1+1$ dimensions has a rather rich spectrum: mesons, solitons,[*] bound states and scattering states in the soliton-antisoliton sector,[†] this seems to be an ideal test case for the various approaches to scalar zero modes on the LF. So far, all works dealing with ϕ^4 on the LF have concentrated on demonstrating that spontaneous symmetry breaking occurs and on reproducing the numerical value of the critical coupling constant from ET quantization.[‡]

One of the most striking consequences of spontaneous symmetry breaking in ϕ^4_{1+1} is the emergence of solitons. While most LF workers choose boundary conditions that make it impossible to study solitons, soliton-antisoliton scattering states are often still possible. These states often have a very clear signature[(33)] and one can easily determine their threshold. Considering the extensive literature on LF ϕ^4_{1+1} (see, e.g., Refs. 55-57 and references cited therein), it is surprising that solitons have been ignored so far.

3.2.2. Fermionic Zero Modes

Consider the free Dirac equation

$$0 = \left(i\gamma_\mu \partial^\mu - M\right)\psi = \left(i\gamma_- \partial_+ + i\gamma_+ \partial_- - i\vec{\gamma}_\perp \vec{\partial}_\perp - M\right)\psi \quad (3.9)$$

Multiplying Eq. (3.9) with $\mathcal{P}^{(+)}$, where $\mathcal{P}^{(\pm)} = \gamma^\mp \gamma^\pm / 2$ are the projection matrices introduced in Section 2.3.2, one obtains

$$i\gamma^- \partial_- \psi^{(-)} = \left(i\vec{\gamma}_\perp \vec{\partial}_\perp + M\right)\psi^{(+)} \quad (3.10)$$

with $\psi^{(\pm)} = \mathcal{P}^{(\pm)}\psi$. Clearly Eq. (3.10) is a constraint equation and one must eliminate $\psi^{(-)}$ before one can canonically quantize the theory (the kinetic term in the fermionic Lagrangian does not contain a LF-time derivative of $\psi^{(-)}$). For all modes but the zero modes this is straightforward. However, Eq. (3.10) does not determine the x^--independent components of $\psi^{(-)}$. In other words, because of possible "integration constants," there is some ambiguity in defining the inverse of the differential operator ∂_-.

---

[*]Often excluded by boundary conditions on the fields,

[†]In general not excluded by boundary conditions.

[‡]In view of the nontrivial renormalization effects on the LF (see Section 4), comparing critical coupling constants on the LF with those from ET quantization is very treacherous.

For scalar fields, the time derivative is always accompanied by a space derivative (kinetic term: $\phi\partial_+\partial_-\phi$). Therefore, the zero mode for scalar fields is not a dynamical degree of freedom, since its time derivative does not enter the Lagrangian. For Dirac fields this is different, since there the Lagrangian is linear in the derivatives, and the fermionic zero mode is a dynamical degree of freedom. Little is known in this case beyond perturbation theory (see, e.g., Refs. 28 and 60).

3.2.3. Gauge Field Zero Modes

For practical reasons one would like to work in the LF gauge $A_- = 0$ when quantizing gauge fields on the LF. The reason is that, only in the LF gauge are canonical field momenta simple. For example, in QCD, the kinetic term for the gauge field in the Lagrangian, $-\frac{1}{4}F_{\mu\nu}F^{\mu\nu}$ contains terms like $\left[D_+, \vec{A}_\perp\right]\left[D_-, \vec{A}_\perp\right]$, i.e., in general, the term multiplying $\partial_+\vec{A}_\perp$ contains interactions. As usual in LF coordinates, the canonically conjugate momentum satisfies a constraint equation

$$\vec{\Pi}_\perp = \frac{\delta\mathcal{L}}{\delta\partial_+\vec{A}_\perp} = \partial_-\vec{A}_\perp - ig\left[A_-, \vec{A}_\perp\right] \qquad (3.11)$$

Only in the LF gauge is the constraint equation for $\vec{\Pi}_\perp$ linear in the fields, and one obtains simple commutation relations between the fields.

The problem with the LF gauge, as with axial gauges in general, has to do with infrared singularities, particularly in the nonabelian case. In order to arrive at a well defined formulation of the theory, it is often very helpful to formulate the theory in a finite 'box' with periodic boundary conditions (i.e., a torus). That way, it is generally easier to keep track of surface terms that appear in formal manipulations which include integrations by parts.

If one starts from an arbitrary gauge field configuration on a torus, it is in general not possible to reach the LF gauge (or spatial axial gauges) by means of a gauge transformation.[52,61] This can be easily shown by considering the Wilson loop around the torus in the x^- direction: $W = P\exp(ig\oint dx^- A_-)$. This is a gauge invariant quantity and thus does not change under a gauge transformation. If it were possible to reach the LF gauge, $A_- = 0$, by means of a gauge transformation this would mean transforming W to 1, which is a contradiction. It turns out that on a torus, the closest one can get to the LF gauge is $\partial_- A_- = 0$, i.e., the zero modes for A_- remain and, due to their relation to the Wilson loop around the torus, they have a gauge invariant meaning.[52] They are dynamical degrees of freedom (their ∂_+ derivative enters the Lagrangian). The zero modes of a^i behave very similar to a scalar

field, in the sense that their time derivative does not enter the Lagrangian and hence they are not dynamical degrees of freedom. Recently, Kalloniatis, Robertson, and collaborators[52] have developed a systematic scheme to disentangle and resolve the various zero-mode problems that appear in QED and QCD. For example, projecting the QED Maxwell equations onto the proper zero-mode sector, they obtain

$$-\partial_\perp^2 \, \overset{o}{A}{}^+ = g \, \overset{o}{J}{}^+ \tag{3.12}$$

$$-2\partial_+^2 \, \overset{o}{A}{}^- - \partial_\perp^2 \, \overset{o}{A}{}^- - 2\partial_i\partial_+ \, \overset{o}{A}{}^i = g\partial_\perp^2 \, \overset{o}{J}{}^- \tag{3.13}$$

$$-\partial_\perp^2 \, \overset{o}{A}{}^+ + \partial_i\partial_+ \, \overset{o}{A}{}^+ + \partial_i\partial_j \, \overset{o}{A}{}^j = g\partial_\perp^2 \, \overset{o}{J}{}^j \tag{3.14}$$

where J^μ is the fermionic current operator. The first of these equations (3.12) is a constraint equation and can be used to eliminate the proper zero mode of A^+ in terms of the current J^+*

$$\overset{o}{A}{}^+ = -g\frac{1}{\partial_\perp^2} \, \overset{o}{J}{}^+ \tag{3.15}$$

which again demonstrates that $A^+ = 0$ is in general not consistent with the equations of motion.

Further simplification can be obtained by taking the (transverse) divergence of Eq. (3.14), yielding

$$\partial_+ \, \overset{o}{A}{}^+ = g\frac{1}{\partial_\perp^2}\partial_i \, \overset{o}{J}{}^i \tag{3.16}$$

Inserting this back into Eq. (3.14), one finds

$$-\partial_\perp^2 \left(\delta_{ij} - \frac{\partial_i\partial_j}{\partial_\perp^2}\right) \overset{o}{A}{}^j = g \left(\delta_{ij} - \frac{\partial_i\partial_j}{\partial_\perp^2}\right) \overset{o}{J}{}^j \tag{3.17}$$

which can be used to eliminate the transverse projection of the proper zero mode of A^j. Note that so far we have not yet completely fixed the gauge, since $\partial_- A^+$ sill leaves the freedom of purely transverse gauge transformations, $A^\mu \to A^\mu + \partial^\mu\Omega$, where $\Omega = \Omega(x^+, x_\perp)$. One can use this residual gauge freedom to set $\partial_i \, \overset{o}{A}{}^i = 0$. In combination with Eq. (3.17), this completely determines the proper zero mode of A^i. Up to this point, it seems that the zero modes in QED pose no real problems in the LF formulation.

---

*In the charge neutral sector, the global zero mode of J^+ vanishes and thus the inverse Laplace is well defined.

The real problems in this formalism arise when one tries to implement these results in a quantum formulation that includes fermions. This can be seen when one inserts the solution for $\int dx^- A_-$ back into the Lagrangian, yielding a four Fermi interaction term of the form

$$\Delta\mathcal{L} \propto \frac{1}{2L} \, \overset{o}{J}{}^+ \, \frac{1}{\partial_\perp^2} \, \overset{o}{J}{}^- \tag{3.18}$$

Similarly, inserting the solution for $\overset{o}{A}{}^i$ into the Lagrangian yields

$$\Delta\mathcal{L} \propto \frac{1}{2L} \, \overset{o}{J}{}^i \, \frac{\delta_{ij} - \frac{\partial_i \partial_j}{\partial_\perp^2}}{\partial_\perp^2} \, \overset{o}{J}{}^j \tag{3.19}$$

The presence of such terms, which contain the "bad" current $j_+ = \sqrt{2}e\psi_{(-)}^\dagger \psi_{(-)}$, leads to nonlinear constraint equations for $\psi_{(-)}$. Because of the difficulties in solving this nonlinear constraint equation, it has so far not been possible to write down the LF hamiltonian for QED or QCD in terms of physical degrees of freedom and including all zero modes, in closed form. Only perturbative expressions for the hamiltonian in terms of physical degrees of freedom have been found so far.[52] Similar problems arise in the DLCQ formulation of QCD with additional complications arising from the difficulties in quantizing the gauge field when $A^+ \neq 0$, arising from the nonlinear constraint relation between fields and their canonical momenta (3.11).

From the practitioner's viewpoint, it would be helpful to know to what extent this elaborate machinery is actually necessary if one is interested only in the large volume limit. On a finite interval, gauge field zero modes clearly play an important role. For example, they are essential to generate the correct potential for a heavy quark–antiquark pair in $1 + 1$ dimensions on a circle in Coulomb gauge.[62,63] However, in the latter example, zero-mode effects for color singlet states disappear in the limit of a large interval. Unfortunately, it is not clear whether this result carries through to higher-dimensional gauge theories.

3.2.4. Perturbative Zero Modes

The zero modes discussed are either connected to purely nonperturbative effects (like in the case of spontaneous symmetry breaking for scalar fields) or seem to be at least connected with nonperturbative physics (like infrared singular long range effects for gauge fields). There are, however, plenty of examples where zero-mode effects appear already on the level of perturbation theory. Examples include disconnected vacuum diagrams,[64] "generalized

tadpoles" for self-interacting scalar fields,[33,65] as well as "rainbow diagrams" for the fermion self-energy.[60,66] These examples will be discussed in more detail in Section 4.

In perturbation theory in LF gauge the gauge field propagator

$$D_{\mu\nu}(k) = \frac{g_{\mu\nu} - \frac{k_\mu n_\nu + k_\nu n_\mu}{k \cdot n}}{k^2 + i\varepsilon} \tag{3.20}$$

$(n \cdot A = A_-)$ becomes singular as $k_- \to 0$. There exist several "prescriptions" to handle this singularity. The most useful for perturbative calculations is the Mandelstam–Leibbrandt (ML) prescription,[38] where one replaces

$$\frac{1}{k \cdot n} \equiv \frac{1}{k_-} \xrightarrow{\text{ML}} \frac{1}{k_- + i\varepsilon \, \text{sign}(k_+)} = \frac{k_+}{k_+ k_- + i\varepsilon} \tag{3.21}$$

The crucial property of this prescription is that the pole structure is similar to the one of a typical Feynman propagator, with poles in the second and fourth quadrant of the complex k_0-plane, and thus allows one to perform a Wick rotation. This is not the case for the principal value (PV) prescription

$$\frac{1}{k_-} \xrightarrow{\text{PV}} \frac{1}{2}\left(\frac{1}{k_- + i\varepsilon} + \frac{1}{k_- - i\varepsilon}\right) \tag{3.22}$$

with poles in the first and fourth quadrant.

One of the major disadvantages of the ML prescription is the fact that it introduces additional energy (k_+) dependencies in the propagator, which cannot be generated by a canonical LF hamiltonian.[67] However, recently the ML prescription has been successfully implemented in a LF Bethe-Salpeter approach to bound states.[68] Conversely, in $\text{QCD}_{1+1}(N_C \to \infty)$ the ML prescription[40] yielded a spectrum that disagreed with the canonical LF approach[25] as well as with the result from equal time quantization.[23] More recently, light-like Wilson loops in $1 + 1$ dimensions have been calculated, using various prescriptions for gauge field propagator,[69] and it was found that only the principal value prescription yields the exact area law one expects for gauge fields in $1 + 1$ dimensions (on noncompact manifolds).

3.3. Zero Modes and the Vacuum in ε-Coordinates

3.3.1. General Considerations

For a free particle $p_+ = \frac{L}{2\varepsilon}\left(-p_- + \sqrt{p_-^2 + 2\varepsilon m^2/L}\right)$ and p_- is no longer restricted to positive values (Fig. 2.1). Therefore, for all finite values

of ε/L, the vacuum in ε-coordinates is nontrivial. Since ε-coordinates (see Section 2.2) provide a controlled and well defined approach to the LF, it seems very natural to employ this framework for studying the LF vacuum.

Let us first consider the canonical LF limit *(L fixed, $\varepsilon \to 0$)*. In this case it is straightforward to derive an effective LF hamiltonian from the ε-hamiltonian[29] (for a related work, see Refs. 70 and 71). For finite L the momenta are discrete. Without interactions the energy of the zero mode $[p_+(0) = m\sqrt{\frac{L}{2\varepsilon}}]$ and the energy of modes with negative momenta $[p_+(-n) \approx \frac{2\pi n}{\varepsilon}]$ diverge as $\varepsilon \to 0$, while the energy of all positive momentum modes $[p_-(n) \approx \frac{m^2 L}{4\pi n}]$ remains finite. For interacting fields there will be some slight quantitative changes, but the general picture should remain the same: zero modes and negative momentum modes are high energy modes — separated from positive momentum modes by an energy gap of $\mathcal{O}\left(\sqrt{\frac{1}{\varepsilon}}\right)$ and $\mathcal{O}\left(\frac{1}{\varepsilon}\right)$ respectively. Thus although $p_- \leq 0$ modes may acquire nontrivial occupations, $p_- > 0$ modes have too little energy to cause any excitations within the $p_- \leq 0$ sector for $\varepsilon \to 0$: the $p_- \leq 0$ modes freeze out and can be replaced by their vacuum expectation value (VEV).

At this point it seems that we have succeeded in deriving a nontrivial effective LF hamiltonian. Unfortunately, we arrived at this result by approaching the LF in such a way that the invariant length of the interval $(\propto L\varepsilon)$ approaches zero, i.e., as discussed in Ref. 29, the effective theory that we have obtained is not necessarily equivalent to the original covariant theory. This can be easily illustrated by means of a perturbative example. Consider a simple tadpole with a mass insertion (to make it convergent) in $1 + 1$ dimensions

$$\tilde{\Sigma} = \int \frac{d^2k}{(2\pi)^2} \frac{1}{\left(k^2 - m^2 + i0\right)^2} = \frac{i}{4\pi m^2} \tag{3.23}$$

On a finite interval (with ε coordinates) one obtains instead $[k_-(n) = \frac{2\pi}{L}n]$

$$\tilde{\Sigma} = \frac{1}{L} \sum_{k_-} \int \frac{dk_+}{2\pi} \frac{1}{\left(\frac{2\varepsilon}{L}k_+^2 + 2k_+ k_- - m^2 + i0\right)^2}$$

$$= \frac{i}{4\sqrt{2\varepsilon L}} \sum_{n=-\infty}^{\infty} \left[\frac{(2\pi n)^2}{2\varepsilon L} + m^2\right]^{-3/2} \tag{3.24}$$

Clearly, in order to recover the continuum result (3.23) one must take limits in such a way that the invariant length of the interval becomes infinite. If one takes the LF limit first $(\varepsilon \to 0, L$ fixed), one obtains a divergent contribution from the zero mode.

A different result is obtained if one performs the continuum limit first ($L \to \infty$, ε/L fixed). Since this corresponds to $\varepsilon L \to \infty$ no problems with perturbation theory arises. However, since the spectrum is now continuous, there is no mass gap and the derivation of the effective hamiltonian for $\varepsilon/L \to 0$ becomes more complicated. Nevertheless, it is still possible: first, note that the momentum scale of the continuum hamiltonian is $m^2 \varepsilon/L$ since momentum dependent terms in the continuum hamiltonian appear only in the kinetic term $\propto \frac{L}{2\varepsilon} \left[-k_- + \sqrt{k_-^2 + m^2 2\varepsilon/L} \right]$ and in vertex factors $\propto \left(k_-^2 + m^2 2\varepsilon/L \right)$. Thus the typical momentum scale in the vacuum is given by $p_-^{\text{vac}} = \mathcal{O}\left(\sqrt{\frac{\varepsilon}{L}} m \right)$. Similarly the energy scale for vacuum excitations (zero total P_-) is of the order $\mathcal{O}\left(\sqrt{\frac{L}{\varepsilon}} m \right)$. Suppose one is interested in the effective hamiltonian for a physical particle of total momentum p_-^{tot} moving in the vacuum. If $\frac{\varepsilon}{L} \ll 1$ then there is almost no overlap between the wave function of the vacuum $p_-^{\text{vac}} = \mathcal{O}\left(\sqrt{\frac{\varepsilon}{L}} m \right)$ and the wave function of the partons in the particle p_-^{parton} because the parton wave function (calculated, for example, with a typical LF hamiltonian) vanishes for small momenta. Thus one can introduce an energy gap *by hand* without affecting the dynamics in the limit $\frac{\varepsilon}{L} \to 0$: for example, by selecting cutoffs Λ_1 and Λ_2 such that

$$ m\sqrt{\frac{\varepsilon}{L}} \ll \Lambda_1 \ll \Lambda_2 \ll p_-^{\text{tot}} \tag{3.25} $$

and removing all modes with $\Lambda_1 < k_- < \Lambda_2$. First, this gives rise to a mass gap and one can argue that the modes with $k_- < \Lambda_1$ remain frozen (energy scale $k_+ > \frac{m^2}{2\Lambda_1}$) when excitations with $k_- > \Lambda_2$ are present (energy scale $k_+ < \frac{m^2}{2\Lambda_2}$): in second-order perturbation theory, the energy shift for modes with $k_- > \Lambda_2$ due to excitations of n modes with $k_- < \Lambda_1$ is given by

$$ \Delta^{(2)} E \propto \frac{\left| \Lambda_1^{-n/2} \right|^2}{-\frac{1}{\Lambda_1}} \Lambda_1^n = -\Lambda_1 \overset{\Lambda_1 \to 0}{\longrightarrow} 0 \tag{3.26} $$

Here $\Lambda_1^{-n/2}$ is a vertex factor, arising from the factor $\frac{1}{\sqrt{\omega_n}}$ in the expansion of the fields ϕ [Eq. (2.10)], the factor Λ_1^n is the phase space factor for n modes with $k_- = \mathcal{O}(\Lambda_1)$ and states with $k_- < \Lambda_1$ excitations are off-shell by at least $\frac{1}{\Lambda_1}$.

Since $k_- < \Lambda_1$ excitations are suppressed, the effective LF hamiltonian for the modes with $k_- > \Lambda_2$ contains the $k_- < \Lambda_1$ modes only via their VEV (which may be nontrivial!)

$$ V_{k_- > \Lambda_2}^{\text{eff}} = \langle 0_{k_- < \Lambda_1} | V | 0_{k_- < \Lambda_1} \rangle \tag{3.27} $$

The crucial point is that the parton distribution calculated with such an effective LF hamiltonian vanishes for small momenta in the above superrenormalizable example.* Thus as long as Λ_2 is small enough compared to the total momentum of the particle p, the parton distribution vanishes already for momenta much larger than Λ_2 and the presence of the cutoff does not affect the parton dynamics. Since the VEVs are nearly independent of ε/L, so is the effective hamiltonian. Thus the suppression of the parton distribution due to the kinetic energy sets in at a value cp_-^{tot}, where c is nearly independent of ε/L. Thus, for $\varepsilon/L \to 0$, Λ_2 can easily be chosen smaller than cp_-^{tot} while Eq. (3.25) remains satisfied. In other words, Λ_2 can be chosen such that the parton dynamics is independent of the exact position of the cutoff. Similarly, since vacuum momenta are restricted to $p_-^{\text{vac}} = \mathcal{O}\left(\sqrt{\frac{\varepsilon}{L}}m\right) \ll \Lambda_1$, the presence of the cutoff does not affect the dynamics of the vacuum either, i.e., the numerical value of the VEVs which enter Eq. (3.27) is independent of the cutoff.

In the second-order perturbation theory argument above, we made use of $\Lambda_1 \ll \Lambda_2$ to make sure that the energy denominator in Eq. (3.26) is of the order $\mathcal{O}(1/\Lambda_1)$. This is actually not necessary, since the occupation of these modes is anyway *dynamically* suppressed for $k_- < cp_-$ and, as long as $\Lambda_1 \ll cp_-$, the energy denominator will automatically be $\mathcal{O}(1/\Lambda_1)$ or smaller.

Thus we can actually let $\Lambda_2 \to \Lambda_1$, i.e., remove the cutoff, without altering the conclusion. Introducing a mass gap was helpful in deriving an effective hamiltonian for modes with $p_- \gg m\sqrt{\varepsilon/L}$. However, since the solutions of the effective hamiltonian vanish at small p_- anyway, there is no need for a cutoff: a region void of excitations between $m\sqrt{\varepsilon/L}$ and cp_- develops dynamically (Fig. 3.1) and this is sufficient to derive an effective hamiltonian.

In the end, the following result is obtained. Suppose we started from some polynomial interaction

$$\mathcal{L}^{\text{int}} = -\sum_n \lambda_n \frac{\phi^n}{n!} \tag{3.28}$$

Then, using Eq. (3.27) (after some combinatorics) the effective interaction, which enters the LF hamiltonian for $p_- > 0$ modes in the limit $\varepsilon/L \to 0$, is given by

$$\mathcal{L}^{\text{int}}_{\text{eff}} = -\sum_n \lambda_n \sum_{k=0}^n \frac{\phi^{(n-k)}}{(n-k)!} \langle 0| \frac{\phi^k}{k!} |0\rangle \tag{3.29}$$

---

* Roughly speaking, the LF kinetic energy T, which one can calculate from the parton momentum distribution $f(k_-)$, using $T = m^2 \int_0^{P_-^{\text{tot}}} dk_- \frac{f(k_-)}{2k_-}$, has to remain finite.
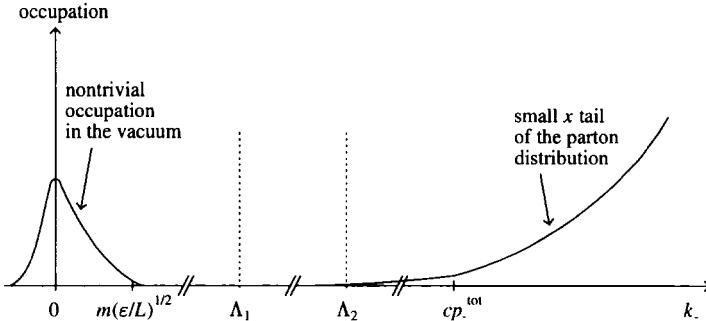
Fig. 3.1. Schematic occupation of modes in the presence of a particle with momentum p_- for $\varepsilon/L \ll 1$ (i.e., "close to the LF"). The modes near $k_- = 0$ are already present in the vacuum and are dynamically restricted to $k_- = \mathcal{O}\left(m(\varepsilon/L)^{(1/2)}\right)$ The "parton distribution," i.e., the modes which are occupied in the presence of the particle but not in the vacuum, vanish at small k_- at a momentum scale which remains finite as $\varepsilon/L \to 0$. The presence of the cutoffs has almost no effect on the dynamics.

(in order to obtain this result one also uses that, after normal ordering, the $p_- > 0$ modes do not contribute to the VEVs). Equation (3.29) is a remarkable result. It states that nontrivial vacuum effects enter the LF hamiltonian only via effective interactions. The effective coupling constants depend on the vacuum condensates which, in general, cannot be obtained directly from a LF calculation.* They must be considered as renormalization parameters of the LF theory. Equation (3.29) is also valid in situations where spontaneous symmetry breaking occurs. For example, in ϕ^4 theory, $\langle 0|\phi|0\rangle$ may become nonzero and a ϕ^3 interaction will thus appear in the effective Lagrangian.[†] However, note that only *a finite* number of condensates is necessary to specify the effective LF hamiltonian: if N is the highest power of ϕ entering the canonical LF hamiltonian, then only condensates $\langle 0|\phi^k|0\rangle$ with $k < N$ need to be considered.

At several points in the above discussion it was important that the theory is free of divergences (up to a finite number of diagrams which can always be subtracted before applying the above argumentation). First, this was important to insure that the momentum scale in the vacuum is finite. Second, it was important because only in the absence of divergences can one apply the kinetic energy argument to prove that the parton momentum distribution vanishes for

---

*However, there are exceptions where one can use sum rules or consistency conditions to determine the effective couplings iteratively. Examples will be discussed in the following section.
[†]It should be emphasized that we did not make any mean field assumptions, such as $\langle 0|\phi^k|0\rangle = \langle 0|\phi|0\rangle^k$, in order to arrive at this result.

small parton momenta. Therefore one must be very careful when generalizing the above results to higher-dimensional field theories. Equation (3.29) can be used in renormalizable field theories only *after* a cutoff has been imposed. This is, for example, the case for the transverse lattice which will be discussed in Section 5.3.

3.3.2. A Simple Example for the Limit $L \to \infty$, $\varepsilon/L \to 0$

The appearance of the gap as $L \to \infty$ (first) and $\varepsilon/L \to 0$ is best understood by studying a concrete example. Ideally this implies considering some nontrivial interacting field theory and calculating the occupation of the modes nonperturbatively for various ε/L and $L \to \infty$. However, even in integrable models, such as the sine-Gordon model, the occupation of the modes is not known exactly! Since numerical calculations at small but finite ε/L and $L \to \infty$ are very complicated — particularly if one is interested in momenta of the order of $m\sqrt{\varepsilon/L}$ — we will proceed by studying a perturbative example. Due to the fact that the appearance of the gap is mostly a consequence of dimensional analysis, this will be sufficient to highlight the essential physics of the limit $\varepsilon/L \to 0$, $L \to \infty$ ($L \to \infty$ first). The example which we will consider is a scalar field theory in $1 + 1$ dimensions with polynomial self-interactions

$$\mathcal{L} = \frac{1}{2}\partial_\mu \phi \partial^\mu \phi - \frac{m^2}{2}\phi^2 - \frac{\lambda_4}{4!}\phi^4 - \frac{\lambda_6}{6!}\phi^6 \tag{3.30}$$

In ε-coordinates the hamiltonian for this model reads after normal ordering

$$H = \sum_n p_+(k_n)a_{k_n}^\dagger a_{k_n} + \int_0^L dx^- \left[\frac{\lambda_4}{4!} : \phi^4 : + \frac{\lambda_6}{6!} : \phi^6 : \right] \tag{3.31}$$

where the same notation as in Section 2.2 has been used. In lowest (zeroth) order in λ_4 and λ_6 the vacuum is the Fock vacuum, defined by $a_{k_n}|0\rangle = 0$. This changes of course for nonvanishing couplings. For example, in second-order perturbation theory in λ_4 one finds for the occupation of states in the vacuum

$$\rho_0(k, \frac{\varepsilon}{L}, L) \equiv \langle \tilde{0}|a_k^\dagger a_k|\tilde{0}\rangle$$

$$= \frac{\lambda_4^2}{3!}L^2 \sum_{k_2, k_3} \frac{1}{[p_+(k) + p_+(k_2) + p_+(k_3) + p_+(k_4)]^2}$$

$$\times \frac{1}{2\omega(k)} \frac{1}{2\omega(k_2)} \frac{1}{2\omega(k_3)} \frac{1}{2\omega(k_4)} \tag{3.32}$$

where $\omega(q) = L\sqrt{q^2 + 2\varepsilon m^2/L}$, $p_+(q) = \left(-q + \sqrt{q^2 + 2\varepsilon m^2/L}\right) L/2\varepsilon$ and $k_4 = -k - k_2 - k_3$. A similar expression is found for the $\mathcal{O}(\lambda_6^2)$-term, which will be omitted for simplicity. In the limit $L \to \infty$ one thus finds

$$\rho_0\left(k, \frac{\varepsilon}{L}\right) \equiv \lim_{L \to \infty} \frac{L}{2\pi} \frac{1}{\sqrt{2\varepsilon L m^2}} \rho_0\left(k, \frac{\varepsilon}{L}, L\right)$$

$$= \frac{\lambda_4^2}{96\pi m^5} \sqrt{\frac{L}{2\varepsilon}} \hat{\rho}_0\left(k\sqrt{\frac{L}{2\varepsilon m^2}}\right) \tag{3.33}$$

where

$$\hat{\rho}_0(z) = \int_{-\infty}^{\infty} \frac{dz_2}{2\pi} \int_{-\infty}^{\infty} \frac{dz_3}{2\pi} \frac{\hat{\omega}(z)^{-1} \hat{\omega}(z_2)^{-1} \hat{\omega}(z_3)^{-1} \hat{\omega}(z_4)^{-1}}{[\hat{\omega}(z) + \hat{\omega}(z_2) + \hat{\omega}(z_3) + \hat{\omega}(z_4)]^2} \tag{3.34}$$

with $\hat{\omega}(z) = \sqrt{z^2 + 1}$ and $z_4 = -z - z_2 - z_3$. The factor $L/2\pi$ arises from going from discrete to continuous momentum k and we divided by the invariant length of the interval because the occupation in the vacuum trivially scales like the invariant length.

Most importantly, the momentum scale in the occupation of the vacuum is set by $m\sqrt{2\varepsilon}/L$. The momentum density in the vacuum is sharply peaked around $k = 0$ with width $\mathcal{O}(\sqrt{2\varepsilon/L})$ and height $\mathcal{O}(\sqrt{L/2\varepsilon})$, i.e., it resembles a δ-function as $\varepsilon/L \to 0$.

Let us now consider a state with momentum P, where P is taken independent of L or ε. To lowest order

$$|P\rangle = a_P^\dagger |0\rangle \tag{3.35}$$

and thus

$$\rho_P\left(k, \frac{\varepsilon}{L}, L\right) \equiv \langle P|a_k^\dagger a_k|P\rangle = \delta_{k,P} + \mathcal{O}(\lambda^2) \tag{3.36}$$

Three classes of corrections contribute to ρ_P: insertions in disconnected vacuum diagrams (Fig. 3.2a) [yielding again Eq. (3.33)], insertions in tadpoles (Fig. 3.2b), and the rest, i.e., insertions in nontadpole connected corrections (Fig. 3.2c).

The tadpole term yields

$$\tilde{\rho}_P^{\text{tadpole}}\left(k, \sqrt{\frac{\varepsilon}{L}}\right) \equiv \lim_{L \to \infty} \frac{L}{2\pi} \rho_P^{\text{tadpole}}\left(k, \sqrt{\frac{\varepsilon}{L}}, L\right)$$

$$= \frac{\lambda_4 \lambda_6}{96\pi m^4 P} \hat{\rho}_0\left(k\sqrt{\frac{L}{2\varepsilon m^2}}\right) \tag{3.37}$$
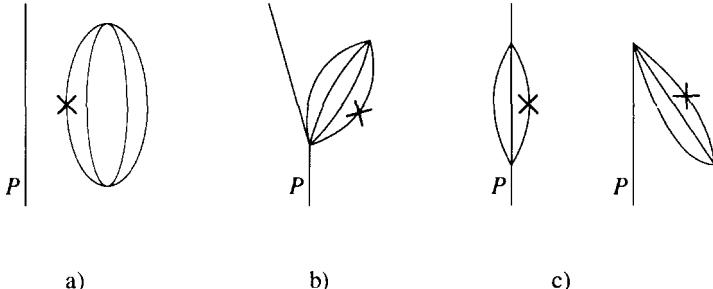
Fig. 3.2. $\mathcal{O}(\lambda^2)$-corrections to the mode density in the presence of a particle with momentum P: (a) disconnected corrections, (b) insertions into generalized tadpoles (i.e., diagrams where a subgraph is connected with the rest of the diagram at one point only), and (c) nontadpole connected corrections.

and for the nontadpole, connected term one finds

$$\tilde{\rho}_P^{nt}\left(k, \sqrt{\frac{\varepsilon}{L}}\right) \equiv \lim_{L \to \infty} \frac{L}{2\pi} \rho_P^{nt}\left(k, \sqrt{\frac{\varepsilon}{L}}, L\right) \tag{3.38}$$

$$= \frac{\lambda_4^2}{32\pi} \int_{-\infty}^{\infty} \frac{dk_2}{2\pi} \left[\frac{1}{E_A^2} + \frac{1}{E_B^2}\right] \frac{1}{\omega(P)} \frac{1}{\omega(k)} \frac{1}{\omega(k_2)} \frac{1}{\omega(k_3)}$$

($k_3 = P - k - k_2$) plus a similar term proportional to λ^6, which will be omitted in the following for simplicity. The energy denominators in Eq. (3.38), corresponding to the two time orderings, are given by

$$E_A = p_+(P) - p_+(k) - p_+(k_2) - p_+(k_3)$$

and

$$E_B = -p_+(P) - p_+(k) - p_+(k_2) - p_+(k_3) \tag{3.39}$$

The various contributions to the occupations in the presence of a particle with momentum P are shown in Fig. 3.3 for a number of values for ε/L. The numerical values for m and P, as well as the coupling constants λ_4 and λ_6, in the plots are taken to be 1. Several effects can be observed:

- The nontadpole connected (dispersive) contribution scales in the limit $L \to \infty$, $\varepsilon/L \to 0$. The scaling function is the LF momentum distribution.

- Both the disconnected contribution as well as the tadpole contribution are restricted to a region $k^2 = \mathcal{O}(\varepsilon/L)\Lambda^2$ near the origin, where Λ is some mass scale ($\Lambda = m$ to lowest nontrivial order).
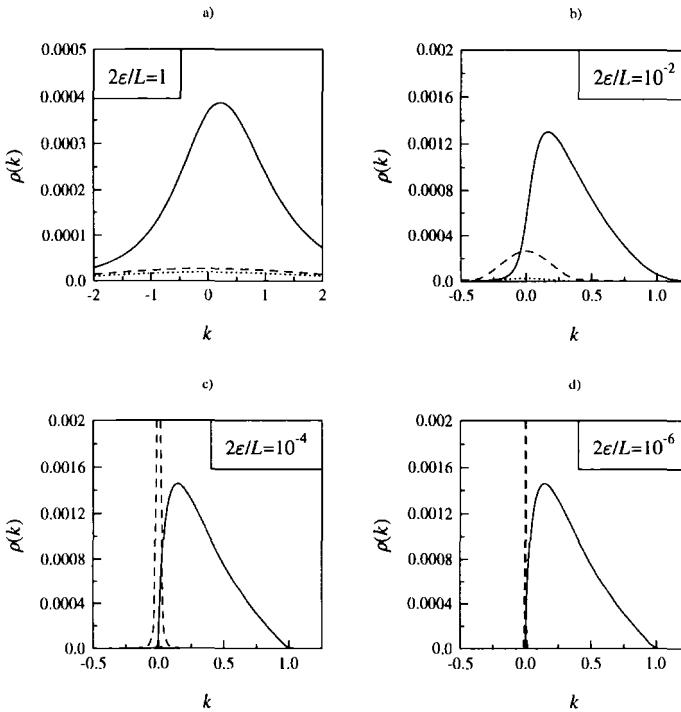
Fig. 3.3. $\mathcal{O}(\lambda^2)$-contributions to the occupation density $\tilde{\rho}(k)$ in the presence of an excitation with momentum $P = 1$ and mass $m = 1$ for various values of the parameter ε/L. Dashed line: disconnected vacuum contribution, dotted line: tadpole contribution, full line: nontadpole connected (dispersive) contribution.

- The integral over the disconnected vacuum contribution is independent of ε/L.

- Compared to the vacuum contribution, the tadpole term is suppressed by one power of $\sqrt{\varepsilon/L}$ and thus can be neglected as $\varepsilon/L \to 0$

The gap can be most easily observed by plotting the density over a logarithmic momentum scale (Fig. 3.4).

For very small values of ε/L, the momentum distributions from the disconnected diagrams [momentum scale $\mathcal{O}(\sqrt{\varepsilon/L})$] and from the dispersive contributions [momentum scale 0.1–1] no longer overlap and a gap arises. The disconnected contributions were already present in the vacuum (ground state for $P = 0$) and are unaltered by the presence of the excitation with momentum P. The only change in occupation within the small momentum
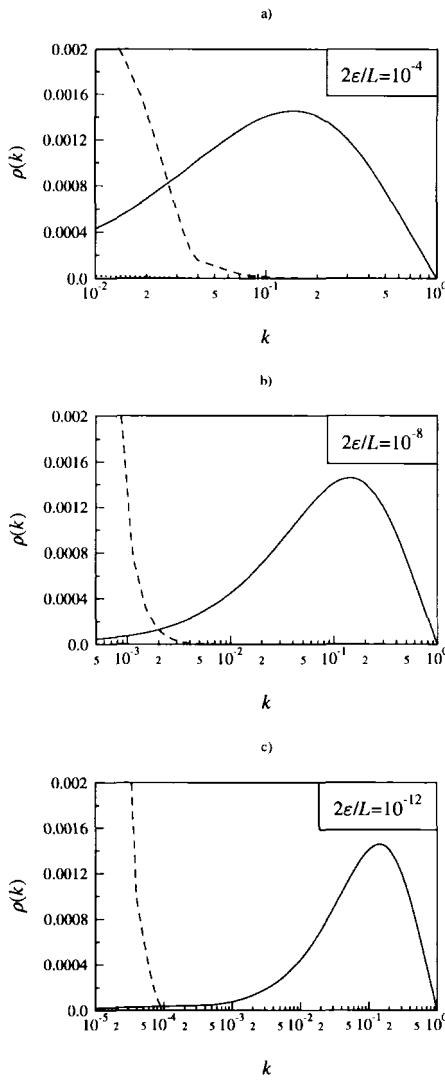
Fig. 3.4. Same as in Fig. 3.3 but for smaller values of ε/L and plotted over a logarithmic momentum scale.

region arises from the tadpoles, but its integrated contribution vanishes as $\varepsilon/L \to 0$ and becomes negligible in that limit. Note that $\sqrt{\varepsilon/L}$ must be extremely small for the gap to be clearly visible. This makes nonperturbative studies of the gap forbiddingly difficult numerically, because one would have to cover a huge number of scales (from $\sqrt{\varepsilon/L}$ to 1) while keeping the invariant volume large.

3.4. Vacuum Condensates and Sum Rules

In the previous section we explained that vacuum condensates may enter the effective (zero-mode free) LF hamiltonian via induced coupling constants. The condensates cannot be calculated directly unless one includes dynamical zero modes. However, even without zero modes, it is possible to calculate at least some of the condensates indirectly using sum rule techniques. As an example, let us consider the two point function in a self-interacting scalar field theory

$$G(x) \equiv \langle 0|\phi(0)\phi(x)|0\rangle \tag{3.40}$$

($x^0 < 0$, $x^2 < 0$). Inserting a complete set of states one obtains

$$G(x) = \langle 0|\phi|0\rangle^2 + \sum_n \int_0^\infty \frac{dp_-}{2p_-} \langle 0|\phi(0)|n,p\rangle\langle n,p|\phi(x)|0\rangle \tag{3.41}$$

$$= \langle 0|\phi|0\rangle^2 + \sum_n \int_0^\infty \frac{dp_-}{2p_-} |\langle 0|\phi(0)|n,p\rangle|^2 \exp\left(i(p_- x^- + p_+^n x^+)\right)$$

where the sum is over all particle states. The normalization of the states is $\langle n,p|m,p'\rangle = 2p_- \delta(p_- - p'_-)\delta_{nm}$ and the energies are given by the on-shell dispersion relation $p_+^n = M_n^2/2p_-$. By boost invariance (in the continuum limit), the vacuum to "hadron" matrix elements are independent of the momentum

$$\langle 0|\phi|n,p\rangle = \frac{g_n}{\sqrt{2\pi}} \tag{3.42}$$

and thus

$$G(x) = \langle 0|\phi|0\rangle^2 - \sum_n \frac{|g_n|^2}{4\pi} K_0(M_n \sqrt{-x^2}) \tag{3.43}$$

where K_0 is a modified Bessel function.[72] In the limit $x^2 \to 0$ one thus finds

$$\langle 0|\phi^2|0\rangle - \langle 0|\phi^2|0\rangle_{\text{free}} \equiv \lim_{x^2 \to 0} [G(x) - G(x)_{\text{free}}]$$

$$= \langle 0|\phi|0\rangle^2 + \sum_n \frac{|g_n|^2}{4\pi} \log \frac{M_n}{M_{\text{free}}} \qquad (3.44)$$

where we used $\sum_n |g_n|^2 = 1$ while M_{free} and $G_{\text{free}}(x)$ are the invariant mass and the two point function for noninteracting fields. Equation (3.44) is very interesting because it allows one to calculate $\langle 0|\phi^2|0\rangle$ in terms of $\langle 0|\phi|0\rangle$ and quantities (M_n and g_n) which are calculable in a canonical LF calculation without any dynamical zero modes.

A similar trick works for the cubic condensates. Of course one has to be careful to separate the disconnected contributions first:

$$\langle 0|\phi(x)\phi(y)\phi(z)|0\rangle = \langle 0|\phi|0\rangle^3 + \langle 0|\phi(x)\phi(y)\phi(z)|0\rangle_C^3$$
$$+ \langle 0|\phi|0\rangle [\langle 0|\phi(x)\phi(y)|0\rangle_C + \langle 0|\phi(x)\phi(z)|0\rangle_C$$
$$+ \langle 0|\phi(y)\phi(z)|0\rangle_C] \qquad (3.45)$$

The connected piece is calculated similar to $\langle 0|\phi^2|0\rangle$ by inserting a complete set of states. In the limit $(x-y)^2 \to 0$, $(y-z)^2 \to 0$ one finds

$$\langle 0|\phi^3|0\rangle = \langle 0|\phi|0\rangle^3 + 3\langle 0|\phi|0\rangle \langle 0|\phi^2|0\rangle_C$$
$$+ \sum_n \int_0^\infty \frac{dp_-}{2p_-} \langle 0|\phi|n, p_-\rangle \langle n, p_-|\phi^2|0\rangle_C$$
$$= \langle 0|\phi|0\rangle^3 + 3\langle 0|\phi|0\rangle \langle 0|\phi^2|0\rangle_C$$
$$+ \sum_n \frac{g_n h_n}{4\pi} \log M_n \qquad (3.46)$$

where $h_n \equiv \sqrt{2\pi} \langle 0|\phi^2|n, p_-\rangle_C$ (independent of p_-) and $\langle 0|\phi^2|0\rangle_C$ can be taken from Eq. (3.44). Note that $\sum_n g_n h_n = 0$ because the states $\int dp_- \exp(ip_- x^-)\phi(x^-)|0\rangle$ and $\int dp_- \exp(ip_- x^-)\phi^2(x^-)|0\rangle$ are orthogonal. Like g_n, h_n can be calculated in a LF calculation without dynamical zero modes.

The generalization of these results to higher condensates is straightforward and, by recursion, one can express them in terms of $\langle 0|\phi|0\rangle$ and matrix elements which are accessible in a LF calculation. These matrix elements (g_n and h_n) depend on the states, and thus implicitly on the coupling constants in the effective LF hamiltonian. Since the coupling constants in the effective LF

hamiltonian also involve the condensates (3.29), this implies that it may be possible to determine the coupling constants in the effective LF hamiltonian self-consistently.

Similar results may be derived for Yukawa theories. In Section 4.2 we will relate the effective coupling constants in the LF hamiltonian to the spectral densities (4.16), which are also accessible in a LF calculation.

Extracting vacuum condensates from a canonical LF calculation via sum rules has, for example, been done in Ref. 73 for the $m_q \to 0$ quark condensate in $QCD_2(N_C \to \infty)$. The numerical result for $\bar{\psi}\psi$ was confirmed later in Ref. 23 in an equal time framework. A finite quark mass calculation, based on LF wave functions and sum rule techniques, was first conducted in Refs. 47 and 74. Again the result agreed with that from equal time quantization.[75]

4. PERTURBATIVE RENORMALIZATION

In practical applications of LF quantization, such as calculating parton distributions, nonperturbative effects play a major role. Nevertheless, it makes sense to study renormalization of LF field theories first from a perturbative point of view because this allows one to resolve some issues which would also appear in a nonperturbative bound state equation.

Most terms in the perturbation series generated by the LF hamiltonian of QED or QCD are UV-divergent. This is not very surprising. After all, we have become used to the fact that most quantum field theories contain divergences. However, as we will see in the following, the structure of the divergences in light front perturbation theory (LFPTh) is different from the divergences in covariant perturbation theory (CPTh). Because LF quantization is a noncovariant formulation of field theory, different Lorentz components of a divergent expression are not necessarily related to each other. In addition, in many examples the degree of divergence in LFPTh is worse than in CPTh.

On the one hand this is caused by the choice of regulators. On a formal level, LFPTh and CPTh are equivalent.[21] However, the "equivalence proof" involves steps which are ill defined in the presence of divergences and singularities. In practice, if one wants to demonstrate the equivalence between LFPTh and CPTh, it is very helpful to completely regularize the theory at the level of the Lagrangian — before quantizing. One possibility to do this is Pauli–Villars regularization, where one can introduce as many regulators as are necessary to render the theory free of divergences and light-cone singularities.[21,76] Obviously, it is then not difficult to es-

tablish the equivalence between LFPTh and CPTh. However, for practical applications, Pauli–Villars regularization is not very useful. On the one hand, the hamiltonian for a Pauli–Villars regularized theory is either non-hermitian or unbounded from below or both.* On the other hand, Pauli–Villars regulators are not very useful for nonabelian gauge theories, because there one would have to introduce massive vector fields, which will in general destroy the renormalizability of nonabelian gauge theories. For these reasons, one is not interested in employing these regulators in the context of LF quantization.

For practical applications, it is very useful to use regulators that are compatible with the kinematic symmetries[†] of the LF.[‡] In the literature one finds, for example, the Brodsky–Lepage regulator

$$\sum_i \frac{\vec{k}_{\perp i}^2 + m_i^2}{x_i} < \Lambda_{BL}^2 \qquad (4.1)$$

where the sum extends over all particles and $x_i = k_{i-}/P_-^{\rm tot} \in (0; 1)$ are LF momentum fractions. Other regulators are a transverse momentum cutoff

$$\vec{k}_\perp^2 < \Lambda_\perp^2 \qquad (4.2)$$

or dimensional regularization in the transverse direction[66,77]

$$\int d^2 k_\perp \to \int d^{2(1-\epsilon)} k_\perp \qquad (4.3)$$

Very often it is also necessary to introduce a cutoff for small longitudinal momenta, such as

$$\Theta(x_i - \delta) \qquad (4.4)$$

and/or a cutoff in the number of particles (Tamm-Dancoff approximation). What all these regulators have in common is that they are in general not compatible with Lorentz transformations that are not kinematic symmetries of the LF (like rotations around any axis other than the z-axis). Thus when using one of these regulators, one should not be surprised if matrix

---

*The Pauli–Villars ghosts must be quantized with the "wrong" commutation relations in order to contribute with opposite signs in loops, which is necessary to cancel the divergences. The properties of the hamiltonian then follow from the spin statistics theorem.
[†]These are all Poincaré transformations, which leave the $x^+ = 0$ initial surface invariant, such as translations, rotations around the z-axis or longitudinal boosts.
[‡]This excludes, e.g., Euclidean lattices.

elements do not exhibit the full Lorentz invariance — unless one compensates for this effect by means of a more general counterterm structure. This last point will be the main subject of the rest of this chapter. The Tamm–Dancoff approximation will be discussed in more detail in Section 5.4.

4.1. Scalar Fields

The following observation is very helpful in analyzing the perturbative equivalence between CPTh and LFPTh: hamiltonian (with x^0 or x^+ as time) perturbation theory can be obtained from covariant perturbation theory after integrating the energies (i.e., the momentum variable which is canonically conjugate to the "time") first. Thus from the mathematical point of view, the question about equivalence between LFPTh and CPTh has been reduced to the question whether the order of integration plays a role in a Feynman integral.

As an example, let us consider the 1-loop self-energy Σ in ϕ^3-theory in $1 + 1$ dimensions (Figure 4.1)

$$\Sigma = \frac{ig^2}{2} \int \frac{dk_-dk_+}{(2\pi)^2} \frac{1}{k^2 - m^2 + i\varepsilon} \frac{1}{(p-k)^2 - m^2 + i\varepsilon} \qquad (4.5)$$

$$= \frac{g^2}{2} \int \frac{dk_-}{2\pi} \frac{\Theta(k_-)}{2k_-} \frac{\Theta(p_- - k_-)}{2(p_- - k_-)} \frac{1}{p_+ - \frac{m^2}{2k_-} - \frac{m^2}{2(p_- - k_-)}} \qquad (4.6)$$

First, without going into the details, it is easy to convince oneself that Eq. (4.6) is exactly what one obtains in LF-hamiltonian perturbation theory: $p_+ - (m^2/2k_-) - [m^2/2(p_- - k_-)]$ is the energy denominator and the Θ-functions ensure that all momenta are positive. The other factors arise from a vertex factor proportional to $[k_-(p_- - k_-)]^{-1/2}$ at each vertex. It is also easy to see that Eq. (4.6) agrees with the covariant calculation with symmetric integration. After substituting $k_- = xp_-$ in Eq. (4.6) one finds

$$\Sigma = \frac{g^2}{2} \int_0^1 \frac{dx}{4\pi} \frac{1}{p^2 x(1 - x) - \lambda^2} \qquad (4.7)$$

In the covariant calculation one first combines the two denominators in Eq. (4.5) with a Feynman parameter integral and then one integrates symmetrically over d^2k. This reproduces Eq. (4.7) where the x-integration corresponds to the parameter integral.
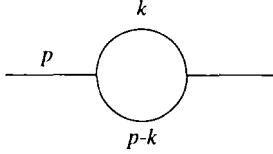
Fig. 4.1. 1-Loop self-energy diagram in ϕ^3_{1+1}.

Our next example will be one where the order of integration does matter, namely, the so-called simple tadpole diagram in ϕ^4 (for simplicity again in $1 + 1$ dimensions)

$$\Sigma = \frac{ig}{2} \int \frac{d^2k}{(2\pi)^2} \left(\frac{1}{k^2 - m^2 + i\varepsilon} - \frac{1}{k^2 - \Lambda^2 + i\varepsilon} \right) \tag{4.8}$$

We have already performed a subtraction because the unregularized integral diverges logarithmically. Symmetric integration over d^2k yields $\Sigma = (g/8\pi) \log \Lambda^2/m^2$. In LFPTh (unsymmetric integration; k_+-integral first) one obtains zero: for $k_- \neq 0$ one can always close a contour integral in the complex k_+ plane such that no poles are enclosed. The surface term vanishes because of the subtraction term. The point $k_- = 0$ is usually omitted in LF quantization without zero modes. The mathematical reason for the difference between the LFPTh result and the CPTh result is a term $\propto \delta(k_-)$, which is omitted if one (as is usually, either explicitly or implicitly done) has a small k_- cutoff, like $\Theta(k_- - \varepsilon)$ at each line — even in the limit $\varepsilon \to 0$.[64]

This result is very typical for pathologies of LFPTh with scalar fields. Compared to CPTh, one omits certain diagrams which are nonzero in CPTh, i.e., LFPTh yields *a priori* wrong results! Fortunately (later we will see that there is a good reason for this) the "mistake" does not depend on the external momenta. Thus one can make up for the mistake by means of a local counterterm in the Lagrangian.

Other diagrams which suffer from the same problem are the generalized tadpole diagrams, i.e., diagrams where part of the diagram is connected with the rest of the diagram only at one single point (examples are shown in Figs. 4.2 and 4.3). As discussed in Ref. 33, they are all zero in LFPTh. However, because the generalized tadpoles in these diagrams are connected to the rest of the diagram only at one point, the covariant calculation yields a momentum-independent result for the tadpole part (just a number), which can thus always be replaced by a local insertion into the diagram. In practice, this means that the fact that all generalized tadpoles are (wrongfully) zero on the LF can be easily compensated by appropriate redefinitions of bare coupling

<center>(a)   (b)</center>
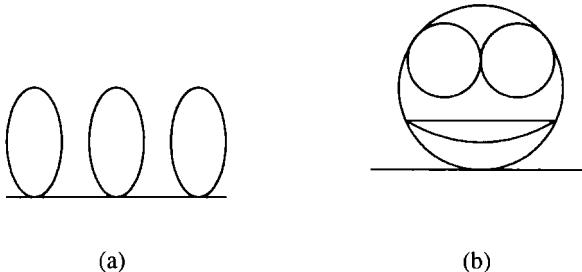
<center>Fig. 4.2. Typical generalized tadpole diagrams for ϕ^4.</center>

constants! Furthermore, tadpole diagrams are the only diagrams which are treated incorrectly in naive LFPTh.

A very interesting result is the relation between the tadpole counterterms and vacuum condensates.[33] For example, each tadpole correction to the propagator in Fig. 4.2a can be written as a mass insertion times the free field vacuum expectation value (VEV) of $\langle 0|\phi^2|0\rangle$. The generalized tadpole in Fig. 4.2b corresponds to a mass insertion times a higher-order correction $\langle 0|\phi^2|0\rangle$. The higher-order tadpoles in Fig. 4.3 correspond to mass (a) and vertex (b) insertions times a term that contributes to $\langle 0|\phi^4|0\rangle$. Suppose the interaction term in the original Lagrangian is

$$\mathcal{L}_{\text{int}} = -\sum_n \frac{\lambda_n}{n!}\phi^n \tag{4.9}$$

Then all the "missing tadpoles" are automatically taken into account if one uses

$$\mathcal{L}_{\text{int,eff}} = -\sum_n \lambda_n \sum_{k=0}^n \frac{\phi^{n-k}}{(n-k)!}\frac{\langle 0|\phi^k|0\rangle}{k!} \tag{4.10}$$

In other words, $\mathcal{L}_{\text{int,eff}}$ with naive LFPTh yields the same results as $\mathcal{L}_{\text{int}}$ (4.9) (4.10) with CPTh to all orders in perturbation theory, if the VEVs in Eq. (4.10) are also given as a perturbative expansion (calculated in CPTh).[33]

First of all, this result is very useful in practice, because, given the original interaction, it allows one immediately to write down an ansatz for the effective LF interaction — even if the VEVs cannot, in general, be calculated from the LF hamiltonian. Second, although derived perturbatively, Eq. (4.10) formally agrees with Eq. (3.29), which was derived nonperturbatively using ε-coordinates. Of course, while Eq. (4.10) was derived only for cases where the VEVs can be calculated perturbatively, Eq. (3.29) is valid in general.
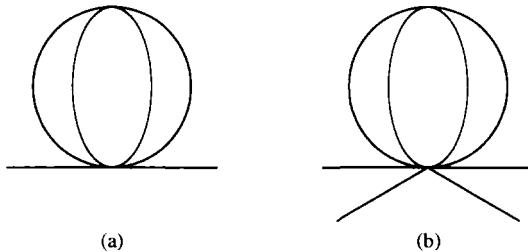
Fig. 4.3. Typical tadpole diagrams arising for scalar fields with more general polynomial self-interactions.

However, the formal agreement between the two results gives us confidence to approach other zero-mode problems using perturbation theory as well.

As it stands, Eq. (4.10) is valid only for superrenormalizable theories because we have only addressed longitudinal divergences in the above discussion. For renormalizable theories one must first cut off the transverse divergences, e.g., by using a transverse lattice (see Section 5.3) or dimensional regularization in the transverse direction.[66,77] However, with such a transverse cutoff in place, Eq. (4.10) is valid for field theories in more than one spatial dimension as well.

4.2. Fermions

For the applications of LF quantization to DIS, we are of course not interested in self-interacting scalar fields but rather in theories with fermions and gauge fields. As a first step toward this direction, let us consider fermions interacting with pseudo-scalar mesons via a Yukawa coupling (see also Section 2.3.2)

$$\mathcal{L}_{\text{int}} = g_p \bar{\psi} i \gamma_5 \psi \chi \tag{4.11}$$

within the framework of LFPTh. First one may be tempted to expect that the above-mentioned perturbative zero-mode problem does not occur here, because *a priori* there are no tadpoles in Yukawa theory with γ_5-coupling. However, after eliminating the nondynamical component of the fermion field ($\psi_{(-)}$) from the theory, the canonical LF hamiltonian (2.28) does contain terms which are fourth order in the fields — giving rise to so-called "seagull"-diagrams (Fig. 4.4).

It is thus not very surprising that the perturbative zero-mode problem arises in diagrams which have the topology of a seagull with one vacuum
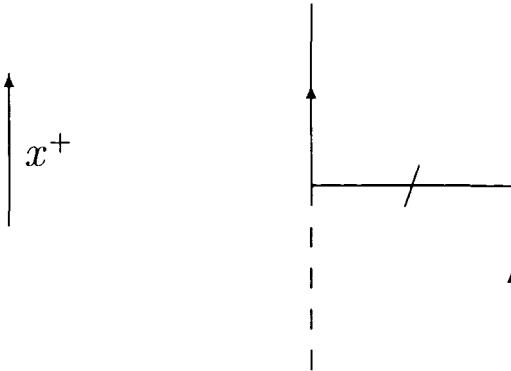
Fig. 4.4. Seagull diagram in x^+ ordered perturbation theory, representing four-point interactions induced by eliminating $\psi_{(-)}$. The dashed lines are bosons and the full lines represent fermions. The "slashed" fermion line corresponds to instantaneous (with respect to LF time) fermion exchange.

contraction (Fig. 4.5), because this is the topology one obtains if one replaces either $\psi^\dagger_{(+)}\partial_-^{-1}\psi_{(+)}$ or ϕ^2 by their VEVs.

In practice, this works out as follows[60,66,78]: Consider, for example, the dressed one loop self-energy diagram for a fermion*

$$\Sigma(p) = g_P^2 \int \frac{d^D k}{(2\pi)^D} \int_0^\infty d\mu^2 \frac{\rho(\mu^2)}{(p-k)^2 - \mu^2 + i\varepsilon}$$
$$\times \int_0^\infty dm^2 i\gamma_5 \frac{\slashed{k}\rho_1(m^2) + \rho_2(m^2)}{k^2 - m^2 + i\varepsilon} i\gamma_5 \qquad (4.12)$$

where the spectral functions (ρ, ρ_1, ρ_2) parameterize the (unspecified) self-energy insertions. They satisfy (it follows from the canonical commutation relations) $\int_0^\infty d\mu^2\rho(\mu^2) = \int_0^\infty dm^2\rho_1(m^2) = 1$. As far as the k_+ integral is concerned, the most singular term in Σ is the one proportional to $\gamma^+ k_+$. We thus consider[†]

$$\Sigma^+ = \frac{\text{tr}(\Sigma\gamma^-)}{4} \qquad (4.13)$$
$$= g_P^2 \int \frac{d^D k}{(2\pi)^D} \int_0^\infty d\mu^2 \frac{\rho(\mu^2)}{(p-k)^2 - \mu^2 + i\varepsilon} \int_0^\infty dm^2 \frac{k_+\rho_1(m^2)}{k^2 - m^2 + i\varepsilon}$$

---

*Here we assume self-consistently that all sub-loop counterterms have been added to the LF result, such that the full fermion propagator is covariant.

[†]A more detailed study shows that the other components are free of trouble.[60,66]
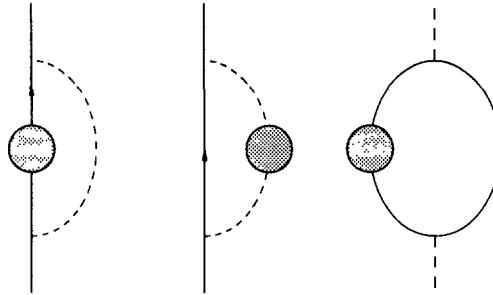
Fig. 4.5. Typical self-energy diagrams in Yukawa theory, which have the same topology as a seagull with one contraction. The blob stands for arbitrary self-energy insertions.

To identify the troublemaker we eliminate k_+ in the numerator using the algebraic identity

$$\frac{k_+}{(k^2 - m^2 + i\varepsilon)\,((p-k)^2 - \mu^2 + i\varepsilon)} =$$

$$\frac{1}{2p_-} \frac{\left[2(p_- - k_-)p_+ - \vec{p}_\perp^2 + 2\vec{p}_\perp \cdot \vec{k}_\perp + m^2 - \mu^2\right]}{(k^2 - m^2 + i\varepsilon)\,((p-k)^2 - \mu^2 + i\varepsilon)}$$

$$-\frac{1}{2p_-}\left[\frac{1}{((p-k)^2 - \mu^2 + i\varepsilon)} - \frac{1}{(k^2 - m^2 + i\varepsilon)}\right] \quad (4.14)$$

The important point here is that the last two terms in Eq. (4.14) give δ-functions in $p_- - k_-$ and k_-, respectively, after the k_+ integration. These δ-functions are missed in the naive LF hamiltonian without zero modes (this is very similar to the tadpoles in self-interacting scalar fields). One finds [we subtract here the one-loop result because this allows us to drop the surface term in the complex k_- plane; $\rho^{\text{free}}(\mu^2) = \delta(\mu^2 - \mu_0^2)$, $\rho_1^{\text{free}}(m^2) = \delta(m^2 - m_0^2)$]

$$\left(\Sigma^+ - \Sigma^+_{\text{1-loop}}\right)_{\text{covariant}} = \left(\Sigma^+ - \Sigma^+_{\text{1-loop}}\right)_{\text{canonical LF}}$$

$$+ \frac{g_P^2}{2p_-} \int \frac{d^D k}{(2\pi)^D} \int_0^\infty d\mu^2 \frac{\rho(\mu^2) - \rho^{\text{free}}(\mu^2)}{k^2 - \mu^2 + i\varepsilon}$$

$$- \frac{g_P^2}{2p_-} \int \frac{d^D k}{(2\pi)^D} \int_0^\infty dm^2 \frac{\rho_1(m^2) - \rho^{\text{free}}(m^2)}{k^2 - m^2 + i\varepsilon} \quad (4.15)$$

Since the other components of Σ have no problems from zero modes, this

immediately implies

$$(\Sigma - \Sigma_{\text{1-loop}})_{\text{covariant}} = (\Sigma - \Sigma_{\text{1-loop}})_{\text{canonical LF}}$$
$$\frac{g_P^2 \gamma^+}{2p_-} \int \frac{d^D k}{(2\pi)^4} \int_0^\infty d\mu^2 \frac{\rho(\mu^2) - \rho^{\text{free}}(\mu^2)}{k^2 - \mu^2 + i\varepsilon}$$
$$\frac{g_P^2 \gamma^+}{2p_-} \int \frac{d^D k}{(2\pi)^4} \int_0^\infty dm^2 \frac{\rho_1(m^2) - \rho_1^{\text{free}}(m^2)}{k^2 - m^2 + i\varepsilon} \quad (4.16)$$

This result is very interesting for the following reasons:

- Canonical LF quantization disagrees with covariant perturbation theory.

- The mistake of canonical LF quantization can be compensated by a counterterm to the mass term in the kinetic energy (but not the mass term appearing in the vertex).

- If one adds the wrong counterterm, rotational invariance and parity invariance for physical observables are broken. This can be used as a renormalization condition to "fine-tune" the coefficient of the counterterm.

- The counterterm is related in a simple way to the spectral function of fermions and bosons which are numerically calculable in a canonical LF calculation!

- The boson contribution in Eq. (4.16) can even be expressed in terms of a local VEV: $\delta\Sigma^{\text{boson}} = \langle 0| : \phi^2 : |0\rangle g_P^2 \gamma^+ / 2p_-$. Unfortunately, this is not possible for the term containing the fermionic spectral density, which would read $\delta\Sigma^{\text{fermion}} = \langle 0| : \bar{\psi} \frac{\gamma^+}{i\partial_-} \psi : |0\rangle g_P^2 \gamma^+ / 2p_-$.

Note that in order to obtain the full counterterm necessary to establish agreement between a covariant calculation and a canonical LF calculation, one still has to add the one-loop counterterm — but this should be obvious and can be easily done. Similar statements hold for fermion loops in the boson self-energy. The only difference to the above example is that the difference between a covariant calculation and a canonical LF calculation results in a difference in the bare boson mass; i.e., no space–time symmetries can be used to fine-tune the counterterm. However, the difference can still be related to the spectral density of the fermions. Besides the "contracted seagulls," only disconnected vacuum diagrams — which are irrelevant for the dynamics of physical states — suffer from the zero-mode problem. It is thus also sufficient to tune the vertex mass and the kinetic mass independently and those masses and the boson mass independently from the corresponding coefficients

in the covariant Lagrangian in order to recover equivalence between covariant calculations and canonical LF calculations. Note, however, that (like in the self-interacting scalar theory) all this holds only *after* rendering the transverse momentum integrals finite [e.g., by means of dimensional regularization[66,77] or a transverse lattice (Section 5.3)].

It should also be noted that perturbative zero modes also play a role in higher-twist parton distributions. There they can lead to violations of naive sum rules as discussed in Refs. 53, 54 and 79.

4.3. Gauge Theories

In gauge theories the situation is much less clear than in scalar field theories or Yukawa theories, because of notorious infrared singularities in the LF gauge $A^+ = 0$. Certain attempts have been made to perturbatively renormalize LF QED[66,77,78] and QCD.[80]

In the context of calculations of the electron's anomalous magnetic moment in QED it has been shown (up to three loops in Feynman gauge and up to two loops in LF gauge) that all $k_- \to 0$ singularities in LFPTh cancel — provided one adds up all diagrams that contribute to a given order in the coupling constant.[78] The regulators used were Pauli–Villars regulators or dimensional regularization in the transverse direction. Furthermore, only two extra* counterterms are necessary to render the theory UV-finite: a kinetic mass counterterm for the electron (similar to the one discussed in Section 4.2) and a mass term for the transverse photon field. The numerical result for $(g-2)$ thus obtained agrees with the known result from covariant calculations.

Perturbative LF calculations of vertex functions, which employ a Tamm–Dancoff truncation, were conducted in Ref. 77 for QED and in Ref. 80 for QCD. Due to incomplete cancellations of $k_- \to 0$ singularities in the Tamm–Dancoff approximation, infrared singular counterterm functions were already in lowest nontrivial order necessary to render the results finite.

The first calculation, relevant for asymptotic freedom, was performed in Ref. 81 (four gluon vertex) and Ref. 82 (quark–gluon vertex). Further discussions on renormalization on QCD in LF gauge (but not LF quantization) can be found in Ref. 39. For demonstrations of asymptotic freedom, employing both LF gauge and LF quantization, see Ref. 83 (and references cited therein).

In both types of calculation (LFPTh and LFTD) even perturbatively the structure of the renormalized LF hatniltonian is not known to higher orders. Perhaps the cleanest way to address the problem would be to start from the axial gauge in ε-coordinates in a finite box[41–43] and to approach the LF by

---

*That is, beyond those counterterms which are required in a covariant calculation.

carefully taking the limit $\varepsilon \to 0$ (as in Section 3.3). While it is conceivable that this is feasible in QED, the axial gauge hamiltonian for QCD_{3+1} in a finite box[43] is perhaps too complicated to allow one to study this limit with appropriate care.

4.4. Summary

In the renormalization of LF field theory, one can distinguish three kinds of counterterms. First the usual renormalizations, which can be handled by making the bare coupling constants in the Lagrangian cutoff-dependent. In the following these will be referred to as canonical counterterms. Second, counterterms that have to be added when one is employing a Tamm–Dancoff cutoff. These will be discussed in Section 5.4. Typically, one needs an *infinite* number of counterterms! Third, effects caused by an improper treatment of zero modes in the canonical approach. In those cases, where these effects are now understood the renormalization of zero-mode effects can be accomplished by adding a *finite* number of counterterms that have the structure of tadpole and seagull diagrams with some lines "ending in the vacuum." In general, the zero-mode counterterms are already included in the list of "Tamm–Dancoff approximation counterterms." This means zero-mode effects become irrelevant when one uses a Tamm–Dancoff approximation. However, in the absence of a Tamm–Dancoff approximation, i.e., in calculations without or with negligible restrictions on the Fock space (see Section 5.3) or in perturbation theory if one adds all diagrams to a given order in the coupling, above-mentioned tadpole or seagull counterterms are quite relevant because they are the only counterterms needed besides the canonical counterterms.

5. NONPERTURBATIVE CALCULATIONS

5.1. Discrete Light-Cone Quantization

The most straightforward method for solving bound state problems in the context of LF quantization is discrete light-cone quantization* (DLCQ).[35] For extensive reviews and more references see Refs. 84–86.

The basic idea in DLCQ is as follows (for simplicity we illustrate the method using the example of ϕ^4_{1+1}). One puts the system into an x^--box of

---

*Like the canonical quantization discussed in Section 2, the quantization surface in DLCQ is the plane $x^+ = 0$, i.e., a front or plane — and not a cone. Thus discrete light *front* quantization (DLFQ) would be a more appropriate terminology. However, because of historical reasons, the method has been named DLCQ in the literature.

length L with periodic or antiperiodic boundary conditions*

$$\phi(x^- + L, x^+) = \pm\phi(x^-, x^+) \tag{5.1}$$

In the following, antiperiodic boundary conditions will be used, which implies for the mode expansion

$$\phi(x^-) = \frac{1}{\sqrt{4\pi}} \sum_{k=1}^{\infty} \frac{\left[a_k e^{-ip_-^k x^-} + a_k^\dagger e^{ip_-^k x^-} \right]}{\sqrt{k - \frac{1}{2}}} \tag{5.2}$$

where

$$p_-^k = \frac{2\pi}{L}\left(k - \frac{1}{2}\right) \tag{5.3}$$

The main reason for choosing antiperiodic boundary conditions is that one does not have to worry about the mode with $p_- = 0$. Another reason is that many numerical problems converge faster when antiperiodic boundary conditions are used (compared to periodic boundary conditions with the $p_- = 0$ mode left out). This can be understood in perturbation theory because there are often nonnegligible contributions to Feynman integrals from the region near $p_- = 0$. Let f be some typical function that appears as the argument of some Feynman integral. Then $\varepsilon \sum_{n=-\infty}^{\infty} f\left((n - \frac{1}{2})\varepsilon\right)$ is usually a better approximation to $\int_{-\infty}^{\infty} f(x)$ than $\varepsilon \sum_{n=-\infty}^{-1} f(n\varepsilon) + \varepsilon \sum_{n=1}^{\infty} f(n\varepsilon)$ because in the latter expression the point $n = 0$ is missing compared to the trapezoidal quadrature formula.

In order for $\phi(x)$ to satisfy the canonical commutation relations (see Section 2),

$$[\partial_-\phi(x), \phi(y)]_{x^+=y^+} = -\frac{i}{2}\delta(x^- - y^-) \tag{5.4}$$

we impose the usual commutation relations for the coefficients a_k,

$$[a_k, a_q^\dagger] = \delta_{kq} \tag{5.5}$$

The above expansion is then inserted into the momentum operator

$$P_- = \int_0^L dx^- : \partial_-\phi\partial_-\phi :$$

$$= \frac{2\pi}{L} \sum_{k=1}^{\infty} a_k^\dagger a_k \left(k - \frac{1}{2}\right) \tag{5.6}$$

---

*In the presence of interactions which contain odd powers of ϕ one has no choice and one must use periodic boundary conditions — otherwise momentum conservation is violated at the boundary!

and the hamiltonian

$$P_+ = \int_0^L dx^- \frac{m^2}{2} : \phi^2 : + \frac{\lambda}{4!} : \phi^4$$

$$= \frac{L}{2\pi} (T + V) \tag{5.7}$$

where

$$T = \frac{m^2}{2} \sum_{k=1}^{\infty} \frac{a_k^\dagger a_k}{k - \frac{1}{2}} \tag{5.8}$$

is the kinetic term and

$$V = \frac{\lambda \delta_{P_f P_i}}{8\pi 4!} \tag{5.9}$$

$$\times \sum_{k_1,k_2,k_3,k_4=1}^{\infty} \frac{: \left(a_{k_1}^\dagger + a_{k_1}\right) \left(a_{k_2}^\dagger + a_{k_2}\right) \left(a_{k_3}^\dagger + a_{k_3}\right) \left(a_{k_4}^\dagger + a_{k_4}\right) :}{\sqrt{k_1 - \frac{1}{2}} \sqrt{k_2 - \frac{1}{2}} \sqrt{k_3 - \frac{1}{2}} \sqrt{k_4 - \frac{1}{2}}}$$

is the interaction term; $\delta_{P_f P_i}$ is a momentum conserving Kronecker δ. Since the length of the box completely factorizes, it is useful to work with the rescaled operators

$$K = P_- \frac{L}{2\pi} \tag{5.10}$$

$$H = P_+ \frac{2\pi}{L} \tag{5.11}$$

Since the momenta of all excitations are discrete and positive, the Fock space is finite dimensional for all K. Thus, at least in principle, one can now proceed as follows: for fixed K (K and H commute) one diagonalizes H (which is a finite matrix for finite K). From the eigenvalues E_i one computes the invariant masses $M_i^2 = 2KE_i$ and from the eigenstates one can compute other physical observables (like parton distributions). In general, physical observables thus computed will of course depend on the "resolution" K. The continuum limit is obtained by extrapolating to $K \to \infty$. The diagonalization is generally done using brute force matrix diagonalization or, if one is only interested in the lowest states, using the Lanczos algorithm[87]

At this point one encounters a problem that is inherent to hamiltonian systems: *the dimension of multiparticle states in the Fock space expansion grows exponentially with the number of particles.* The number of particles, as well as the number of states for a single particle are both limited by the

longitudinal momentum K, i.e., the dimension of the Fock space basis shows factorial growth with K. Fortunately, in $1 + 1$ dimensional examples, the factorial growth sets in only rather slowly and numerical convergence for typical observables can be obtained before the size of the matrices becomes a problem. DLCQ was enormously successful in many $1 + 1$ dimensional field theories.[32,33,44–49,88,89] In all cases, where results from other approaches to field theories were available, agreement could be shown within numerical uncertainties (QED_{1+1}: Refs. 90 vs. Refs. 44 and 45* QCD_{1+1}: Ref. 94 vs. Refs. 46 and 47 sine-Gordon model: Ref. 95 vs. Ref. 33). Beyond reproducing known results, DLCQ has been used to calculate new and interesting results in QCD_{1+1}: the most notable results are the existence of a nucleon–nucleon bound state and the analysis of the nuclear quark distribution in comparison with the nucleon quark distribution. Not only does the $1 + 1$ dimensional "deuteron" exhibit an EMC-effect, but it can also be understood analytically due to the simplified dynamics in $1 + 1$ dimensions.[48] Typical Euclidean lattice calculations are too "noisy" to even demonstrate binding of hadrons. Another remarkable result from DLCQ calculations in QCD_{1+1} dimensions is "Anti-Pauli-Blocking"[49,89]: contrary to the naive expectation, sea quarks in nucleons in QCD_{1+1} tend to have the same flavor as the majority flavor among the valence quarks (i.e., more $\bar{u}$ than $\bar{d}$ in a nucleon $\psi_{\text{valence}} = uud$).

In $2 + 1$ or $3 + 1$ dimensions the situation changes drastically, because there the exponential growth is much more rapid. The basic reason is that there are now transverse degrees of freedom besides the longitudinal degrees of freedom. Suppose that each particle can occupy N states for each spatial dimension. Then the Fock space basis size grows like $N^{3N_{\text{part}}}$ with the number of particles in $3 + 1$ dimensions, while the corresponding growth would be only $N^{N_{\text{part}}}$ in $1 + 1$ dimensions. For a concrete example (ϕ^4 with antiperiodic boundary conditions in the longitudinal direction) this works out as follows. For a longitudinal momentum $K = \frac{15}{2}$ (8 longitudinal momentum states accessible) the Fock space basis size is 27. If one has just two transverse degrees of freedom (e.g., two points in the transverse direction) the basis size grows to 426. For 8 x 8 = 64 degrees of freedom in the transverse direction, that number grows to $6 \cdot 10^{15}$. These astronomical numbers clearly demonstrate that any direct matrix diagonalization approach or even a Lanczos-type algorithm is doomed to fail because one is not even able to store the wave function in a computer.[34]

---

*However, there is still a 1% difference in the fundamental meson mass for the term linear in m_e in QED_{1+1} as calculated from bosonization[90] and in LF quantization.[91] It is not clear whether this deviation is due to the finite Fock space truncation or whether this is a real problem.[92,93]

The most simple (and perhaps most drastic) way out of this dilemma is to impose additional cutoffs, like restricting the number of particles. Typically, this means restricting the Fock space to 3 (perhaps 4) particles or less.[37,51] In QED, since the coupling is small, this is a good approximation. However, to the same order in α within which the 3-particle truncation is a good approximation one can calculate the parton distributions analytically.[96] That is, even in QED there is not much point in doing numerical DLCQ calculations with Fock space truncations to the lowest nontrivial order! In QCD, where one faces an intrinsically strong coupling problem, restricting the Fock space to the lowest nontrivial component seems entirely useless. For example, even if one allows up to 4 particles (which is about the maximum that can be handled numerically using the Lanczos algorithm), this means one allows at most one gluon in addition to the three valence quarks in a proton. That is, there is no chance one can "see" any effects from nonlinear gluon–gluon couplings.*

It should be emphasized that this problem is not specific for LF field theories, but occurs in many hamiltonian approaches to field theory — and in many cases could be solved. Thus there are many numerical methods available which can potentially be useful in overcoming the difficulties associated with exponential basis size growth.

5.2. Functional Integration on a Longitudinal Lattice

Functional integrals on Euclidean lattices have been very successful in solving ground state properties of QCD (e.g., vacuum properties, hadron masses, and ground state matrix elements). However, since two points on a Euclidean lattice are always separated by a space-like distance, it is only very indirectly possible to extract information about light-cone correlation functions from these calculations. Of course, this is because in conventional Euclidean field theory $\exp(-\beta P_E^0)$ is used to project on the ground state wave function of P^0 at equal time. Thus as a caveat one might be tempted to consider a similar formalism for LF hamiltonians. Suppose one discretizes the x^- direction† and uses a functional integral to project on the ground state of P_+.[97,98] This results in an immediate problem because the LF energy *decreases* with increasing momentum [$P_+ = M^2/2P_-$ in the continuum, on a lattice there is a minimum for $P_- = \mathcal{O}(1/a)$]. Due to Bragg reflections, momentum is not conserved and the particles tend to accumulate near the minimum. However, since the momentum near that minimum is of the order of the inverse lattice spacing, the particles always "see" the lattice and no

---

*A caveat to this pessimistic point of view will be discussed in Section 5.4.
†The transverse coordinates are irrelevant in this argument.
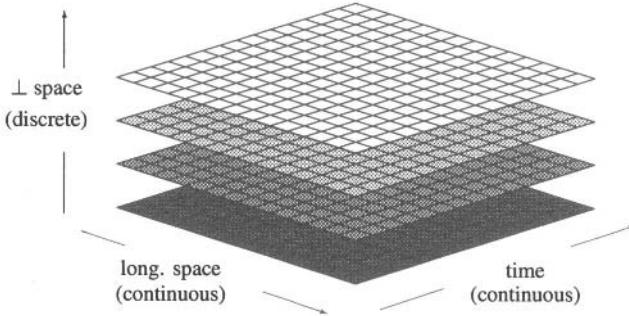
Fig. 5.1. Space–time view of a transverse lattice.

meaningful continuum limit is obtained. It is conceivable that this problem can be cured by adding a Lagrange multiplier proportional to the total LF momentum to the lattice action (in the continuum limit this amounts to minimizing $\tilde{P}_+ = P_+ + \lambda P_-$ instead of P_+). However, this idea will not be investigated here any further. Another difficulty of the longitudinal LF lattice is species doubling for bosons[97]!

5.3. Hamiltonian Monte Carlo on a Transverse Lattice

While Monte Carlo calculations for longitudinal LF lattices seem to be plagued with difficulties, this is not the case for the transverse lattice.[34] On a transverse lattice one keeps the longitudinal directions (x^+ and x^-) continuous, while discretizing the transverse coordinate (Fig. 5.1).[99]

For simplicity, let us consider self-interacting scalar fields in $2 + 1$ dimensions on such a transverse lattice characterized by the action

$$A^{\text{cont.}} = \int d^3x \left[\sum_{\mu=0}^{2} \frac{\partial_\mu \phi \partial^\mu \phi}{2} - \frac{m^2}{2}\phi^2 - \mathcal{L}_{\text{int}}(\phi) \right] \tag{5.12}$$

Upon discretizing the transverse direction (spacing a) one thus obtains

$$A^{\perp \text{ latt.}} = a \sum_n \int d^2x \tag{5.13}$$

$$\times \left[\sum_{\mu=0}^{1} \frac{\partial_\mu \phi_n \partial^\mu \phi_n}{2} - \frac{(\phi_{n+1} - \phi_n)^2}{2a^2} - \frac{m^2}{2}\phi_n^2 - \mathcal{L}_{\text{int}}(\phi_n) \right]$$

Up to a factor of a (which can be absorbed into a redefinition of the field ϕ_n), Eq. (5.14) looks like the action for a multiflavor theory in $1 + 1$ dimensions

(where the site index n corresponds to the "flavor" index). In the next step one constructs the DLCQ hamiltonian for this "multiflavor" $1+1$ dimensional theory. The important point here is that the action is local in the transverse direction, i.e., there are only nearest neighbor interactions. Since the DLCQ hamiltonian is thus also local,

$$H_{\text{DLCQ}} = \sum_n [H_n + V_{n,n+1}] \tag{5.14}$$

one can apply many Monte Carlo techniques which have been developed for other hamiltonian systems (see e.g., Ref. 100). One technique which turns out to be particularly useful for LF hamiltonians on a transverse lattice is the ensemble projector Monte Carlo technique[101] based on the so called checkerboard decomposition of the hamiltonian.[102] Using locality of the hamiltonian one can write

$$H_{\text{DLCQ}} = H_a + H_b \tag{5.15}$$

where

$$H_a = \sum_{n=1,2,3,\ldots} \frac{H_n}{2} + \sum_{n=1,3,5,\ldots} V_{n,n+1} = H_{1,2} + H_{3,4} + \ldots$$

$$H_b = \sum_{n=1,2,3,\ldots} \frac{H_n}{2} + \sum_{n=2,4,6,\ldots} V_{n,n+1} = H_{2,3} + H_{4,5} + \ldots \tag{5.16}$$

In other words, the DLCQ hamiltonian can be written as a sum of two terms, each of which can be written as a direct sum of two-site hamiltonians. The point to all this is that while the dimension of the space on which H_{DLCQ} acts is astronomical, the two-site hamiltonians act only on a very small Hilbert space [for our above example with $K = \frac{15}{2}$ and say 16 transverse sites: $\dim(H_{\text{DLCQ}}) = 7.8 \cdot 10^8$ but $\dim(H_{n,n+1}) = 426$]. The method is called checkerboard algorithm because one approximates the time evolution operator of the system by alternating infinitesimal time evolution operators generated by H_a and H_b respectively,

$$e^{-\varepsilon H_{\text{DLCQ}}} = e^{-\frac{\varepsilon}{2} H_a} e^{-\varepsilon H_b} e^{-\frac{\varepsilon}{2} H_a} + \mathcal{O}(\varepsilon^3) \tag{5.17}$$

If one axis of the checkerboard is the discretized space direction and the other the time, Eq. (5.16) can be interpreted as if interactions between sites occur only across the black squares.[102]

Before we explain how the infinitesimal time evolution operators are multiplied together, let us pause here for a moment and understand the advantage

of the transverse lattice with DLCQ over the longitudinal lattice discussed in
the previous section. The main cause of the problem in the previous section
was lack of longitudinal momentum conservation. In DLCQ P_-, the longitu-
dinal momentum, is manifestly conserved. Furthermore, P_- is just the sum
of momenta at each site

$$P_- = \sum_n P_-^n \tag{5.18}$$

and the checkerboard algorithm is compatible with longitudinal momentum
conservation ($[H_a, P_-] = [H_b, P_-] = 0$). In other words, with DLCQ on
a transverse lattice, longitudinal momentum is conserved at each step of the
calculation. Hence, one can minimize P_+ while keeping P_- manifestly fixed
and there are no "runaway solutions."

   In the actual calculations one uses Monte Carlo techniques to calculate
$\left(e^{-\varepsilon H}\right)^N |\psi_i(K)\rangle$ by alternate application of $e^{-\frac{\varepsilon}{2}H_a}$, $e^{-\varepsilon H_b}$, $e^{-\varepsilon H_a}$, ...,
$e^{-\frac{\varepsilon}{2}H_a}$ to $|\psi_i(K)\rangle$. Here $|\psi_i(K)\rangle$ is an initial guess for the ground state wave
function with longitudinal momentum K. For $N \to \infty$ one thus obtains an
approximation (because ε is finite, the result is not exact) to the ground state
hadron with the same good* quantum numbers as $|\psi_i(K)\rangle$. One very useful
technique is the ensemble projector Monte Carlo method,[100,101] which works
as follows for these systems:

(1) Let $|n\rangle$ be a complete set of states
    (here product basis of Fock state bases at each site).

(2) Make a good guess for $|\psi_i(K)\rangle$ (here a valence state with $P_\perp = 0$:
    $|\psi_i(K)\rangle = \sum_{n_\perp} a^\dagger_{K,n_\perp} |0\rangle$).

(3) Start from ensemble $|i_\nu^{(0)}\rangle$ of states (from set $|n\rangle$).

(4) For each $|i_\nu^{(0)}\rangle$ select a new state $|i_\nu^{(1)}\rangle$ with probability

$$W(i_\nu^{(1)}, i_\nu^{(0)}) = \frac{|\langle i_\nu^{(1)}|e^{-\frac{\varepsilon}{2}H_a}|i_\nu^{(0)}\rangle|}{\sum_n |\langle n|e^{-\frac{\varepsilon}{2}H_a}|i_\nu^{(0)}\rangle|}$$

and calculate the score

$$S_\nu^{(1,0)} = \frac{\langle i_\nu^{(1)}|e^{-\frac{\varepsilon}{2}H_a}|i_\nu^{(0)}\rangle}{W(i_\nu^{(1)}, i_\nu^{(0)})}$$

---

*Of course, only those quantum numbers which are associated with exact symmetries of DLCQ
 on a transverse lattice (like C parity or baryon number in QCD) are relevant here.

note: $W(i_\nu^{(1)}, i_\nu^{(0)})$ factorizes into two-site probabilities
$\hookrightarrow$ local (one pair of sites at a time) "updating" possible.

(5) Replicate states with multiplicity:
$$\int \left[\frac{|S_\nu^{(k,k-1)}|}{\bar{S}} + \text{random number} \in (0; 1) \right]$$
($\bar{S}$: av. score).

Thus paths with large scores contribute with multiple weight, while paths with small scores get eliminated.

(6) Repeat while alternating H_a and H_b
($\frac{1}{2}$ in exponent only in first and last step!).

(7) Observables from ensemble average, e.g., energy of ground state hadron:
$$E_0 = \lim_{N \to \infty} \frac{\sum_\nu \langle \psi_f(K)|H|i_\nu^{(N)}\rangle \, \text{sign}\left[S_\nu^{(N,N-1)} \cdot \ldots \cdot S_\nu^{(1,0)} \right]}{\sum_\nu \langle \psi_f(K)|i_\nu^{(N)}\rangle \, \text{sign}\left[S_\nu^{(N,N-1)} \cdot \ldots \cdot S_\nu^{(1,0)} \right]}$$

other observables (e.g., an observable diagonal in the basis):
$$\langle \psi_0(K)|\hat{O}|\psi_0(K)\rangle =$$
$$\lim_{\substack{M \to \infty \\ N \to \infty}} \frac{\sum_\nu \langle \psi_f(K)|i_\nu^{(N+M)}\rangle \, \text{sign}\left[S_\nu^{(N+M,N+M-1)} \cdot \ldots \cdot S_\nu^{(1,0)} \right] \langle i_\nu^{(N)}|\hat{O}|i_\nu^{(N)}\rangle}{\sum_\nu \langle \psi_f(K)|i_\nu^{(N+M)}\rangle \, \text{sign}\left[S_\nu^{(N+M,N+M-1)} \cdot \ldots \cdot S_\nu^{(1,0)} \right]}$$

In this Monte Carlo procedure, one only has to store the ensemble of states at one "timeslice" plus the result of the measurement of the observable after N slices. Thus, at least in principle, one can handle very large lattices. The main advantages of the transverse lattice are as follows[34]:

- Longitudinal momentum is manifestly conserved $\to$ no runaway solutions.

- Parton distributions are diagonal in the DLCQ-basis.

- LF vacuum is trivial $\to$ no statistical fluctuations from updating the vacuum far away from physical states on huge lattices.

- Species doubling for fermions occurs only for the latticized transverse dimensions $\to$ can be easily compensated by staggering.[103]

- Excited states are suppressed by the square of their masses:
$\exp(-N\epsilon P_+) = \sum_n |n\rangle \exp(-N\epsilon M_n^2/2P_-)\langle n|$ instead of
$\exp(-N\epsilon P^0) = \sum_n |n\rangle \exp(-N\epsilon M_n)\langle n|$ which one encounters in a conventional hamiltonian formulation.

It is interesting to see how confinement emerges on the transverse lattice in the limit of large lattice spacing: In this limit, the coupling between the sheets is weak and the energy scale associated with link field excitations is high. Therefore, when one separates two test charges in the longitudinal direction, the transverse lattice behaves similar to QCD_{1+1} and linear confinement results trivially. For transverse separations between the charges, a different mechanism is at work. Gauge invariance demands that the two charges are connected by a string of link fields. In the limit of large spacing the link fields fluctuate only little, and the energy of such a configuration can be estimated by counting the number of link fields needed to connect the charges, which again yields linear confinement.

Some of the disadvantages of the transverse lattice are: Since $x^+ \rightarrow ix^+$ is *not* a Wick rotation (it is just a mathematical trick to project on the ground state of P_+), the metric is not Euclidean and thus propagators oscillate. Hence, negative scores occur already for bosons which leads to an increase in the statistical fluctuations. However, these negative scores turn out to have only a small statistical weight and the resulting "sign-problem" is not serious. Very often in LF calculations, large cancellations occur between different terms in the hamiltonian. For example, the instantaneous photon exchange has a $1/q_-^2$ singularity which is canceled by vertex factors in photon exchange. In general, it is difficult to obtain such cancellations from a Monte Carlo calculation. Another difficulty is that gauge invariance on a lattice can only be maintained if one introduces link fields. On a transverse lattice this amounts to introducing $1 + 1$-dimensional gauged nonlinear sigma model fields on each link.[99] Constructing a Fock space basis out of these nonlinear degrees of freedom and calculating appropriate matrix elements is a nontrivial task.[104,105]

The sign problem associated with fermions is a notorious difficulty for Monte Carlo algorithms: due to the minus sign in exchange terms, the infinitesimal time evolution operator tends to contain many negative matrix elements. This very general problem is also expected to afflict Mont Carlo calculations on transverse lattices. However, since the LF vacuum is trivial, there are no sign fluctuations from Z-graphs and vacuum diagrams. Thus one expects that the sign problem on the LF is less severe than usual. Whether this improvement is sufficient to render fermions tractable on transverse lattices has not yet been investigated.

Obviously, the transverse lattice lacks manifest rotational invariance, which must be restored in the process of renormalization. Recently, a technique has been described that allows easy computation of the potential between infinitely heavy quarks in a LF framework.[106] Demanding rotational invariance for this observable may prove to be a powerful tool in such a procedure.

5.4. Light-Front Tamm-Dancoff

As we have discussed already in Section 5.1, the dimensionality of the Fock space grows dramatically as one includes higher Fock components. Clearly, since α_S is fairly large at a low momentum scale, a numerical solution of bound state problems in QCD (which includes all scales) necessarily involves many Fock components. In this section we will discuss the light-front Tamm–Dancoff (LFTD) approach to LF problems (for a comprehensive review see Ref. 107). The basic idea is very simple[108,109]: Hadrons are complicated objects only if one tries to build them in terms of bare quarks and gluons whose masses and couplings are renormalized at a scale of 1 GeV or higher. In terms of collective excitations (constituent quarks) ground state hadrons are rather simple. One of the problems with the constituent quark model is that *a priori* the interactions among the quarks are *ad hoc*.

The goal of LFTD field theory is to systematically eliminate higher Fock components and high energy degrees of freedom.* As one goes to lower and lower scales the interaction between the (dressed) constituents thus becomes more and more complicated. If the whole program is successful, constituent quarks will emerge as the quasiparticles of QCD at intermediate energies. A major virtue of using LF quantization in this approach is that it stays close both to physical intuition (which may prove very helpful when it comes to developing variational methods to analyze the hamiltonian) as well as to experimental observables at large momentum transfer (useful for phenomenological applications).

A systematic Fock space expansion, based on a hamiltonian formulation, for field theory was originally developed by Tamm[111] and independently by Dancoff.[112] It turns out that such an approach is doomed to fail if the perturbative ground state (the starting point of the expansion) is too far from the actual ground state. In such a situation one needs very (or infinitely) complicated Fock states just to build the ground state. LF quantization is advantageous at this point, because the vacuum of a LF hamiltonian is trivial.

In fact, because of the vacuum, LF quantization is probably the *only* framework where such a program can possibly work.

In practice, even within LF quantization, it is of course not possible to integrate out high energy states and higher Fock states exactly. Instead one writes down a catalog of all interaction terms that are allowed by power

---

*This procedure is explicitly demonstrated for the simple example of ϕ^4_{3+1} in the two-particle sector in Ref. 110.

counting[113,114]: on the LF there are two length scales x^- and $x_\perp$. The engineering dimensions of the various operators and terms that enter the LF hamiltonian in 3+1 dimensions can be easily derived from free field theory[114] (ϕ stands for a scalar field or for $A_\perp$ — the transverse gauge field components which have the same engineering dimension as scalar fields; $\psi^{(+)}$ is the dynamical component of a fermion field):

$$\partial_- = \left[\frac{1}{x^-}\right], \quad \partial_\perp = \left[\frac{1}{x_\perp}\right], \quad m = \left[\frac{1}{x_\perp}\right]$$

$$\psi^{(+)} = \left[\frac{1}{x_\perp \sqrt{x^-}}\right], \quad \phi = \left[\frac{1}{x_\perp}\right] \tag{5.19}$$

The hamiltonian and the hamiltonian density have dimensions

$$H = \left[\frac{x^-}{x_\perp^2}\right], \quad \mathcal{H} = \left[\frac{1}{x_\perp^4}\right] \tag{5.20}$$

Thus all allowed terms without fermion fields are[114]

$$m^3\phi, \ m^2\phi^2, \ \partial_\perp^2\phi^2, \ m\phi^3, \ \phi^4 \tag{5.21}$$

Including fermion fields one obtains[114]*

$$\frac{1}{\partial_-}\psi^{(+)\dagger}\Gamma\left\{m^2, \partial_\perp^2, m\vec{\gamma}_\perp\vec{\partial}_\perp, m\phi, \phi^2\right\}\psi^{(+)} \tag{5.22}$$

$$\frac{1}{\partial_-^2}\psi^{(+)\dagger}\Gamma_1\psi^{(+)}\psi^{(+)\dagger}\Gamma_2\psi^{(+)} \tag{5.23}$$

(Γ, Γ_1, and Γ_2 are some Dirac matrices). Unfortunately, this is not the whole story. Already free LF-field theory is nonlocal in the longitudinal direction {e.g., for scalar fields because of the fundamental commutator $[\phi(x^-, x^+), \phi(y^-, x^+)] = -\frac{i}{4}\varepsilon(x^- - y^-)$ and for fermions because an inverse derivative of ∂_- appears in the kinetic energy term (2.28)}. Thus longitudinal locality is no longer a restriction on the functional form of the possible terms in the hamiltonian. As a result, any of the operators in the above catalog may be multiplied by arbitrary functions of ratios of longitudinal momenta! In fact, there are examples known where complicated functions of ratios of incoming and outgoing momenta, multiplying a four-fermion counterterm, are necessary to cancel UV divergences.[115]

---

*See the discussion in Ref. 114 why terms with negative powers of m are excluded.

As a result of this infinitely complicated counterterm structure, it seems one loses predictive power and one thus might be forced to abandon LFTD as a *fundamental* theory of hadrons. It should be emphasized that, even if one does have to abandon LFTD as a fundamental theory, it might still have many virtues in parton phenomenology. However, there has been recent progress toward understanding how to apply renormalization group techniques to LFTD that may help restore its predictive power[107] (for an excellent pedagogical review, see Ref. 83).

Unless one works with the full hamiltonian, nonperturbative bound state calculations in QCD almost inevitably violate gauge invariance.* Therefore, if one wants to derive a constituent picture from QCD, one is forced to allow that explicit gauge invariance is violated: *gauge invariance becomes a hidden symmetry*.[83,107] In LFTD one introduces cutoffs that violate symmetries which normally prevent a constituent picture from arising (gauge invariance and full Lorentz invariance). In a sense, the counterterm functions that complicate renormalization offer a possible resolution of apparent contradictions between the constituent picture and QCD.[83]

The technique to remove cutoff dependence from physical results is renormalization: for example, the functions of momentum fractions that appear in the relevant and marginal operators can be fixed by demanding covariance and gauge invariance in physical observables. An alternative way to fix the marginal and relevant counterterms is *coupling constant coherence* (CCC): one insists that functions appearing in noncanonical relevant and marginal operators are not independent functions of the cutoff, but depend on the cutoff implicitly through their dependence on canonical couplings.[83,116] This automatically fixed the way in which new variables evolve with the cutoff, and it also fixes their value at all cutoffs if one insists that the new counterterms vanish when the canonical couplings are turned of.[83] Remarkably, in the examples studied in Ref. 116, 117, this procedure provided the precise values for the noncanonical terms that were required to restore Lorentz covariance for physical observables. For an explicit example for CCC, the reader is referred to Ref. 83.

Even without assuming CCC, one can employ renormalization group techniques[118] to help determine the counterterm functions: using the powerful tool of trial and error, one makes an ansatz for these functions, which one can improve by repeatedly applying renormalization group transformations to the effective LF hamiltonians with these functions included. The fact that the QCD hamiltonian should be an ultraviolet stable fixed point under these transformations can be exploited to improve the original ansatz for the

---

*Lattice gauge theory being the only exception.

counterterm functions.[107] Probably, such transformations alone are not suf-
ficient to completely determine the renormalized LF hamiltonian for QCD,
but one can improve this approach considerably by using perturbation theory,
CCC, and perhaps phenomenology to guide the ansatz functions used in the
renormalization group approach to LF hamiltonians.

Another promising idea in the context of LFTD is the *similarity
transformation.*[119] Whenever one derives an effective hamiltonian by elim-
inating states above a certain cutoff perturbatively, one faces small energy
denominators, and thus large and uncertain corrections, for states that are
close to (and below) the cutoff. This feature makes it very difficult to repeat-
edly apply renormalization group transformations because matrix elements of
states near the cutoff are large. To resolve this problem, Glazek and Wilson
have suggested applying a cutoff to *energy differences* instead of to *single
particle energies.* By construction, this resolves the problem of small energy
denominators, but it also provides a band diagonal hamiltonian. The *simi-
larity transformation* exploits this type of cutoff and thus provides a way to
apply renormalization group techniques to LF hamiltonians (and other many
body problems).[119]

6. SUMMARY, CONCLUSIONS, AND OUTLOOK

LF field theory is a very promising approach toward calculating correla-
tion functions along a light-like direction. Such correlation functions appear
in the theoretical analysis of a variety of hard scattering processes, such as
deep inelastic lepton–hadron scattering and asymptotic form factors. Proba-
bly the most intriguing and controversial property of LF hamiltonians is the
triviality of the ground state. Recent developments indicate that LF hamil-
tonians must be regarded as effective hamiltonians in the sense that some
of the interactions acquire nonperturbative renormalizations with coefficients
proportional to vacuum condensates. So far one understands the LF vacuum
and is able to construct the effective LF hamiltonian only in a few toy models.
However, in these examples only a finite number of condensates are necessary
to completely specify the hamiltonian. It would be extremely useful if one
could construct and approximately solve such an effective LF hamiltonian for
QCD, not only for the analysis of hard processes, but also for our understand-
ing of low energy QCD: due to the triviality of the LF vacuum, a constituent
picture makes sense and an effective LF hamiltonian for QCD would offer
the opportunity for deriving a constituent picture as an approximation to the
QCD bound state problem.

Three mainstream directions can be distinguished in the endeavor toward

constructing a LF hamiltonian for QCD: First, a *fundamental* approach where all zero modes are included as dynamical degrees of freedom. Second, an *effective* approach where one attempts to absorb all zero modes and associated vacuum effects into *effective* interactions and coupling constants. Third, the *LF Tamm–Dancoff* approach, where not only vacuum effects but also effects from high energy and high Fock components are "integrated out" and absorbed into effective interaction terms. In the *fundamental* approach (this includes all formulations of LF field theory where explicit zero-mode degrees of freedom are included) the vacuum as well as the physical particle states are complicated and one partly loses the dynamical advantages of the LF framework. While it seems easier to construct the hamiltonian than in the other two approaches, the main difficulty of the *fundamental* approach lies in the fact that the equations of motion are extremely complicated. It is not clear whether such an approach provides any computational advantage over a conventional hamiltonian approach. Nevertheless, it is very useful to pursue this approach further in order to provide a solid theoretical basis for other, more practical, approaches to LF field theory. For example, studies that include zero modes can be useful for deriving an ansatz for the effective LF hamiltonian in the large volume limit.

The *LF Tamm–Dancoff* approach corresponds to the other extreme. The vacuum is trivial and the physical particle states are very simple — by construction they contain only the low energy effective degrees of freedom. A major virtue of this approach is that it stays close to physical intuition and thus potentially offers a connection between the constituent picture and QCD.[83] While the *LF Tamm–Dancoff* approach is thus very appealing from the intuitive point of view its main disadvantage is the enormous complexity of the effective Tamm–Dancoff hamiltonian. In principle, an infinite number of counterterms are possible. These counterterm functions are heavily constrained by imposing Lorentz covariance on physical observables or by demanding cancellation of unphysical divergences. However, so far it is not clear to what extent one can employ renormalization group techniques to constrain the possible interactions to the point where only a few (instead of infinitely many) free parameters enter the LF Tamm–Dancoff hamiltonian of QCD. The second (*effective,* in the sense of zero-mode free) approach toward constructing the LF hamiltonian for QCD stands in between the other two in several respects. The vacuum is trivial but physical particles will in general have a complicated wave function. Some of the interactions in the effective LF hamiltonian have coefficients proportional to vacuum condensates. Those can either be regarded as free parameters or (in some cases) they can be determined from self-consistency conditions. Surprisingly, in those cases where the construction of such an effective hamiltonian has been accomplished, al-

ready a finite number of condensates is sufficient to specify the hamiltonian.* This is a very encouraging result. Perturbative calculations up to two loops indicate a similar result for QED, where the two loop calculations do not require any counterterms which are not already present at the one loop level. LF perturbation theory in QCD has so far only been performed up to one loop.

Although there has been considerable progress recently, so far none of these three approaches has been successful to the point where it was possible to construct a useful LF hamiltonian for QCD. The initial optimism about LF quantization, spurred by the very successful application to $1 + 1$ dimensional field theories, was premature. Much work remains to be done before LF quantization can be applied to QCD.

For example, it is still not completely understood to what extent LF hamiltonians, with a trivial vacuum, can account for the phenomenon of spontaneous symmetry breaking. The only examples where this subject seems to be mostly understood are ϕ^4 theory in $1 + 1$ dimensions and field theories in the mean field approximation. It would be interesting to study cases where the order parameter for the symmetry breaking does not enter the hamiltonian — which is, for example, the case in the spontaneous breakdown of chiral symmetry in QCD.

A possibly related issue, which requires further study, concerns the *noncovariant counterterms.* In the context of perturbation theory it has been shown that a finite number of such counterterms are necessary in the bare hamiltonian to recover full Lorentz covariance for physical observables. However, so far it has not been demonstrated that the proposed counterterms are sufficient to restore Lorentz covariance for physical observables in a nonperturbative calculation.

Within the context of LF Tamm–Dancoff it is still necessary to demonstrate that the renormalization group, combined with constraints from Lorentz invariance, is sufficient to fix the infinite number of counterterms which are possible on general grounds.

For the transverse lattice approach to be useful, it must be shown that the fermion sign problem, which usually limits hamiltonian Monte Carlo calculations with fermions considerably, is tractable. Since vacuum fluctuations are suppressed in LF quantization, any sign problems arising from vacuum diagrams are trivially absent. While this is a very encouraging observation, it resolves only part of the problem — sign problems arising from exchange diagrams within a hadronic state are of course still there. Another difficulty

---

*This approach should not be confused with the standard QCD-sum rules approach to the strong interactions,[120] where one does *not* solve a hamiltonian and where practically all the dynamics is buried in the condensates. Hence it is not surprising that less condensates are necessary as an input in the LF effective hamiltonian approach than in the sum rule approach.

for transverse lattice calculations occurs because gauge invariance on such a lattice requires the introduction of $1 + 1$-dimensional link fields. One must learn to work with these "nonlinear sigma model" degrees of freedom in the context of LF quantization before one can apply the transverse lattice to QCD.

Besides QCD oriented applications of the LF formalism, it may turn out to be very useful to consider phenomenological and/or more nuclear physics oriented applications as well. For example, it may be interesting to reconsider the pion contribution to nuclear structure functions[121] from the point of view of LF quantization. On the one hand, this could be helpful in clarifying the role of binding effects in such calculations. On the other hand, such works may help to demonstrate the usefulness of LF quantization to people who are not directly involved in the field.

LF quantization is very closely related to the *infinite momentum frame* formulation of field theory. Intuitively one would thus expect that the LF formulation of QCD offers a new theoretical approach to relativistic heavy ion collisions. So far, this connection has been exploited only very little.[122]

ACKNOWLEDGMENTS

7. APPENDIX: THE DIRAC-BERGMANN FORMALISM

In this appendix, a brief introduction to the Dirac–Bergmann quantization procedure[123–125] is given. Quite generally, it replaces the canonical quantization procedure in the presence of constraints. However, it can also be used to derive the correct fundamental commutation relations for theories where the Lagrangian contains at most linear terms in the time derivative.*

This is, for example, the case for many field theories when expressed in terms of LF variables.[127] For example, for a noninteracting massive scalar field in $1 + 1$ dimensions one obtains

$$\mathcal{L} = \partial_+ \phi \partial_- \phi - \frac{m^2}{2} \phi^2 \tag{7.1}$$

---

*It should be noted that, in the latter case, alternate treatments are possible as well.[126]

which contains no terms quadratic in $\partial/\partial x^+$. Naive canonical quantization, i.e.,

$$\pi = \frac{\delta \mathcal{L}}{\delta \partial_+ \phi} = \partial_- \phi \tag{7.2}$$

$$[\pi(x), \phi(y)]_{x^+ = y^+} = -i\delta(x^- - y^-) \tag{7.3}$$

with

$$P_+ = \int dx^- T_{+-} = \int dx^- \frac{m^2}{2} \phi^2 \tag{7.4}$$

yields

$$-\partial_\mu \partial^\mu \phi = -2\partial_+ \partial_- \phi = -i\left[P_+, \partial_- \phi\right] = 2m^2 \phi \tag{7.5}$$

Clearly, Eq. (7.5) differs from the (correct) Euler–Lagrange equation $-2\partial_+ \partial_- \phi = m^2 \phi$ by a factor of two.[20] This mistake arises because the kinetic term in Eq. (7.1) is only linear in the time derivative ∂_+. Thus the equation relating the canonical momenta to the fields (7.2) is a constraint equation since it contains no time derivative and therefore the phase space variables $\pi(x)$ and $\phi(x)$ for a given time are not independent.

    Quantizing a system with constraints is a nontrivial task. Fortunately, the Dirac–Bergmann algorithm provides a step by step prescription for the proper quantization procedure. The basic steps of this procedure will be illustrated in an example below. To keep the discussion simple, zero modes will be deliberately left out in the discussion. A complete discussion, which includes zero modes, can be found in Refs. 128–131. Furthermore, the discussion here will be restricted to a system with a finite number of degrees of freedom [which can, for example, be obtained from Eq. (7.1) by discretizing the x^- direction]

$$L(\phi_i, \dot{\phi}_i) = \sum_{i,j=1}^{N} A_{i,j} \dot{\phi}_i \phi_j - \sum_i V(\phi_i) \tag{7.6}$$

with $A_{ij} = -A_{ji}$ (the symmetric part of A_{ij} corresponds to a total time derivative and can be subtracted). The canonical momenta are given by

$$\pi_i = \frac{\partial \mathcal{L}}{\partial \dot{\phi}_i} = \sum_j A_{ij} \phi_j \tag{7.7}$$

with Poisson brackets

$$\{\phi_i, \pi_j\} = \delta_{ij}$$
$$\{\phi_i, \phi_j\} = \{\pi_i, \pi_j\} = 0 \tag{7.8}$$

Equation (7.7) does not contain any time derivative, i.e., it should be considered as a constraint

$$\chi_i \equiv \pi_i - \sum_j A_{ij}\phi_j \approx 0 \tag{7.9}$$

$i = 1,\ldots,N$. Here ≈ 0 means *weakly vanishing,* i.e., a constraint on the physical phase space. The *canonical hamiltonian* is constructed as usual

$$H_c = \sum_i \dot{\phi}_i \pi_i - L = \sum_i V(\phi_i) \tag{7.10}$$

The constraints (7.9) have nonvanishing Poisson brackets with H_c

$$\{\chi_i, H_c\} = -V'(\phi_i) \tag{7.11}$$

as well as among themselves

$$\{\chi_i, \chi_j\} = A_{ij} - A_{ji} = 2A_{ij} \tag{7.12}$$

Thus if the time evolution would be generated by Poisson brackets with H_c, the theory would be inconsistent because the constraints would not be satisfied at all times. To remedy the situation one adds Lagrangian multipliers to H_c, yielding the *primary hamiltonian*

$$H_p = H_c + \sum_i \lambda_i \chi_i \tag{7.13}$$

and demands strong vanishing of the Poisson bracket of H_p with the constraints

$$0 = \{\chi_i, H_p\} = \{\chi_i, H_c\} + \sum_k \lambda_k B_{ki} \tag{7.14}$$

where $B_{ki} = 2A_{ki}$. To simplify the discussion, let us suppose that B^{-1} exists.* Then one can satisfy Eq. (7.14) by choosing

$$\lambda_k = \sum_i (B^{-1})_{ki} \{\chi_i, H_c\} \tag{7.15}$$

The primary hamiltonian thus reads

$$H_p = H_c - \sum_{i,j} \chi_i (B^{-1})_{ij} \{\chi_j, H_c\} \tag{7.16}$$

---

*For the LF Lagrangian this is actually not the case. There is one zero eigenvalue — the infamous zero mode — which has to be treated separately. The resulting procedure is known as the modified Dirac–Bergmann algorithm.

Let us now introduce the Dirac brackets between X and Y

$$\{X,Y\}_D = \{X,Y\} - \sum_{i,j} \{X,\chi_i\} (B^{-1})_{ij} \{\chi_j, Y\} \qquad (7.17)$$

By construction one has

$$\dot{X} = \{X, H_c\}_D = \{X, H_p\} \qquad (7.18)$$

Actually, the Dirac bracket of any operator with any of the constraints vanishes identically

$$\{X,\chi_k\}_D = \{X,\chi_k\} - \sum_{i,j} \{X,\chi_i\} (B^{-1})_{ij} \{\chi_j, \chi_k\}$$

$$= \{X,\chi_k\} - \sum_{i,j} \{X,\chi_i\} (B^{-1})_{ij} B_{jk} = 0 \qquad (7.19)$$

i.e., in particular $\{\chi_i, \chi_j\} = 0$. In a sense, the Dirac brackets take all the phase space restrictions from the constraint equations automatically into account. This is in sharp contrast to the Poisson brackets, which are calculated as if all the π_i's and ϕ_i's were independent

$$\{X,Y\} = \sum_i \frac{\partial X}{\partial \phi_i} \frac{\partial Y}{\partial \pi_i} - \frac{\partial Y}{\partial \phi_i} \frac{\partial X}{\partial \pi_i}$$

It thus seems natural to use Dirac brackets, instead of Poisson brackets, when identifying classical brackets with quantum commutators

$$\{X,Y\}_D \to i\,[X,Y] \qquad (7.20)$$

in the quantization process. A more thorough discussion on this subject can, for example, be found in Ref. 127. Here we are more interested in the consequences of Eq. (7.20). For this purpose, let us evaluate the fundamental Dirac brackets

$$\{\phi_i, \pi_j\}_D = \{\phi_i, \pi_j\} - \sum_{k,l} \{\phi_i, \chi_k\} (B^{-1})_{kl} \{\chi_l, \pi_j\}$$

$$= \delta_{i,j} - \sum_{k,l} \delta_{ik} (B^{-1})_{kl} A_{lj} = \frac{1}{2}\delta_{i,j} \qquad (7.21)$$

Roughly speaking, the reduction in the number of independent degrees of freedom by a factor of two manifests itself in a factor $1/2$ in the Dirac bracket, and after applying Eq. (7.20) the factor $1/2$ also appears in the

quantum commutator between π_i and ϕ_j. For the LF quantization of scalar fields this implies

$$[\pi(x), \phi(y)]_{x^+=y^+} = -\frac{i}{2}\delta(x^- - y^-) \tag{7.22}$$

instead of Eq. (7.3). Clearly, this remedies the above-mentioned problem (7.5) with the extra factor of 2 in the LF equation of motion generated by P_+ (7.5).

From the physics point of view,[132] the whole difficulty in quantization with constraints could be avoided if it were possible to choose degrees of freedom which are compatible with the constraints. For the above example this is actually possible, since the constraint (7.9) is linear in the fields. Let us thus make the ansatz

$$\phi_i^D = \alpha \left[\phi_i + \sum_j \beta_{ij}\pi_j \right] \tag{7.23}$$

where α is a constant and the β_{ij} are determined by requiring a vanishing Poisson bracket between ϕ_i^D and the constraints

$$0 = \{\phi_i^D, \chi_j\} = \alpha \left[\delta_{ij} + \sum_k \beta_{ik} A_{kj} \right] \tag{7.24}$$

i.e., $\beta_{ij} = \left(A^{-1}\right)_{ij}$. The normalization α is fixed by demanding that $\phi_i^D \approx \phi_i$, i.e.,

$$
\begin{aligned}
\phi_i^D &= \alpha \left[\phi_i + \sum_j \left(A^{-1}\right)_{ij} \pi_j \right] \\
&\approx \alpha \left[\phi_i + \sum_j \left(A^{-1}\right)_{ij} \sum_k A_{jk}\pi_k \right] \\
&= 2\alpha\phi_i
\end{aligned} \tag{7.25}
$$

yielding $\alpha = \frac{1}{2}$. By construction, ϕ_i^D does not "see" the constraint and one can apply canonical quantization rules directly

$$\left[\pi_i, \phi_j^D\right] = -i\delta_{ij} \tag{7.26}$$

and thus

$$\left[\pi_i, \phi_j\right] = -i\alpha\delta_{ij} = -\frac{i}{2}\delta_{ij} \tag{7.27}$$

In the continuum limit this results in Eq. (7.22).

As already indicated above, there are more points that need to be discussed before the Dirac-Bergmann procedure for constructing the LF hamiltonian is complete. In particular, one has to address the issue of zero modes. In the LF example, the analog of the matrix A_{ij} is the differential operator ∂_-. Fields which are independent of x^- are annihilated by ∂_- and thus correspond to eigenvectors with eigenvalue zero (on a finite interval, with periodic boundary conditions, these zero modes have to be considered for a complete formulation of the theory). In such a situation one first has to project on the Hilbert space orthogonal to the zero modes before the simplified procedure above can be applied. The resulting modified Dirac-Bergmann procedure is quite involved and has been discussed extensively in the literature.[128–131] The basic difficulty arises because the constraint equation for the zero mode is nonlinear. For example, in ϕ^4 theory in a "box" with periodic boundary conditions in the x^--direction, integrating the Euler-Lagrange equation $-2\partial_-\partial_+\phi = m^2\phi + \frac{\lambda}{3!}\phi^3$ over x^- yields[55,56,59]

$$m^2 \int dx^- \phi + \frac{\lambda}{3!} \int dx^- \phi^3 = 0 \qquad (7.28)$$

In the first term in Eq. (7.28) only the zero mode is projected out but in the second term higher modes contribute as well. Because the constraint equation (7.28) is nonlinear, the resulting quantum theory is as complicated as the formulation in usual coordinates. So far, it is not clear whether any dynamical simplifications (like "freezing out" of the zero mode) arise in the infinite volume limit.

REFERENCES

1. F. J. Yndurain, *Quantum Chromodynamics,* Springer, New York (1983).
2. R. L. Jaffe, in: *Los Alamos School on Relativistic Dynamics and Quark–Nuclear Physics,* (M. B. Jackson and A. Picklesimer, eds.), Wiley, New York (1985).
3. T. P. Cheng and L. F. Li, *Gauge Theory of Elementary Particle Physics,* Oxford Univ. Press, Oxford (1984).
4. R. Jackiw, *Springer Tracts in Modern Physics 62,* (G. Höhler, ed.), Springer, Berlin (1972).
5. X. Ji, *Comments Nucl. Part. Phys.* **21,** 123 (1993).
6. P. A. M. Dirac, *Rev. Mod. Phys.* 21, 392 (1949).
7. K. Hornbostel, in: *From Fundamental Fields to Nuclear Phenomena,* (J. A. McNeil and C. E. Price, eds.), World Scientific, Singapore (1991).
8. S. Fubini and G. Furlan, *Physics* 1, 229 (1965).
9. S. J. Brodsky and G. P. Lepage, *Phys. Rev.* **D22,** 2157 (1980).
10. J. D. Bjorken, I. Dunietz, and J. Taron, *Nucl. Phys.* **B371,** 111 (1992).

11. M. Burkardt, *Phys. Rev.* **D46,** R1924, R2751 (1992); M. Burkardt and E. Swanson, *Phys. Rev.* **D46,** 5083 (1992).

12. C.-Y. Cheung, W.-M. Zhang, and G.-L. Lin, *Phys. Rev.* **D52,** 2915 (1995).

13. K. Bardakci and M. B. Halperin, *Phys. Rev.* **176,** 1686 (1968).

14. L. Susskind, *Phys. Rev.* **165,** 1535 (1968).

15. S. Weinberg, *Phys. Rev.* **150,** 1313 (1966).

16. J. B. Kogut and D. E. Soper, *Phys. Rev.* **D1,** 2901 (1970).

17. J. D. Bjorken, J. B. Kogut, and D. E. Soper, *Phys. Rev.* **D3,** 1382 (1971).

18. S. Brodsky, R. Roskies, and R. Suaya, *Phys. Rev.* **D8,** 4574 (1973).

19. J. D. Bjorken and S. D. Drell, *Relativistic Quantum Fields,* McGraw-Hill, New York (1965).

20. S. Chang, R. Root, and T. Yan, *Phys. Rev.* **D7,** 1133 (1973).

21. S.-J. Chang and T.-M. Yan, *Phys. Rev.* **D7,** 1147 (1972).

22. I. Bars and M. B. Green, *Phys. Rev.* **D17,** 537 (1978).

23. M. Li, *Phys. Rev.* **D34,** 3888 (1986); M. Li, L. Wilets, and M. C. Birse, *J. Phys.* **G13,** 915 (1987).

24. S. Huang, J. W. Negele, and J. Polonyi, *Nucl. Phys.* **B307,** 669 (1988).

25. G.'t Hooft, *Nucl. Phys.* **B72,** 461 (1974); *Nucl. Phys.* **B75,** 461 (1974).

26. M. B. Einhorn, *Phys. Rev.* **D14,** 3451 (1976); *Phys. Rev.* **D15,** 1649, 3037 (1977).

27. F. Röhrlich, *Ada Phys. Aust.* **32,** 87 (1970).

28. D. G. Robertson and G. McCartor, *Z. Phys.* **C53,** 661 (1992); G. McCartor and D. G. Robertson, *Z. Phys.* **C53,** 679 (1992).

29. F. Lenz, S. Levit, M. Thies, and K. Yazaki, *Ann. Phys. (N.Y.)* **208,** 1 (1991); F. Lenz, Proceedings of NATO Advanced Study Institute on *Hadrons and Hadronic Matter,* (D. Vautherin *et al.,* eds.), Plenum, New York (1990).

30. E. V. Prokhvatilov and V. A. Franke, *Sov. J. Nucl. Phys.* **49,** 688 (1989).

31. K. Hornbostel, *Phys. Rev.* **D45,** 3781 (1992).

32. A. Harindranath and J. P. Vary, *Phys. Rev.* **D36,** 1141 (1987); **D37,** 1064, 1076, 3010, (1988); W.-M. Zhang, *Chin. J. Phys.* **32,** 717 (1994); C. J. Benesh and J. P. Vary, *Z. Phys.* **C49,** 411 (1991).

33. M. Burkardt, *Phys. Rev.* **D47,** 4628 (1993).

34. M. Burkardt, *Phys. Rev.* **D49,** 5446 (1994).

35. H.-C. Pauli and S. J. Brodsky, *Phys. Rev.* **D32,** 1993, 2001 (1985).

36. A. Harindranath and R. J. Perry, *Phys. Rev.* **D43,** 492 (1991).

37. P. M. Wort, *Phys. Rev.* **D47,** 608 (1993).

38. S. Mandelstam, *Nucl. Phys.* **B213,** 149 (1983); G. Leibbrandt, *Phys. Rev.* **D29,** 1699 (1984); *Rev. Mod Phys.* **59,** 1067 (1987).

39. A. Bassetto, M. Dalbesco, I. Lazzizzera, and R. Soldati, *Phys. Rev.* **D31,** 2012 (1985); A. Basetto, G. Nardelli, and R. Soldati, *Yang–Mills Theories in Algebraic Non-Covariant Gauges,* World Scientific, Singapore (1991).

40. T. T. Wu, *Phys. Lett.* **61B,** 142 (1977); *Phys. Rep.* **49,** 245 (1979).

41. F. Lenz, H. W. L. Naus, K. Ohta, and M. Thies, *Ann. Phys. (N. Y.)* **233,** 17 (1994).

42. F. Lenz, H. W. L. Naus, K. Ohta, and M. Thies, *Ann. Phys. (N.Y.)* **233,** 51 (1994).

43. F. Lenz, H. W. L. Naus, and M. Thies, *Ann. Phys. (N.Y.)* **233,** 317 (1994).

44. T. Eller, H.-C. Pauli, and S. J. Brodsky, *Phys. Rev.* **D35,** 1493 (1987).

45. T. Eller and H.-C. Pauli, *Z. Phys.* **C42,** 59 (1989).

46. K. Hornbostel, H.-C. Pauli, and S. J. Brodsky, Proc. of the Ohio State Workshop on Relativistic Many-Body Physics, World Scientific, Singapore (1988); S. J. Brodsky, Invited talk presented at the Third Lake Louise Winter Institute on QCD: Theory and Experiment, Chateau Lake Louise, Alberta, Canada, March 6–12, 1988; K. Hornbostel, Ph.D. Thesis, SLAC-Report-333; K. Hornbostel, S. J. Brodsky, and H.-C. Pauli, *Phys. Rev.* **D41,** 3814 (1990).

47. M. Burkardt, Doktorarbeit, Erlangen, 1989.

48. M. Burkardt, *Nucl. Phys.* **A504,** 762 (1989).

49. M. Burkardt and R. Busch, contributed to the Lake Louise Winter Institute: Particle Physics — The Factory Era, Lake Louise, Canada, February 17–23, 1991, (B. A. Campbell, A. N. Kamal, P. Kitching, and F. C. Khanna, eds.), World Scientific, Singapore (1991).

50. A. C. Tang, S. J. Brodsky, and H.-C. Pauli, *Phys. Rev.* **D44,** 1842 (1991).

51. M. Kaluža and H.-C. Pauli, *Phys. Rev.* **D45,** 2968 (1992); M. Krautgärtner, H.-C. Pauli, and F. Wölz, *Phys. Rev.* **D45,** 3755 (1992); L. C. L. Hollenberg, K. Higashijima, R. C. Warner, and B. H. J. McKellar, *Prog. Theor. Phys.* **87,** 441 (1992).

52. A. C. Kalloniatis and H. C. Pauli, *2. Phys.* **C60,** 255 (1993); *2. Phys.* **C63,** 161 (1994); A. C. Kalloniatis and D. G. Robertson, *Phys. Rev.* **D50,** 5262 (1994).

53. M. Burkardt, in Proceedings to SPIN 92 (Nagoya, Japan, Nov 92).

54. M. Burkardt, *Phys. Rev.* **D52,** 3841 (1995).

55. S. S. Pinsky and B. Van de Sande, *Phys. Rev.* **D48,** 816 (1993).

56. S. S. Pinsky and B. Van de Sande, *Phys. Rev.* **D49,** 2001 (1994).

57. S. S. Pinsky, B. Van de Sande, and J. R. Hiller, *Phys. Rev.* **D51,** 726 (1995).

58. D. G. Robertson, *Phys. Rev.* **D47,** 2549 (1993).

59. T. Heinzl, S. Krusche, S. Simburger, and E. Werner, *Z. Phys.* **C56,** 415 (1992).

60. M. Burkardt and A. Langnau, *Phys. Rev.* **D44,** 3857 (1991).

61. N. S. Manton, *Ann. Phys. (N.Y.)* **159,** 220 (1985).

62. M. Engelhardt and B. Schreiber, *Z. Phys.* **A 351,** 71 (1995).

63. A. C. Kalloniatis, H.-C. Pauli, and S. S. Pinsky, *Phys. Rev.* **D50,** 6633 (1994).

64. S.-J. Chang and S. K. Ma, *Phys. Rev.* **180,** 1506 (1969).

65. P. A. Griffin, *Phys. Rev.* **D46,** 3538 (1992).

66. M. Burkardt and A. Langnau, *Phys. Rev.* **D44,** 1187 (1991).

67. G. McCartor and D. G. Robertson, *Z Phys.* **C62,** 349 (1994); *Z. Phys.* **C68,** 345 (1995).

68. H.-H. Lin and D. Soper, *Phys. Rev.* **D48,** 1841 (1993).

69. A. Bassetto, F. De Biasio, and L. Griguolo, *Phys. Rev. Lett.* **72,** 3141 (1994).

70. E. V. Prokhvatilov, H. W. L. Naus, and H.-J. Pirner, *Phys. Rev.* **D51,** 2933 (1995).

71. J. Vary and T. J. Fields, Proceedings to *Theory of Hadrons and Light-Front QCD,* Zakopane, August 1994, hep-ph/9411263.

72. M. Abramowitz and I. A. Stegun (Eds.), *Handbook of Mathematical Functions,* Dover, New York (1970).

73. A. R. Zhitnitsky, *Phys. Lett.* **165B,** 405 (1985); *Sov. J. Nucl. Phys.* **43,** 999 (1986); *Sov. J. Nucl. Phys.* **44,** 139 (1986).

74. M. Burkardt, *Workshop on Quantum Infrared Physics,* Paris, France, 1994, hep-ph/9409333; M. Burkardt, to appear in *Phys. Rev.* **D53** (1996).

75. F. Lenz and M. Thies, private communications.

76. C. Buchiat, P. Fayet, and N. Sourlas, *Nuovo Cim. Lett.* **4,** 9 (1972).

77. D. Mustaki, S. Pinsky, J. Shigemitsu, and K. G. Wilson, *Phys. Rev.* **D43,** 3411 (1991).

78. A. Langnau and M. Burkardt, *Phys. Rev.* **D47,** 3452 (1993).

79. M. Burkardt, *Nucl. Phys.* **B373,** 613 (1992).

80. A. Harindranath and W.-M. Zhang, *Phys. Rev.* **D48,** 4868, 4881, 4903 (1993).

81. C. B. Thorn, *Phys. Rev.* **D19,** 639 (1979); *Phys. Rev.* **D20,** 1934 (1979).

82. G. Curci, W. Furmanski, and R. Petronzio, *Nucl. Phys.* **B175,** 27 (1980).
83. R. J. Perry, invited lectures presented at 'Hadrons 94', Gramado, Brasil, April, 1994.
84. S. J. Brodsky and H.-C. Pauli, Invited lectures given at 30th Schladming Winter School in Particle Physics: Field Theory, Schladming, Austria, Feb 27–Mar 8, 1991.
85. H.-C. Pauli, Proceedings of Leipzig Workshop on Quantum Field Theory Theoretical Aspects of High Energy Physics, Bad Frankenhausen, Germany, 20–24 Sept 1993.
86. S. J. Brodsky, G. McCartor, H.-C. Pauli, and S. S. Pinsky; *Part. World* **3,** 109(1993).
87. J. R. Hiller, *Phys. Rev.* **D43,** 2418 (1991); *Phys. Rev.* **D44,** 2504 (1991); J. J. Wivoda and J. R. Hiller, *Phys. Rev.* **D47,** 4647 (1993).
88. G. McCartor, *Z. Phys.* **C41,** 271 (1988); **C52,** 611 (1991); **C64,** 349 (1994).
89. R. Busch, Diplomarbeit, Erlangen 1989.
90. S. Coleman, *Ann. Phys. (N.Y.)* **101,** 239 (1976).
91. H. Bergknoff, *Nucl. Phys.* **B122,** 215 (1977).
92. K. Mahrt, Diplomarbeit, Erlangen, 1992.
93. S. Stampfer, Diplomarbeit, Erlangen, 1992.
94. C. J. Hamer, *Nucl. Phys.* **B195,** 503 (1982).
95. R. F. Dashen, B. Hasslacher, and A. Neveu, *Phys. Rev.* **D11,** 3424 (1975); A. Zamolodchikov and A. Zamolodchikov, *Ann. Phys. (N.Y.)* **120,** 253 (1979).
96. M. Burkardt, *Nucl. Phys.* **B373,** 371 (1992).
97. D. Mustaki, *Phys. Rev.* **D38,** 1260 (1988).
98. S. Huang and W. Lin, *Ann. Phys. (N.Y.)* **226,** 248 (1993).
99. W. A. Bardeen and R. B. Pearson, *Phys. Rev.* **D14,** 547 (1976); W. A. Bardeen, R. B. Pearson, and E. Rabinovici, *Phys. Rev.* **D21,** 1037 (1980).
100. J. W. Negele and H. Orland, *Quantum Many-Particle Systems,* Addison Wesley, Redwood City (1987).
101. T. A. DeGrand and J. Potvin, *Phys. Rev.* **D31,** 871 (1985).
102. J. E. Hirsch, R. L. Sugar, D. J. Scalapino, and R. Blankenbecler, *Phys. Rev.* **B26,** 5033 (1982); J. Potvin and T. A. DeGrand, *Phys. Rev.* **D30,** 1285 (1984).
103. P. A. Griffin, *Phys. Rev.* **D47,** 1530 (1993).
104. P. A. Griffin, *Mod Phys. Lett.* **A7,** 601 (1992); P. A. Griffin, *Nucl. Phys.* **B372,** 270 (1992).
105. P. Griffin, Proceedings to *Theory of Hadrons and Light-Front QCD,* Zakopane, August 1994, hep-ph/9410243.
106. M. Burkardt, Proceedings to *Theory of Hadrons and Light-Front QCD,* Zakopane, August 1994, hep-ph/9410219.
107. K. G. Wilson *et al., Phys. Rev.* **D49,** 6720 (1994).
108. R. J. Perry, A. Harindranath, and K. G. Wilson, *Phys. Rev. Lett.* **65,** 2959 (1990).
109. K. G. Wilson and D. G. Robertson, Proceedings to *Theory of Hadrons and Light-Front QCD,* Zakopane, August 1994, hep-ph/9411007.
110. E. A. Ammons, *Phys. Rev.* **D50,** 980 (1994).
111. I. Tamm, *J. Phys. (USSR)* **9,** 449 (1945).
112. S. M. Dancoff, *Phys. Rev.* **78,** 382 (1950).
113. K. G. Wilson, talk at Aspen Center for Physics, Aspen, CO, 1991 (a video tape of this lecture is available from S. Pinsky).
114. S. D. Glazek and R. J. Perry, *Phys. Rev.* **D45,** 3740 (1992).
115. S. D. Glazek *et al., Phys. Rev.* **D47,** 1599 (1993).
116. R. J. Perry, *Ann. Phys. (N.Y.)* **232,** 116 (1994).
117. R. J. Perry and K. G. Wilson, *Nucl. Phys.* **B403,** 587 (1993).
118. K. G. Wilson, *Rev. Mod Phys.* **47,** 773 (1975).
119. S. D. Glazek and K. G. Wilson, *Phys. Rev.* **D48,** 5863 (1993); *Phys. Rev.* **D49,** 4214 (1994).

120. V. A. Novikov, M. A. Shifman, A. I. Vainshtein, and V. I. Zakharov, *Nucl. Phys.* **B191,** 301 (1981).
121. B. L. Friman, V. R. Pandharipande, and R. B. Wiringa, *Phys. Rev. Lett.* **51,** 763 (1983).
122. L. McLerran and R. Venugopalan, *Phys. Rev.* **D49,** 2233, 3352 (1994); *Phys. Rev.* **D50,** 2225 (1994).
123. P. A. M. Dirac, *Canad. J. Math.* **1,** 1 (1950); *Lectures on Quantum Mechanics,* Benjamin, New York (1964).
124. P. G. Bergmann, *Helv. Phys. Ada Suppl.* **4,** 79 (1956).
125. A. Hanson, T. Regge, and C. Teitelboim, *Constrained Hamiltonian Systems,* Academia Nazionale dei Lincei, Rome (1976).
126. L. Fadeev and R. Jackiw, *Phys. Rev. Lett.* **60,** 1962 (1988).
127. K. Sundermayer, *Constrained Dynamics,* Lecture Notes in Physics 169, Springer, Berlin (1982).
128. T. Heinzl, S. Krusche, and E. Werner, *Z. Phys.* **A334,** 443 (1989).
129. T. Heinzl, S. Krusche, and E. Werner, *Phys. Lett.* **B272,** 54 (1991).
130. T. Heinzl, S. Krusche, and E. Werner, *Phys. Lett.* **B275,** 410 (1992).
131. T. Heinzl, S. Krusche, and E. Werner, *Phys. Lett.* **B256,** 55 (1991).
132. P. Griffin, private communications.
133. C. G. Callan, N. Coote, and D. J. Gross, *Phys. Rev.* **D13,** 1649 (1976).
134. H.-C. Pauli, proceedings of Leipzig Workshop on Quantum Field Theory Theoretical Aspects of High Energy Physics, Bad Frankenhausen, Germany, 20–24 Sept 1993.
135. R. J. Perry and A. Harindranath, *Phys. Rev.* **D43,** 4051 (1991).

5:08 pm, Feb 10, 2005

Chapter 2

NUCLEON KNOCKOUT BY INTERMEDIATE ENERGY ELECTRONS

James J. Kelly

Department of Physics
University of Maryland
College Park, Maryland 20742

1. INTRODUCTION

Nucleon knockout by electron scattering provides a powerful probe of the electromagnetic properties of nucleons and of the momentum distributions in nuclei. Since the nucleus is transparent with respect to the electromagnetic interaction, the entire nuclear volume can be probed uniformly. The weakness of the electromagnetic interaction allows one to separate the soft Coulomb

distortion of the electron scattering process from the hard-scattering event in which, to a very good approximation, a single virtual photon transfers its energy and momentum to the nuclear electromagnetic current. The kinematic flexibility of electron scattering permits the momentum and energy transfers to be varied independently, with various kinematical conditions emphasizing different aspects of the reaction mechanism. For example, under conditions in which a single high-energy nucleon receives most of the energy transfer, the quasifree electron–nucleon scattering process is emphasized.

Quasifree nucleon knockout from few-nucleon systems can be used to measure the nucleon electromagnetic form factors, especially for the neutron which is not available as an elementary target. The neutron can be isolated further either by using a polarized $^3\vec{\text{He}}$ target, in which the target polarization is dominated by the neutron contribution, or by detecting the recoil neutron explicitly in quasifree kinematics. Measurements of neutron form factors made with several different reactions, such as $^3\vec{\text{He}}(\vec{e}, e'n)$ or $\mathbf{d}(\vec{e}, e'\vec{n})$, are being compared to test the models used to extract the desired information and to verify its accuracy. Additional constraints are also provided by proton knockout reactions on the same targets. Variation of the kinematics near quasifree conditions, described as the quasielastic ridge, allows the momentum distribution within the target to be studied for comparison with the nearly exact structure calculations that are possible for few-body systems. Measurements further from the quasielastic ridge emphasize the role of meson-exchange and isobar currents.

Similarly, nucleon knockout from heavier systems can be used to probe the single-nucleon spectral function in complex nuclei. Exclusive measurements for states of the residual nucleus at low excitation energy are sensitive to quasiparticle properties, such as occupation probabilities, spectroscopic factors, binding energies, spreading widths, and momentum distributions. The kinematic flexibility of the knockout reaction can be used to test the models used to extract this structure information, for example, by comparing parallel with nonparallel kinematics or by varying the ejectile energy. The spatial localization of specific orbitals also provides some sensitivity to possible density-dependent modifications of the electromagnetic properties of bound nucleons. Measurements of the azimuthal dependence of the cross section and the recoil polarization of the ejectile can provide detailed tests of the reaction mechanism, which may be useful in delineating the role of two-body currents or in testing off-shell models of the current operator. Measurements at larger missing energy can provide information on the deep-hole spectral function or on multinucleon currents. Measurements at large missing momentum are sensitive to short-range and tensor correlations.

The first systematic survey of single-particle properties of nuclei using the

($e,e'p$) reaction was performed at Saclay during the 1970s and was reviewed in 1984 by Frullani and Mougey in Vol. 14 of this series.[1] Since that time, improvements in accelerator and detector technology have permitted an ever broader kinematic range to be investigated with greater resolution and precision. At Saclay, experiments on few-body systems were performed with larger momentum transfer and larger missing momentum. At MIT–Bates, the reaction mechanism in light nuclei was studied across the quasifree peak, through the dip region, and onto the delta resonance. At NIKHEF, the achievement of 100-keV resolution in missing energy made an extensive survey of spectroscopic factors and momentum distributions possible for many states of many nuclei across the periodic table. The quality and quantity of these data, in particular, have been very stimulating to nuclear many-body theory. More recently polarized beams, polarized targets, and recoil polarimetry have become available at several laboratories and neutron knockout from few-body systems has been observed.

With the advent of continuous duty-cycle electron accelerators, a much greater range of phenomena is becoming accessible. In addition to continued expansion of the kinematic range made available by the reduction of accidental coincidences, we can expect to see qualitatively new phenomena made available to investigation using polarimetry, neutron knockout, multinucleon detection, and out-of-plane measurements. The high duty-factor extracted beam from the NIKHEF pulse stretcher has permitted single-nucleon knockout measurements to be extended to much larger missing momentum and has made triple coincidence measurements possible. Furthermore, a polarized internal target facility is under development. At Mainz, the continuous 855-MeV microtron beam combined with three large acceptance spectrometers provides access to a much larger fraction of the phase space for reaction products. Polarized beam is available and recoil polarimetry soon will be. At CEBAF high intensity 4-GeV polarized beams delivered to three complementary detector stations will soon provide unprecedented kinematic flexibility and precision to electronuclear physics.

The purpose of this chapter is to review recent experimental and theoretical developments in nucleon knockout reactions initiated by intermediate energy electrons (roughly 400 MeV–1 GeV) and to preview some of the investigations planned for the new facilities. Several related review articles have also appeared recently. Dieperink and de Witt Huberts[2] have reviewed the results of high-resolution ($e,e'p$) measurements of spectroscopic factors and momentum distributions. The response of complex nuclei to electromagnetic interactions has been reviewed by Boffi, Giusti, and Pacati.[3] The role of nucleon structure has been re-

viewed by Mulders.[4] Parity violation in electron scattering has been reviewed by Musolf *et al.*[5] A valuable collection of articles on many related topics may also be found in a book edited by Frois and Sick.[6] And, of course, the seminal review by Frullani and Mougey remains an invaluable resource.

In Section 2 we review the formalism of the one-photon-exchange approximation, with particular emphasis on polarization observables. In Section 3 we review the data on the electromagnetic form factors of the nucleon, with particular emphasis on neutron form factors. In Section 4 we discuss briefly some of the recent measurements for few-body systems ($A \leq 4$), emphasizing structure and reaction model issues not directly related to nucleon form factor measurements using those targets. In Section 5 we provide a detailed, critical review of the distorted wave approximation for $(\vec{e}, e'\vec{N})$ reactions. In Section 6 we review the data on single-hole spectral functions for complex nuclei, with particular emphasis on the high-resolution experiments performed at NIKHEF. In Section 7 we review experiments which seek to test various aspects of the electronuclear reaction mechanism. Finally, a summary of our conclusions is presented in Section 8.

2. ONE-PHOTON-EXCHANGE APPROXIMATION

In this section we examine the general structure of electromagnetic reactions in the one-photon-exchange approximation, including polarization observables. The formalism for polarization in inclusive and coincident electron scattering from nuclei was originally developed elsewhere.[7–15] The most comprehensive discussions are given by Donnelly and Raskin.[10,14] The derivations are sketched here so that the nomenclature can be introduced. We generally conform to the conventions of Bjorken and Drell[16] and consider only the extreme relativistic limit ($m_e \rightarrow 0$). We also consider the specific results for elastic scattering from the nucleon and, for the sake of later use in the elementary off-shell cross section, scattering from a moving nucleon.

2.1. Definition of the Response Tensors for *A(e,e′x)B*

Consider the reaction *A(e,e′x)B* diagrammed in Fig. 2.1, where $k_i = (\varepsilon_i, \mathbf{k}_i)$ and $k_f = (\varepsilon_f, \mathbf{k}_f)$ are the initial and final electron momenta, $p_A = (\varepsilon_A, \mathbf{p}_A)$ and $p_B = (\varepsilon_B, \mathbf{p}_B)$ are the initial and final target momenta, $p_x = (\varepsilon_x, \mathbf{p}_x)$ is the ejectile momentum, and $q = k_i - k_f = (\omega, \mathbf{q})$ is the momentum transfer carried by the virtual photon. The invariant cross section has the

general form[16]

$$d\sigma = \nu_r^{-1} \mathcal{N}_i \mathcal{N}_A \overline{\sum_i} \sum_f |\mathcal{M}^{fi}|^2 \mathcal{N}_f \frac{d^3k_f}{(2\pi)^3}$$

$$\times \left(\prod_{j=1}^n \mathcal{N}_j \frac{d^3p_j}{(2\pi)^3} \right) (2\pi)^4 \delta^4 (p_f - q - p_A) \qquad (2.1)$$

where the relative velocity for collinear collisions

$$\nu_r = \frac{\left[(k_i \cdot p_A)^2 - (m_e m_A)^2 \right]^{1/2}}{\varepsilon_i \varepsilon_A}$$

is practically unity and where the normalization of plane waves is given by

$$\mathcal{N}_i \langle p_i | p_i' \rangle = (2\pi)^3 \delta^3 (\mathbf{p}_i - \mathbf{p}_i')$$

Note that for the covariant normalization used by Bjorken and Drell, $\mathcal{N} = m/\varepsilon$ for hadrons or $\mathcal{N} = 1/2\varepsilon$ for massless electrons, but when the nuclear physics is treated nonrelativistically, the noncovariant normalization $\mathcal{N} = 1$ is usually employed. Averaging over initial states is indicated by $\overline{\sum_i}$ and summation over undetected final states by $\sum_f$. In the one-photon-exchange approximation, the invariant matrix element $\mathcal{M}^{fi}$ becomes

$$\mathcal{M}^{fi} = \frac{4\pi\alpha}{Q^2} \langle k_f \lambda_f | j_\mu | k_i \lambda_i \rangle \langle B_f \mathbf{p}_x | J^\mu | A_i \rangle \qquad (2.2)$$

where $\alpha = 1/137$ is the fine structure constant, $Q^2 = -q_\mu q^\mu = \mathbf{q}^2 - \omega^2$ is the space-like invariant mass of the virtual photon, λ_i and λ_f are initial and final helicities for the electron, while A_i and B_f are the initial and final nuclear states including spin variables.

The momenta required to specify the phase space of the final hadronic system are indicated by the set $\{p_j, j = 1, n\}$, where n is equal to one plus the number of detected hadrons and where $p_f = \sum_1^n p_j$. No hadrons are detected for inclusive electron scattering, in which case $n = 1$ and p_f is the total momentum of a hadronic system with invariant mass

$$m_f^2 = m_A^2 - Q^2 + 2m_A\nu$$

where $\nu = p_A \cdot q/m_A$ is an invariant which equals the energy transfer in the laboratory frame. For semi-inclusive reactions one or more hadrons is detected in coincidence with the scattered electron, leaving a residual system with invariant mass

$$m_B^2 = (p_A + q - p_x)^2$$
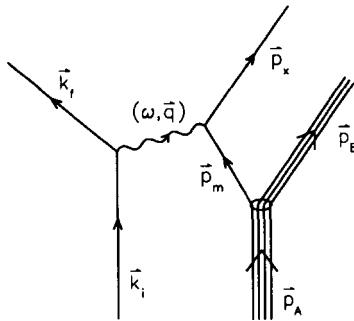
Fig. 2.1. One-photon exchange for the $A(e, e'x)B$ reaction.

where p_x is the net four momentum of the detected hadrons. For exclusive reactions the momenta of the detected particles is sufficient to uniquely specify the state of the residual nucleus.

The unpolarized electron current is given by

$$\langle k_f \lambda_f | j^\mu | k_i \lambda_i \rangle = \bar{u}_f \gamma^\mu u_i \tag{2.3}$$

where u_i and u_f are the initial and final electron spinors normalized according to the convention

$$\bar{u}(p, \lambda) u(p, \lambda') = \delta_{\lambda, \lambda'} \tag{2.4}$$

If the electron helicities are not observed, the electron portion of $|\mathcal{M}|^2$ becomes

$$\frac{1}{2} \sum_{\lambda_i \lambda_f} \langle k_f \lambda_f | j_\mu | k_i \lambda_i \rangle \langle k_i \lambda_i | j_\nu^\dagger | k_f \lambda_f \rangle = \frac{1}{2} \text{Trace} \sum_{\lambda_i \lambda_f} \bar{u}_f \gamma_\mu u_i \bar{u}_i \gamma_\nu u_f \tag{2.5}$$

The helicity sums are performed using the spinor identity

$$\sum_\lambda u(k, \lambda) \bar{u}(k, \lambda) = \frac{k + m_e}{2 m_e} \tag{2.6}$$

Hence, it is convenient to define an electron response tensor $\eta_{\mu\nu}$ such that

$$\eta_{\mu\nu} = 2 m_e^2 \, \text{Trace} \, \gamma_\mu \frac{k_i + m_e}{2 m_e} \gamma_\nu \frac{k_f + m_e}{2 m_e} \tag{2.7}$$

or

$$\eta_{\mu\nu} = 2 \left(k_{i\mu} k_{f\nu} + k_{f\mu} k_{i\nu} - k_i \cdot k_f g_{\mu\nu} \right) \tag{2.8}$$

where the electron mass has been neglected.

Similarly, we can define nuclear response tensors $\mathcal{W}^{\mu\nu}$ that are bilinear in matrix elements of the nuclear current and which contain most of the phase space factors relevant to each application.

For semi-inclusive reactions it is convenient to define the nuclear response tensor as

$$\mathcal{W}_{\mu\nu} = \mathcal{N}_A\mathcal{N}_x\mathcal{N}_B\overline{\sum_{A_i}\sum_{B_f}}\int d^3p_B \, \langle B_f\mathbf{p}_x|J_\mu|A_i\rangle\langle A_i|J_\nu^\dagger|B_f\mathbf{p}_x\rangle$$
$$\times\delta^4(p_x + p_B - q - p_A) \tag{2.9}$$

The invariant cross section then becomes

$$d\sigma = (2\pi)^{-3}\frac{\varepsilon_f}{\varepsilon_i}\frac{\alpha^2}{Q^4}\eta_{\mu\nu}\mathcal{W}^{\mu\nu}d\varepsilon_f d\Omega_e d^3p_x \tag{2.10}$$

where $d\Omega_e$ is the solid angle for the electron momentum in the laboratory. Hence, using

$$d^3p_x = \varepsilon_x p_x d\varepsilon_x d\Omega_x$$

where $d\Omega_x$ is the solid angle for the ejectile momentum in the laboratory, we obtain

$$\frac{d^6\sigma}{d\varepsilon_f d\Omega_e d\varepsilon_x d\Omega_x} = \frac{p_x\varepsilon_x}{(2\pi)^3}\frac{\varepsilon_f}{\varepsilon_i}\frac{\alpha^2}{Q^4}\eta_{\mu\nu}\mathcal{W}^{\mu\nu} \tag{2.11}$$

as the sixfold differential cross section.

For exclusive reactions in which only a single discrete state or narrow resonance of the target is excited, we use

$$\mathcal{R} = \int d\varepsilon_x\,\delta(\varepsilon_x + \varepsilon_B - \omega - m_A) = \left|1 - \frac{\varepsilon_x}{\varepsilon_B}\frac{\mathbf{p}_x\cdot\mathbf{p}_B}{\mathbf{p}_x\cdot\mathbf{p}_x}\right|^{-1} \tag{2.12}$$

to integrate over the peak in missing energy and thus to obtain a fivefold differential cross section of the form

$$\frac{d^5\sigma}{d\varepsilon_f d\Omega_e d\Omega_x} = \mathcal{R}\frac{p_x\varepsilon_x}{(2\pi)^3}\frac{\varepsilon_f}{\varepsilon_i}\frac{\alpha^2}{Q^4}\eta_{\mu\nu}\mathcal{W}^{\mu\nu} \tag{2.13}$$

where R is a recoil factor which adjusts the nuclear phase space.[17] For inclusive electron scattering, we use

$$\int\frac{d^3p_B}{\varepsilon_B}\delta^4(p_B - q - p_A) = \delta((p_A + q)^2 - m_B^2)$$

and

$$\int_0^\infty d\varepsilon_f \delta((p_A + q)^2 - m_B^2) = \frac{1}{2m_A}\left(1 + \frac{2\varepsilon_i}{m_A}\sin^2\frac{\theta_e}{2}\right)^{-1}$$

to remove the momentum-conserving delta function from the definition of the nuclear response tensor. Thus, it is convenient to define the nuclear response tensor for inclusive reactions as

$$\mathcal{W}_{\mu\nu} = \frac{1}{2m_A^2}\overline{\sum_{A_i}}\sum_{B_f}\langle B_f \mathbf{p}_x|J_\mu|A_i\rangle\langle A_i|J_\nu^\dagger|B_f \mathbf{p}_x\rangle \qquad (2.14)$$

Hence, we obtain the simple formula

$$\frac{d\sigma}{d\Omega} = f_{\text{rec}}\frac{\varepsilon_f}{\varepsilon_i}\frac{\alpha^2}{Q^4}\eta_{\mu\nu}\mathcal{W}^{\mu\nu} \qquad (2.15)$$

where

$$f_{\text{rec}} = \left(1 + \frac{2\varepsilon_i}{m_A}\sin^2\frac{\theta_e}{2}\right)^{-1}$$

is the recoil factor and m_A is the target mass. Note that

$$\frac{\varepsilon_f}{\varepsilon_i} = f_{\text{rec}}\left(1 - \frac{m_B^2 - m_A^2}{2m_A\varepsilon_i}\right)$$

where

$$m_B^2 = m_A^2 - Q^2 + 2m_A\omega$$

is the invariant mass of the final hadronic system and that

$$\varepsilon_f/\varepsilon_i \to f_{\text{rec}}$$

for elastic scattering.

2.2. Basic Response Functions for Electron Scattering

The nuclear response tensor describes the electromagnetic structure of the target and contains all of the dynamics of interest. Recognizing that the response tensors are bilinear in matrix elements of the current operator, it is useful to establish the schematic notation

$$\mathcal{W}_{\mu\nu} = \langle J_\mu J_\nu^\dagger\rangle$$

where the angle brackets denote products of matrix elements appropriately averaged over initial states and summed over final states with whatever phase

space factors are relevant to the application at hand. We also note that the electron tensor can be expressed in the alternative form

$$\eta_{\mu\nu} = K_\mu K_\nu - q_\mu q_\nu - Q^2 g_{\mu\nu}$$

where $K = k_i + k_f$. Thus, since conservation of the nuclear electromagnetic current requires

$$q_\mu \mathcal{W}^{\mu\nu} = \mathcal{W}^{\mu\nu} q_\nu = 0$$

the contraction of electron and nuclear response tensors reduces to the form

$$\eta_{\mu\nu} \mathcal{W}^{\mu\nu} = \langle K \cdot J K \cdot J^\dagger - Q^2 J \cdot J^\dagger \rangle$$

It is convenient to define a right-handed coordinate system with

$$\hat{\mathbf{z}} = \hat{\mathbf{q}} \tag{2.16a}$$

$$\hat{\mathbf{y}} = \frac{\mathbf{k}_i \otimes \mathbf{k}_f}{|\mathbf{k}_i \otimes \mathbf{k}_f|} \tag{2.16b}$$

$$\hat{\mathbf{x}} = \hat{\mathbf{y}} \otimes \hat{\mathbf{z}} \tag{2.16c}$$

The continuity equation

$$J_z = \frac{\omega}{|\mathbf{q}|} \rho \tag{2.17}$$

can now be used to eliminate the longitudinal component of the current in favor of the charge, such that

$$
\begin{aligned}
K \cdot J K \cdot J^\dagger - Q^2 J \cdot J^\dagger &= \left[\left(K_0 - \frac{\omega}{|\mathbf{q}|} K_z \right)^2 - Q^2 \left(1 - \frac{\omega^2}{|\mathbf{q}|^2} \right) \right] \rho\rho^\dagger \\
&\quad + \left(K_x^2 + Q^2 \right) J_x J_x^\dagger + Q^2 J_y J_y^\dagger \\
&\quad - K_x \left(K_0 - \frac{\omega}{|\mathbf{q}|} K_z \right) \left(\rho J_x^\dagger + J_x \rho^\dagger \right)
\end{aligned}
$$

Upon evaluation of the components of K in this basis, some tedious but straightforward algebra reveals

$$
\begin{aligned}
K \cdot J K \cdot J^\dagger - Q^2 J \cdot J^\dagger &= 4\varepsilon_i \varepsilon_f \cos^2 \frac{\theta}{2} \\
&\times \left[V_{00} \rho\rho^\dagger + V_{xx} J_x J_x^\dagger + V_{yy} J_y J_y^\dagger - V_{0x} \left(\rho J_x^\dagger + J_x \rho^\dagger \right) \right]
\end{aligned}
$$

where θ is the electron scattering angle and where the coefficients

$$V_{00} = \frac{Q^4}{\mathbf{q}^4}$$

$$V_{xx} = \frac{Q^2}{\mathbf{q}^2} + \tan^2 \frac{\theta}{2}$$

$$V_{yy} = \tan^2 \frac{\theta}{2}$$

$$V_{0x} = \frac{Q^2}{\mathbf{q}^2} \left(\frac{Q^2}{\mathbf{q}^2} + \tan^2 \frac{\theta}{2} \right)^{1/2}$$

depend only upon electron kinematics. The appearance of terms of the type $Q^2/\mathbf{q}^2$ in these coupling coefficients is associated with retardation effects involved in the transformation from the Lorentz gauge to the Coulomb gauge during the elimination of the longitudinal current in favor of the charge.[18] Therefore, whatever the dynamics of the hadronic component of the system, gauge invariance and the one-photon-exchange approximation require the unpolarized cross section to have the general structure

$$\eta_{\mu\nu} \mathcal{W}^{\mu\nu} = 4\varepsilon_i \varepsilon_f \cos^2 \frac{\theta}{2} \qquad (2.18)$$
$$\times \left[V_{00} W_{00} + V_{xx} W_{xx} + V_{yy} W_{yy} - V_{0x} (W_{0x} + W_{x0}) \right]$$

The structure of the nuclear response tensor can be analyzed further by expressing it as a linear combination of the tensors based upon the available vectors.[19] Since current conservation requires $q_\mu \mathcal{W}^{\mu\nu} = \mathcal{W}^{\mu\nu} q_\nu = 0$, it is convenient to orthogonalize the basis with respect to q, using

$$\tilde{p}_x = p_x + \frac{p_x \cdot q}{Q^2} q \qquad (2.19)$$

$$\tilde{p}_A = p_A + \frac{p_A \cdot q}{Q^2} q \qquad (2.20)$$

Without loss of generality, we can evaluate the structure of $\mathcal{W}^{\mu\nu}$ in the lab frame and later boost to another frame if desired. In the lab frame, the momenta can be expressed as

$$p_A = (m_A, 0, 0, 0)$$
$$p_x = (\varepsilon_x, |\mathbf{p}_x| \sin \theta_{pq} \cos \phi, |\mathbf{p}_x| \sin \theta_{pq} \sin \phi, |\mathbf{p}_x| \cos \theta_{pq})$$

where θ_{pq} is the polar angle between $\mathbf{p}_x$ and $\mathbf{q}$ and where ϕ is the azimuthal

angle defining the reaction plane. Hence, the vectors orthogonal to q become

$$\tilde{p}_A = m_A \frac{\mathbf{q}^2}{Q^2}\left(1,0,0,\frac{\omega}{q}\right)$$

$$\tilde{p}_x = |\mathbf{p}_x| \sin\theta_{pq}(0,\cos\phi,\sin\phi,0)$$

It is convenient to remove the extraneous kinematic factors and to use basis vectors

$$V_1 = \left(1,0,0,\frac{\omega}{q}\right) \tag{2.21a}$$

$$V_2 = (0,\cos\phi,\sin\phi,0) \tag{2.21b}$$

which remain well-defined in the limit $\theta_{pq} \to 0$. Finally, we define the photon projection operator as

$$\tilde{g}^{\mu\nu} = g^{\mu\nu} + \frac{q^\mu q^\nu}{Q^2} \tag{2.22}$$

which is orthogonal to q and is related to the virtual photon polarization basis vectors

$$\epsilon^\mu_{\pm 1} = \mp 2^{-\frac{1}{2}}(0,1,\pm i,0) \tag{2.23a}$$

$$\epsilon^\mu_0 = \left(\frac{|\mathbf{q}|}{Q},0,0,\frac{\omega}{Q}\right) \tag{2.23b}$$

by

$$\tilde{g}^{\mu\nu} = \sum_\lambda (-)^\lambda \epsilon^{\mu*}_\lambda \epsilon^\nu_\lambda \tag{2.24}$$

Therefore, we expand the symmetric part of the nuclear response tensor as

$$\mathcal{W}^{\mu\nu}_S = W_1 \tilde{g}^{\mu\nu} + W_2 V_1^\mu V_1^\nu + W_3 V_2^\mu V_2^\nu + W_4 [V_1^\mu V_2^\nu]_S \tag{2.25}$$

where

$$[A^\mu B^\nu]_{S,A} = (A^\mu B^\nu \pm B^\mu A^\nu)/2 \tag{2.26}$$

represent symmetric and antisymmetric tensor products. Note that the anti-symmetric part, $\mathcal{W}^{\mu\nu}_A$, does not contribute to unpolarized electron scattering because $\eta_{\mu\nu}$ is symmetric. Each of the four independent response functions, W_i, depends only on Lorentz scalars involving the momentum transfer and

the hadron momenta. Thus, the kinematic and dynamic dependencies are isolated in the general form

$$\eta_{\mu\nu} W^{\mu\nu} = 4\varepsilon_i \varepsilon_f \cos^2 \frac{\theta}{2} \tag{2.27}$$
$$\times (V_L R_L + V_T R_T + V_{LT} R_{LT} \cos\phi + V_{TT} R_{TT} \cos 2\phi)$$

where

$$V_L = \frac{Q^4}{\mathbf{q}^4} \tag{2.28a}$$

$$V_T = \frac{Q^2}{2\mathbf{q}^2} + \tan^2 \frac{\theta}{2} \tag{2.28b}$$

$$V_{LT} = \frac{Q^2}{\mathbf{q}^2} \left(\frac{Q^2}{\mathbf{q}^2} + \tan^2 \frac{\theta}{2} \right)^{1/2} \tag{2.28c}$$

$$V_{TT} = \frac{Q^2}{2\mathbf{q}^2} \tag{2.28d}$$

are the electron coupling coefficients and where

$$
\begin{aligned}
R_L &= & W'^{00} &= \frac{\mathbf{q}^2}{Q^2} W_1 + W_2 \\
R_T &= W^{xx} + W^{yy} &= -2W_1 + W_3 \\
R_{LT} \cos\phi &= -W^{0x} - W^{x0} &= -W_4 \cos\phi \\
R_{TT} \cos 2\phi &= W^{xx} - W^{yy} &= W_5 \cos 2\phi
\end{aligned}
$$

are the four independent response functions which describe the electromagnetic properties of the hadronic system. These response functions contain all of the dynamical information concerning the electromagnetic structure of the target that is available from this reaction.

Several characteristics of these results bear further discussion. First, the derivation was quite general and can be applied to elastic or inelastic scattering, quasifree scattering, or knockout using the appropriate definition of the hadronic response tensor. Second, additional response functions become available when the polarizations of either the electron or the ejectile are observed and can be readily analyzed by extending the derivation above to include antisymmetric tensors and a suitable pseudovector. Third, the structure of the cross section simplifies considerably for parallel kinematics in which the ejectile momentum is parallel to the momentum transfer. Under these conditions the cross section must be independent of the undefined azimuthal angle ϕ, such that both R_{LT} and R_{TT} vanish in the limit $\theta_{pq} \to 0, \pi$. Thus, only two independent response functions

survive for quasifree scattering in parallel kinematics, namely, R_L and R_T. Similarly, because the momentum of the residual system is necessarily parallel to the momentum transfer in the laboratory, only two response functions are relevant to inclusive electron scattering.

Finally, combining the helicity projection $\cos^2(\theta/2)$ with the photon propagator, we obtain the semi-inclusive unpolarized cross section in the form

$$\frac{d^6\sigma}{d\varepsilon_f d\Omega_e d\varepsilon_x d\Omega_x} = \frac{p_x \varepsilon_x}{(2\pi)^3}\sigma_M \tag{2.29}$$
$$\times (V_L R_L + V_T R_T + V_{LT} R_{LT}\cos\phi + V_{TT} R_{TT}\cos 2\phi)$$

where the Mott cross section

$$\sigma_M = \frac{\alpha^2 \cos^2(\theta/2)}{4\varepsilon_i^2 \sin^4(\theta/2)} \tag{2.30}$$

represents the elementary cross section for electron scattering from a heavy structureless target. In general, the response functions for a particular reaction, specified by the invariant masses $\{m_A, m_x, m_B\}$, depend upon the four remaining independent Lorentz scalars $\{Q^2, q \cdot p_A, q \cdot p_x, p_x \cdot p_A\}$, but it is usually more convenient to employ the more familiar laboratory variables $\{Q^2, \omega, p_x, \theta_{pq}\}$. Similarly, the inclusive electron scattering cross section reduces to

$$\frac{d\sigma}{d\Omega} = f_{rec}\sigma_M (V_L R_L + V_T R_T) \tag{2.31}$$

where the response functions now depend only upon Q^2 and ω.

Thus, we find that in the one-photon-exchange approximation, the unpolarized electron scattering cross section depends upon at most four independent response functions. Having isolated the explicit dependence on azimuthal angle, the current matrix elements can be evaluated for any convenient ϕ. Hence the response functions can be expressed in the alternative forms

$$R_L = W_{00} = \langle \rho\rho^\dagger \rangle$$
$$R_T = \langle W_{xx} + W_{yy} \rangle = \langle J_\parallel J_\parallel^\dagger + J_\perp J_\perp^\dagger \rangle$$
$$R_{LT}\cos\phi = -\langle W_{0x} + W_{x0} \rangle = -\langle \rho J_\parallel^\dagger + J_\parallel\rho^\dagger \rangle$$
$$R_{TT}\cos 2\phi = \langle W_{xx} - W_{yy} \rangle = \langle J_\parallel J_\parallel^\dagger - J_\perp J_\perp^\dagger \rangle$$

where $J_\parallel$ lies in the scattering plane, and $J_\perp$ is orthogonal to that plane and both are orthogonal to $\mathbf{q}$. The longitudinal response function R_L is due to

the charge and the longitudinal component of the current. The transverse response function R_T is the incoherent sum of contributions from the two components of the current orthogonal to the direction of the virtual photon. The longitudinal–transverse interference response function R_{LT} is due to the interference of the longitudinal current with the transverse component of the current that lies in the reaction plane. The transverse–transverse interference response function R_{TT} is due to the interference between the two transverse components of the current.

2.3. Electron Polarization

In the extreme relativistic limit, only the longitudinal component of the electron polarization is relevant. Thus, the electron response tensor can be separated into two contributions of the form[20]

$$\eta_{\mu\nu} = \frac{1}{2}[\eta_{\mu\nu}^u + h\eta_{\mu\nu}^h] \tag{2.32}$$

where $\eta_{\mu\nu}^u$, presently adorned with the superscript u, is the unpolarized tensor developed previously and where $\eta_{\mu\nu}^h$ is the helicity-dependent response tensor. The helicity dependence can be explicated by inserting the projection operator

$$\Pi_h = \frac{1}{2}(1 + h\gamma_5) \tag{2.33}$$

into the current matrix elements

$$j^\mu = \bar{u}_f \gamma^\mu \Pi_h u_i$$

such that

$$\eta_{\mu\nu}^h = \frac{1}{2} \text{Trace} \, \gamma_\mu \gamma_5 \, \not{k}_i \gamma_\nu \, \not{k}_f$$

in the limit of vanishing electron mass. Thus, we find

$$\eta_{\mu\nu}^h = -2i\varepsilon_{\mu\nu\alpha\beta}k_i^\alpha k_f^\beta$$

where $\varepsilon_{\mu\nu\alpha\beta}$ is the completely antisymmetric tensor. Finally, using $K = k_i + k_f$ and $q = k_i - k_f$, we obtain a form,

$$\eta_{\mu\nu}^h = -i\varepsilon_{\mu\nu\alpha\beta}q_i^\alpha K_f^\beta \tag{2.34}$$

with which current conservation is readily enforced.

The same methods used in Section 2.2 to contract the spin-independent tensors can now be used to evaluate their helicity dependence, with the result[7,9,10,21]

$$\eta_{\mu\nu}^h \mathcal{W}_A^{\mu\nu} = 4\varepsilon_i\varepsilon_f \cos^2\frac{\theta}{2}\left[iV'_{LT}(\mathcal{W}^{0y} - \mathcal{W}^{y0}) - iV'_{TT}(\mathcal{W}^{xy} - \mathcal{W}^{yx})\right]$$

(2.35)

where

$$V'_{LT} = \frac{Q^2}{\mathbf{q}^2}\tan(\theta/2)$$

(2.36a)

$$V'_{TT} = \left[\frac{Q^2}{\mathbf{q}^2} + \tan^2(\theta/2)\right]^{\frac{1}{2}}\tan(\theta/2)$$

(2.36b)

The response functions can be evaluated by generalizing the expansion developed in Eq. (2.25) to include an antisymmetric contribution

$$\mathcal{W}_A^{\mu\nu} = W_7[V_1^\mu V_2^\nu]_A$$

(2.37)

[Note: the subscript on W_7 was based upon the more general expansion employed in Section 2.4.] Thus, we find that

$$i(\mathcal{W}^{0y} - \mathcal{W}^{y0}) = \sin\phi R'_{LT}$$

(2.38)

where $R'_{LT} = -iW_7$, but that $\mathcal{W}^{xy} - \mathcal{W}^{yx} = 0$ without polarization of either the target or the ejectile.

Therefore, if the electron beam is longitudinally polarized, the differential cross section can be expressed in the form

$$\frac{d\sigma_h}{d\epsilon_f d\Omega_e d\Omega_x} = \sigma_0\frac{1}{2}(1 + hA)$$

(2.39)

where σ_0 is the unpolarized cross section, h is the electron helicity, and A is the beam analyzing power. The beam analyzing power involves a single new response function, sometimes known as the *fifth* response function,[7,9] arising from the interference between the longitudinal current and the transverse current that is normal to the scattering plane. Being proportional to $\sin\phi$, this fifth response function and the corresponding analyzing power vanish in coplanar kinematics. Furthermore, if R'_{LT} is expressed in terms of matrix elements of the nuclear current, such that

$$R'_{LT}\sin\phi = -2\,\text{Im}\langle\rho J_y^\dagger\rangle$$

(2.40)

we find that it vanishes in the plane wave limit where both matrix elements are real.[7] Thus, the beam analyzing power depends upon the presence of final-state interactions. Further elaboration of this point is given in Section 2.4.
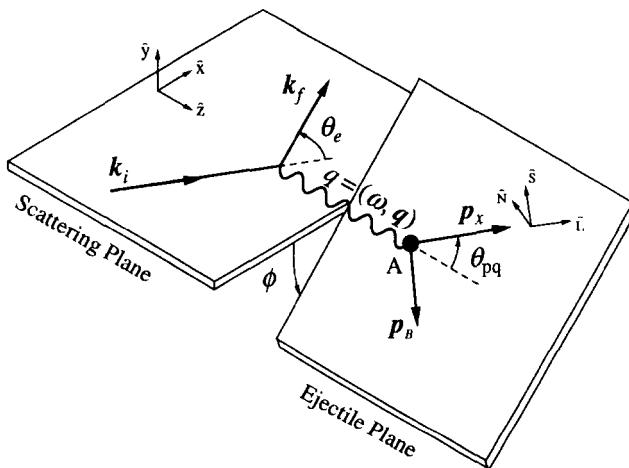
Fig. 2.2. Kinematic definitions for $A(\vec{e}, e'\vec{N})B$ **reactions.**

2.4. Response Functions for Recoil Polarization

Next we consider the properties of the nuclear response tensor for nucleon knockout reactions of the type $A(\vec{e}, e'\vec{N})B$ initiated by a polarized beam and for which the ejectile polarization is detected. The formalism for describing these reactions was developed elsewhere.[11,13,15] A diagram of the reaction may be found in Fig. 2.2. The detected nucleon emerges with momentum $\mathbf{p}_x$ at an angle θ_{pq} with respect to q, leaving the residual nucleus with recoil momentum $\mathbf{p}_B = \mathbf{q} - \mathbf{p}_x$. The polarization of the outgoing nucleon is expressed in the (S, N, L) basis defined with $\hat{L}$ in the direction of the nucleon momentum $\mathbf{p}_x$ and $\hat{N}$ along the normal to the reaction plane, which makes a dihedral angle ϕ with respect to the (electron) scattering plane.

2.4.1. Spin Structure of the Nuclear Response Tensor

Recognizing that $\eta^u_{\mu\nu}$ is symmetric with respect to exchange of the indices $\mu\nu$ while $\eta^h_{\mu\nu}$ is antisymmetric, the contraction of the lepton and hadron tensors can be written in the form

$$\eta_{\mu\nu}\mathcal{W}^{\mu\nu} = \eta^u_{\mu\nu}\mathcal{W}^{\mu\nu}_S + \eta^h_{\mu\nu}\mathcal{W}^{\mu\nu}_A$$

The general form exhibited by the contraction of the symmetric tensors was evaluated in Section 2.2. The same methods can also be used to evaluate the

contraction of the antisymmetric tensors, with the result

$$\eta_{\mu\nu}^{u}\mathcal{W}_{S}^{\mu\nu} = 4\varepsilon_i\varepsilon_f\cos^2\frac{\theta}{2}\left[V_L\mathcal{W}^{00} + V_T(\mathcal{W}^{xx} + \mathcal{W}^{yy})\right.$$
$$\left. -V_{LT}(\mathcal{W}^{0x} + \mathcal{W}^{x0}) + V_{TT}(\mathcal{W}^{xx} - \mathcal{W}^{yy})\right] \quad (2.41a)$$

$$\eta_{\mu\nu}^{h}\mathcal{W}_{A}^{\mu\nu} = 4\varepsilon_i\varepsilon_f\cos^2\frac{\theta}{2}\left[iV_{LT}'(\mathcal{W}^{0y} - \mathcal{W}^{y0})\right.$$
$$\left. -iV_{TT}'(\mathcal{W}^{xy} - \mathcal{W}^{yx})\right] \quad (2.41b)$$

where the kinematic factors were specified above. Note that because $\mathcal{W}^{\mu\nu}$ is hermitian, each term of $\mathcal{W}_S^{\mu\nu}$ must be purely real, while each term of $\mathcal{W}_A^{\mu\nu}$ must be purely imaginary, such that every contribution to the contraction of $\eta_{\mu\nu}\mathcal{W}^{\mu\nu}$ is real.

If the ejectile polarization is detected, the hadron tensor can be expanded in terms of the four independent four-vectors q, p_x, p_A, and s_x. Alternatively, to avoid problems that might occur when the ejectile spin and all three momentum vectors lie in the same plane, it is more convenient to employ

$$\xi^\mu = \varepsilon^{\mu\nu\alpha\beta}q_\nu V_{1\alpha}V_{2\beta}$$

where $\varepsilon^{\mu\nu\alpha\beta}$ is the completely antisymmetric tensor and where V_1 and V_2 are vectors related to p_A and p_x that were defined in Eq. (2.21). With this choice, ξ is automatically orthogonal to the other three basis vectors. As before, it is convenient to extract common kinematic factors from the definitions of the basis vectors in the lab frame. Therefore, to simplify the algebra, we choose

$$A = (0, -\sin\phi, \cos\phi, 0) \quad (2.42)$$

to be the pseudovector member of the expansion basis. Recognizing that terms involving q do not contribute and that

$$A^\mu A^\nu = \frac{\mathbf{q}^2}{Q^2}V_1^\mu V_1^\nu - V_2^\mu V_2^\nu - \tilde{g}^{\mu\nu}$$

is not independent of the other tensors, the symmetric and antisymmetric parts of $\mathcal{W}^{\mu\nu}$ can be expanded in the form

$$\mathcal{W}_S^{\mu\nu} = \mathcal{W}_1\tilde{g}^{\mu\nu} + \mathcal{W}_2 V_1^\mu V_1^\nu + \mathcal{W}_3 V_2^\mu V_2^\nu + \mathcal{W}_4[V_1^\mu V_2^\nu]_S$$
$$+\mathcal{W}_5[V_1^\mu A^\nu]_S + \mathcal{W}_6[V_2^\mu A^\nu]_S \quad (2.43a)$$

$$\mathcal{W}_A^{\mu\nu} = \mathcal{W}_7[V_1^\mu V_2^\nu]_A + \mathcal{W}_8[V_1^\mu A^\nu]_A + \mathcal{W}_9[V_2^\mu A^\nu]_A \quad (2.43b)$$

Given that the electromagnetic current is conserved, these $3^2 = 9$ independent tensors are sufficient to fully characterize $\mathcal{W}^{\mu\nu}$.

The coefficients $\mathcal{W}_i$ depend upon the independent scalars and are at most linear in the ejectile spin. Assuming that parity is conserved, terms linear in A, which is a pseudovector, must be multiplied by pseudoscalar coefficients, while terms independent of A must be multiplied by scalar coefficients. Thus, the coefficients can be expressed in the form

$$\begin{aligned}
\mathcal{W}_i &= W_i^u + W_i^N \vec{\sigma} \cdot \hat{N} & (i = 1 - 4, 7) \\
\mathcal{W}_i &= W_i^L \vec{\sigma} \cdot \hat{L} + W_i^S \vec{\sigma} \cdot \hat{S} & (i = 5, 6, 8, 9)
\end{aligned}$$

where the superscript u, indicating an unpolarized response, is often omitted. Therefore, nucleon knockout by a polarized electron beam in which the ejectile polarization is detected is described by 18 independent response functions. However, if parity is not conserved, 36 response functions are required. These arise from the 9 independent tensors that can be constructed for the unpolarized case and for each of the 3 possible polarization states.

It is now a simple, albeit tedious, exercise to evaluate the response functions and to extract their dependencies on the azimuthal angle ϕ. These azimuthal dependencies are given in the following defining relations:

$$R_L + R_L^N \vec{\sigma} \cdot \hat{N} = \mathcal{W}^{00} \tag{2.44a}$$

$$R_T + R_T^N \vec{\sigma} \cdot \hat{N} = \mathcal{W}^{xx} + \mathcal{W}^{yy} \tag{2.44b}$$

$$\begin{aligned}
(R_{LT} + R_{LT}^N \vec{\sigma} \cdot \hat{N}) \cos\phi & \\
+ (R_{LT}^L \vec{\sigma} \cdot \hat{L} + R_{LT}^S \vec{\sigma} \cdot \hat{S}) \sin\phi &= -(\mathcal{W}^{0x} + \mathcal{W}^{x0})
\end{aligned} \tag{2.44c}$$

$$\begin{aligned}
(R_{TT} + R_{TT}^N \vec{\sigma} \cdot \hat{N}) \cos 2\phi & \\
+ (R_{TT}^L \vec{\sigma} \cdot \hat{L} + R_{TT}^S \vec{\sigma} \cdot \hat{S}) \sin 2\phi &= \mathcal{W}^{xx} - \mathcal{W}^{yy}
\end{aligned} \tag{2.44d}$$

$$\begin{aligned}
(R'_{LT} + R_{LT}^{\prime N} \vec{\sigma} \cdot \hat{N}) \sin\phi & \\
+ (R_{LT}^{\prime L} \vec{\sigma} \cdot \hat{L} + R_{LT}^{\prime S} \vec{\sigma} \cdot \hat{S}) \cos\phi &= i(\mathcal{W}^{0y} - \mathcal{W}^{y0})
\end{aligned} \tag{2.44e}$$

$$R_{TT}^{\prime L} \vec{\sigma} \cdot \hat{L} + R_{TT}^{\prime S} \vec{\sigma} \cdot \hat{S} = -i(\mathcal{W}^{xy} - \mathcal{W}^{yx}) \tag{2.44f}$$

where

$$\begin{aligned}
R_L^m &= \frac{\mathbf{q}^2}{Q^2} W_1^m + W_2^m & (m = u, N) \\
R_T^m &= -2W_1^m + W_3^m & (m = u, N) \\
R_{LT}^m &= -W_4^m & (m = u, N) \\
R_{LT}^m &= W_5^m & (m = L, S) \\
R_{TT}^m &= -W_3^m & (m = u, N) \\
R_{TT}^m &= -W_6^m & (m = L, S) \\
R_{LT}^{\prime m} &= -iW_7^m & (m = u, N) \\
R_{LT}^{\prime m} &= -iW_8^m & (m = L, S) \\
R_{TT}^{\prime m} &= iW_9^m & (m = L, S)
\end{aligned}$$

Obviously, terms proportional to $\sin\phi$ or $\sin 2\phi$ cannot contribute in coplanar kinematics. Terms proportional to $\cos\phi$ can be isolated in coplanar kinematics by comparing measurements for $\phi = 0, \pi$.

The dependence of the nuclear response functions upon recoil polarization can be extracted from the defining relationships, Eq. (2.44), by the introduction of appropriate projection operators into the nuclear response tensor. Recognizing that the conceptual definition

$$\mathcal{W}_{\mu\nu} = \langle J_\mu J_\nu^\dagger \rangle$$

where the angle brackets denote products of matrix elements appropriately averaged over initial states and summed over final states with appropriate phase-space factors, includes summation over both target and ejectile spins, we can isolate the desired nucleon polarization component $\hat{\mathbf{a}}$ using the generalization

$$\mathcal{W}_{\mu\nu}(\hat{\mathbf{a}}) = \langle J_\mu J_\nu^\dagger \boldsymbol{\sigma} \cdot \hat{\mathbf{a}} \rangle \tag{2.45}$$

where the Pauli matrix refers to the ejectile spin. If the ejectile spin is not detected, the spin-operator simply reverts to a unit matrix and the previous results are recovered.

2.4.2. Parallel Kinematics

The requirement that the observables for parallel kinematics, in which the orientation of the reaction plane becomes undefined, be independent of the azimuthal angle ϕ leads to constraints among the response functions in the limit $\theta_{pq} \to 0$. Consider the limiting process in which $\theta_{pq} \to 0$ with constant ϕ. The ejectile helicity basis $(\hat{S}, \hat{N}, \hat{L})$ is then related to the laboratory basis $(\hat{x}, \hat{y}, \hat{z})$ by a right-handed rotation about the common $\hat{L} = \hat{z} = \hat{q}$ axis by the angle ϕ. The requirement that the contributions of the transverse polarization,

$$R_{LT}^N \vec{\sigma} \cdot \hat{N} + R_{LT}^S \vec{\sigma} \cdot \hat{S} = \vec{\sigma} \cdot \hat{x}(-R_{LT}^N + R_{LT}^S) \sin\phi \cos\phi$$
$$+ \vec{\sigma} \cdot \hat{y}(R_{LT}^N \cos^2\phi + R_{LT}^S \sin^2\phi)$$

be independent of ϕ implies that $R_{LT}^N = R_{LT}^S$ in parallel kinematics. Applying similar conditions to the polarization transfer and to antiparallel kinematics $(\theta_{pq} \to \pi)$ then gives

$$R_{LT}^N = \pm R_{LT}^S \tag{2.46}$$
$$R_{LT}'^N = \mp R_{LT}'^S \tag{2.47}$$

where the upper sign refers to parallel and the lower to antiparallel kinematics. All other response functions whose contributions to the observables retain explicit dependencies on the undefined azimuthal angle must vanish in parallel kinematics. Therefore, only five independent response functions survive in parallel or antiparallel kinematics.

2.4.3. Plane-Wave Limit

In the plane-wave (PWIA) limit, the symmetries of the operators and the states with respect to the combined symmetry operation $\Theta = \mathcal{PT}$, where $\mathcal{P}$ represents parity inversion and $\mathcal{T}$ represents time reversal, gives rise to important constraints upon the properties of $\mathcal{W}^{\mu\nu}$. Here we give a slightly simplified derivation; more rigorous considerations may be found in Refs. 7, 11 and 14, for example. In PWIA, both the initial state of the target and the final state, consisting of the ejectile and the residual nucleus, are represented as products of plane wave functions for a nucleon and the residual nucleus, one of which absorbs a virtual photon while the other is a spectator. Each of these states has the following transformation property:

$$\Theta \mid \vec{p}_i, m_i \rangle = \eta_i \mid \vec{p}_i, -m_i \rangle^*$$

where m_i is the magnetic quantum number and η_i is a phase factor of unit magnitude. Similarly, the electromagnetic current is represented by a one-body operator which is invariant with respect to Θ, such that

$$\Theta J^\mu \Theta^{-1} = J^\mu$$

Hence, current matrix elements have the symmetry property

$$\langle \vec{p}_x m_x, \vec{p}_B m_B \mid \Theta^{-1} \Theta J^\mu \Theta^{-1} \Theta \mid \vec{p}_A m_A \rangle$$
$$= \eta_x^* \eta_B^* \eta_A \langle \vec{p}_A, -m_A \mid J^\mu \mid \vec{p}_x, -m_x, \vec{p}_B, -m_B \rangle$$

Ignoring phase space and normalization factors, the unpolarized nuclear response tensor

$$\mathcal{W}^{\mu\nu} = \sum_{m_x m_B m_A} \langle \vec{p}_x m_x, \vec{p}_B m_B \mid J^\mu \mid \vec{p}_A m_A \rangle$$
$$\times \langle \vec{p}_A m_A \mid J^\nu \mid \vec{p}_x m_x, \vec{p}_B m_B \rangle \tag{2.48}$$

becomes

$$\mathcal{W}^{\mu\nu} = \sum_{m_x m_B m_A} \langle \vec{p}_x, -m_x, \vec{p}_B, -m_B \mid J^\nu \mid \vec{p}_A, -m_A \rangle$$
$$\times \langle \vec{p}_A, -m_A \mid J^\mu \mid \vec{p}_x, -m_x, \vec{p}_B, -m_B \rangle \tag{2.49}$$

under the action of Θ. Note that the phase factors drop out because $\mathcal{W}$ is bilinear in the matrix elements. Simply changing the signs of dummy summation indices, we find that the unpolarized response tensor must be symmetric in the plane wave limit:

$$PWIA \Longrightarrow \mathcal{W}^{\mu\nu} = \mathcal{W}^{\nu\mu} \qquad (2.50)$$

Combining this result with the hermiticity of $\mathcal{W}$, we conclude that the unpolarized response tensor is purely real in the plane-wave limit.

On the other hand, the Pauli spin matrix is odd with respect to Θ,

$$\Theta\vec{\sigma}\Theta^{-1} = -\vec{\sigma}$$

so that the response tensor for recoil polarization

$$
\mathcal{W}^{\mu\nu}(\hat{a}) = \sum_{m_x m'_x m_B m_A} \langle \vec{p}_x m_x, \vec{p}_B m_B \mid J^\mu \mid \vec{p}_A m_A \rangle
$$
$$
\times \langle \vec{p}_A m_A \mid J^\nu \mid \vec{p}_x m'_x, \vec{p}_B m_B \rangle \langle m'_x \mid \vec{\sigma} \cdot \hat{a} \mid m_x \rangle \quad (2.51)
$$

becomes

$$
\mathcal{W}^{\mu\nu} = \sum_{m_x m'_x m_B m_A} \langle \vec{p}_x, -m'_x, \vec{p}_B, -m_B \mid J^\nu \mid \vec{p}_A, -m_A \rangle
$$
$$
\times \langle \vec{p}_A, -m_A \mid J^\mu \mid \vec{p}_x, -m_x, \vec{p}_B, -m_B \rangle
$$
$$
\times \langle -m_x \mid -\vec{\sigma} \cdot \hat{a} \mid -m'_x \rangle \qquad (2.52)
$$

such that

$$\mathcal{W}^{\mu\nu}(\hat{a}) = -\mathcal{W}^{\nu\mu}(\hat{a}) = \mathcal{W}^{\nu\mu}(-\hat{a}) \qquad (2.53)$$

is symmetric with respect to exchange of its indices combined with inversion of spins. If the spins are not inverted, contributions to $\mathcal{W}$ which are linear in one of the spins are antisymmetric, and thus must be purely imaginary since $\mathcal{W}$ is hermitian.

Therefore, we conclude that $\mathcal{W}_S^{\mu\nu}$ does not contribute to the recoil polarization in PWIA. Similarly, $\mathcal{W}_A^{\mu\nu}$ does not contribute in PWIA to the part of the cross section that is independent of nucleon spin.

2.4.4. *Classification of the Response Functions*

It is useful to classify the 18 response functions required to describe fully the $A(\vec{e}, e'\vec{N})B$ reaction according to their dependencies upon opening angle

TABLE 2.1

Properties of the Response Functions for the $A(\vec{e}, e'\vec{N})B$ Reaction

The constraints among response functions for parallel/antiparallel kinematics are indicated by the upper/lower choices of signs.

Response function	Helicity dependence	Survives in plane	Survives parallel	Survives PWIA	Azimuthal dependence
R_L	X	✓	✓	✓	1
R_T	X	✓	✓	✓	1
R_{LT}	X	✓	X	✓	$\cos\phi$
R_{TT}	X	✓	X	✓	$\cos 2\phi$
R'_{LT}	✓	X	X	X	$\sin\phi$
R_L^N	X	✓	X	X	1
R_T^N	X	✓	X	X	1
R_{LT}^N	X	✓	✓	X	$\cos\phi$
R_{TT}^N	X	✓	X	X	$\cos 2\phi$
R'^N_{LT}	✓	X	$\mp R'^S_{LT}$	✓	$\sin\phi$
R_{LT}^L	X	X	X	X	$\sin\phi$
R'^L_{LT}	✓	✓	X	✓	$\cos\phi$
R_{TT}^L	X	X	X	X	$\sin 2\phi$
R'^L_{TT}	✓	✓	✓	✓	1
R_{LT}^S	X	X	$\pm R_{LT}^N$	X	$\sin\phi$
R'^S_{LT}	✓	✓	✓	✓	$\cos\phi$
R_{TT}^S	X	X	X	X	$\sin 2\phi$
R'^S_{TT}	✓	✓	X	✓	1

θ_{pq}, out-of-plane angle ϕ, and final-state interactions.[11] These characteristics are summarized in Table 2.1.

Although, strictly speaking, the plane-wave limit does not apply to knockout reactions, it does help to distinguish between those response functions that are governed primarily by the elementary electron–nucleon vertex and those which would vanish in the absence of final-state interactions (FSI). The former tend to be relatively insensitive to details of FSI, while the latter depend strongly upon FSI and tend to be more sensitive to their details. To the extent that one-photon exchange is valid, electron scattering from free nucleons involves only those response functions allowed in PWIA. Similarly, quasifree knockout for few-body systems is dominated by the same responses.

It is important to recognize that none of these developments depends upon the characteristics of the undetected system. Therefore, electroproduction reactions of the type $A(\vec{e}, e'\vec{N})X$, where $X = B + \pi$ might include a pion or other meson, for example, are also described by the same formalism. The

formalism of pion electroproduction with recoil polarization has been considered by Raskin and Donnelly,[14] Nozawa, Blankleider, and Lee,[22–24] and Drechsel and Tiator,[25] among others. Although the plane-wave limit does not apply to the pion electroproduction reaction, similar selection rules can be developed for the case of an isolated resonance. According to the Fermi–Watson theorem[26] all scattering amplitudes for an isolated resonance are characterized by a common phase. Under those circumstances the imaginary part of the interference between two components of the current, $\mathrm{Im}(J_k J_l^*) = 0$, vanishes identically. Consequently, the same set of response functions shown to vanish in Table 2.1 for PWIA knockout also vanish for any electroproduction dominated by an isolated resonance. Therefore, these response functions require interference between resonant and nonresonant (background) amplitudes or between two different resonances.

2.5. Recoil Polarization Observables

Nucleon knockout reactions of the type $(\vec{e}, e'\vec{N})$ initiated by a polarized beam and for which the ejectile polarization is detected may be described by a differential cross section of the general form[13,15]

$$\frac{d^6\sigma_{hs}}{d\varepsilon_f d\Omega_e d\varepsilon_x d\Omega_x} = \sigma_0 \frac{1}{2}\left[1 + \mathbf{P}\cdot\boldsymbol{\sigma} + h(A + \mathbf{P}'\cdot\boldsymbol{\sigma})\right] \qquad (2.54)$$

where σ_0 is the unpolarized cross section, h is the electron helicity, s indicates the nucleon spin projection upon $\boldsymbol{\sigma}$, $\mathbf{P}$ is the induced polarization, A is the beam analyzing power, and $\mathbf{P}'$ is the polarization transfer coefficient. Thus, the net polarization of the recoil nucleon $\boldsymbol{\Pi}$ has two contributions of the form

$$\boldsymbol{\Pi} = \mathbf{P} + h\mathbf{P}' \qquad (2.55)$$

where $|h| \leq 1$ is interpreted as the longitudinal beam polarization. Recapitulating the results of preceding sections, each of the observables may be described in terms of kinematical factors $V_{\alpha\beta}$ and response functions $R_{\alpha\beta}$, according to

$$\begin{aligned}
\sigma_0 &= K\sigma_M \left(V_L R_L + V_T R_T + V_{LT} R_{LT}\cos\phi + V_{TT} R_{TT}\cos 2\phi\right)\\
\sigma_0 A &= K\sigma_M V'_{LT} R'_{LT}\sin\phi\\
\sigma_0 P_N &= K\sigma_M \left(V_L R_L^N + V_T R_T^N + V_{LT} R_{LT}^N\cos\phi + V_{TT} R_{TT}^N\cos 2\phi\right)\\
\sigma_0 P_m &= K\sigma_M \left(V_{LT} R_{LT}^m\sin\phi + V_{TT} R_{TT}^m\sin 2\phi\right) \qquad (m=L,S)\\
\sigma_0 P'_N &= K\sigma_M V'_{LT} R'^N_{LT}\sin\phi\\
\sigma_0 P'_m &= K\sigma_M \left(V'_{LT} R'^m_{LT}\cos\phi + V'_{TT} R'^m_{TT}\right) \qquad (m=L,S)
\end{aligned}$$

where the kinematical factors

$$K = \frac{\varepsilon_x p_x}{(2\pi)^3} \qquad\qquad \sigma_M = \frac{\alpha^2}{4\epsilon_i^2} \frac{\cos^2(\theta/2)}{\sin^4(\theta/2)}$$

$$V_L = \frac{Q^4}{\mathbf{q}^4} \qquad\qquad V_T = \frac{Q^2}{2\mathbf{q}^2} + \tan^2(\tfrac{\theta}{2})$$

$$V_{LT} = \frac{Q^2}{\mathbf{q}^2}\left[\frac{Q^2}{\mathbf{q}^2} + \tan^2(\tfrac{\theta}{2})\right]^{\frac{1}{2}} \qquad V_{TT} = \frac{Q^2}{2\mathbf{q}^2}$$

$$V'_{LT} = \frac{Q^2}{\mathbf{q}^2}\tan(\tfrac{\theta}{2}) \qquad\qquad V'_{TT} = \left[\frac{Q^2}{\mathbf{q}^2} + \tan^2(\tfrac{\theta}{2})\right]^{\frac{1}{2}}\tan(\tfrac{\theta}{2})$$

are expressed in terms of the electron scattering angle θ, the angle ϕ between the reaction and scattering planes, and the four-momentum transfer $Q^2 = -q_\mu q^\mu = \mathbf{q}^2 - \omega^2$. The detected nucleon emerges with momentum $\mathbf{p}_N$ at an angle θ_{pq} with respect to $\mathbf{q}$, leaving the residual nucleus with recoil momentum $\mathbf{p}_r = \mathbf{q} - \mathbf{p}_N$. In the plane-wave impulse approximation, the struck nucleon is found with initial or missing momentum $\mathbf{p}_m = -\mathbf{p}_r$. A diagram of the reaction may be found in Fig. 2.2. The polarization of the outgoing nucleon is expressed in the (S, N, L) basis defined with $\hat{L}$ in the direction of the nucleon momentum $\mathbf{p}$ and $\hat{N}$ along the normal to the reaction plane.

Considerable simplification of the spin structure of the reaction is obtained for parallel kinematics. Azimuthal symmetry around $\mathbf{q}$ eliminates those response functions whose contributions to the observables depend upon the orientation of the reaction plane and also requires $R_{LT}^N = R_{LT}^S$ and $R_{LT}'^N = -R_{LT}'^S$. Hence, there remain at most five independent response functions in parallel kinematics. The expressions relating observables to response functions then reduce to

$$\sigma_0/K\sigma_M = V_L R_L + V_T R_T \qquad\qquad (2.56a)$$

$$\Pi_N \sigma_0/K\sigma_M = V_{LT} R_{LT}^N \qquad\qquad (2.56b)$$

$$\Pi_S \sigma_0/K\sigma_M = h V'_{LT} R_{LT}'^S \qquad\qquad (2.56c)$$

$$\Pi_L \sigma_0/K\sigma_M = h V'_{TT} R_{TT}'^L \qquad\qquad (2.56d)$$

Thus, polarization measurements permit certain individual response functions to be isolated. Measurement of the induced polarization P_N for parallel kinematics yields R_{LT}^N at $\theta_{pq} = 0°$ or $180°$ directly, while measurement of P'_S or P'_L yields $R_{LT}'^S$ or $R_{TT}'^L$, respectively.

Further simplifications are obtained when either the target or the residual nucleus has **spin-$\frac{1}{2}$** and the other is spinless. Examples include pion electroproduction on the nucleon or $p_{1/2}$ knockout from a spin-zero nucleus. The

current matrix elements can then be expressed in terms of six independent complex helicity amplitudes, but since only two of these helicity amplitudes survive in parallel kinematics only four independent response functions can contribute to the observables for parallel or antiparallel kinematics.[13] Under these conditions, the additional constraint $R_{TT}^{\prime L} = R_T$ then applies. Therefore, measurements of the two transverse polarization components combined with Rosenbluth separation of the cross section suffice to completely determine the two relevant helicity amplitudes. Also note that different helicity amplitudes are obtained for $\theta_{pq} = 0°$ and $\theta_{pq} = 180°$. On the other hand, Rosenbluth separation of the cross section is often difficult and plagued by systematic errors in the subtraction of two nearly equal cross sections with rapid kinematic dependencies. Hence it may be advantageous to exploit the relationship between longitudinal polarization and R_T to either replace or supplement Rosenbluth separation.

2.6. Target Polarization

2.6.1. Spin-$\frac{1}{2}$

The scattering of polarized electrons from polarized **spin-$\frac{1}{2}$** targets without detection of final-state polarizations can be analyzed in exactly the same manner as employed in Sections 2.4 and 2.5. Thus, the cross section is expressed as[3]

$$\frac{d^6\sigma_{hs}}{d\varepsilon_f d\Omega_e d\varepsilon_x d\Omega_x} = \sigma_0 \frac{1}{2}\left[1 + \mathbf{P}^T \cdot \mathbf{A}^T + h(A + \mathbf{P}^T \cdot \mathbf{A}'^T)\right] \quad (2.57)$$

where $\mathbf{P}^T$ is the target polarization vector, $\mathbf{A}^T$ is the target analyzing power, A is the beam analyzing power, and $\mathbf{A}'^T$ is the correlation vector. Although the correlation between beam and target polarizations is normally described by a matrix,[27] often known as the efficiency correlation matrix,[28] the fact that only the helicity of the electron beam is relevant at high energies permits the correlation matrix to be reduced to vector form.

The new observables $\mathbf{A}^T$ and $\mathbf{A}'^T$ are analogous to the recoil polarization observables $\mathbf{P}$ and $\mathbf{P}'$ and can be expanded in terms of the same set of response functions adorned by a superscript T to indicate their role in target, rather than recoil, polarization. These response functions are projected from the polarization tensor in precisely the same manner specified by Eq. (2.45) except that the Pauli matrix refers to the target spin rather than the ejectile spin. In principle, these response functions are independent of those for recoil polarization, although in some special cases, such as simplified models

of pion electroproduction, some of the target and recoil polarization response functions coincide.

Polarized ^{3}He targets are the most important example of this type. To the extent that the spin is carried entirely by the neutron, and that final-state interactions and other complications can be calculated accurately, polarized ^{3}He provides a good polarized neutron target. Hence, the polarization observables can be used to isolate the neutron and to determine its electromagnetic properties. Work along these lines will be reviewed in Sections 3.3.2 and 3.3.3.

2.6.2. $\vec{A}(\vec{e}, e'\vec{x})\vec{B}$

The nuclear response tensor for the general case in which the target, an ejectile, and the residual nucleus are all polarized can be represented schematically as[29]

$$
\mathcal{W}^{\mu\nu} = \overline{\sum_{if}} \sum_{m_x m'_x} \sum_{m_A m'_A} \sum_{m_B m'_B} \langle m_x m_B \mid J^\mu \mid m_A \rangle \langle m'_A \mid J^\nu \mid m'_x m'_B \rangle^*
$$
$$
\times \rho^x_{m_x m'_x} \rho^B_{m_B m'_B} \rho^A_{m_A m'_A} \delta(E_i - E_f) \tag{2.58}
$$

where ρ^A, ρ^x, and ρ^B are polarization density matrices for the target, the ejectile, and the residual nucleus, respectively. The summation over final and average over initial states implicitly includes all relevant phase space factors. The m-indices label magnetic substrates, but other quantum numbers are suppressed for brevity. The density matrices can be expressed in terms of irreducible statistical tensors t_{kq} according to Ref. 28, 30

$$
\rho_{mm'} = (2s+1)^{-1} \sum_{kq} (-)^{s-m} \left\langle \begin{array}{cc|c} s & s & k \\ m' & -m & q \end{array} \right\rangle t_{kq} \tag{2.59}
$$

where s is the intrinsic spin of the particle.

The combinatorics of the general case can produce a daunting number of response functions. For example, the $9 \times 18 = 162$ independent response functions required to fully describe the $^2\vec{H}(\vec{e}, e'\vec{p})n$ reaction have been developed in some detail by Dmitrasinovic and Gross.[31] A complete catalogue of polarization observables for electrodisintegration of polarized deuterons by longitudinally polarized electrons in which the recoil polarization is also analyzed has been prepared by Arenhövel *et al.*[32] However, it remains to be seen which of these many observables might yield valuable information.

2.7. Basic PWIA for $A(e, e'x)B$

In nonrelativistic PWIA, the knockout cross section factorizes in the form

$$\frac{d\sigma}{d\varepsilon_f d\Omega_e d\varepsilon_x d\Omega_x} = K\sigma_{ex}S(E_m, \mathbf{p}_m) \tag{2.60}$$

where

$$K = \frac{\varepsilon_x p_x}{(2\pi)^3} \tag{2.61}$$

is a kinematical factor which adjusts the phase space, σ_{ex} is the half off-shell cross section for scattering of an electron by constituent x, and S is the spectral function relating the ground state of the target A to the final state of the residual nucleus B. The kinematics of the process are indicated in Fig. 2.1. The ejectile is usually a nucleon, but similar results pertain to more complex clusters. In PWIA we assume that the virtual photon $(\omega, \mathbf{q})$ is absorbed by a preformed but off-shell constituent x with initial momentum $\mathbf{p}$ and energy E before knockout. These quantities are determined by applying energy and momentum conservation at the $\gamma + x$ vertex, whereby

$$E = \varepsilon_x - \omega = m_x - E_m - T_B + T_A \tag{2.62a}$$
$$\mathbf{p} = \mathbf{p}_x - \mathbf{q} \tag{2.62b}$$

The kinetic energies of the target and the residual nuclei are denoted here by T_A and T_B, respectively. Henceforth we assume $T_A = 0$, i.e., the lab frame. The missing energy*

$$E_m = m_x + m_B - m_A = \omega - T_x - T_B \tag{2.63}$$

represents the separation energy for a particular final configuration of the hadronic system and is related to the excitation energy ε_B^* of the residual nucleus by

$$E_m = E_S + \varepsilon_B^* \tag{2.64}$$

where E_S is minimum separation energy for the ground state. Similarly, we define the missing momentum as

$$\mathbf{p}_m = \mathbf{p}_x - \mathbf{q} = -\mathbf{p}_B \tag{2.65}$$

---

* Although the present definition of missing energy is more properly called missing mass, with $\omega - T_x$ being the missing energy, we have decided to conform with the more prevalent nomenclature despite its minor inconsistency.

Obviously $\mathbf{p}_m$ is simply the inverse of the recoil momentum and in PWIA may be interpreted as the momentum the ejectile must have had prior to knockout.

The spectral function

$$S(E, \mathbf{p}) = \sum_f |\langle B_f | a(\mathbf{p}) | A_i \rangle|^2 \delta(E - E_m) \qquad (2.66)$$

represents the probability that a nucleon with initial momentum $\mathbf{p}$ and binding energy E can be removed from initial state A_i of target A and leave the residual target B in any final state B_f that has missing energy E_m. Clearly, the initial energy and momentum the ejectile must have had before knockout are identified with the missing energy and momentum for the reaction

$$PWIA \implies (E, \mathbf{p}) \longrightarrow (E_m, \mathbf{p}_m) \qquad (2.67)$$

The spectral function plays a central role in many-body theory and in the description of single-nucleon removal processes, but is not a true observable since it is not actually possible to cause a nucleon to suddenly disappear from the system. Nucleon knockout by electron scattering, under kinematical conditions which emphasize the direct single-nucleon mechanism in which a single virtual photon delivers a large momentum transfer to a single nucleon, comes about as close to this ideal as possible, but in analyzing experiments we must still account for final-state interactions and more complicated mechanisms for sharing the energy transfer.

2.8. Kinematical Conventions

Most experiments have been performed using either of two types of kinematical conventions, which are illustrated in Fig. 2.3. *In parallel kinematics* the ejectile momentum is parallel to the momentum transfer such that the missing momentum $p_m = p_x - q$ is positive if $p_x > q$ or negative if $p_x < q$. Since the ejectile momentum is usually held constant or nearly constant, the missing momentum is varied by changing the momentum transfer, which is larger for negative p_m and smaller for positive p_m. To minimize variations of final-state interactions (FSI), one usually prefers to hold the ejectile momentum p_x^* constant in the $x + B$ center of mass, although many experiments have chosen to maintain constant laboratory momentum instead.

Alternatively, one can keep both the four-momentum transfer $(\omega, \mathbf{q})$ and p_x constant and vary p_m by changing the angle θ_{pq} between them. Since both q and p_x are usually large enough for the relevant range of p_m to be covered with relatively small angles, p_m is nearly perpendicular to q (and to p_x). Hence, these conditions are often called *quasiperpendicular kinematics*.
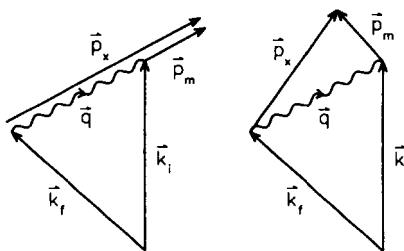
Fig. 2.3. Arrangements for parallel (left) and quasiperpendicular (right) kinematics.

So that $p_m = 0$ is obtained at $\theta_{pq} = 0$, it is customary to choose $q = p_x$ for quasiperpendicular kinematics.

Although the literature exhibits little uniformity regarding these conventions, based upon Fig. 2.2 it is natural in quasiperpendicular kinematics to identify ejectile momenta between the beam and momentum transfer directions with positive θ_{pq}, positive p_m, and $\phi = 0$ and to identify ejectile momenta at angles larger than θ_q either with negative p_m or with negative θ_{pq} or with $\phi = \pi$. Furthermore, treating parallel kinematics as the limit $\theta_{pq} \longrightarrow 0^+$, we define the   direction in parallel kinematics to point toward smaller ejectile angles.

Note that the literature contains two different definitions of missing momentum for parallel kinematics. The Saclay group defines the missing momentum to be the recoil momentum carried by the residual nucleus,[1,33] while the NIKHEF group usually defines the missing momentum to be the undistorted initial momentum according to Eq. (2.65). Hence, these two conventions are opposite in sign. We have chosen to adopt the NIKHEF convention for parallel kinematics. Furthermore, we arbitrarily assign $\hat{\mathbf{N}}$ for parallel kinematics to the direction of $\mathbf{k}_i \otimes \mathbf{k}_f$ for parallel kinematics. Similarly, the Saclay group assigns positive recoil momenta to $\theta_p < \theta_q$, while most NIKHEF papers assign positive missing momenta to $\theta_p > \theta_q$ because those conditions tend to be easier experimentally and hence are more common. Since large missing momenta are more accessible at $\phi = \pi$, we have again chosen to adopt the NIKHEF convention and assign $p_m > 0$ for coplanar nonparalllel kinematics with $\phi = \pi$ and $\theta_p > \theta_q$. With these choices, $\hat{\mathbf{N}}$ is directed downward (upward) for positive (negative) p_m.

Finally, we define *antiparallel kinematics* to be when the ejectile momentum is parallel to the momentum transfer, but in the opposite direction. It has been suggested[34] that these conditions can be used to observe short-range correlations in which a pair of nucleons have large momenta relative to each

other, but the pair has a small momentum relative to the residual nucleus. A virtual photon is absorbed by the partner whose initial momentum is parallel to **q,** and hence is ejected from the nucleus with relatively small momentum transferred and correspondingly large probability, while the correlated partner, which is a spectator to the scattering event, emerges with large momentum antiparallel to **q.**

2.9. Electron Scattering from a Moving Nucleon

The unpolarized nucleon response tensor is defined as

$$\mathcal{W}_{\mu\nu} = \frac{1}{2} \sum_{s_i s_f} \langle p_f s_f | J_\mu | p_i s_i \rangle \langle p_i s_i | J_\nu^\dagger | p_f s_f \rangle \tag{2.68}$$

where p_i and p_f are the momenta while s_i and s_f are the spin four-vectors for the initial and final states. Matrix elements of the nucleon current can be expressed in the form

$$\langle p_f s_f | J^\mu | p_i s_i \rangle = \bar{U}_f \Gamma^\mu (p_f, p_i) U_i \tag{2.69}$$

where Γ^μ is the electromagnetic vertex function for the nucleon and where the spinors are denoted by U_i and U_f. The vertex function for a Dirac particle with internal structure has the general form

$$\Gamma_2^\mu = \gamma^\mu F_1(Q^2) + i\sigma^{\mu\nu} \frac{q_\nu}{2M} \kappa F_2(Q^2) \tag{2.70}$$

where F_1 is sometimes called the Dirac form factor and F_2 the Pauli form factor and where k is the anomalous part of the magnetic moment. Alternatively, the Gordon identity[16,35] can be used to express this current in the form

$$\Gamma_1^\mu = \gamma^\mu \left(F_1(Q^2) + \kappa F_2(Q^2) \right) - \frac{P^\mu}{2M} \kappa F_2(Q^2) \tag{2.71}$$

where $P = p_i + p_f$ and where p_i and p_f are the initial and final nucleon momenta. Although these forms are equivalent on-shell, they need not be equivalent off-shell. Moreover, as discussed in Section 5.5.3, the structure of the vertex function can be considerably more complicated off-shell.

Anticipating that we will require the cross section for scattering from a quasifree nucleon that is moving in its initial state (within the nucleus), it will be helpful to analyze the general structure of the cross section without the simplifying assumption of a stationary target. To evaluate the cross section

for a moving but free nucleon, it is simpler to use the Γ_1 form of the current. Upon evaluation of the traces, the nucleon response tensor becomes

$$4m^2 \mathcal{W}_{\mu\nu} = \left[F_1^2 + \frac{Q^2}{4m^2}(\kappa F_2)^2 \right] P_\mu P_\nu - (F_1 + \kappa F_2)^2 Q^2 \tilde{g}_{\mu\nu}$$

where

$$\tilde{g}_{\mu\nu} = g_{\mu\nu} + \frac{q_\mu q_\nu}{Q^2}$$

Thus, the electron-nucleon cross section involves response functions of the form[18]

$$R_L = \frac{(E_i + E_f)^2}{4m^2} W_1 - \frac{\mathbf{q}^2}{4m^2} W_2 \qquad (2.72a)$$

$$R_T = 2\tau W_2 + \frac{\mathbf{p}_f^2 \sin^2 \theta_{pq}}{m^2} W_1 \qquad (2.72b)$$

$$R_{LT} = -\frac{(E_i + E_f)|\mathbf{p}_f| \sin \theta_{pq}}{m^2} W_1 \qquad (2.72c)$$

$$R_{TT} = \frac{\mathbf{p}_f^2 \sin^2 \theta_{pq}}{m^2} W_1 \qquad (2.72d)$$

where

$$W_1 = F_1^2 + \tau(\kappa F_2)^2 \qquad (2.73a)$$
$$W_2 = (F_1 + \kappa F_2)^2 \qquad (2.73b)$$

are the two independent form factors and where

$$\tau = \frac{Q^2}{4m^2}$$

The simplest approximation to nucleon knockout stipulates quasifree scattering from a nucleon that is moving in the mean field of the residual nucleus but is otherwise free. We also assume that the nucleon that is observed is the same as the nucleon that absorbed the virtual photon. If this nucleon were initially at rest, then the R_{LT} and R_{TT} response functions would vanish. Thus, in the absence of final-state interactions, these response functions depend upon the Fermi motion in the target and hence can be considered to be recoil corrections due to the initial velocity of the struck nucleon. Such effects are expected to be sensitive to ambiguities in the off-shell extrapolation of the nucleon current. However, final-state interactions also contribute to these form factors.

3. NUCLEON FORM FACTORS

Accurate knowledge of the electromagnetic properties of nucleons is essential to the evaluation of models of nucleon structure.[4] For example, Gari and Krümpelmann[36,37] have suggested that strange quark coupling to the nucleon, via the ϕ-meson, could have a large effect on the neutron electric form factor without significantly affecting other nucleon electromagnetic form factors for moderate Q^2. Unfortunately, G_{En} is very poorly known and the present experimental precision of proton form factors and of G_{Mn} also leaves much to be desired. Furthermore, uncertainties in the nucleon electromagnetic form factors sometimes dominate the theoretical uncertainties in electronuclear calculations. For example, Schiavilla and Riska[38] identify nucleon form factors as the largest source of theoretical uncertainty for threshold electrodisintegration of the deuteron at large momentum transfer.

3.1. Sachs Form Factors

Proton form factors can be readily determined from measurements of elastic electron scattering from hydrogen. In the absence of free-neutron targets, measurements of neutron form factors rely on experiments upon few-body systems under conditions that optimize the accuracy of the impulse approximation. Quasifree scattering requires that the recoil momentum, and hence the initial nucleon momentum, be negligible. Furthermore, detection of a recoil neutron in quasifree kinematics minimizes the unwanted contributions of protons.

For free eN elastic scattering, one ordinarily works in the lab frame, for which $R_{LT} = R_{TT} = 0$. It is then more convenient to work with the Sachs form factors,[39] defined as

$$G_E(Q^2) = F_1(Q^2) - \tau\kappa F_2(Q^2) \tag{3.1a}$$
$$G_M(Q^2) = F_1(Q^2) + \kappa F_2(Q^2) \tag{3.1b}$$

such that

$$W_1 = \frac{G_E^2 + \tau G_M^2}{1 + \tau} \tag{3.2a}$$
$$W_2 = G_M^2 \tag{3.2b}$$

For elastic scattering from a stationary nucleon, the kinematic and angular

factors can be simplified considerably using

$$\omega = \frac{Q^2}{2m} = 2m\tau, \qquad \frac{m + E_f}{2m} = 1 + \tau$$

$$\frac{\mathbf{q}^2}{4m^2} = (1+\tau)\tau \qquad \frac{Q^2}{\mathbf{q}^2} = (1+\tau)^{-1}$$

such that

$$V_L R_L + V_T R_T = W_1 + 2\tau \tan^2 \frac{\theta}{2} W_2$$

Thus, the familiar Rosenbluth formula is obtained in the form[40]

$$\frac{d\sigma}{d\Omega} = f_{\text{rec}}\sigma_M \left(\frac{G_E^2 + \tau G_M^2}{1 + \tau} + 2\tau G_M^2 \tan^2 \frac{\theta}{2} \right) \qquad (3.3)$$

or, alternatively,

$$\frac{d\sigma}{d\Omega} = f_{\text{rec}}\sigma_M \left[A(Q^2) + B(Q^2)\tan^2 \frac{\theta}{2} \right] \qquad (3.4)$$

In this way the interference between the nucleon form factors is eliminated, greatly simplifying their extraction from cross-section data. A Rosenbluth separation is performed using measurements at the same Q^2 but different angles to determine both $A(Q^2)$ and $B(Q^2)$ independently, and from them the Sachs form factors. However, for large Q^2 the magnetic contribution dominates both A and B and it becomes difficult to isolate the electric form factor using only cross-section measurements.

Similarly, the nucleon polarization produced by a longitudinally polarized electron beam,

$$P_L' = G_M^2 \frac{2\tau(1+\tau)^{1/2}[1 + (1+\tau)\tan^2(\theta/2)]^{1/2}\tan(\theta/2)}{G_E^2 + [\tau + 2\tau(1+\tau)\tan^2(\theta/2)]G_M^2} \qquad (3.5a)$$

$$P_S' = -G_E G_M \frac{2[\tau(1+\tau)]^{1/2}\tan(\theta/2)}{G_E^2 + [\tau + 2\tau(1+\tau)\tan^2(\theta/2)]G_M^2} \qquad (3.5b)$$

has two nonvanishing components.[41] In the one-photon-exchange approximation there is no recoil polarization unless the beam is polarized and there is no beam analyzing power. It is also useful to observe that the ratio

$$\frac{P_S'}{P_L'} = -\frac{G_E}{G_M}\left[\tau\left(1 + (1+\tau)\tan^2 \frac{\theta}{2}\right)\right]^{-1/2} \qquad (3.6)$$

provides a means of measuring G_E/G_M that is relatively insensitive to systematic errors in the beam polarization and in the analyzing power of the

polarimeter. Since G_M can be determined with good accuracy from cross-section measurements, G_E can then be obtained by combining the polarization ratio with the cross-section information.

For low Q^2, it has been found (see Section 3.2) that the nucleon form factors can be represented qualitatively by the dipole parametrizations

$$G_{Ep}(Q^2) \approx \frac{G_{Mp}(Q^2)}{\mu_p} \approx \frac{G_{Mn}(Q^2)}{\mu_n} \approx G_D(Q^2) \qquad (3.7)$$

where the dipole form factor is

$$G_D(Q^2) = \left(1 + \frac{Q^2}{\Lambda_D^2}\right)^{-2} \qquad (3.8)$$

and where the scale parameter is $\Lambda_D^2 = 0.71 \ (\text{GeV}/c)^2$. It is actually surprising that such a simple ansatz should be so successful, since there appears to be no fundamental reason for it. Similarly, a simple and commonly used parametrization of the neutron electric form factor due to Galster et al.[42] is

$$G_{En}(Q^2) = -\mu_n G_D(Q^2) \frac{\tau}{1 + b\tau} \qquad (3.9)$$

where $b = 5.6$ gives the best, albeit poorly determined, fit to their elastic electron–deuteron scattering data.

A more fundamental representation of the nucleon form factors can be obtained from the vector meson dominance (VMD) model of Sakurai[43] in which the virtual photon couples either to a core with only a Dirac form factor F_1 or via conversion to a neutral vector meson with both vector and tensor coupling to the photon. It is convenient to separate the Dirac and Pauli form factors, F_1 and F_2, into isoscalar and isovector contributions, such that

$$F_1 = \frac{1}{2}(F_{1S} + \tau_3 F_{1V}) \qquad (3.10a)$$

$$\kappa F_2 = \frac{1}{2}(\kappa_S F_{1S} + \tau_3 \kappa_V F_{2V}) \qquad (3.10b)$$

where $\tau_3 = +1(-1)$ for the proton (neutron). A simple parametrization, suggested by Iachello, Jackson, and Lande,[44] which incorporates the necessary constraints upon charges and magnetic moments, can then be expressed as

$$F_1^S(Q^2) = F_0(Q^2)\left[(1 - \beta_\omega - \beta_\phi) + \beta_\omega F_\omega(Q^2) + \beta_\phi F_\phi(Q^2)\right] \quad (3.11a)$$

$$F_1^V(Q^2) = F_0(Q^2)\left[(1 - \beta_\rho) + \beta_\rho F_\rho(Q^2)\right] \qquad (3.11b)$$

$$\kappa_S F_2^S(Q^2) = F_0(Q^2)\left[(\kappa_S - \alpha_\phi)F_\omega(Q^2) + \alpha_\phi F_\phi(Q^2)\right] \qquad (3.11c)$$

$$\kappa_V F_2^V(Q^2) = F_0(Q^2)\left[\kappa_V F_\rho(Q^2)\right] \qquad (3.11d)$$

where F_0 is a common intrinsic form factor and where each form factor is normalized such that $F_i(0) = 1$. Each meson contributes a monopole form factor

$$F_i(Q^2) = \left(1 + \frac{Q^2}{m_i^2}\right)^{-1} \qquad (i = \rho, \omega, \phi) \qquad (3.12)$$

with a pole at $Q^2 = -m_i^2$ for time-like momentum transfer. Modifications of the ρ form factor are often included to correct for its width and other extensions and variations have also been proposed. Each of the coefficients (β_i, α_i) represents a combination of meson–photon $(V\gamma)$ and VNN coupling constants. Although the VMD model provides constraints among the various coupling constants, and should also describe VNN and $V\pi\pi$ couplings in other contexts consistently, phenomenological analyses of nucleon form factors usually fit the strengths independently.

Probably the most accurate parametrization of the proton form factor data for $Q^2 < 2$ (GeV/c)^2 is the four-pole fit performed by Simon *et al.*[45] Although loosely based upon the vector meson dominance model, the masses were chosen to fit the data without regard to their identification with known mesons and neutron form factors were not considered. Alternatively, the dispersion-theory analysis of Höhler *et al.*[46] also provides fits to the neutron form factors. Dispersion theory was used to deduce $F_{i\rho}$ from spectral information obtained from data for πN and $\pi\pi$ scattering and for $F_\pi(Q^2)$. The ω contribution and a set of "effective" mesons with adjustable masses m_i were included as simple poles with adjustable residues.

In this form, the VMD model begins to break down for large Q^2 because its superposition of monopoles is neither able to reproduce the dipole form factor nor to conform with the asymptotic behavior predicted by perturbative QCD (PQCD). At large Q^2, helicity conservation by the photon–quark interaction requires $Q^2 F_2/F_1$ to approach a constant. Furthermore, for $Q^2 \gg \Lambda^2_{\text{QCD}}$, quark counting rules combined with the evolution of the strong coupling constant, $\alpha_s(Q^2)$, require

$$F_1 \propto \frac{\alpha_s^2(Q^2)}{Q^4} \qquad (3.13a)$$

$$\alpha_s(Q^2) = \frac{12\pi}{(33 - 2N_f) \log Q^2/\Lambda^2_{\text{QCD}}} \qquad (3.13b)$$

where N_f is the number of flavors active for QCD renormalization scale Λ_{QCD}.[47,48] Additional logarithmic corrections and higher twist contributions have also been evaluated.[49,50] Thus, aside from logarithmic corrections, we expect $F_1 \propto Q^{-4}$ and $F_2 \propto Q^{-6}$. Accordingly, F_1 should dominate G_M for

large Q^2, but $G_E = F_1 - \tau \kappa F_2$ receives comparable contributions from both F_1 and F_2, such that G_{Ep} in particular may be susceptible to cancellations which could accentuate differences between models.[51]

Also note that the VMD universality condition would suggest $\beta_\omega \approx \beta_\rho$ and the OZI rule would suggest $\beta_\phi \approx 0$, such that $F_{1S} \approx F_{1V}$. Hence, it is commonly assumed that

$$F_{1n} \approx 0 \Rightarrow G_{En} \approx -\tau G_{Mn} \tag{3.14}$$

Thus, if F_{1n} is negligible, F_{2n} would determine the asymptotic behavior of the neutron magnetic form factor, leading to $G_{Mn} \propto Q^{-6}$. Under those circumstances the absolute value of G_{En} would eventually exceed that of G_{Mn} (provided that F_{1n} remains negligible). However, if one also assumes that $G_{Mn} = \kappa_n G_D$, the model $G_{En} = -\tau \kappa_n G_D$ does not agree with the expected Q^{-4} asymptotic behavior.[52]

Gari and Krümpelmann[51,52] have proposed a synthesis of the VMD model with perturbative QCD, denoted VMD-PQCD, in which the intrinsic form factors are modified to interpolate between monopole form at low Q^2 and PQCD at high Q^2. Their original model was limited to ρ and ω coupling, but they have extended the model to include coupling to the ϕ via a two-step process.[36,37] The coupling constants, an intrinsic form factor, and two scale parameters which govern the onset of PQCD behavior are fitted to nucleon elastic form factor data. The most important difference between the earlier and later models appears to be the strong effect that ϕ coupling has upon G_{En}. We denote these two models, labelled models 1 and 3 in Ref. 37, as GK1 and GK3, respectively.

3.2.   Unpolarized Measurements of Nucleon Form Factors

Most measurements of proton form factors have been made using elastic scattering of unpolarized electrons from hydrogen, while most determinations of the neutron form factors depend upon either elastic or quasielastic scattering from deuterium. Although subtraction of the proton contribution to inclusive quasielastic scattering from deuterium can be used to measure neutron form factors, more accurate measurements can be obtained by detecting the neutron in coincidence. Hofstadter[53] first suggested that G_{Mn} be obtained from quasifree electron scattering by the neutron in deuterium via the $d(e, e'n)p$ reaction. The major difficulty with that technique is accurate measurement of the neutron efficiency. Alternatively, several anticoincidence measurements have also been performed in which the requirement that a coincident proton *not* be present is imposed. In principle that method is equivalent to the coincident detection of a neutron, but requires exquisite knowledge of detection

efficiencies to be successful. Finally, it has been suggested that uncertainties in the deuteron wave function and final state interactions are minimized by measuring the ratio of $(e, e'n)/(e, e'p)$ cross sections for electrodistintegration of deuterium[54,55] and a few experiments have been performed using this ratio technique.

The available unpolarized data are summarized in Table 3.1. Dates are included to distinguish between *classical* and *modern* experiments. We have not attempted to be truly exhaustive in the citation of older experiments, but have included several representative examples of each technique, where available, in several kinematic regimes. Selected data for the nucleon Sachs form factors are compared with representative models in Figs. 3.1 and 3.2. For each quantity we display the most precise data sets that are available in each range of Q^2.

3.2.1. Proton Form Factors

The proton electric form factor is known to a few percent for $Q^2 \lesssim 1$ (GeV/c)^2, but for large Q^2 the dominance of G_M makes accurate determination of the electric form factor difficult and only G_{Mp} is known with good precision for $Q^2 > 2$ (GeV/c)^2. Recent high-precision measurements made at SLAC[63,64,66–69] extend G_{Ep} to about 7 (GeV/c)^2 with $\sim \pm 20\%$ uncertainties and remain consistent with $G_{Ep}/G_D \approx 1$. The magnetic form factor is now known to a few percent for $Q^2 < 20$ (GeV/c)^2 and to about $\pm 10\%$ at 31 (GeV/c)^2, but it should be noted that the assumption $G_{Ep} = G_{Mp}/\mu_p$ was used to subtract the small contribution of G_{Ep} in the analysis of the E136 data covering $2.9 < Q^2 < 31.3$ (GeV/c)^2.[68,69]

The asymptotic behavior of proton form factors is compared in Fig. 3.3 with the PQCD predictions of Brodsky and Lepage,[89] wherein

$$G_{Mp} \propto \left[Q^2 \log \left(\frac{Q^2}{\Lambda_{\text{QCD}}^2} \right) \left(1 + \frac{m_\rho^2}{Q^2} \right) \right]^{-2} \tag{3.15}$$

The factor involving m_ρ was applied somewhat arbitrarily to account for the VMD behavior expected at low Q^2. Normalizing this model to the high Q^2 data, we find good agreement with the G_{Mp} data for $Q^2 > 10$ (GeV/c)^2. Similarly, the ratio $Q^2 F_2/F_1$ may be approaching asymptopia for $Q^2 > 5$ (GeV/c)^2,[64] but the data do not extend to large enough Q^2 and are not yet precise enough to reach that conclusion with confidence.

Several representative models are also compared with the proton form factor data in Figs. 3.1 and 3.3. The four-pole fit of Simon *et al.*[45] gives a somewhat more accurate fit to the data than does the dispersion model of

TABLE 3.1

Summary of ^{1}H(e, e) and ^{2}H(e, e') Experiments

| Target	Type	Q^2 (GeV/c)^2	Deduced quantities	Date	Reference
^{1}H	elastic	0.004–0.014	G_{Ep}/G_{Mp}	1974	56
^{1}H	elastic	0.006–0.032	G_{Ep}, G_{Mp}	1974	57
^{1}H	elastic	0.007–0.056	G_{Ep}, G_{Mp}	1980	45
^{1}H	elastic	0.005–0.19	G_{Ep}, G_{Mp}	1975	58
^{1}H	elastic	0.24–1.2	G_{Ep}, G_{Mp}	1966	59
^{1}H	elastic	0.49–1.75	G_{Mp}	1990	60
^{1}H	elastic	0.4–2.0	G_{Ep}, G_{Mp}	1971	61
^{1}H	elastic	0.67–3.0	G_{Ep}, G_{Mp}	1973	62
^{1}H	elastic	1.0–3.0	G_{Ep}, G_{Mp}	1989	63, 64
^{1}H	elastic	1.0–3.75	G_{Ep}/G_{Mp}	1970	65
^{1}H	elastic	1.75–8.83	G_{Ep}, G_{Mp}	1992	66, 67
^{1}H	elastic	2.9–31.3	G_{Mp}	1986	68, 69
^{2}H	elastic	0.004–0.032	G_{En}	1970	70
^{2}H	elastic	0.002–0.16	G_{En}	1981	71
^{2}H	ratio	0.11	G_{Mn}	1994	72
^{2}H	ratio	0.125–0.605	G_{Mn}	1995	73
^{2}H	quasielastic	0.11–0.16	G_{En}, G_{Mn}	1966	74
^{2}H	coincidence	0.109–0.255	G_{Mn}	1993	75
^{2}H	quasielastic	0.06–0.3	G_{En}, G_{Mn}	1966	76
^{2}H	elastic	0.2–0.56	G_{En}	1971	42
^{2}H	ratio	0.22–0.58	G_{En}, G_{Mn}	1966	77
^{2}H	elastic	0.04–0.72	G_{En}	1990	78
^{2}H	ratio	0.39–0.78	G_{En}, G_{Mn}	1969	79
^{2}H	quasielastic	0.48–0.83	G_{Mn}	1987	80
^{2}H	quasielastic	0.04–1.2	G_{En}, G_{Mn}	1965	81, 82
^{2}H	quasielastic	0.39–1.5	G_{En}, G_{Mn}	1973	62
^{2}H	ratio	1.0–1.53	G_{En}, G_{Mn}	1972	83
^{2}H	anticoincidence	0.28–1.8	G_{En}, G_{Mn}	1973	84
^{2}H	quasielastic	0.75–2.57	G_{Mn}	1988	85
^{2}H	quasielastic	1.75–4.0	G_{En}, G_{Mn}	1993	86
^{2}H	anticoincidence	0.27–4.47	G_{En}, G_{Mn}	1968	87
^{2}H	quasielastic	2.5–10.0	G_{Mn}	1982	88
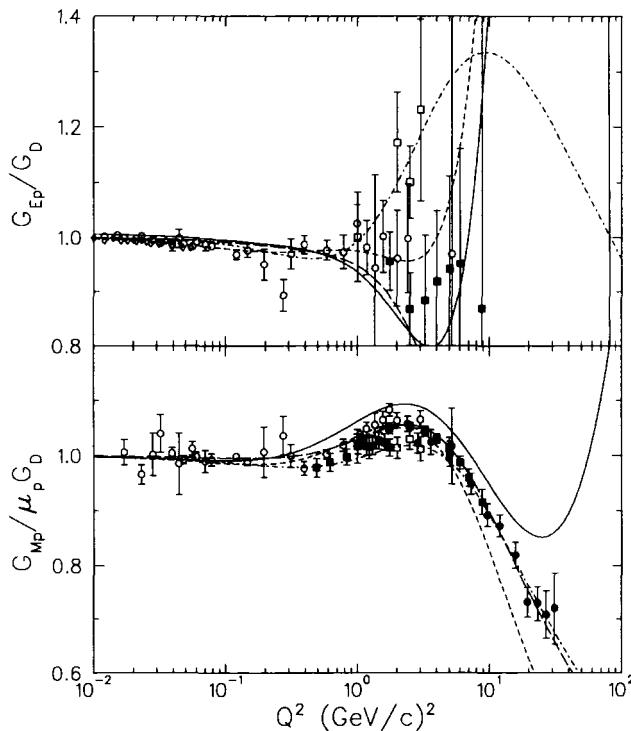
Fig. 3.1. Sachs form factors for the proton. Data: open diamonds,[45] open circles,[46] open squares,[64] filled squares,[60,67] filled circles,[69] Models: short dashes, Mainz four-pole fit,[45] solid line, dispersion-theoretical fit 8.2;[46] long dashes and dash-dot curves, VMD-PQCD models 1 and 3,[36,37]

Höhler *et al.*,[46] but both models clearly fail for $Q^2 > 10$ (GeV/c)^2. The more realistic asymptotic behavior of the VMD-PQCD model makes it more successful at large Q^2. Although there is little difference in G_{Mp} between VMD-PQCD models 1 (GK1)[51] and 3 (GK3),[36,37] the more recent GK3 model seems to give a better description of the G_{Ep} data for $Q^2 > 2$ (GeV/c)^2. However, because the various experiments do not agree with each other very well for large Q^2, despite their large error bars, the experimental situation remains unresolved. Yet, the vicinity of $Q^2 \sim 10$ (GeV/c)^2 is where these models exhibit their largest differences. It is important to realize that since $G_{Ep} = F_{1p} - \tau \kappa_p F_{2p}$ with $Q^2 F_2 \propto F_1$ for large Q^2, G_{Ep} may be susceptible to severe cancellations which would accentuate differences between models. In this case the most important difference between these models seems to be
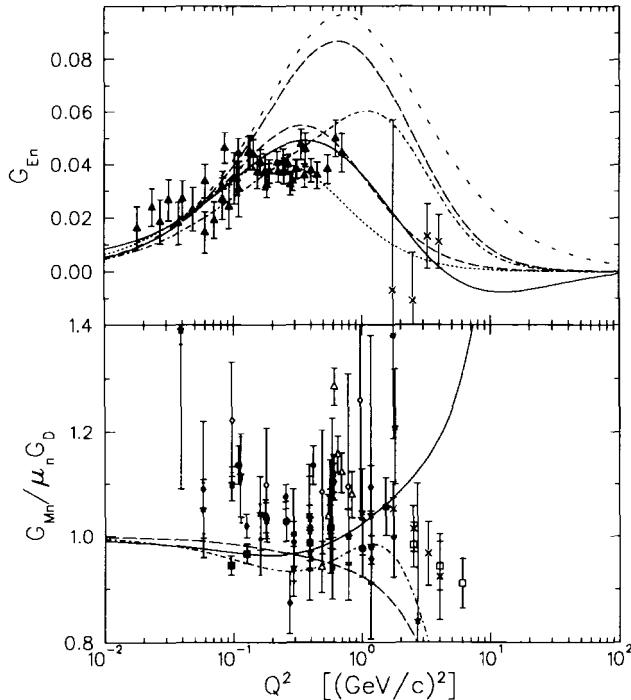
Fig. 3.2. Sachs form factors for the neutron. Coincidence measurements: filled circles,[75] Ratio measurements: filled squares[72] open circles,[79,83] open stars.[77] Elastic measurements: filled triangles.[78] Quasielastic measurements: crosses,[86] open squares,[88] open triangles,[80] open diamonds,[81] filled stars,[62] small filled circles,[74] small filled diamonds.[82] Anticoincidence measurements: filled diamonds,[84] asterisks.[87] Note that for the inclusive quasielastic data of[86] (crosses), the sign of G_{En}^2 was arbitrarily assigned to G_{En}. Models: short dashes, Platchkov fit based on Paris potential;[78] medium dashes, Galster model;[42] widely-spaced dashes, $G_{En} = -\tau\kappa_n G_D$; solid line, dispersion-theoretical fit 8.2;[46] long dashes and dash-dot curves, VMD-PQCD models 1 and 3.[36,37]

the scale parameter that governs suppression of the helicity-flip form factor. Figure 3.3 shows that $Q^2 F_{2p}/F_{1p}$ is quite sensitive to the difference between these models of helicity-flip suppression, with the data suggesting that an intermediate scale would be more appropriate. Therefore, it will be important to obtain accurate G_{Ep} data for $Q^2 \sim 10$ (GeV/c)^2. As Rosenbluth separation becomes impractical, polarization measurements that exploit Eq. (3.6) will be needed.
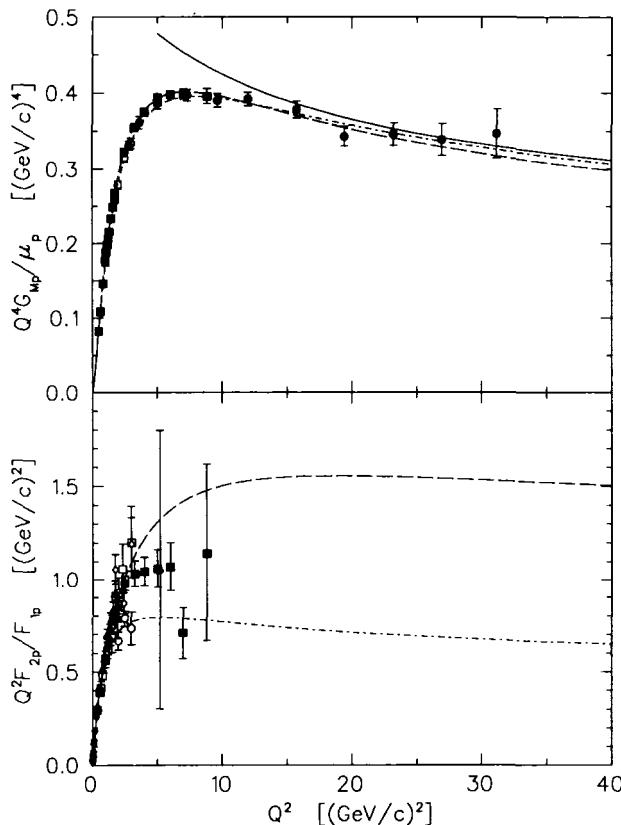
Fig. 3.3. Asymptotic behavior of proton form factors. Data: open diamonds,[46] open squares,[62] filled triangles,[61] open circles,[64] filled squares,[67] filled circles,[69] Models: Brodsky-Lepage, solid line; VMD-PQCD model 1, dashed lines; VMD-PQCD model 3, dash-dot lines.

3.2.2. *Magnetic Form Factor of the Neutron*

The data collected in Fig. 3.2 show that the magnetic form factor of the neutron remains very poorly determined. Most measurements of G_{Mn} have been made using inclusive electron scattering from deuterium and subtracting the proton contribution. However, that method requires a longitudinal-transverse separation and accurate knowledge of the deuteron wave function. As discussed by Markowitz *et al.*,[75] most previous analyses omitted or underestimated their systematic and model uncertainties; consequently, the error bars plotted for those experiments are unduly optimistic. Indeed, most data

sets shown in Fig. 3.2 exhibit more internal scatter than expected from their error bars and some exhibit unexpectedly large dependences on Q^2, suggesting that systematic errors are larger than reported, while the differences between sets suggest that model dependencies are not under adequate control. Therefore, the uncertainties in previous generations of G_{Mn} measurements are at least $\pm 10\%$ for $Q^2 < 6$ $(\text{GeV}/c)^2$. At that present level of precision, G_{Mn} remains consistent with the dipole parametrization for $Q^2 \lesssim 2$ $(\text{GeV}/c)^2$ and appears to fall more rapidly at larger Q, as expected from PQCD.[85,86]

Despite the limitations of the available data, it is clear that the Höhler parametrization fails for $Q^2 > 2$ $(\text{GeV}/c)^2$. The data do not reach large enough Q^2 to test the asymptotic behavior of the VMD-PQCD models, but it does appear that those models underestimate G_{Mn} for Q^2 near enough to the scaling regime to indicate the normalization of the Q^{-4} fall-off. The data for moderate Q^2 are also not sufficiently precise to distinguish between these two versions of the VMD-PQCD model. Furthermore, the low Q^2 region remains interesting because several quark models of nucleon structure predict significant deviations with respect to the dipole parametrization.

A recent measurement of G_{Mn} using $d(e,e'n)p$ that was performed at the MIT-Bates laboratory by Markowitz *et al.*[75] employed the associated particle reaction $d(\gamma, pn)$ to measure the efficiency of the neutron detector. In that kinematically complete calibration reaction, a proton detected in a magnetic spectrometer must be accompanied by a neutron in the neutron time-of-flight detector. Consequently, the neutron efficiency could be determined accurately and the total systematic uncertainty was less than $\pm 3\%$. Furthermore, the uncertainty in G_{Mn} due to variations of the wave function with the choice of *NN* potential, contributions of two-body currents, and uncertainties in G_{En} is typically less than $\pm 2\%$ for quasifree kinematics.[90,91] Measurements were made for $Q^2 = 0.109$, 0.176, and 0.255 $(\text{GeV}/c)^2$ and are compared with the dipole parametrization and with previous data in Fig. 3.2. The older data had suggested that for Q^2 near 0.1 $(\text{GeV}/c)^2$ there might be an enhancement of G_{Mn} with respect to the dipole form factor, and the results of Markowitz *et al.* are consistent with that suggestion.

Experiments using the ratio technique have also been performed recently at NIKHEF[72] and Bonn.[73] The results from NIKHEF for $Q^2 = 0.11$ $(\text{GeV}/c)^2$ give $G_{Mn}/\mu_n G_D = 0.957 \pm 0.016$ which, being slightly smaller than unity, disagrees with the result of Markowitz *et al.* by several standard deviations. In the ratio method, both neutrons and protons are detected simultaneously, thereby eliminating systematic errors due to luminosity. The efficiency for neutron detection was measured at PSI using the associated particle method based upon the $^1\text{H}(n, np)$ reaction. Careful pulse height calibration is needed to use calibrations performed at another laboratory and

to remove dependence upon threshold. Although the ratio method tends to minimize uncertainties due to target structure, radiative corrections are still different for the two reactions. More importantly, the multiple scattering and edge corrections are different for protons and neutrons, and must be modelled quite carefully.[92,93] The multiple scattering corrections for protons are large and contribute to the systematic uncertainties, but the authors claim to have evaluated those corrections precisely. The Bonn experiment[73] also employed the ratio technique and a similar arrangement of nucleon detectors, but the efficiency calibration was based upon the $^1H(\gamma, \pi^+)n$ reaction *in situ*. The results for $Q^2 \approx 0.1$ $(GeV/c)^2$ agree with the NIKHEF experiment and disagree with MIT. At larger Q^2 both MIT and Bonn obtain comparable results, but the Bonn experiment extends to large Q^2.

The recent data for G_{Mn} are compared with representative models in Fig. 3.4. The data obtained prior to 1980 are omitted, as are the data of Esaulov *et al.*[80] which display an implausibly rapid dependence on Q^2. The new data suggest that the ratio $G_{Mn}/\mu_n G_D$ possesses a broad enhancement near 0.6 $(GeV/c)^2$ that is qualitatively similar to a parallel structure in $G_{Mp}/\mu_p G_D$. None of the models presently available reproduces the structure suggested by the recent data for $G_{Mn}/\mu_n G_D$.

Therefore, much work remains to be done to obtain accurate and definitive measurements of the neutron magnetic form factor. The coincidence and ratio techniques appear to be the most promising, and both should be employed over a wide range of Q^2 using the new generation of high duty factor electron accelerators. More care should be given to the control of systematic errors and model dependencies. The present uncertainties in G_{Mn} seriously limit the accuracy of many theoretical calculations for few-body systems. Moreover, unless improved, the uncertainty in G_{Mn} will limit the accuracy of anticipated G_{En} measurements which rely upon polarization measurements of G_{En}/G_{Mn}.

3.2.3. *Neutron Mean-Square Charge Radius*

The mean-square charge radius of the neutron $\langle r_n^2 \rangle_{ch}$ is related to the slope of G_{En} for $Q^2 \to 0$ and can be obtained from the scattering length b_{ne} for low-energy neutrons scattered by atomic electrons via the relationships[94–96]

$$\langle r_n^2 \rangle_{ch} = -6 \left. \frac{dG_{En}}{dQ^2} \right|_{Q^2 \to 0} = \frac{3\hbar c}{\alpha m_n c^2} b_{ne} \tag{3.16}$$

However, the results extracted from measurements of the energy dependence of the total cross section for neutron atomic scattering by two groups disagree
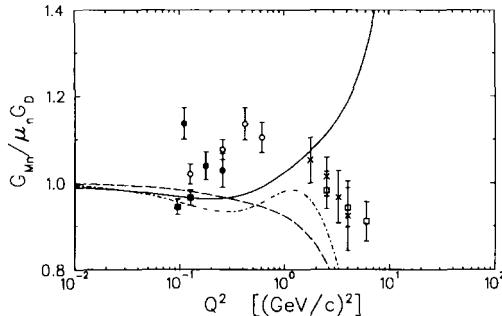
Fig. 3.4. Recent measurements of G_{Mn} are compared with representative models. Coincidence measurements: filled circles.[75] Ratio measurements: filled squares.[72] open circles.[73] Quasielastic measurements: crosses,[86] open squares.[88] Models: solid line, dispersion-theoretical fit 8.2[46]; long dashes and dash-dot curves, VMD-PQCD models 1 and 3.[36,37]

by about 20% even though the data themselves are consistent. Koester *et al.*[97,98] obtain $b_{ne} = (-1.32 \pm 0.04) \times 10^{-3}$ fm, while Alexandrov *et al.*[99] obtain $b_{ne} = (-1.55 \pm 0.11) \times 10^{-3}$ fm. Leeb and Teichtmeister[100] have analyzed the methods employed by both groups and trace the discrepancy to the treatment of resonance corrections. The extracted scattering length is strongly correlated with the resonance correction, which is not unambiguously determined by the data. Leeb and Teichtmeister argue that the correction deduced by Alexandrov *et al.* requires large contributions from negative energy levels that they believe are unlikely. On the other hand, Alexandrov[101] argues that the energy-independent resonance correction should be fitted to the data and that in the absence of definitive theoretical knowledge a negative contribution cannot be excluded. Alexandrov also emphasizes that neutron diffraction from single crystals[102] provides a larger signal and a result, $b_{ne} = (-1.60 \pm 0.05) \times 10^{-3}$ fin, that is consistent with their analysis of the total cross-section data. Unfortunately, we cannot resolve this dispute here. Therefore, we must conclude that the uncertainty in the neutron charge radius remains uncomfortably large, about 20%, and that development of an unambiguous method for extracting this important quantity should have a high priority.

3.2.4. G_{En} from Electron-Deuteron Elastic Scattering

The data for $A(Q^2)$ for elastic scattering from deuterium in the range $0.4 \leq Q^2 \leq 18$ fm^{-2} has recently been improved by Platchkov *et al.* such that the estimated accuracy varies from about 2% for $Q^2 < 10$ fm^{-2} to
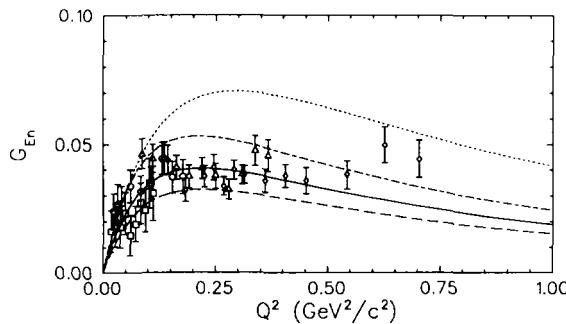
Fig. 3.5. Neutron electric form factor extracted from elastic electron–deuteron scattering by Platchkov et al.[78] The symbols and the solid line represent the results of an analysis based upon the Paris potential, where squares, circles, triangles, and diamonds correspond to beam energies of 200, 300, 500, and 650 MeV, respectively. The dashed, dash-dotted, dotted lines represent fits based upon the RSC, Argonne V14, and Nijmegen potentials, respectively.

about 6% at the largest Q^2.[78] However, the extraction of G_{En} from these data is complicated and there are many sources of possible error. An effective $A_{IA}(Q^2)$ that is intended to represent the impulse approximation was deduced by subtraction of calculated corrections for relativistic effects and meson-exchange currents. It is also necessary to subtract the magnetic dipole contribution using fitted experimental information, yielding a quantity labelled $A'_{IA}(Q^2)$. Next, deuteron S- and D-state wave functions based upon various nonrelativistic potentials were used to unfold the nuclear structure from $A'_{IA}(Q^2)$ to obtain the electric isoscalar form factor $G_{IA}(Q^2)$. Finally, the proton form factor is subtracted leaving $G_{En}(Q^2)$ to be parametrized in the form

$$G_{En}(Q^2) = -\mu_n G_D(Q^2) \frac{a\tau}{1+b\tau} \tag{3.17}$$

where G_D is the standard dipole form factor. The fit to the neutron electric form factor extracted using the Paris potential,[103,104] with $a = 1.25 \pm 0.13$ and $b = 18.3 \pm 3.4$, is shown as the solid line in Fig. 3.5. Also shown are results based on the Reid soft core (RSC),[105] Argonne V14,[106] and Nijmegen[107] potentials.*

Despite the excellent statistical precision of the $A(Q^2)$ data, the uncertainties in the extracted neutron electric form factor remain quite large. The uncertainty in the corrections to $A_{IA}(Q^2)$ for relativistic effects and meson-exchange currents was estimated by Platchkov *et al.* to be $\pm 5\%$, but this

---

* Note that there is an error in Table 2 of Ref. 78 where the Argonne V14 result should have had $b = 19.7 \pm 2.7$ instead of 11.2 ± 2.7.[108]

modest uncertainty is amplified for G_{En} to about $\pm20\%$. The uncertainties due to subtraction of the magnetic dipole and proton form factors were claimed to be negligible. An estimate of the possible model dependence of G_{En} due to variations of the nucleon–nucleon potential is also given in Fig. 3.5. The form factors deduced using the Paris or RSC potentials give slopes at $Q^2 \to 0$ in good agreement with the data of Koester *et al.*[97,98] for the scattering of low-energy neutrons by atomic electrons, but the form factors deduced using the Argonne V14 or Nijmegen potentials give slopes which are about 50% larger. However, the Platchkov data themselves do not determine this slope very well — the value deduced for the slope is determined by the parameter a in Eq. (3.17) and hence is clearly model dependent. Furthermore, as discussed in Section 3.2.3, there remains considerable ambiguity in the extraction of the neutron charge radius from measurements of the neutron–electron scattering length[100,101] Therefore, it is not clear that the form factors deduced using the V14 or Nijmegen potentials should be rejected upon the basis of the a parameter alone. If one limits consideration to the Paris and RSC potentials the estimated model dependence would be about $\pm10\%$ at $Q^2 \approx 15$ fm^{-2}, but this estimate rises to about $\pm40\%$ if all four potentials are considered. Therefore, even an optimistic assessment of the uncertainties in $G_{En}(Q^2)$ still gives a net uncertainty of at least $\pm50\%$.

The uncertainties due to corrections for relativistic effects and meson-exchange currents and the model dependence due to uncertainties in the nucleon-nucleon potential grow with Q^2 such that for $Q^2 > 1$ (GeV/c)^2 it becomes very difficult to extract $G_{En}(Q^2)$ from $A(Q^2)$ regardless of the accuracy of the data.

3.3. Polarized Measurements of Nucleon Form Factors

Despite its obvious importance to the evaluation of models of nucleon structure, G_{En} remains the least known of the nucleon electromagnetic form factors. Substantial improvement of our present limited knowledge of the neutron electric form factor and extension to higher momentum transfer will require new techniques. Exploitation of the polarization of the neutron detected in quasifree scattering from deuterium or of the spin of a polarized ^{3}He target is expected to yield more precise and less model-dependent measurements of the neutron electric form factor. These polarization observables are expected to distinguish between neutron and proton contributions so that the neutron form factors may be isolated. Several pioneering measurements of recoil and target polarizations have been performed recently and will be reviewed in this section. Although these experiments do not yet offer adequate precision, they do demonstrate the experimental feasibility of their techniques
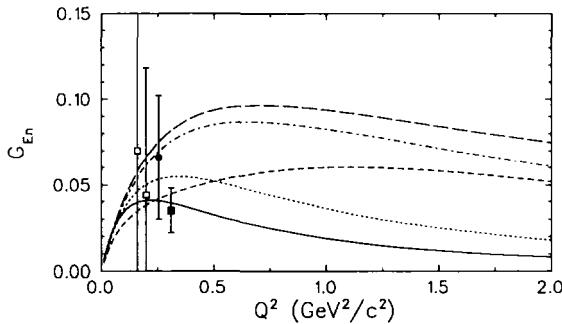
Fig. 3.6. Recent determinations of G_{En} from polarization measurements are compared with selected models. The data are from quasielastic $^2\mathrm{H}(\vec{e}, e'\vec{n})^1\mathrm{H}$ (filled circles),[109] inclusive $^3\vec{\mathrm{He}}(\vec{e}, e')$ (open squares),[110,111] and exclusive $^3\vec{\mathrm{He}}(\vec{e}, e'n)$ (filled squares).[112] The parametrizations are: Platchkov *et al.*[78] (solid), Galster[42] (dotted), $F_{1n} = 0$ (long dashes), and Gari-Krümpelmann[36,37] VMD-PQCD models 1 (dash-dot) and 3 (short dashes).

and will soon be improved at new and upgraded high duty-factor facilities.

The recent data using polarization measurements are summarized in Fig. 3.6 and the various techniques are reviewed below. Unfortunately, these low-Q^2 data are not yet sufficiently accurate to clearly distinguish among the models shown. The unpolarized data for G_{En} are shown in Fig. 3.2. Note that for the data of Lung *et al.*,[86] covering $1.75 < Q^2 < 4.0$ $(\mathrm{GeV}/c)^2$, we have arbitrarily assigned the sign of G_{En}^2 to G_{En}. These data are consistent with zero, or with the Höhler, Galster, or Platchkov parametrizations, but clearly exclude the popular ansatz: $F_{1n} = 0 \Rightarrow G_{En} = -\tau G_{Mn}$.

For G_{En}, the most important difference between VMD-PQCD models 1 and 3 is coupling to the ø meson in model 3, which is related to the strangeness content of the nucleon. Accurate data for $Q^2 > 0.5$ $(\mathrm{GeV}/c)^2$ could easily distinguish between these models, both of which adequately fit the other nucleon form factors. Thus, G_{En} appears to be uniquely sensitive to the ϕ coupling and thereby to strangeness.

3.3.1. G_{En} from $d(\vec{e}, e'\vec{n})p$

Arnold, Carlson, and Gross[41] have suggested that G_{En} might be determined more precisely from the recoil polarization of a neutron from quasifree scattering. For a free neutron at rest, the sideways component of the polarization transfer is given by

$$P'_S = \frac{-2G_{En}G_{Mn}[\tau(1+\tau)]^{1/2}\tan(\theta_e/2)}{G_{En}^2 + G_{Mn}^2\tau[1 + 2(1+\tau)\tan^2(\theta_e/2)]} \qquad (3.18)$$

Since G_{En} is quite small, this quantity is approximately equal to the ratio of the electric and magnetic form factors times a kinematic factor of the form

$$P'_S \approx \frac{G_{En}}{G_{Mn}} \frac{-2[\tau(1+\tau)]^{1/2}\tan(\theta_e/2)}{\tau[1+2(1+\tau)\tan^2(\theta_e/2)]}$$

Arenhövel[90,91] has demonstrated that the dependence of P'_S upon variations of the deuteron wave function due to reasonable choices of *NN* potential is negligible in quasifree kinematics. Similarly, contributions due to meson-exchange currents and intermediate isobar excitation may also be neglected for $\theta_{np} < 20°$, where θ_{np} is the center-of-mass angle between **q** and the neutron–proton relative momentum. Therefore, P'_S for the $d(\vec{e}, e'\vec{n})p$ reaction in quasifree kinematics appears to provide a nearly model-independent signal for G_{En}/G_{Mn}.

The first measurement of neutron polarization for $d(\vec{e}, e'\vec{n})p$ was made at $Q^2 = 0.255$ (GeV/c)^2 by Eden *et al.*[109] using a polarimeter[113] based upon neutron scattering by the hydrogen in mineral-oil scintillators. The neutron energy was determined from time of flight. The result is $G_{En} = 0.066 \pm 0.036 \pm 0.009$, where the uncertainties are separated into statistical followed by systematic contributions. Although the relative precision of this measurement was only about 60%, limited primarily by statistics and the signal/noise ratio that could be achieved with the 0.8% duty factor beam that was then available at the MIT–Bates laboratory, it demonstrates the feasibility of the technique, which will be used to make much higher precision measurements with high duty-factor beams at MIT–Bates and CEBAF in the near future. A similar experiment has also been performed at Mainz, but the analyzing power of their polarimeter had not yet been calibrated at the time of this writing.[114]

The systematic errors in this technique can be reduced by measuring the ratio of the sideways and longitudinal polarizations, where the latter is obtained by using a magnet to precess the longitudinal spin into the sideways direction. Uncertainties due to the analyzing power of the detector and the beam polarization then cancel to first order, with only small residual uncertainties due to differences between the angular distributions of the two polarization components remaining. Systematic uncertainties due to variations of the precession angle with neutron momentum and angle are expected to be very small.

3.3.2. Neutron Form Factors from $^3\vec{\mathrm{He}}(\vec{e}, e')$

Inclusive measurements on polarized targets offer two new response functions. Recognizing that inclusive measurements are necessarily restricted to

parallel kinematics, we infer from Table 2.1 that

$$A = A_x^T = A_z^T = A_y'^T = 0$$

where, in the notation of Section 2.6, A is the beam analyzing power, $\mathbf{A}^T$ is the target analyzing power, and $\mathbf{A}'^T$ is the polarization correlation vector. Furthermore, in PWIA we find that $A_y^T = 0$. Thus, the inclusive PWIA cross section reduces to[10]

$$\frac{d\sigma_{hs}}{d\varepsilon_f d\Omega_e} = \sigma_0 \frac{1}{2}\left[1 + hP^T(\cos\theta_s A_z'^T + \sin\theta_s \cos\phi_s A_x'^T)\right] \quad (3.19)$$

where

$$\mathbf{P}^T = P^T(\hat{\mathbf{x}}\sin\theta_s\cos\phi_s + \hat{\mathbf{y}}\sin\theta_s\sin\phi_s + \hat{\mathbf{z}}\cos\theta_s)$$

is the target polarization and where

$$\sigma_0/K\sigma_M = V_L R_L + V_T R_T \quad (3.20a)$$
$$A_x'^T \sigma_0/K\sigma_M = V_{LT}' R_{LT}'^T(\hat{\mathbf{x}}) \quad (3.20b)$$
$$A_z'^T \sigma_0/K\sigma_M = V_{TT}' R_{TT}'^T(\hat{\mathbf{z}}) \quad (3.20c)$$

To reduce clutter among the superscripts, the spin-projection used in evaluating the polarized-target response functions has been given as an argument instead of a superscript. Note that our notation and the normalization of the response functions differs somewhat from that used by Donnelly and Raskin,[10] but the results are equivalent.

Clearly, two polarized-target response functions can be isolated using measurements with $\theta_s = 0$ for $R_{TT}'^T(\hat{\mathbf{z}})$ or with $\theta_s = 90°$ for $R_{LT}'^T(\hat{\mathbf{x}})$. Optimal sensitivity is obtained when the target polarization lies in the scattering plane ($\phi_s = 0, \pi$). For a polarized nucleon target, the response functions are given by[115]

$$R_{LT}'^T(\hat{\mathbf{x}}) = 2\left[\tau(1+\tau)\right]^{1/2} G_E G_M \quad (3.21a)$$
$$R_{TT}'^T(\hat{\mathbf{z}}) = 2\tau G_M^2 \quad (3.21b)$$

Thus, since G_{En} is small, the transverse target asymmetry $A_x'^T$ for polarized neutrons is proportional to G_{En}/G_{Mn}.

Although polarized neutron targets are not available, the next best source of polarized neutrons is found in polarized $^3\vec{\text{He}}$ whose spin is carried primarily by the unpaired neutron while the protons are preferentially paired to spin zero. The ground state wave function for ^{3}He is dominated by the spatially symmetric S-state ($\approx 88\%$) with small admixtures of D-state ($\approx 8\%$),

mixed symmetry S'-state ($\approx$ 1.5%), and more complicated configurations. Recognizing that the depolarizing contributions predicted by a wide variety of nuclear models are strongly correlated with binding energy, Friar et al.[116] estimated the nucleon polarizations in $^3\vec{\text{He}}$ to be $P_n = 0.87 \pm 0.02$ for the neutron and $P_p = -0.027 \pm 0.004$ for protons, with the remainder of the spin residing in orbital motions. This estimate is based upon fits to the correlation between depolarization and binding energy and includes a subjective estimate of theoretical uncertainty.

Blankleider and Woloshyn[115] calculated spin-dependent momentum distributions using the closure approximation and a Faddeev wave function based upon a separable expansion of the Reid soft-core potential.[117] In quasifree kinematics, they predicted that the neutron contribution dominates the asymmetry for $\theta_s = 0$, but that the proton and neutron contributions for $\theta_s = 90°$ are similar. Furthermore, the proton contribution for $\theta_s = 90°$ also depends strongly on ω, complicating the extraction of G_{En}. They also noted that the target asymmetry passes through zero at an angle for which the uncertainty due to G_{Mn} is minimized. Since that angle depends primarily upon G_{En}, it provides another technique for measuring the neutron electric form factor.

Degli Atti, Pace, and Salmé[118] have calculated the spin-dependent spectral functions and evaluated the accuracy of the closure approximation and the dependence of the target asymmetries on nucleon form factors. Closure is accurate to about 15% near the quasifree peak ($y = 0$) for $Q^2 \approx 0.2$ (GeV/c)^2 and improves as Q^2 increases, but is quite poor for $|y| > 50$ MeV/c. (See Section 7.1.1 for the definition and a discussion of the y-scaling variable.) The proton contribution can be quite large and is underestimated by the closure approximation, but can be minimized by judicious choice of target orientation.

The more detailed calculations of Schulze and Sauer[119] lead to similar conclusions, although the authors appear to underappreciate the experimental uncertainties. Furthermore, they compared several methods for evaluating the nuclear response tensor which differ in their treatment of violations of current conservation that inevitably attend the impulse approximation and find that the ambiguities are significant. The method used by Blankleider and Woloshyn was least favored. Consequently, since the proton contributions are larger and less certain than originally thought, Schulze and Sauer are pessimistic about the use of $^3\vec{\text{He}}(\vec{e}, e')$ for measurement of G_{En}. Although it might appear that a $^3\vec{\text{H}}(\vec{e}, e')$ calibration measurement of G_{Ep} could help to resolve some of the ambiguities, the fact that the neutron contamination of the latter is so much smaller than the proton contamination of the former vitiates the usefulness of the comparison.[119]

The origin of the differences between the calculations of Refs. 119 and 118 has been clarified by degli Atti et al.,[120,121] who find that the procedure

TABLE 3.2

Summary of $^3\vec{\text{He}}(\vec{e}, e')$ Experiments

Experimental measurements are given in the form: value ± statistical uncertainty ± systematic uncertainty. When given, the third uncertainty for deduced quantities is a theoretical estimate of model dependence

θ_s (deg)	Q^2 $(\text{GeV}/c)^2$	ω range (MeV)	A'^T (%)	Deduced quantity	Reference
3	0.20	70–160	$-2.6 \pm 0.9 \pm 0.5$		110
8	0.20	90–138	$-3.8 \pm 1.4 \pm 0.7$		122, 111
9	0.19	95–145	$-10.2 \pm 1.1 \pm 0.6$	$(G_{Mn}/(\mu_n G_D))^2$ $= 1.00 \pm 0.12$ $\pm 0.06 \pm 0.03$	123
102	0.16	58–161	$+2.4 \pm 1.3 \pm 0.4$	$G_{En} = +0.070$ $\pm 0.100 \pm 0.035$	124, 111
90	0.20	70–160	$+1.8 \pm 1.2 \pm 0.3$	$G_{En} = +0.044$ ± 0.074	110
87	0.14	72–99	$+1.5 \pm 0.6 \pm 0.2$		125

used by Blankleider and Woloshyn, which they also used in their own previous paper,[118] to extract the polarization response functions is inconsistent in its application of current conservation and consequently lacks a significant longitudinal contribution. When that contribution is included consistently, they obtain very good agreement with Schulze and Sauer,[119] using the same preferred method of extraction.

A series of inclusive measurements of the polarized-target asymmetries made at the MIT—Bates laboratory is summarized in Table 3.2. The values given for θ_s generally represent approximate averages over several similar values. Each data set includes a reversal of the target polarization.

The set of measurements with small θ_s can either be interpreted as testing the reaction models and the ^{3}He wave function[110,111] or as measurements of G_{Mn}.[123] At the present level of precision, these results are consistent with both the impulse approximation and with the dipole parametrization of G_{Mn}, but the improved precision anticipated for future experiments will be needed to make more incisive comparisons.

It was hoped originally that the measurements with the target polarization nearly orthogonal to the momentum transfer would be sensitive to G_{En}. However, at low Q^2 the size of the proton contribution and the uncertainties due to the choice of NN potential, nucleon form factors, and off-shell prescriptions severely limit sensitivity to G_{En}. A representative example is shown in Fig. 3.7, where the relative contributions of neutrons and protons, as estimated by
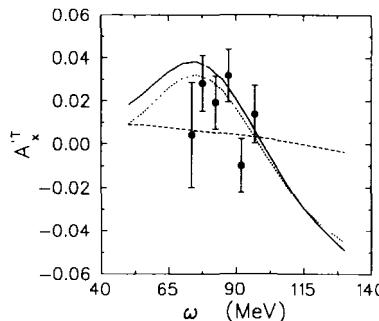
Fig. 3.7. **The target asymmetry data**[125] **for inclusive quasielastic scattering by polarized**
^{3}He for $E_i = 370$ MeV and $\theta_e = 70.1°$ are compared with calculations by Schulze and
Sauer[119] The full calculation is shown by the solid curve, while the dotted and dashed curves
show the separate contributions of protons and neutrons, respectively.

Schulze and Sauer *et al.*[119] are compared with the data of Hansen *et al.*[125]
The proton contribution is clearly dominant at low Q^2. These calculations
use 18-channel Faddeev wave functions based on the Paris potential, Galster
form factors, and the ccl off-shell prescription, but do not include FSI or
MEC. Variations of these choices give integrated quasielastic asymmetries in
the range 2.1–2.9%, compared with 1.5 ± 0.6 experimentally. The residual
discrepancy may be due to FSI or MEC effects presently omitted from the
model.

Although these experiments demonstrate the feasibility of a technique
which should be more successful in future experiments with higher duty-factor
beams, their statistical significance is not yet useful. More importantly, the
proton contribution and model uncertainties remain too large to permit reliable
extraction of G_{En} from the inclusive measurements at low Q^2 that have been
performed so far. The relative contribution due to neutrons is expected to
increase at larger Q^2 and may become favorable for $Q^2 > 0.6$ (GeV/c)^2. On
the other hand, degli Atti *et al.*[121] emphasized that the proton contribution
can be minimized and the sensitivity to G_{En} optimized by choosing a target
orientation not quite orthogonal to $\vec{q}$. They find that for a wide range of
electron kinematics and form factor models, a target polarization angle of
about $105°$ with respect to the beam direction, rather than orthogonal to
$\vec{q}$, optimizes the sensitivity of quasifree $^3\vec{\text{He}}(\vec{e}, e')$ to G_{En}. Nevertheless,
exclusive measurements appear to be more promising.

3.3.3. Neutron Form Factors from $^3\vec{\text{He}}(\vec{e}, e'n)$

Extraction of G_{En} from inclusive measurements of the $^3\vec{\text{He}}$ target asymmetry is complicated by the size of the proton contribution and uncertainties in its form factors. Exclusive measurements of the type $^3\vec{\text{He}}(\vec{e}, e'n)$ are more promising for $Q^2 > 0.3$ (GeV/c)^2 because the proton contributions are suppressed by detection of the coincident neutron. Laget[126] has studied the corrections to PWIA for this reaction due to final state interactions and meson exchange currents and finds these effects to significantly affect the target asymmetries for small Q^2. Similar conclusions were reached for $d(\vec{e}, e'\vec{n})p$ at nonzero recoil momentum. Fortunately, these effects are calculated to become negligible for $Q^2 > 0.3$ (GeV/c)^2.

Additional support for this proposition is available from $^3\vec{\text{He}}(\vec{p}, pN)$ reactions. Miller *et al.*[127] find that for small p_m the target analyzing power is suppressed unless the momentum transfer is large enough, $q > 500$ MeV/c, but that the PWIA prediction is recovered for large ejectile momenta. Furthermore, the beam and target analyzing powers for $^3\vec{\text{He}}(\vec{p}, pn)$ should be equal in PWIA and are for $q > 500$ MeV/c. These results are interpreted as evidence that spin-dependent final-state interactions are important for small Q^2, but may be negligible for $Q^2 > 0.3$ (GeV/c)^2. However, a more detailed theoretical analysis of the proton-induced knockout reaction is still required.

The first measurement of target asymmetries for exclusive $^3\vec{\text{He}}(\vec{e}, e'n)$ reaction has been made at Mainz by Meyerhoff *et al.*[112] At $Q^2 = 0.31$ (GeV/c)^2, they find $A_z'^T = (-7.40 \pm 0.73)\%$ and $A_x'^T = (+0.89 \pm 0.30)\%$. Using the PWIA ratio

$$\frac{G_{En}}{G_{Mn}} = \left[\tau + \tau(1 + \tau)\tan^2\frac{\theta_e}{2}\right]^{1/2}\frac{A_x'^T}{A_z'^T} \qquad (3.23)$$

to minimize systematic errors and the dipole parametrization for G_{Mn}, they find $G_{En} = 0.035 \pm 0.012 \pm 0.005$, where the remaining systematic uncertainty is dominated by G_{Mn}. The result agrees with the Platchkov analysis[78] based upon either the Paris, Reid soft-core, or Argonne V14 potentials, and seems to exclude the result based upon the Nijmegen potential. However, their acceptances were quite large and it will be important to average theoretical models that include FSI effects over the experimental acceptances properly before their result can be considered definitive.

3.3.4. Other Methods for Measuring G_{En}

Several improved measurements using $d(\vec{e}, e'\vec{n})$, $^3\vec{\text{He}}(\vec{e}, e')$, and $^3\vec{\text{He}}(\vec{e}, e'n)$ which exploit the higher duty-factor beams now available at MIT–Bates

and Mainz are either in progress or planned. These new data should have smaller statistical and systematic uncertainties and will cover more extensive kinematic ranges. Similar experiments are also planned at CEBAF with continuous beams of higher energy. Experiments with polarized beams and polarized internal targets are being developed at NIKHEF. Studies of $^3\vec{\text{He}}(\vec{e}, e'N)$ for both neutron and proton knockout can be used to test details of the wave functions and the reaction model.[128]

Experiments using polarized deuterated-ammonia targets to study the $\vec{d}(\vec{e}, e'N)$ reaction are also being planned. The sensitivity to G_{En} of the deuteron-polarization observables in the $\vec{d}(\vec{e}, e'n)p$ reaction has been studied by Arenhövel et al.,[91] who suggest that the helicity-dependent target vector-polarization asymmetry with the spin orthogonal to $\mathbf{q}$ is the most promising observable of that type. An experiment of that type has been proposed by Day.[129] Alternatively, Rekalo et al.[130] have suggested that the $\vec{d}(\vec{e}, e'p)n$ reaction could be used in antiparallel kinematics, in which the proton is detected in the direction opposite to $\mathbf{q}$, is also sensitive to G_{En}. In that case the target asymmetry due to a vector polarization orthogonal to $\mathbf{q}$ offers the best signal.

Donnelly et al.[131] have also suggested that the parity-violating asymmetry in $^1\text{H}(\vec{e}, e)^1\text{H}$ is sensitive through isospin symmetry to G_{En}, provided that the contribution due to strange quarks is neglected. However, these contributions are expected to be of the same order.[5]

3.4. Summary

The nucleon electromagnetic form factors are fundamental quantities required for evaluating models of nucleon structure. However, the dominance of the magnetic form factor at large Q^2 makes extraction of the electric form factor from cross-section measurements difficult and vulnerable to large systematic errors. The proton magnetic form factor is known with good precision for $Q^2 \lesssim 30$ (GeV/c)^2 and is described well by models which combine vector meson dominance at low Q^2 with perturbative QCD at high Q^2. However, the proton electric form factor is essentially unknown for $Q^2 \gtrsim 1$ (GeV/c)^2.

Despite significant improvements achieved recently for neutron detection in $\text{d}(e, e'n)$ reactions, the data for neutron form factors remains relatively poor. High-quality coincidence data for the magnetic form factor are limited to $0.1 \lesssim Q^2 \lesssim 0.6$ (GeV/c)^2 and for $1.0 \lesssim Q^2 \lesssim 6.0$ (GeV/c)^2 we must rely on inclusive quasielastic measurements with subtraction of the proton contribution. These data for $G_{Mn}/\mu G_D$ display a broad enhancement for $Q^2 \sim 0.6$ (GeV/c)^2 that is not well described by the available models. Although G_{En} has been extracted from very precise data for elastic scattering

by deuterium, the analysis is quite model dependent. Alternatively, the ratio of G_E/G_M can be obtained from polarization measurements involving either the recoil neutron or a polarized target in conjunction with a polarized electron beam. The feasibility of these techniques has been demonstrated and systematic high-precision measurements of the electric form factors of both protons and neutrons are expected in the near future using the new high duty-factor facilities with high intensity polarized beams that are now becoming available.

4. PROTON KNOCKOUT EXPERIMENTS ON FEW-BODY SYSTEMS

Electromagnetic reactions upon the few-body systems, those with $A \leq 4$, continue to provide a fertile laboratory for exploration of fundamental properties of nucleons and NN interactions, three-body forces, and subnucleonic degrees of freedom. Exact calculations can be performed for the deuteron, whose low density limits possible medium modifications of the electromagnetic properties of nucleons. Nevertheless subnucleonic degrees of freedom, represented as meson exchange currents (MEC), play a vital role in many of the electromagnetic processes involving the deuteron. Perhaps the most striking example is found in threshold electrodisintegration of the deuteron[132] for which a deep interference minimum in the PWIA prediction is completely obliterated by strong MEC effects.

Given a model of the NN interaction, the ground-state wave functions for trinucleon systems would be solvable exactly if there were no explicit three-body interactions. However, with the exception of the Bonn potential, most modern NN interactions underbind the triton by about 1 MeV.[148] This deficit is generally attributed to three-body forces which are then adjusted empirically because there is no unambiguous theory of three-body forces. Nor do fits to NN and πN scattering data uniquely determine all of the parameters needed to calculate meson-exchange currents in nuclei. These two-body currents are closely related to, and perhaps indistinguishable from, possible medium modifications of the electromagnetic properties of bound nucleons. Furthermore, although final-state interactions (FSI) are in principle calculable exactly, at least in nonrelativistic Faddeev approaches, practical calculations have not yet included complete NN interactions and generally omit MEC effects. Similarly, nearly exact calculations of the ground-state wave functions for $A = 4$ systems can be performed with Green function[149] or variational[150] Monte Carlo methods, but FSI and MEC are more difficult to treat exactly. Alternatively, diagrammatic expansions[151,152] can include MEC, but the convergence of the rescattering series is questionable. With

TABLE 4.1
Summary of $(e, e'p)$ Experiments on Few-Body Systems

Target	Observables	E^* (MeV)	p_m (MeV/c)
^{2}H$(e,e'p)$	R_{LT}, R_{TT}	17.9 ± 1.7	
^{2}H$(e,e'p)$	ρ^D		0–180
			150–340
^{2}H$(e,e'p)$	ρ^D		295–500
^{2}H$(e,e'p)$	R_L, R_T		39–110
	R_T/R_L		
^{2}H$(e,e'p)$	R_L, R_T, R_{LT}		36–170
^{2}H$(e,e'p)$	A_ϕ		8–95
^{2}H$(e,e'p)$	R_L, R_T		20
			100
			-100
			$-20,-50,-100,-150$
			150
	R_L, R_T, R_{LT}		50,100,150
^{3}He$(e,e'p)$	ρ^D	0–70	0–200
^{3}He$(e,e'p)$	ρ^D	0–70	150–310
^{3}He$(e,e'p)$	ρ^D		225–370
^{3}He$(e,e'd)$	ρ^D		370–500
^{3}He$(e,e'p)$	ρ^D	0–90	300–600
^{4}He$(e,e'p)$	ρ^D		(10,210)
			(110,350)
	FSI		$\pm100 \pm 15$
	FSI		100 ± 15
^{4}He$(e,e'p)$	R_L, R_T		30
			90
			190
^{4}He$(e,e'p)$	R_L, R_T		265
	R_{LT}		265
^{4}He$(e,e'p)$	ρ^D	0–140	250–380
			440–600

density and binding energy typical of complex nuclei, but with structure simple enough to calculate exactly, the $A = 4$ system provides a transition to the electromagnetic response of complex nuclei.

Therefore, there remain fundamental issues which can be addressed with $(e, e'N)$ reactions on few-body targets and the relative simplicity of these targets suggests that the results might be interpretable with relatively little ambiguity, at least as compared with complex nuclei with $A > 4$. The recent proton knockout data for electron scattering on $A \leq 4$ systems is summarized in Table

TABLE 4.1

(Continued)

T_p (MeV)	(ω, q) (MeV, MeV/c)	Type	Refs.
	$30 \leq \theta_p \leq 120°$		153
	$(105, 450)$	$\perp$	133
	$(147, 350)$		133
	$(200, 279)$	$\perp$	134
	$(75, 299)$	$\parallel$	135
	$0.05 \leq Q^2 \leq 0.27$ (GeV/c)^2		
	$(95.4, 463)$	$\perp$	136
	$(79, 388)$	$\perp$	137
	$q = 300, 400, 500, 600, 670$	$\parallel$	138
	$q = 400, 500, 600, 670$		
	$q = 200, 300, 400, 500, 920$		
	$q = 825$		
	$q = 650$		
	$q = 400$	$\perp$	
	$(330\text{--}470, 430)$	$\perp$	139
	$(300\text{--}430, 300)$	$\perp$	
	$(113, 250)$	$\perp$	140
	$(113, 250)$	$\perp$	
	$(200, 279)$	$\perp$	141
97	$(116, 431)$	$\perp$	142–144
97	$(100, 250)$	$\perp$	
	$(75\text{--}141, 262\text{--}538)$	$\parallel$	143, 144
	$(73\text{--}148, 400)$	$\perp$	
	$(98, 421)$	$\parallel$	145
	$(65\text{--}277, 299\text{--}829)$		
	$(147, 682)$		
	$(200, 324)$	$\parallel$	146
	$(200, 360)$	$\perp$	
	$(159, 261)$	$\perp$	147
	$(199, 278)$		

4.1. The tabulated kinematic variables are intended for general guidance only— more precise values can be obtained from the original sources.

4.1. The $D(e, e'p)$ Reaction

Electromagnetic reactions upon the deuteron play a central role in evaluating models of the *NN* interaction and of meson-exchange currents.[154] In the quasielastic regime, interaction effects and two-body currents are relatively unimportant so that nucleon form factors, particularly neutron form

factors, become accessible to investigation subject to relatively little model dependence. Away from the quasielastic ridge, subnucleonic degrees of freedom become more important and can again be investigated with relatively little complication due to uncertainties in the ground-state wave function.

A series of measurements has been performed at Saclay using kinematics which emphasize the longitudinal response, minimizing the corrections to the impulse approximation due to meson-exchange currents.[133,134] After the small MEC effects are included, the deduced experimental momentum distribution for $p_m \leq 500$ MeV/c agrees very well with predictions based upon the Paris potential.[152,155] However, somewhat surprisingly, the experimental momentum density for $p_m \to 0$ is suppressed by about 15% relative to theory, perhaps reflecting a small suppression of the longitudinal response.[138] More detailed investigation of the nuclear current for bound nucleons requires separation of the nuclear response function into its various components. For example, in nonrelativistic (NR) calculations R_{LT} is expected to be particularly sensitive to relativistic corrections of the current operator,[156] while R_{TT} is expected to be particularly sensitive to meson-exchange and isobar contributions (NR+MEC+IC).[154,155] The first $(e, e'p)$ experiment to use out-of-plane detection of the ejectile was made using the pulse-stretcher ring at Sendai by Tamae et al.[153] for the $d(e, e'p)$ reaction using 129 MeV electrons scattered by $\theta_e = 30°$. Protons emerging at polar angles $0 \leq \theta_{pq} \leq 120°$ with respect to $\mathbf{q}$, in 30° steps, were detected for azimuthal angles of $\phi = 45, 90,$ and 135°, allowing measurements to be made of the ratios $\sigma_{LT}(\theta_{pq})/\sigma_0$ and $\sigma_{TT}(\theta_{pq})/\sigma_0$, where σ_0 refers to the coincidence cross section for parallel kinematics. The measurements were made for a very low excitation energy, $E_{np} = 18$ MeV, and agree very well with nonrelativistic (NR) calculations made by Fabian and Arenhövel[154] based upon the Paris potential, but were not sufficiently precise to clearly establish the role of subnucleonic degrees of freedom. Furthermore, the normalization of the interference response functions was not measured. More precise data for larger excitation energies are needed to make more discriminating tests.

Separated response functions have been measured for larger momentum transfers by van der Schaar et al.[135,136] at NIKHEF. In parallel kinematics, measurements of the ratio R_L/R_T for $0.05 \leq Q^2 \leq 0.27$ (GeV/$c)^2$ are consistent with PWIA or with a small suppression. Calculations based upon either nonrelativistic or relativistic models, which are practically indistinguishable, describe the small deviations of this ratio from the PWIA limit equally well. However, there remains a small (2σ) discrepancy, which cancels in the ratio, between theory and experiment for both response functions. Measurements were also made in nonparallel kinematics with constant $(\omega, q) = (95$ MeV, 463 MeV/$c)$,[136] allowing R_T and R_{LT} to be separated

for $50 \leq p_m \leq 175$ MeV/c, but the systematic uncertainty in R_{LT}, which arises from the subtraction of similar cross sections with strong energy and angular dependencies, varies between about 59% at small p_m to 27% at high p_m despite the 1 mrad accuracy with which the spectrometer angles were known. Hence, these data are presented in Fig. 4.1 in the form of a left–right asymmetry[157]

$$A_\phi = \frac{\sigma(\phi = 0) - \sigma(\phi = \pi)}{\sigma(\phi = 0) + \sigma(\phi = \pi)}$$

where $\sigma(\phi)$ here refers to the differential cross section in the scattering plane with $\phi = 0$ referring to an ejectile momentum between $\mathbf{q}$ and the beam direction. This ratio is proportional to R_{LT}, but is less vulnerable to systematic uncertainties, here amounting to $\delta A_\phi = \pm 0.05$. The data for A_ϕ are compared with several theoretical calculations. The relativistic (R) calculations of Hummel and Tjon[158] appear to give a slightly better description of R_{LT} than the nonrelativistic NR or NR+MEC+IC calculations due to Arenhövel,[155] but appear to be definitely superior when presented as the left–right asymmetry A_ϕ.The relativistic calculations do not include meson-exchange or isobar currents, but the NR+MEC+IC calculation suggests that their effect is small for these nearly quasifree kinematics; to investigate those effects one must move further from the quasielastic ridge. On the other hand, the NR calculations were truncated at first order in q/m, while Mosconi and Ricci[156] have demonstrated that higher-order contributions, primarily the Darwin–Foldy term, significantly enhance R_{LT} and suppress R'_{LT} for these kinematics. The measurements of A_ϕ made at Bonn by Frommberger et al.[137] for $8 \leq p_m \leq 73$ MeV/c are consistent with those of NIKHEF where they overlap and are also described better when relativistic corrections to the NR+MEC+IC model are applied.[159]

Recently, measurements were made at Saclay by Ducret et al.[138] of R_L and R_T for $20 \leq p_m \leq 150$ MeV/c and $200 \leq q \leq 825$ MeV/c and of R_{LT} for $50 < p_m < 150$ MeV/c at $q = 400$ MeV/c. The Saclay data for R_L/R_T are consistent with those of NIKHEF where they overlap, but suggest that the longitudinal response is suppressed for $q < 500$ MeV/c. This suppression appears to be smaller than found for complex nuclei but may explain the suppression of the deuteron momentum density for small p_m. For $q > 500$ MeV/c, R_L/R_T is consistent with unity for deuterium but remains suppressed for $A \geq 4$. For R_{LT} systematic errors better than ± 11% were claimed, and the data for both R_{LT} and A_ϕ are qualitatively consistent with those of NIKHEF. These response functions were compared with four non-relativistic calculations,[91,152,156,159] which all use the same deuteron wave function based upon the Paris potential but which differ primarily in their
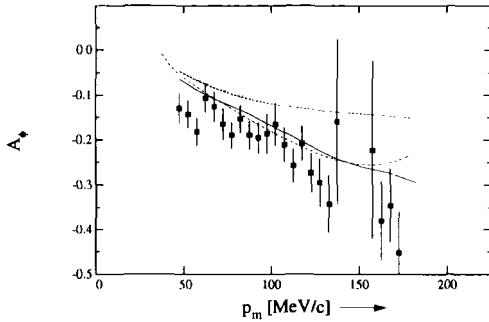
Fig. 4.1. Left–right asymmetry, A_ϕ for $d(e, e'p)$. The NIHKEF data of van der Schaar *et al.*[136] are compared with NR (dotted) and NR+MEC+IC (dashed) calculations by Fabian and Arenhövel,[154,155] calculations by Mosconi and Ricci (dot–dash)[156] which include relativistic corrections, and fully relativistic calculations by Hummel and Tjon (solid).[158,160]

prescriptions for inclusion of relativistic corrections. These calculations differ amongst themselves by 10–25% and from the data by similar amounts, with none being systematically superior to another. Unfortunately, the relativistic calculations of Hummel and Tjon[160] fare little better, reproducing some of the response functions for some kinematics, but not others. Contrary to the NIKHEF findings, these R_{LT} data appear to be described better by the Arenhövel calculation, with the Hummel and Tjon calculation being about 20% too large.

The apparent disagreement between the Saclay and NIKHEF interpretations of the role of relativistic corrections in reproducing the R_{LT} data has been discussed by van der Steenhoven[157] in terms of the effects that errors in R_L or R_T could have upon A_ϕ. The persistence of differences of up to 20% between various recent measurements of these separated response functions makes unambiguous conclusions difficult.

Therefore, although the experimental deuteron momentum density is accurately reproduced, the available data for separated response functions are only explained at the 10–15% level by standard $NN + MEC$ models which appear to suffer from substantial ambiguities in their relativistic corrections. Experimentally, further progress requires either dramatic reduction of the systematic errors for interference response functions or extension to polarization observables. Theoretically, further progress requires either resolution of the present ambiguities in the application of relativistic corrections or a fully relativistic calculation that incorporates a consistent treatment of meson exchange currents.

4.2. The ^{3}He$(e, e'p)$ Reaction

Calculations of inclusive and exclusive electron scattering on ^{3}He were per-formed in PWIA using Faddeev wave functions based upon either the Paris or the RSC potentials by Meier–Hadjuk et al.[161] who interpreted the significant disagreement with data as evidence for the need of final-state interactions and proper antisymmetrization of the final state. Alternatively, momentum distribu-tions have been computed using the variational Monte Carlo method[150] with the Urbana or Argonne NN interactions in conjunction with a phenomenological model of the three-nucleon interaction. The three-nucleon interaction is needed to reproduce experimental binding energies and radii for the three-nucleon sys-tem. These calculations provide relatively good descriptions of the experimental momentum distributions for both the ^{3}He$(e, e'p)^2$H and ^{3}He$(e, e'p)$np. channels for $p_m \leq 600$ MeV/c.[139,141]

Final state interactions (FSI) for the ^{3}He$(e, e'p)$ can be evaluated either using a diagrammatic expansion[151,152] or by solving the Feddeev equations.[162,163] The diagrammatic expansion has the advantage that meson-exchange currents (MEC) can also be included to the same order, but has the disadvantage that convergence of FSI is not guaranteed. In principle, the Faddeev approach per-mits the FSI to evaluated completely, but most practical calculations performed to date have used truncated forms of the NN interaction and have not included MEC.

Faddeev calculations for ^{3}He$(e, e'p)$ were performed by van Meijgaard and Tjon[162,163] using a separable unitary pole expansion (UPE) based upon a local spin-dependent s-wave potential containing both attractive and repulsive con-tributions. This model provides a good fit to the Nd phase shifts. The lowest-order calculation for the direct deuteron knockout, seen either in ^{3}He$(e, e'd)p$ or in ^{3}He$(e, e'p)d$ for antiparallel kinematics, was shown to be a poor approxima-tion, while the Faddeev calculation gives a good account of the data. However, s-wave FSI are not sufficient to describe the ^{3}He$(e, e'p)d$ data for large missing momenta. The method has been extended to three-body electrodisintegration[164] and compared with the inclusive data of Dow et al.[165] Van Meijgaard and Tjon find that proper treatment of FSI significantly affects the inclusive longitudinal response functions, giving a good account of the data, and that the prescription for connecting relativistic kinematics with nonrelativistic dynamics plays an im-portant role. However, lacking MEC, that calculation underpredicts the trans-verse response.

More realistic NN interactions were employed by Ishikawa et al.,[166] who evaluated the convergence of the multiple scattering series for the two-body breakup channel using a nonrelativistic Faddeev approach. The 34-channel ground-state wave function was evaluated with either Paris or Bonn potentials,
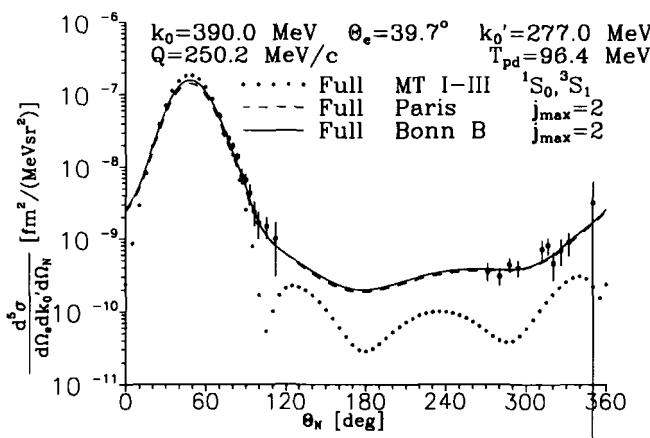
Fig. 4.2. Data for the _pd_ electrodisintegration of ^{3}He[140] are compared with complete FSI calculations by Golak _et a/._[167] using the Paris (dashed) or Bonn B (solid) potentials. Calculations based upon the UPE model of van Meijgaard and Tjon[162,163] are also shown as the dotted line. Here Θ_N is the nucleon angle with respect to the beam.

but _NN_ interactions in the continuum were limited to the $^1S_0$ and $^3S_1 - ^3D_1$ states and the Coulomb interaction was neglected. Although meson-exchange currents and relativistic corrections were omitted, the rescattering contributions could be compared order by order with the exact solution for that model. They find that, except in the immediate vicinity of the quasielastic peak, the multiple scattering series converges quite slowly, if at all. Therefore, caution must be exercised in interpreting finite-order diagrammatic expansions of final-state interactions, as employed by Laget, particularly for large angles with respect to **q**. Furthermore, the tensor interaction, neglected by van Meijgaard and Tjon, was also found to be important for large missing momenta in nonparallel kinematics.

These calculations have been extended by Golak _et al._[167] to include complete representations of the _NN_ interaction and enough partial waves to obtain convergence of FSI for realistic interactions. Representative calculations for the _pd_ two-body channel are compared in Figs. 4.2 and 4.3 with data from Keizer _et al._[140] The data were obtained for constant $(\omega, q) = (113$ MeV, 250 MeV/c) with protons being detected for $32° < \emptyset_{pq} < 63°$ and deuterons for $55° \leq -\theta_{dq} \leq 120°$, corresponding to missing momenta in the range $225 \leq p_m \leq 500$ MeV/c. In order to enhance the cross section for large recoil momenta, the momentum transfer q for these kinematics was chosen to be relatively small and ω to be substantially above the quasifree peak. The calculations in Fig. 4.3 show that, even in the peak, FSI effects
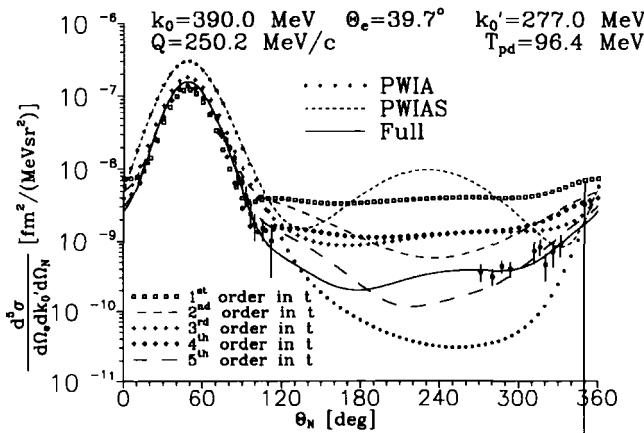
Fig. 4.3. The convergence of the multiple scattering series for the *pd* electrodisintegration of
^{3}He is compared with full FSI calculations and with ordinary (PVVIA) and antisymmetrized
(PWIAS) plane-wave impulse approximation. The data are from Ref. 140 and the calculations
are from Ref. 167. Here Θ_N is the nucleon angle with respect to the beam.

remain quite important for these large-ω kinematics and that the antisymmetrized plane-wave impulse approximation (PWIAS) is not useful. There is little variation among the complete FSI calculations based upon realistic *NN* interactions, such as Paris versus Bonn B, and those calculations reproduce the data quite well. However, the simpler UPE model fails for large recoil momenta. Furthermore, away from the peak cross section the multiple scattering series converges quite slowly, with large differences remaining between fourth and fifth orders. Therefore, low-order diagrammatic calculations cannot be trusted except in the immediate vicinity of the peak. Similarly, for three-body breakup it is equally important to perform complete FSI calculations with realistic interactions — PWIAS and/or diagrammatic approaches are not adequate. On the other hand, the diagrammatic calculations indicate that meson exchange and isobar currents can become important away from quasifree kinematics and these contributions have not yet been included in the Faddeev calculations.

4.3. The ^{4}He$(e, e'p)$ Reaction

The momentum distribution for the ground-state transition in the ^{4}He$(e, e'p)$ reaction has been studied by van den Brand *et al.*[142-144] for $p_m \leq 350$ MeV/c using two kinematical conditions. The first, with con-

stant $(\omega, q) = (116$ MeV, 431 MeV/c) and $\theta_e = 70°$, tends to emphasize the transverse response, while the second, with $(\omega, q) = (100$ MeV, 250 MeV/c) and $\theta_e = 36°$, tends to emphasize the longitudinal response. In both cases the center-of-mass kinetic energy of 75 MeV, corresponding to a laboratory kinetic energy of 97 MeV for proton scattering in the rest frame of the residual nucleus, was held constant to minimize variations in the final-state interactions. The role of charge-exchange contributions of the type $(e, e'n)(n, p)$ and $(e, e'p)(p, n)$ was investigated using the Lane model with phenomenological optical potentials. Those calculations demonstrate that charge-exchange effects are important, but do not reproduce the data very well.

The Saclay group[145] have studied the q-dependence of R_L/R_T for $^4\text{He}(e, e'p)^3\text{H}$ at several values of p_m and find that ratio is reduced with respect to PWIA (unity) and decreases as q increases. Charge exchange contributions to $^4\text{He}(e, e'N)$ reactions have been studied by Buballa *et al.*[168] using a random-phase approximation based upon a meson-exchange model to develop a G-matrix residual interaction. The charge exchange contribution to $^4\text{He}(e, e'p)$ reduces the longitudinal contribution with respect to the transverse, in good agreement with the Saclay data. Similar results, although not quite enough suppression, were obtained by Warmann and Langanke[169] using a resonating group method to calculate both the bound states and the scattering states from the same interaction with antisymmetrization and orthogonality enforced exactly. For $p_m > 300$ MeV/c, the Buballa calculation suggests that the longitudinal cross section for $^4\text{He}(e, e'n)$ is as large or larger than the longitudinal cross section for $^4\text{He}(e, e'p)$; obviously, it would be interesting to test that prediction.

Momentum distributions for $^4\text{He}(e, e'p)^3\text{H}$ have been calculated by Schiavilla *et al.*[150] using the variational Monte Carlo method with the Urbana or Argonne NN interactions in conjunction with the model VII three-nucleon interaction. Those wave functions were used by Laget in diagrammatic calculations which include rescattering, charge exchange, and meson-exchange currents. These microscopic reproduce the data for kinematics I very well and both charge exchange and meson-exchange currents are found to be important. However, the calculations for kinematics II fall below the data for $p_m < 300$ MeV/c by up to 20%, while for larger p_m the calculated momentum distribution flattens out more than the data. Since these conditions are far from the quasielastic peak, higher-order final-state interactions may be important. Also note that recoil contributions, where the virtual photon is absorbed by the residual nucleus rather than the ejected nucleon, become important under these conditions and may be overestimated by the calculation.

5.   DISTORTED WAVE ANALYSIS OF $(\vec{e}, e'\vec{N})$ REACTIONS

In this section we provide a critical review of the assumptions and ambiguities involved in the distorted wave approximation (DWA) for $(\vec{e}, e'\vec{N})$ reactions on complex nuclei. For the present purposes we assume that one hard virtual photon is absorbed by a single nucleon and postpone consideration of multinucleon currents to Section 7. Most such calculations for finite nuclei that have been performed to date employ nonrelativistic wave functions for the target nucleus and distorted waves obtained as solutions to the Schrödinger equation. The effects of optical-model ambiguities upon knockout calculations are reviewed in considerable detail, and recommendations for minimizing such ambiguities are made. The nonrelativistic models also require reduction of the current operator to a nonrelativistic form, and we review the attendant ambiguities as well. Furthermore, most nonrelativistic calculations evaluate electron distortion using an eikonal expansion which is quite accurate for light- and medium-weight nuclei, but which converges slowly at best and is not sufficiently accurate for heavy nuclei, such as the lead region. More recently, relativistic calculations have been performed in which electron distortion is evaluated essentially exactly. Such calculations do improve the shape of missing momentum distributions for heavy nuclei, due to improvements in the accuracy of Coulomb distortion, but ambiguities due to the choice of optical potential and approximations to the off-shell current operator remain unabated.

Data analyzed using the distorted wave approximation will be reviewed in Section 6. Experiments designed to test the reaction model and various refinements of the DWA are reviewed in Section 7.

5.1.   Distorted Wave Amplitude

A conceptual diagram of the distorted wave approximation (DWA) for the single-nucleon knockout reaction, *A(e,éN)B, is* given in Fig. 5.1. The one-photon exchange amplitude for this process can be expressed in the form[19]

$$\mathcal{M} = \int \frac{d^3q'}{(2\pi)^3} \, \mathcal{J}^e_\mu(\mathbf{q}') \frac{1}{Q'^2} \mathcal{J}^\mu_N(\mathbf{q}') \tag{5.1}$$

where the electron and nuclear currents are

$$\mathcal{J}^e_\mu(\mathbf{q}') = \int d^3r \, e^{-i\mathbf{q}'\cdot\mathbf{r}} \bar{\psi}^e_f(\mathbf{r})\gamma_\mu\psi^e_i(\mathbf{r}) \tag{5.2a}$$

$$\mathcal{J}^N_\mu(\mathbf{q}') = \int d^3r \, e^{i\tilde{\mathbf{q}}'\cdot\mathbf{r}} \bar{\psi}^N_f(\mathbf{r})\Gamma_\mu\psi^N_i(\mathbf{r}) \tag{5.2b}$$
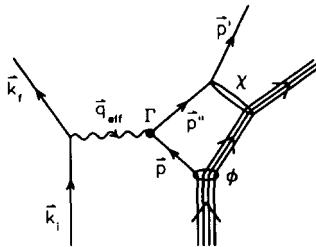
Fig. 5.1. Conceptual diagram for the distorted wave approximation to single-nucleon knockout reactions.

and where Γ_μ is the vertex operator for the nucleon current. In these expressions the electron wave functions relative to the target of mass m_A are denoted by the spinors ψ_i^e and ψ_f^e for the initial and final states, respectively. Since it is more convenient to express the ejectile wave functions ψ^N relative to the residual nucleus of mass m_B, the radial scale is adjusted by means of the reduced momentum transfer[170] $\tilde{\mathbf{q}}' = \mathbf{q}' m_B / m_A$.

If we assume that a virtual photon with momentum $\mathbf{q}'$ is absorbed by a single nucleon with initial momentum $\mathbf{p}$, the nuclear current at position r becomes

$$\mathcal{J}_\mu^N(\mathbf{r}) = \int \frac{d^3p}{(2\pi)^3} \frac{d^3p''}{(2\pi)^3} \, e^{-i\tilde{\mathbf{q}}'\cdot\mathbf{r}} \tilde{\chi}^{(-)*}(\mathbf{p}',\mathbf{p}'') \Gamma_\mu(\mathbf{p}'',\mathbf{p}) \tilde{\phi}(\mathbf{p}) \quad (5.3)$$

where the single-nucleon wave function is the amplitude for removing a nucleon from the initial state of target A and reaching the final state of residual nucleus B, such that

$$\tilde{\phi}(\mathbf{p}) = \langle B | a(\mathbf{p}) | A \rangle \quad (5.4)$$

The distorted wave $\tilde{\chi}^{(-)*}(\mathbf{p}',\mathbf{p}'')$ is the amplitude that an ejectile with initial momentum $\mathbf{p}'' = \mathbf{p} + \mathbf{q}'$ emerges from the nuclear field with final momentum $\mathbf{p}'$. Inclusion of inelastic processes within the final-state interactions can be accomplished using a coupled-channels model of the distorted waves, as discussed in Section 7.5. In coordinate space these wave functions are expressed as

$$\phi(\mathbf{r}) = \int \frac{d^3p}{(2\pi)^3} \, e^{i\mathbf{p}\cdot\mathbf{r}} \tilde{\phi}(\mathbf{p}) \quad (5.5a)$$

$$\chi(\mathbf{p}',\mathbf{r}) = \int \frac{d^3p''}{(2\pi)^3} \, e^{i\mathbf{p}''\cdot\mathbf{r}} \tilde{\chi}(\mathbf{p}',\mathbf{p}'') \quad (5.5b)$$

Thus, the nuclear current becomes

$$\mathcal{J}_\mu^N(\mathbf{q}') = \int \frac{d^3p}{(2\pi)^3}\, \tilde{\chi}^{(-)*}(\mathbf{p}', \mathbf{p} + \mathbf{q}')\Gamma_\mu(\mathbf{p} + \mathbf{q}', \mathbf{p})\tilde{\phi}(\mathbf{p}) \qquad (5.6)$$

where $\mathbf{q}'$ is the local momentum transfer supplied by the electron.

In the absence of Coulomb distortion, the electron current would be proportional to $\delta^3(\mathbf{q}' - \mathbf{q})$, so that the nuclear current could be evaluated for a unique value of the momentum transfer obtained from asymptotic kinematics. Fortunately, even in the presence of Coulomb distortion, the electron current tends to be sharply peaked about a local or effective momentum transfer, $\mathbf{q}' \approx \mathbf{q}_{\text{eff}}$, so that for light nuclei it remains a good approximation to evaluate the vertex function in the effective momentum approximation (EMA),

$$\Gamma_\mu(\mathbf{p}'', \mathbf{p}) \approx \Gamma_\mu(\mathbf{p}', \mathbf{p}_{m,\text{eff}}) \qquad (5.7)$$

where the effective missing momentum, $\mathbf{p}_{m,\text{eff}} = \mathbf{p}' - \mathbf{q}_{\text{eff}}$, includes the effect of Coulomb distortion. Further details of the effective momentum approximation for Coulomb distortion are given in Section 5.6.

Therefore, we obtain

$$\mathcal{J}_\mu^N(\mathbf{q}') \approx \int d^3r\, e^{i\tilde{\mathbf{q}}_{\text{eff}}\cdot\mathbf{r}}\chi^{(-)*}(\mathbf{p}', \mathbf{r})\Gamma_\mu(\mathbf{p}', \mathbf{p}_{m,\text{eff}})\phi(\mathbf{r}) \qquad (5.8)$$

where the vertex function has now been reduced to a matrix, acting on nucleon spins, whose elements are evaluated using effective kinematics. This approach greatly simplifies the numerical evaluation of the transition amplitude and is a suitable starting point for nonrelativistic models that use nonrelativistic wave functions χ and ϕ and a nonrelativistic reduction of Γ. It also has the advantage of preserving the response function structure of the one-photon exchange approximation.

Several other processes may contribute to the transition amplitude. Dispersion corrections involving electromagnetic excitation of either the initial or the residual nucleus require exchange of two or more hard photons and hence are inhibited by α^2 relative to the lowest-order DWA amplitude. Coherent (elastic or inelastic) electron scattering by the residual nucleus may also permit an energetic nucleon to emerge. Recoil contributions of this type are important in some kinematical situations for very light nuclei, but are expected to be negligible for complex nuclei. Similarly, exchange contributions in which a nucleon emerges other than that which absorbs the virtual photon are expected to be minimized when the ejectile momentum is large and the missing momentum small. However, these effects may become important for $(e, e'p)$ experiments at large missing momenta which seek to study short-range

correlations. These and several additional processes have been discussed in Ref. 1 but, since realistic calculations are not yet practical, no further discussion of those issues will be given here. Two-body currents involving meson exchange and/or isobar excitation are discussed in Section 7.4.

5.2. Distorted Momentum Distributions

The distorted momentum distribution $\rho^D(\mathbf{p}_m, \mathbf{p}')$ is obtained by dividing the unpolarized differential cross section σ_0 by the elementary electron–nucleon cross section σ_{eN} for initial (final) nucleon momenta $\mathbf{p}_m$ $(\mathbf{p}')$, such that

$$\rho^D(\mathbf{p}_m, \mathbf{p}') = \frac{\sigma_0}{K\sigma_{eN}} \tag{5.9}$$

where

$$\sigma_{eN} = \sigma_M \left(V_L R_L^{eN} + V_T R_T^{eN} + V_{LT} R_{LT}^{eN} \cos\phi + V_{TT} R_{TT}^{eN} \cos 2\phi \right) \tag{5.10}$$

does not include the phase-space factor K. To be consistent, the eN response functions must be computed from the same current operator used to evaluate the nuclear response functions. The normalization is determined by the requirement that in the plane-wave approximation the momentum distribution, $\rho_j(p_m)$, for a fully occupied orbital with total angular momentum j be normalized to its occupancy, such that

$$4\pi \int dp_m \, p_m^2 \, \rho_j(p_m) = 2j + 1 \tag{5.11}$$

for the independent-particle shell model.

Similarly, the experimental momentum distribution is also obtained using Eq. (5.9), but the off-shell electron–nucleon cross section, σ_{cc1}, developed by de Forest[18] is normally used for σ_{eN}. Further details may be found in Section 5.5.3.

5.3. Bound State Wave Functions

The radial overlap function for removing a nucleon from the ground state of an A-body system, $\Psi_0^{(A)}$, and leaving the residual $(A-1)$-body system in a specific final state, $\Psi_\alpha^{(A-1)}$, can be expanded in the form

$$\langle \Psi_\alpha^{(A-1)} | \Psi_0^{(A)} \rangle = \sum_\beta c_{\alpha\beta} \phi_\beta(\mathbf{r}) \tag{5.12}$$

where $c_{\alpha\beta}$ is a parentage or pickup coefficient and where the labels α and β stand for all required quantum numbers. We assume that the basis functions closely resemble single-particle orbitals in the Hartree–Fock mean field. Thus, we assume that

$$\left[-\frac{\hbar^2}{2m}\nabla^2 + V(r) \right]\phi_\beta = \varepsilon_\beta \phi_\beta \tag{5.13}$$

where the separation-energy prescription for the single-particle energies stipulates that

$$\varepsilon_\beta = E_0^{(A)} - E_\beta^{(A-1)} - m_N \tag{5.14}$$

The single-particle potential is usually parametrized in the Woods-Saxon form

$$V(r) = V^Z(r) + V^C(r) + V^{LS}\mathbf{L}\cdot\sigma \tag{5.15}$$

where $V^Z(r)$ is the Coulomb potential for a uniformly charged sphere of radius R_Z and where

$$V^C(r) = -V_0 f(r) \tag{5.16a}$$

$$V^{LS}(r) = -V_0^{LS}\frac{2}{r}\frac{\partial}{\partial r}f(r) \tag{5.16b}$$

with

$$f(r) = [1 + \exp((r-R)/a)]^{-1} \tag{5.17}$$

The radius of the Coulomb potential for residual charge $(Z - 1)$ is parametrized as $R_Z = r_Z(A-1)^{1/3}$ where r_Z is typically 1.2 fm. The radius of the nuclear potential is parametrized as $R = r_0(A-1)^{1/3}$ and the radius parameter r_0 is adjusted to fit the shape of the momentum distribution for each state separately. The diffuseness parameter a is usually held constant, where typically $a = 0.65$ fm is assumed. The central and spin–orbit potentials are usually assigned the same geometrical parameters. Either the strength V_0^{LS} or the ratio V_0^{LS}/V_0^C is also held constant. Typically, one chooses $V_0^{LS} \approx 6$ MeV or uses the Thomas form[171]

$$V_0^{LS} = \frac{1}{2}\left(\frac{\hbar}{2m_p c}\right)^2 \lambda V_0 = 0.00553\lambda V_0 \tag{5.18}$$

with $\lambda = 25$. The depth of the central potential is then adjusted to reproduce the experimental separation energy.

Many analyses also include a Perey nonlocality correction of the radial wave function[172,173] in the form of a multiplicative factor

$$P(r) = \left[1 + \frac{\mu}{2\hbar^2}\beta^2 V_0 f(r)\right]^{-1/2} \tag{5.19}$$

where $\mu = m_p(A - 1)/A$ is the reduced mass. The nonlocality parameter is typically chosen as $\beta = 0.85$ fm. The wave function must be renormalized and the quoted rms radius includes the change due to the nonlocality correction.

5.4. Ejectile Distortion

The ejectile distorted wave is assumed to satisfy a Schrödinger equation of the form

$$\left[\nabla^2 + k^2 - 2\mu\left(U^C + U^{LS}\mathbf{L}\cdot\boldsymbol{\sigma}\right)\right]\chi = 0 \tag{5.20}$$

where the central and spin–orbit optical potentials are U^C and U^{LS}. Relativistic kinematics are incorporated by using the exact relativistic wave number k and by replacing the reduced mass with the reduced energy

$$\mu = \frac{E_N E_{A-1}}{E_N + E_{A-1}} \tag{5.21}$$

where E_N and E_{A-1} are the relativistic total energies of the ejectile and the residual nucleus. The optical potentials may be obtained from fits to elastic scattering data, performed either with the Schrödinger or with the Dirac equation followed by transformation to an equivalent Schrödinger equation, or from folding model calculations using density-dependent effective interactions. These methods are reviewed below.

5.4.1. Woods–Saxon Parametrizations

Most analyses are performed using optical potentials fitted to proton elastic scattering data using simple Woods-Saxon (WS) shapes of the form

$$U^C(r) = V^Z(r) + V^C f(x_V) + iW^C f(x_W) + 4ia_S W^S g(x_S) \tag{5.22a}$$

$$U^{LS}(r) = \frac{2}{r}\left[V^{LS}g(x_{VLS}) + iW^{LS}g(x_{WLS})\right] \tag{5.22b}$$

where

$$f(x_i) = [1 + e^{x_i}]^{-1}, \qquad g(x_i) = -\partial f(x_i)/\partial r$$
$$x_i = (r - R_i)/a_i, \qquad R_i = r_i A^{1/3}$$

The factor $-4a_S$ is included to normalize the surface-absorption form factor to unity at its peak. The Coulomb potential V^Z is usually obtained for a uniformly charged sphere of radius $R_Z = r_Z A^{1/3}$ with $r_Z \approx 1.25$ fm, but is sometimes obtained, more consistently, by folding the Coulomb interaction over the nuclear charge density. For low energies, typically $T_p < 100$ MeV, surface absorption is parametrized by W_S, usually with $r_S = r_W$ and $a_S = a_W$. The real and imaginary spin–orbit potentials are usually assigned common geometrical parameters, $r_{WLS} = r_{VLS} = r_{LS}$ and $a_{WLS} = a_{VLS} = a_{LS}$.

The parameters may be obtained either from single-energy fits made to the data for each ejectile energy independently or from energy-dependent analyses which consider a broad range of proton energies. The former usually produce superior fits to the elastic scattering data, but the parameters may vary erratically with energy due to uncontrollable correlations among the parameters or to defects in the reaction mechanism. Energy-dependent optical models impose a smooth energy dependence upon the potentials, usually at the expense of local fit quality. Furthermore, global optical potentials also impose smooth functions upon the mass dependence of the geometrical parameters. However, one must be careful not to employ such potentials significantly beyond the ranges of either mass or energy originally fitted — they usually do not extrapolate well.

The potential fitted by Schwandt et al.[174] to cross section and analyzing power for proton elastic scattering for $A \geq 40$ and $80 \leq T_p \leq 180$ MeV is commonly employed for knockout analyses. It may be used for either proton or neutron scattering since it contains a parametrization of the symmetry potential. Although the Schwandt potential does not bear extrapolation in either mass or energy well, it is nevertheless often used for lighter nuclei, sometimes even for mass 12. A potential developed by Abdul-Jalil and Jackson[175, 176] for $A \approx 12$ and $50 \leq T_p \leq 160$ MeV has sometimes been used for knockout studies, but in our opinion its description of proton scattering data is unsatisfactory. Alternatively, the $p+^{12}C$ potential of Comfort and Karp[177] for $T_p \leq 185$ MeV is preferred. Unfortunately, a global nonrelativistic optical potential for $A \geq 12$ and a broad range of energy does not appear to exist. For that we must appeal to Dirac phenomenology (DP).

5.4.2. Dirac Phenomenology

Suppose that a four-component Dirac spinor

$$\Psi(\mathbf{r}) = \begin{pmatrix} \psi_+(\mathbf{r}) \\ \psi_-(\mathbf{r}) \end{pmatrix}$$

where ψ_+ and ψ_- are two-component Pauli spinors for positive and negative energy components, satisfies a Dirac equation of the form

$$[\boldsymbol{\alpha} \cdot \mathbf{p} + \beta(m + S)] \Psi = (E - V - V^Z)\Psi \tag{5.23}$$

with scalar and vector potentials S and V. Upon elimination of the lower components, an equivalent Schrödinger equation of the form

$$\left[\nabla^2 + k^2 - 2\mu\left(U^Z + U^C + U^{LS}\mathbf{L} \cdot \boldsymbol{\sigma}\right)\right]\phi = 0 \tag{5.24}$$

can be obtained, where ψ_+ is related to ϕ by the Darwin transformation

$$\psi_+ = B^{1/2}\phi \tag{5.25a}$$

$$B = 1 + \frac{S - V - V^Z}{E + m} \tag{5.25b}$$

The equivalent Schrödinger potentials are then

$$U^Z = \frac{E}{\mu}V^Z \tag{5.26a}$$

$$U^C = \frac{E}{\mu}\left[V + \frac{m}{E} + \frac{S^2 - V^2}{2E} - \frac{V^Z(V^Z + 2V)}{2E}\right] + U^D \tag{5.26b}$$

$$U^D = \frac{1}{2\mu}\left[-\frac{1}{2r^2B}\frac{d}{dr}(r^2B') + \frac{3}{4}\left(\frac{B'}{B}\right)^2\right] \tag{5.26c}$$

$$U^{LS} = -\frac{1}{2\mu}\frac{B'}{rB} \tag{5.26d}$$

where U^D is the Darwin potential. The Schrödinger solutions are phase-equivalent to the Dirac solutions in the sense that the asymptotic phase shifts, and hence observables for elastic scattering, are the same. However, the Dirac wave function is modified in the interior by a nonlocality factor similar in form to the Perey–Buck nonlocality factor, except that it depends upon $S - V$, which is closely related to the spin–orbit potential, rather than upon the central potential. Hence, C_{rel} can also be deduced from the spin–orbit potential directly.[178] When used in nonrelativistic calculations, the positive energy spinor ψ_+, including the Darwin factor, is identified with the distorted wave χ.

Hama et al.[179] produced global Dirac optical potentials for $A \geq 40$ and $65 \leq T_p \leq 1040$ MeV. The scalar and vector potentials were parametrized by symmetrized Woods–Saxon functions, of the form

$$f(x) = \left[(1 + e^{-x})(1 + e^x)\right]^{-1} \tag{5.27}$$

where $x = (r - R)/a$ for each component, as before. In addition, surface absorption proportional to $f'(x)$ was included. Two fits were made, here designated DP1 and DP2. The strengths and shape parameters for DP1 were expanded in the form

$$V_i = R_i \sum_{j=0}^{3} V_{ij} E^{-j}$$

$$R_i = A^{1/3} \left(\sum_{j=0}^{2} R_{ij} A^{-j} + \sum_{j=3}^{5} R_{ij} E^{2-j} \right)$$

$$a_i = \sum_{j=0}^{2} a_{ij} A^{-j} + \sum_{j=3}^{5} a_{ij} E^{2-j}$$

where the subscript i refers to real and imaginary parts of the scalar and vector potentials. A slightly different parametrization was employed for DP2. DP1 has 77 parameters, compared with 84 for DP2, but both give approximately the same reduced $\chi_\nu^2 \approx 8.3$ for more than 4500 degrees of freedom.

The global Dirac optical potential was then extended to the ranges $A \geq 12$ and $20 \leq T_p \leq 1040$ MeV, including more than 8700 data points, by Cooper et al.[180] The parametrizations are more complicated and several essentially equivalent variations of the global potential were provided. In addition, best-fit energy-dependent potentials were produced for everyone's favorite targets: ^{12}C, ^{16}O, ^{40}Ca, ^{90}Zr, and ^{208}Pb.

Although the scalar+vector (SV) model of Dirac phenomenolgy is not unique, and relatively simple but arbitrary shapes are employed for the potentials, this work represents the most extensive and systematic analyses of proton optical potentials available. The data are described very well by potentials whose properties vary smoothly with both mass and energy.

5.4.3. *Microscopic Optical Models*

Further guidance may be sought in microscopic models of the nucleon optical potential based upon the local density approximation (LDA). In recent years it has become clear that the nucleon-nucleon effective interaction depends strongly upon the density in the interaction region. Several calculations of the effective interaction in nuclear matter have been made following the seminal work of Hüfner and Mahaux.[181] Jeukenne, Lejeune, and Mahaux[182–185] computed the self-energy and the optical potential for $0 \leq E_p \leq 160$ MeV using the Reid soft-core potential.[105] Brieva, Rook, and von Geramb[186–190] used the Hamada–Johnston potential[191] and later

von Geramb and collaborators[192, 193] used the Paris potential[103] to calculate the pair wave function and then to deduce a local pseudopotential using a generalization of the Siemens averaging procedure.[194] Similar calculations using the Hamada–Johnston potential have also been performed by Yamaguchi, Nagata, and Michiyama (YNM),[195, 196] who parametrized their results in Gaussian rather than Yukawa form. Nakayama and Love[197] used the Bonn potential[198] to calculate a local pseudopotential that reproduces on-shell matrix elements of the G-matrix. These theories are all based upon the Bethe-Goldstone equation and include Pauli blocking and self-energy corrections self-consistently. Finally, Ray[199] used a coupled channels nucleon-isobar model and Watson multiple scattering theory to calculate a density-dependent t-matrix applicable to nucleon energies above 200 MeV that includes some of the effects of pion production. All of these calculations predict strong density dependence of the nucleon–nucleon effective interaction. In fact, Ray's calculations predict that surprisingly strong density dependence persists even to energies as high as 800 MeV.

Although the qualitative features of the medium modifications are essentially the same, the quantitative differences among the various theories are surprisingly large, much larger than would be expected from the variations among the underlying nucleon–nucleon potentials that are employed, suggesting that the approximations required to evaluate the effective interaction are not yet under good control. The effect of these differences upon elastic and inelastic scattering calculations has been surveyed in a series of papers by Kelly and collaborators in which transition densities measured by electroexcitation are used to minimize uncertainties due to nuclear structure and to isolate the effective interaction for detailed examination.[200–204] Transition densities which are strong in the interior provide information about the high-density properties of the effective interaction, while surface-peaked transition densities reveal the low-density properties. The systematic comparison of such cases demonstrates quite clearly that the effective interaction depends upon local density and that estimates based upon nuclear matter theory have qualitatively correct characteristics, but that none of the theories presently available is sufficiently accurate for quantitative applications to nuclear structure. Therefore, an empirical model of the effective interaction has been developed in which medium modifications similar to those predicted by nuclear matter theory are parametrized in a form suitable to phenomenological analysis of data. The parameters are adjusted to reproduce inelastic scattering data for several states in one or more targets simultaneously. Empirical effective interactions have been extracted from data for several energies in the range $100 \leq E_p \leq 650$ MeV. For each energy we find that a unique effective interaction describes data for several inelastic transitions in a single nucleus and

that the fitted interaction is essentially independent of target. These findings confirm the basic hypothesis of the local density approximation, namely, that the interaction depends primarily upon local density and is independent of the detailed structure of any particular target or transition. The fitted parameters also exhibit a relatively smooth energy dependence.

Although slightly better fits to some of the data sets may be found in the original analyses, for the present purposes we choose to employ the empirical effective interactions (EEI) tabulated by Kelly and Wallace.[205] For this set of interactions, the medium modifications are applied to the Franey–Love (FL)[206] parametrization of the free *t*-matrix, which is available for all relevant energies, and common fitting strategies and constraints were used to help smooth the energy dependence of the fitted parameters. These choices are made primarily for aesthetic reasons and have very little effect upon knockout calculations.

The potentials which emerge from all microscopic models exhibit much more complicated radial shapes than posited by the Woods–Saxon model of the optical potential. The detailed shapes depend upon the density dependence and range of the effective interaction and upon the nuclear density, which especially for light targets is not well approximated by the Fermi shape. For energies between about 100 and 300 MeV, for example, the real central potential exhibits a characteristic "wine-bottle" shape. Similar shapes also arise from the nonrelativistic reduction of either Dirac phenomenolgy or the relativistic impulse approximation. Although good fits to elastic scattering data may be achieved with simplistic models of the potential, artificially simple geometries cannot be justified on more fundamental grounds.

Basing the phenomenology of the effective interaction primarily upon inelastic scattering actually offers two advantages over the determination of the optical potential via elastic scattering. First, the various radial shapes of transition densities provide differential sensitivity to the density dependence of the effective interaction, while the elastic optical potential requires only a global average over density. Second, since the distorted waves are determined self-consistently using optical potentials constructed from the same interaction that drives the inelastic transitions, the inelastic observables depend upon overlap integrals and are sensitive to the wave functions in the nuclear interior, thereby helping to determine the interior optical potential. Elastic scattering, on the other hand, depends on asymptotic phase shifts and all potentials which share the same asymptotic wave functions predict the same elastic scattering despite differences in the interior. Therefore, provided that a consistent description of both elastic and inelastic scattering emerges from the phenomenological analysis of the effective interaction, the resultant optical potential should represent a more realistic description of the nuclear

interior than models restricted to simple geometries, even if the latter yield better χ^2 fits to the elastic scattering data alone.

A disadvantage of this procedure is that it depends upon the relationship between elastic and inelastic t-matrices

$$t_{\text{inel}}(q, \rho) = (1 + \partial/\partial\rho)t_{\text{el}}(q, \rho)$$

first derived for proton scattering by Cheon *et al.*[207,208] The rearrangement factor $(1 + \partial/\partial\rho)$ arises quite naturally in the collective model for which the effective interaction is interpreted as a functional derivative of the optical potential with respect to the local density. Cheon *et al.* then argue that this result also represents an approximation to the hole-line expansion of the transition potential, but the additional approximations required to perform a practical calculation render their numerical demonstration of its accuracy somewhat unconvincing. Nevertheless, this factor has been found to be a crucial ingredient in the self-consistent analysis of the empirical effective interaction.[201] If the interaction depends linearly upon density, the effect of the rearrangement factor is to double the density dependence for inelastic scattering relative to the elastic interaction. Also note that it is the elastic interaction that is predicted by nuclear matter theory. However, for low energies the rearrangement contribution is so large that it can even change the sign of $\text{Im}\, t^C$ at saturation density. Thus, it is likely that higher-order contributions become important in this regime. In fact, the phenomenology encounters severe difficulties which have so far stymied efforts to extract a satisfactory empirical effective interaction applicable to nucleon energies below 100 MeV. Unfortunately, most of the high-resolution $(e, e'p)$ data presently available is confined to proton energies below 100 MeV.

5.4.4. Comparison of Optical Potentials

Optical potentials for $p + {}^{40}\text{Ca}$ at $T_p = 135$ MeV are compared for several models in Fig. 5.2. The suppression of t_{00}^C in the surface region makes $\text{Re}\, U^C$ smaller for the EEI than for the PH model at large radii. Otherwise, the EEI $\text{Re}\, U^C$ potential is similar to PH and is intermediate between the DP and Schwandt models, though with a more complicated radial shape. Similarly, for $\text{Re}\, U^{LS}$ the EEI potential is slightly smaller than PH, but both have larger radii and more complicated radial shapes than the Woods-Saxon parametrizations, either relativistic or nonrelativistic. Perhaps the most important differences between these models are found in the absorptive potential, $\text{Im}\, U^C$. At this energy the Schwandt model is less absorptive and the DP model more absorptive than the EEI model. The PH model is considerably

^{40}Ca(p,p) E_p = 135 MeV
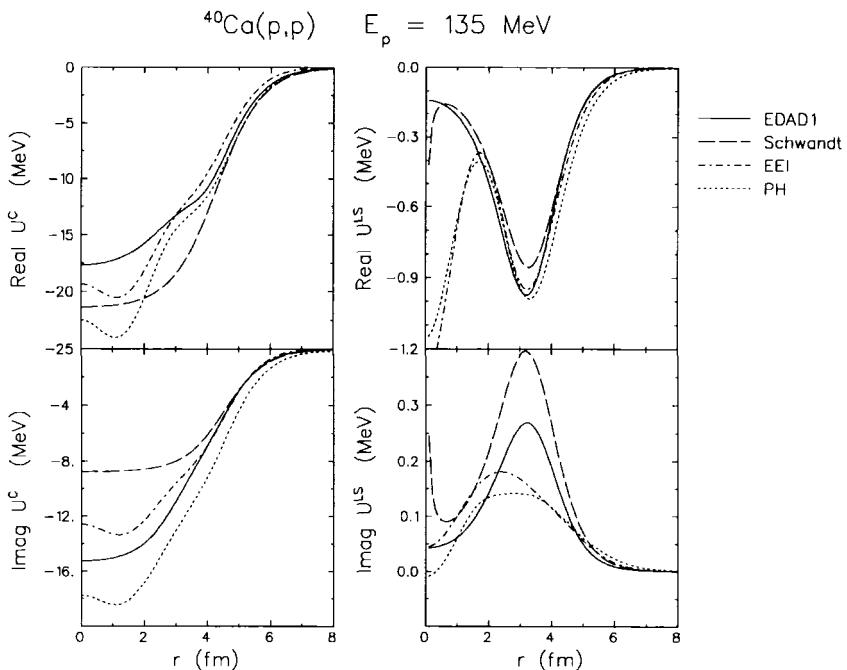
Fig. 5.2. Several models of the optical potential for $p+^{40}$Ca at $T_p = 135$ MeV.

more absorptive than any of the others. As we shall see in the next sec-
tion, these absorptive properties are directly correlated with the spectroscopic
factors deduced from knockout data using these potentials.

A convenient means of comparing various models of the optical potential
is provided by the volume integrals

$$J[U_i] = 4\pi \int dr \ r^2 U_i(r) \tag{5.28}$$

where Ui is either the real or imaginary part of either the central or spin–orbit
potential. It is found that J/A for central potentials and $J/A^{1/3}$ for spin-
orbit potentials depend only weakly on A.[209] The r^2 weighting makes these
quantities most sensitive to the surface properties of the potentials. We will
see later that spectroscopic factors are also sensitive to the interior properties
of the potentials.

The energy dependence of the volume integrals of the optical potentials
for $p+^{40}$Ca are compared for several models in Fig. 5.3. The solid curve
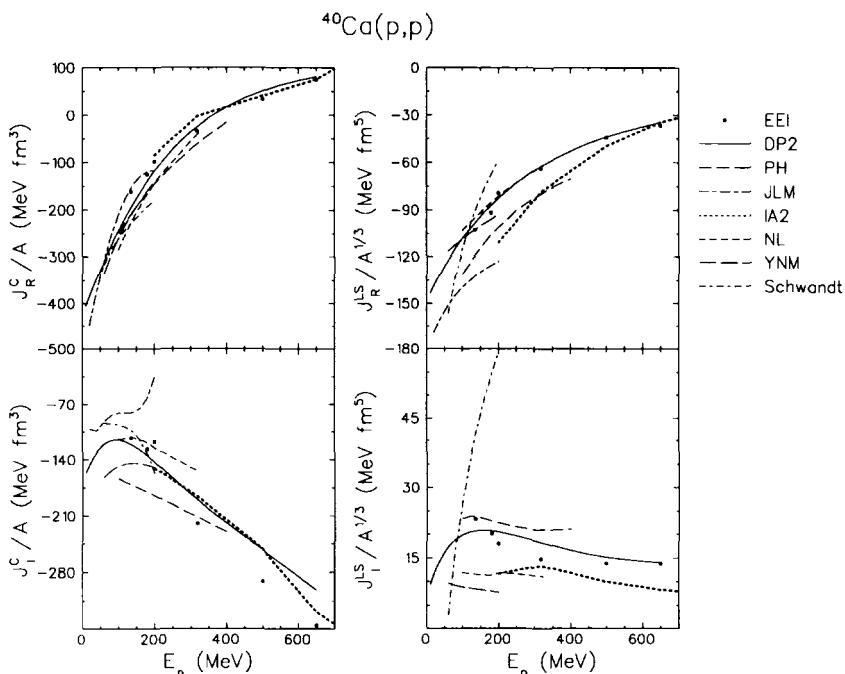
Fig. 5.3. Volume integrals for several models of the optical potential for $p+{}^{40}\mathrm{Ca}$ are compared as functions of proton kinetic energy.

portrays "fit 2" global Dirac phenomenology,[179] designated (DP2), which provides good fits to elastic scattering data covering the broadest ranges of mass and energy available in phenomenological potentials; other versions of Dirac phenomenology give similar results. The empirical effective interaction (EEI) fitted to both elastic and inelastic scattering data gives results that are similar to DP in their range of overlap.

The energy dependence of the Schwandt potentials is quite different from the DP and EEI results. The Schwandt spin–orbit potentials depend much more strongly on energy than do any of the other models, phenomenological or theoretical. Although the imaginary spin–orbit potential is fairly weak, that component of the Schwandt model is unrealistically strong above 100 MeV. The energy dependence of the imaginary central potential also becomes quite steep for $T_p > 150$ MeV. Since the DP model provides an equally good fit to the data analyzed by Schwandt *et al.,* it is clear that these properties of the Schwandt model are not dictated by the data. The Schwandt model is less

(more) absorptive than the EEI model below (above) by about 150 MeV.

Predicted proton absorption cross sections are compared with data in Fig. 5.4. Unfortunately, the available proton data are scarce and of uneven quality.[210] Nevertheless, the EEI model provides accurate predictions for these data, although the 200 MeV interaction appears to give results which are systematically low compared to the trends for other energies. It is important to remember that the EEI model is dominated by inelastic data, but gives good fits to elastic data whether or not they are included in the analysis. Furthermore, neither absorption nor total cross-section data were included in the analysis, but are nevertheless predicted accurately. Dirac phenomenology also provides good predictions for proton absorption cross sections, but its calculations for both ^{12}C and ^{40}Ca appear to be slightly too large. Below about 150 MeV the Schwandt model also agrees with the data, but its energy dependence appears to be unreasonable and it begins to diverge from the data for higher energies. The earlier version of that model due to Nadasen[209] gives a better description of the energy dependence of the absorption cross section.

Finally, we compare in Fig. 5.5 predictions for neutron total cross sections with the high-quality neutron total cross-section data recently obtained at LAMPF.[211] Neutron total cross sections computed from the Schwandt potential are substantially larger than the data. For self-conjugate targets Dirac phenomenology provides good predictions over broad ranges of mass and energy, but, lacking a parametrization of the symmetry potential, the DP model fails to reproduce σ_n for $N > Z$.[212] As for the proton absorption cross section, DP predictions for the ^{12}C neutron total cross sections appear to be slightly too large in the energy range relevant to existing proton knockout data. The EEI model also provides good predictions for self-conjugate targets and appears to be more accurate than DP for light nuclei, such as ^{12}C. The result at 200 MeV appears to be slightly too small, as also observed in the proton absorption cross sections. Below about below 300 MeV, the EEI calculations for heavier targets with significant neutron excesses also appear to be more accurate than DP, but tend to be too high at higher energies, particularly for ^{208}Pb. For these EEI calculations the symmetry potential is obtained by folding the isovector density with the density-independent isovector interaction from the FL t-matrix. Although the isovector interaction has not been calibrated to nucleon-nucleus scattering data with the same care as the isoscalar interaction, its contribution is small enough that residual errors in theoretical models of that term should not be too serious. Similarly, calculations using the relativistic impulse approximation, with[205] or without[213] density dependence, also reproduce the neutron total cross-section data for ^{208}Pb.

Each of the theoretical effective interactions available in the 100–200
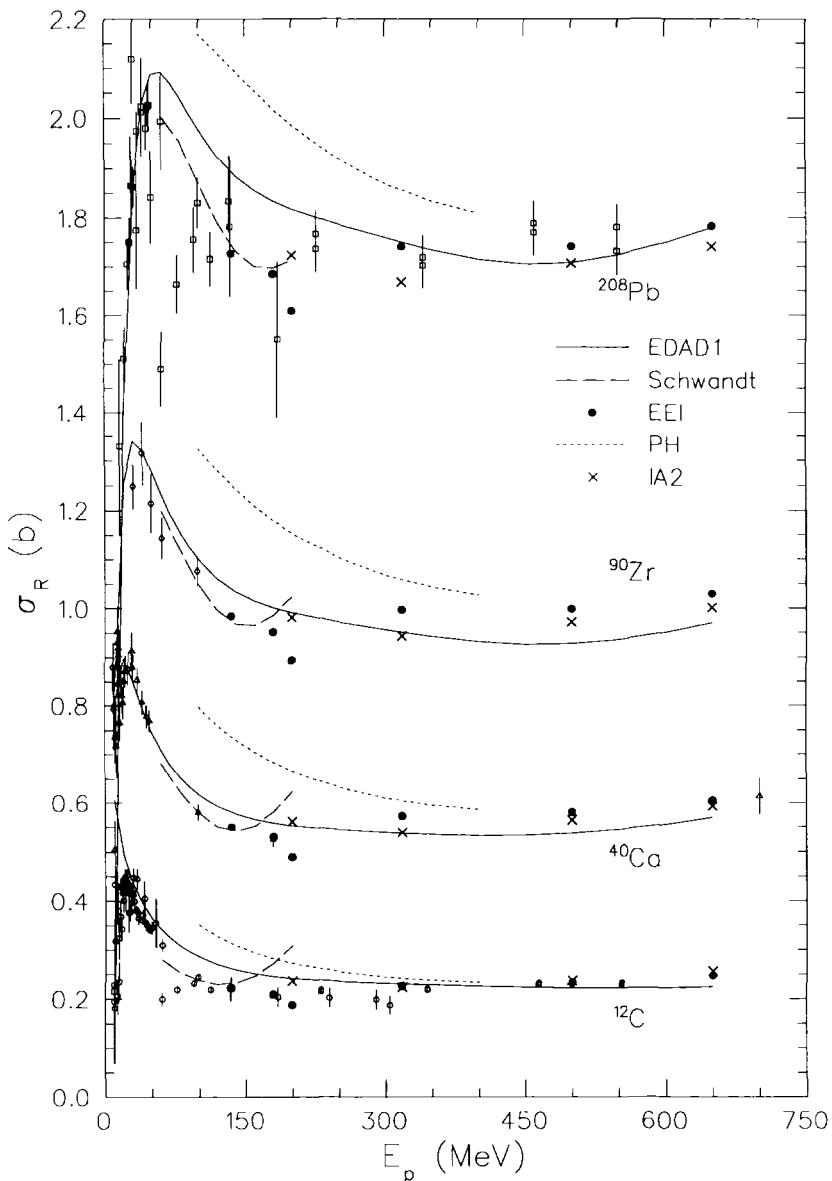
Fig. 5.4. Proton absorption cross sections for several optical models are compared with data. Note that for ^{12}C and ^{40}Ca the IA2 and EEI calculations sometimes almost coincide and the EEI calculations sometimes obscure data points.
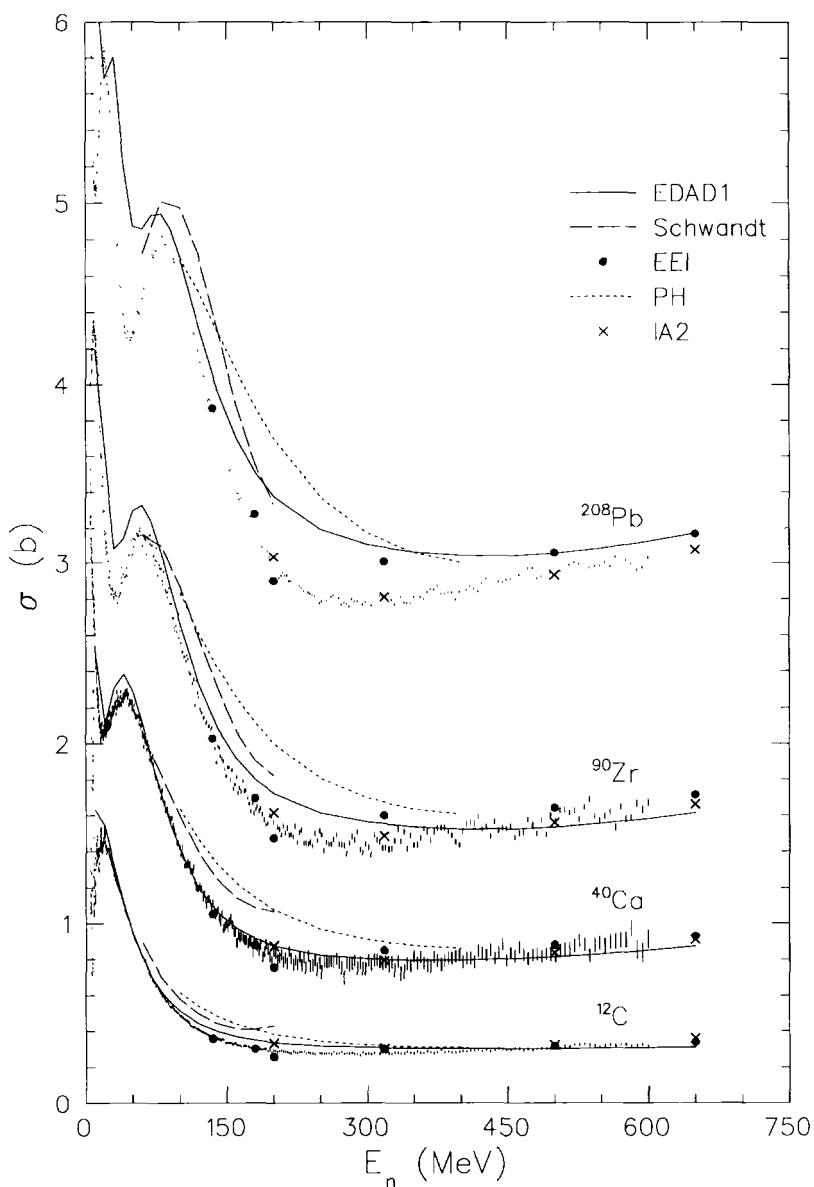
Fig. 5.5. Neutron total cross sections for several optical models are compared with data.

MeV regime produce neutron total cross sections that are too large. Since the JLM model does not provide shapes for its interaction components and is mainly intended for use at lower energies, it will not be considered further. The other models give larger volume integrals for the real parts of the central and spin–orbit potentials than obtained from either the DP or the EEI models. Although the PH interaction generally gives the most accurate elastic scattering predictions among the LDA models, its absorption is clearly too strong. Except for the NL interaction, which has an unusually strong density dependence for that component, the LDA also gives stronger volume integrals for the imaginary central potential. The most important difference between these components of the empirical and theoretical effective interactions is reduction of the low-density interaction strength in the EEI model, which is needed to fit inelastic scattering data for surface-peaked transition densities. This result has been interpreted as an effect for finite nuclei that is not described by the local density interaction: the density dependence for large (small) radii is stronger (weaker) than for infinite nuclear matter with the corresponding local density. However, since the EEI model was fitted to data for self-conjugate targets with $A \leq 40$, the fact that it begins to deviate from the total cross section data for heavier nuclei may indicate either that it lacks a dependence on neutron excess or that the finite-nucleus corrections to the LDA must be reduced for larger nuclei.

5.4.5. Sensitivity of Knockout to Optical Model Ambiguities

Due to the transparency of the nucleus to the electromagnetic interaction, the knockout reaction may be initiated anywhere within the nuclear volume. Hence the distortion of the emergent nucleon wave function can be sensitive to the details of the optical potential in the interior. Since knockout samples the radial dependence of the optical potential rather differently than does proton elastic scattering, it is not *a priori* clear that the phenomenological optical potential which provides the most accurate fit to proton scattering data will also provide the most accurate description of knockout.

Several studies of the sensitivity of *(e, e'p)* distortion to variations of the optical potential have been performed. Blok *et al.*[214] compared the sensitivity of *(p, p')* and *(e, e'p)* reactions in the $A \approx 90$ region to the interior of the optical potential. For ^{88}Sr(p, p') to the second 2^+ state, a state whose transition density peaks in the nuclear interior, they found that the data at $E_p = 200$ MeV favors an absorptive potential that is stronger in the interior than the global optical potential of Schwandt *et al.*,[174] but that is similar to the microscopic potential based upon the Paris–Hamburg G-matrix.[193] Similarly, the interior lobe of the $2p_{3/2}$ wave function provides the ^{90}Zr$(e, e'p)$

reaction with interior sensitivity. It was found that the data for 70 and 100 MeV protons could not be adequately described by standard optical potentials, but that a consistent description of the data for both energies using the same bound-state wave function could be obtained by increasing the strength of the interior optical potential. Den Herder *et al.*[215] studied the sensitivity of the distorted momentum distribution to the lower integration limit and found that for missing momenta $p_m \approx 160$ MeV/c a substantial contribution is obtained from the interior lobe of the $2p_{3/2}$ wave function. Although *(e, e'p)* is obviously not the reaction of choice for determination of the proton optical potential, it can be used to test the consistency of assumptions made in the analysis of proton elastic scattering that are based upon simple phenomenological models of the optical potential.

These studies of the sensitivity of spectroscopic factors to uncertainties in the optical potential usually conclude that this source of systematic error is typically about 5–7%, of which about 3% is attributed to the optical potential and the rest to uncertainties in Coulomb distortion and other variations of the model.[215] However, Weinstein *et al.*[216] report much larger optical-model dependence of spectroscopic factors for $1p$ knockout from ^{12}C, amounting to uncertainties as large as 20%. Furthermore, most such studies are limited to optical potentials of simple Woods–Saxon geometry, while microscopic models of the proton optical potential almost always predict potentials with more complicated shapes.

The sensitivity of electromagnetic knockout of protons to models of the optical potential is illustrated in Fig. 5.6, in which distorted momentum distributions for the $2s_{1/2}$ and $1d_{3/2}$ orbitals calculated using several representative optical models are compared with the data of Raben *et al.*[217] Data for both parallel and quasiperpendicular kinematics were acquired with electron beam energies near 500 MeV. The ejectile energy was chosen to be equivalent to proton scattering at 135 MeV in the lab, an energy for which both theoretical and empirical effective interactions are available. For the purposes of this study, we use the same overlap functions for each choice of potential and kinematics; these wave functions were obtained from a Skyrme–Hartree–Fock calculation using the interaction designated Z_σ by Refs. 218 and 219 and are similar to those fitted by Kramer *et al.*[220] to (e, *e'p*) data. No attempt has been made here to fit either the shape or the normalization of the overlap function to the data, which are shown merely to indicate the qualitative agreement between NRDWIA calculations and the data. The dashed curves use the global optical model of Schwandt *et al.*,[174] the dash-dotted curves use folded optical potentials based upon the Paris-Hamburg (PH) effective interaction,[192,193] and the solid curves use the empirical effective interaction (EEI) fitted to proton inelastic scattering by ^{16}O.[201] These potentials were

compared in Fig. 5.2. To isolate the dependence upon optical potential, all other aspects of the calculations were the same for all cases. In particular, nonlocality corrections were not applied to any of the nonrelativistic models. The Darwin factor is applied for Dirac phenomenology, of course.

The sensitivity of spectroscopie factors for *(e, e'p)* to differences between various optical models is illustrated in Table 5.1 for ^{40}Ca and $T_p = 135$ MeV. The relative spectroscopie factors, S/S_{EEI}, are compared to the EEI model by scaling the positive p_m peak of the distorted momentum density to match the EEI calculation. Among the effective interactions considered, the NL model is least absorptive and the PH model most absorptive, and consequently the spectroscopie factor for $1d_{3/2}$ knockout is larger for PH than NL, with EEI in between. However, for $2s_{1/2}$ knockout, which peaks at larger radius, $S_{NL}/S_{EEI} > 1$ shows that the potential shapes also matter. At this energy the Schwandt potential is slightly less absorptive and hence its spectroscopie factors are slightly smaller than for the EEI model, with the difference tending to decrease at larger radius. The absorptive potential remains stronger and hence the spectroscopie factors remain larger at large radii for the PH model than for the EEI model.

The comparison between the EEI and DP models is a little more complicated than the results of Section 5.4.4 might suggest. Although the EDAD1 absorptive potential shown in Fig. 5.2 is only a little larger than for EEI and is significantly smaller than for PH, the $1d_{3/2}$ spectroscopie factor for the EDAD1 model is about 15% greater than for EEI and is almost as large as for PH. However, it is the interior wave function that matters, not the equivalent Schrödinger absorptive potential itself, and the wave function is smaller by the Darwin factor than would be obtained in a local model using the same potential. Since the Darwin factor is closer to unity the difference from EEI decreases at larger radius. The role of the Darwin factor in suppressing the interior wave function, and thus enhancing spectroscopie factors deduced using DP potentials, was first studied by Boffi *et al.*[221] However, as shown in Section 5.4.7, there is evidence that the DP potentials are too absorptive and hence that its spectroscopie factors are too large.

Therefore, these results suggest that there is considerably more model dependence in the extraction of spectroscopie factors than commonly quoted. Near the peaks of the distorted momentum distributions, we find spreads of about ±7% for the 2s orbital or ±15% for the ld orbital. The spread among the calculations for the *2s* orbital is much larger at the second peak of the momentum distribution, beyond 150 MeV/c, because that feature arises from the interior lobe of the bound-state wave function where differences between the various models of the ejectile wave function are most pronounced. These features of the missing momentum distributions are clearly correlated
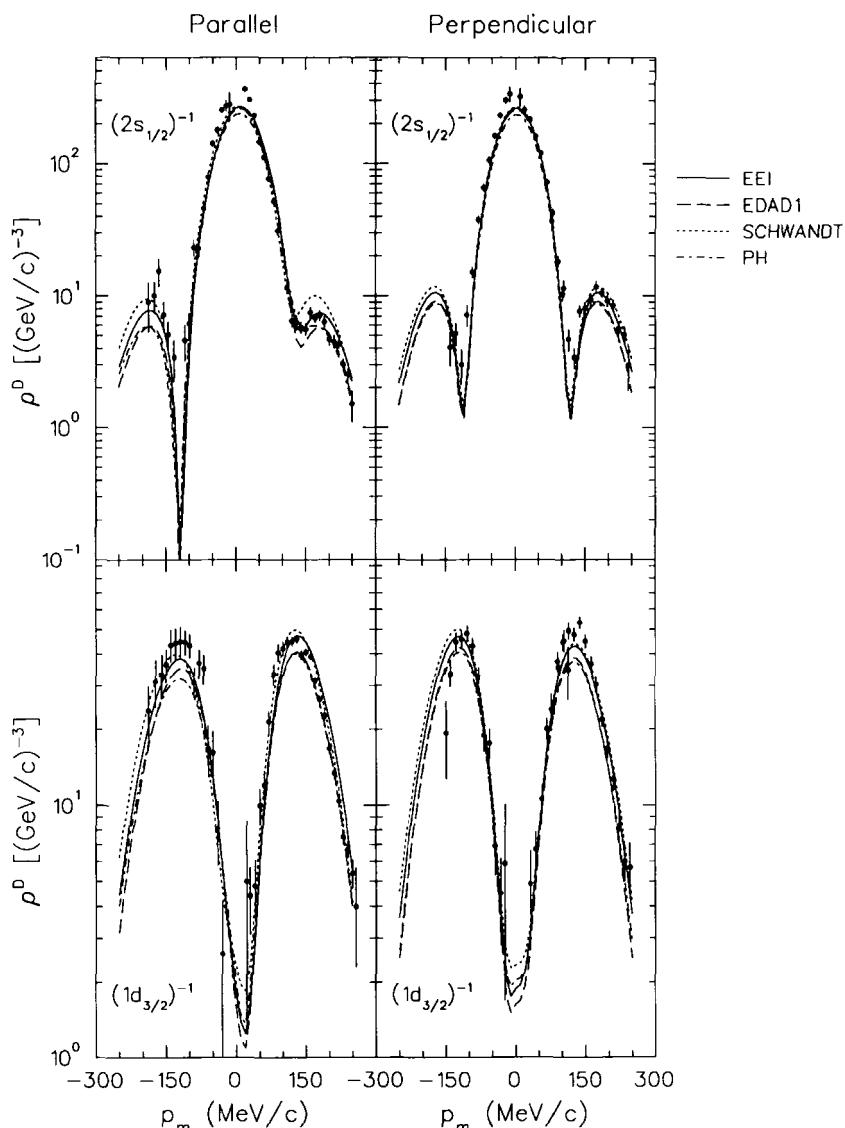
Fig. 5.6. Calculations for ^{40}Ca$(e, e'p)$ at $T_p = 135$ MeV are compared for several optical models. The same overlap functions were used for both parallel and quasiperpendicular kinematics and for each choice of potential. Perey factors are not included for nonrelativistic potentials.

TABLE 5.1

Sensitivity of Spectroscopic Factors for ^{40}Ca$(e, e'p)$ to the Choice of Optical Model, with $\varepsilon_i = 500$ MeV and $T_p = 135$ MeV

For each potential, spectroscopic factors for parallel ($\parallel$) and for quasiperpendicular ($\perp$) kinematics are compared with the EEI potential

Potential	$1d_{3/2}$		$2s_{1/2}$	
	$(S/S_{EEI})_\parallel$	$(S/S_{EEI})_\perp$	$(S/S_{EEI})_\parallel$	$(S/S_{EEI})_\perp$
EEI	1.0	1.0	1.0	1.0
PH	1.18	1.17	1.13	1.12
NL	0.90	1.01	1.05	1.03
Schwandt	0.95	0.98	1.00	0.97
EDAD1	1.16	1.12	1.04	1.03

with the interior wave function and thus with the depth of the absorptive potential for each model. Nonlocality and/or Darwin factors also affect the interior wave function and the deduced spectroscopic factor. Inasmuch as the empirical effective interaction is sensitive to the attenuation of the distorted waves through the inelastic scattering data to which it was fitted, we expect that model to produce the most reliable estimates of the interior wave functions for knockout.

5.4.6.   Nonlocality Corrections

Most nonrelativistic analyses of $(e, e'p)$ reactions include a Perey factor of the form[172,173]

$$C_P(r) = \left[1 - \frac{m\beta^2}{2\hbar^2} \operatorname{Re} U^C(r)\right]^{-1/2} \tag{5.29}$$

where $\operatorname{Re} U^C(r)$ is the real part of the central optical potential and typically one assumes that $\beta = 0.85$ fm. If ψ_L is the solution of a Schrödinger equation based upon a local optical potential that is supposed to be phase equivalent to a more fundamental nonlocal potential, the phase-equivalent solution to the original nonlocal Schrödinger equation is then supposed to be $\psi_{NL} \approx C_P \psi_L$. Since the Perey factor for an attractive potential is less than unity in the interior, the amplitude of the nonlocal wave function is reduced relative to the local wave function and thus the spectroscopic factor deduced by scaling the calculation to knockout data is increased by use of the Perey factor.

However, the justification for this procedure is fairly weak. Although there are many sources of nonlocality in the final-state interaction, there is

no rigorous derivation of any general relationship between wave functions in nonlocal and equivalent local potentials. For example, Fiedeldey *et al.*[222] have shown that the Perey factors for potentials whose nonlocalities are due to channel coupling can be very different from those due to exchange, with the former being much closer to unity. The appropriate Perey factor also depends upon the prescription used to construct the equivalent local potential, such that different prescriptions applied to the same nonlocal interaction can lead to different Perey factors. Despite its intuitive appeal, the Perey prescription is only an ansatz which must be justified by many-body theory, preferably for finite systems.

The optical potential $U = V + iW$ is closely related to the proper self-energy $\mathcal{U}(k, E) = \mathcal{V}(k, E) + i\mathcal{W}(k, E)$ via[183,223–225]

$$E(k) = \frac{k^2}{2m} + \mathcal{U}(k, E) \tag{5.30}$$

Assuming that E is real and substituting $k = k_R + ik_I$, we find

$$k_R = \sqrt{2m(E - V)} \tag{5.31a}$$

$$k_I = -\frac{m_k}{k_R}\mathcal{W} = -\frac{m}{k_R}W \tag{5.31b}$$

$$\frac{m_k}{m} = \left[1 + \frac{m}{k}\frac{\partial\mathcal{V}}{\partial k}\right]^{-1} \tag{5.31c}$$

where the potentials on shell are

$$V(E) = \mathcal{V}(k_R(E), E) \tag{5.32a}$$

$$W(E) = \frac{m_k}{m}\mathcal{W}(k_R(E), E) \tag{5.32b}$$

The total effective mass

$$\frac{m^*(E)}{m} = 1 - \frac{dV}{dE} = \frac{m_k}{m}\frac{m_E}{m} \tag{5.33}$$

is the product of the k-mass, m_k, and an E-mass, m_E, defined by

$$\frac{m_E}{m} = 1 - \frac{\partial\mathcal{V}(k, E)}{\partial E} \tag{5.34}$$

on shell. For large k_R, it is found[225] that $m_E \approx m$, so that $m^* \approx m_k$. Thus, to the extent that the energy dependence of the optical potential is dominated by the exchange contribution to a Brueckner–Hartree–Fock potential,

the nonlocality correction can be associated with the quasiparticle effective mass (k-mass) via

$$C_{NL} = \sqrt{m_k/m} \approx \sqrt{m^*/m} \tag{5.35}$$

The traditional parametrization is based upon the ansatz

$$\mathcal{V}(k, E) = \mathcal{V}_0(E)e^{-(\beta k/2)^2} \tag{5.36}$$

where $\beta = 0.85$ fm was derived for low-energy neutron scattering data, $E_n < 20$ MeV.

In Fig. 5.7 we show the Perey factor for $p + {}^{40}\text{Ca}$ at $E_p = 135$ MeV obtained from the local density approximation using the parametrization of m_k provided by Jeukenne, Lejeune, and Mahaux (JLM).[185] Alternatively, the effective mass can be derived from a density-dependent effective interaction $t(q, k, k_F)$ using the local density approximation (LDA)

$$\frac{m_k}{m} = \left[1 + \frac{m}{k}\rho\frac{\partial t(q, k, k_F)}{\partial k}\right]^{-1} \tag{5.37}$$

where ρ, k, and k_F are the local density, wave number, and Fermi momentum and where the q-dependence is attributed to the direct contribution and the k-dependence to the exchange contribution. The Perey factor that results from the Paris–Hamburg (PH) effective interaction[192193] is also shown in Fig. 5.7; other effective interactions, such as NL[197] or YNM,[196] give similar results. Finally, the traditional Perey factor with $\beta = 0.85$ fm is also shown. This choice is seen in Fig. 5.7 to lie between the PH and JLM estimates, and to be closer to PH. However, at higher energies the nonlocality range may change and other sources of nonlocality may give rise to different corrections. Note that $\beta_{PH} = 0.7$ fin gives a good approximation to the PH nonlocality correction in the interior, but that the Perey factor remains below unity for larger radii because of the difference between the radial extents of U and p.

Although several authors have remarked upon its omission, LDA calculations based upon the PH or NL interactions, including those performed by their progenitors, rarely include the m_k nonlocality corrections either to the absorptive potential or to the wave function. The nonlocality corrections to those models would be small: the reduction of the absorptive potential leads to a larger wave function, but is partially compensated by the Perey-factor reduction of the wave function so that inelastic scattering is largely unaffected, provided that either both or neither of the corrections are employed consistently. Calculations based on the YNM interaction usually employ both corrections, following the example of its authors.[196] The nonlocality corrections to the JLM interaction appear to be more important and are usually included.
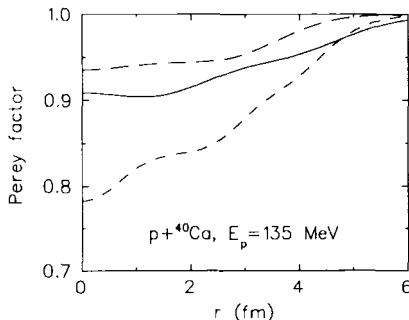
Fig. 5.7. **Comparison between nonlocality corrections for** $p+^{40}$**Ca at** $E_p = 135$ **MeV based upon the the JLM (short-dashed), PH (long-dashed), and Perey models (solid).**

Dirac–Brueckner–Hartree–Fock calculations (e.g., Refs. 226 and 227) also produce an explicit momentum dependence in the optical potential and hence reduction to local form also involves a k-mass correction. Inclusion of the scalar potential, which contributes to a Lorentz effective mass, and energy dependence of the optical potential requires a generalization of Eq. (5.33) for Dirac models, but Eq. (5.31) remains valid.[228] Unlike nonrelativistic many-body theory, m_k/m for relativistic models is slightly greater than unity.[228]

Jin and Onley[178] have argued that Perey and/or Darwin factors should be applied to the EEI model to bring its spectroscopie factors into agreement with Dirac phenomenology. However, we have shown that nonlocality corrections cannot be applied to the EEI model *a posteriori* without destroying the fit to proton inelastic scattering.[229] Inelastic scattering and knockout are similar in that both are sensitive to the interior wave function. A conventional Perey factor would reduce the ^{16}O(p, p') cross section by about 18%; the reduction for a Darwin factor would be about 33% and the reduction for both factors simultaneously is even larger. Obviously, proton inelastic scattering calculations cannot tolerate these modifications of the interior wave function. On the other hand, if nonlocality corrections are made *a priori* as part of the model, the fitting procedure modifies the interaction so that the inelastic scattering is fitted as well as before. However, the spectroscopie factor for the modified model is practically unchanged.[229] Therefore, the discrepancy between the EEI and DP models cannot be eliminated by applying nonlocality corrections to the EEI model.

The sensitivity of $(e, e'p)$ spectroscopie factors to nonlocality corrections is examined in Table 5.2 using ^{40}Ca$(e, e'p)$ in parallel kinematics, with $\varepsilon_\iota = 500$ MeV and $T_p = 135$ MeV, as before. Application of a conventional Perey factor, with $\beta = 0.85$ fm, to the Schwandt model increases its spectroscopie factors by 5–8%, with larger effects for more interior wave

TABLE 5.2

Effect of Nonlocality Corrections on Deduced Spectroscopic Factors for $^{40}Ca(e, e'p)$ in Parallel Kinematics, with $\varepsilon_i = 500$ MeV and $T_p = 135$ MeV

The second (third) column gives the correction to the absorptive potential (wave function). An entry of m_k/m in the second column indicates that the k-mass was obtained from the exchange contribution to the effective interaction. An entry of C_P^2 indicates that the k-mass was inferred from a Perey factor.

Potential	m_k/m	C	S/S_{EEI} for $1d_{3/2}$	S/S_{EEI} for $2s_{1/2}$
EEI	1.0	1.0	1.0	1.0
EEINL	C_P^2	$\beta = 0.85$ fm	1.02	1.06
Schwandt		1.0	0.95	1.00
Schwandt		$\beta = 0.85$ fm	1.03	1.05
PH	1.0	1.0	1.18	1.14
PH	m_k/m	$\sqrt{m_k/m}$	1.19	1.14
NL	1.0	1.0	0.90	1.05
NL	m_k/m	$\sqrt{m_k/m}$	0.90	1.06

functions. For the effective interactions based upon nuclear matter theory, the m_k/m corrections to the absorptive potentials and to the wave functions tend to compensate each other: smaller absorption leads to larger wave functions, but Perey damping reduces the wave function again so mat there is little change in cross sections for either knockout or inelastic scattering. Similarly, an empirical effective interaction fitted using *a priori* nonlocality corrections to both absorption and wave functions, designated EEINL,[229] gives practically the same spectroscopie factors as the original EEI without nonlocality corrections. These effects are essentially independent of kinematical arrangement — for each potential similar calculations for quasiperpendicular kinematics give practically identical ratios between corresponding spectroscopie factors that include or omit nonlocality corrections.

5.4.7. Nuclear Transparency

Due to the distribution of initial momenta, the quasifree single-nucleon knockout strength is spread over a Fermi cone whose opening angle is approximately $\theta_F = \tan^{-1} k_F/q$ and over a range of missing energies that includes the binding energy for the deepest orbital. However, final-state interactions broaden these distributions and transfer some of the flux into more complicated final states. Optical models describe this loss of flux from the initial

single-nucleon channels as absorption. Hence, nuclear transparency can be loosely defined as the ratio between the coincident *(e, e'p)* cross section and the inclusive quasifree electron scattering cross section, where the coincidence cross section is integrated over the Fermi cone and over the range of missing energy populated by direct knockout.

The appropriate weighting factors depend upon the kinematics of the experiment. The simplest situation arises when (ω, q) are held constant, for which the nuclear transparency $\mathcal{T}_\perp$ may be defined as

$$\mathcal{T}_\perp = \frac{\sum_\alpha \int d\theta \sin\theta \, \rho^D(p_m, E_\alpha)}{\sum_\alpha \int d\theta \sin\theta \, \rho^{PW}(p_m, E_\alpha)} \tag{5.38}$$

where E_α is the missing energy for orbital α, and ρ^D and ρ^{PW} are distorted and plane-wave momentum distributions for each orbital. Since the distorted momentum must be evaluated for the appropriate kinematical conditions, its dependence upon variables other than p_m remains implicit. Also note that the weight factor should be expressed in terms of the center-of-mass system, where the ejectile momentum is constant, but for large q the laboratory momentum changes little over the Fermi cone so that the distinction between the lab and cm angles matters little. Since experimental results are usually quoted in terms of laboratory momenta and angles, we use the lab angle in the weighting factor. Alternatively, for parallel kinematics we define

$$\mathcal{T}_\parallel = \frac{\sum_\alpha \int dp_m \, p_m^2 \, \rho^D(p_m, E_\alpha)}{\sum_\alpha \int dp_m \, p_m^2 \, \rho^{PW}(p_m, E_\alpha)} \tag{5.39}$$

but must recognize that the ejectile energy is correlated with p_m and again that the electron scattering kinematics remain implicit.

The first measurements of nuclear transparency for *(e,e'p)* with $150 \leq T_p \leq 210$ MeV were made by Garino *et al.*[230,231] using a 780 MeV electron beam, $\omega = 215 \pm 20$ MeV, and $q \approx 610$ MeV/c. Measurements were made for four in-plane opening angles between about 0° and 23° with $\phi = 180°$, which sample a slice through the Fermi cone for this q. The ratios

$$\mathcal{R}(\theta) = \frac{\int dE_m \, d^5\sigma(e, e'p)/dE_m d\Omega_e d\Omega_p}{d^2\sigma(e, e')/d\Omega_e} \tag{5.40}$$

integrated over a wide range of missing energy (up to about 100 MeV) were measured for ^{12}C, ^{27}Al, ^{58}Ni, and ^{181}Ta. Several methods were used to relate the measured ratios $\mathcal{R}(\theta)$ to the nuclear transparency, but the variations were less than 5%, which can be viewed as an estimate of the systematic error. From our point of view, the experimental realization of Eq. (5.38) would be

$$\mathcal{T}_\perp = \frac{\int d\theta \sin\theta \, \mathcal{R}^{DW}(\theta)}{\int d\theta \sin\theta \, \mathcal{R}^{PW}(\theta)} \tag{5.41}$$
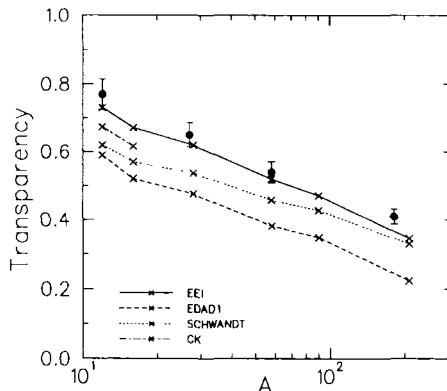
Fig. 5.8. Nuclear transparency data for $(e, e'p)$ are compared with calculations using several optical models. The data (solid points) were obtained using a 780 MeV electron beam, $\omega = 215 \pm 20$ MeV, and $q \approx 610$ MeV/c. Calculations were performed for selected closed sub-shell nuclei with mass numbers indicated by crosses. The solid line employs the EEI, dashes the EDAD1, dots the Schwandt, and dash–dots the Comfort and Karp (CK) potential.

The data for $E_m \leq 80$ **MeV** are shown in Fig. 5.8. Note that for large E_m there is evidence, discussed in Section 7.6, that multinucleon knockout contributes to the transverse response and hence may unduly increase the experimental transparency if the range of missing energy is too large. Garino *et al.* find that increasing the maximum E_m from 60 to 100 MeV increases the transparency by about 5–10% (relative).

We have studied the sensitivity of nuclear transparency to the optical model, comparing the EEI model with Dirac phenomenology, version EDAD1. Although the data extend in both energy and mass beyond their ranges of applicability, we also show calculations based upon the Schwandt and the Comfort and Karp (CK) optical potentials for comparison with other authors who have used those models. Ejectile wave functions for the Schwandt and CK potentials include Perey factors, Eq. (5.29), with $\beta = 0.85$ **fm,** while wave functions based upon Schrödinger-equivalent potentials from Dirac phenomenology include the Darwin factor, Eq. (5.25). Nonlocality corrections are not needed for the EEI model because both elastic and inelastic scattering are fitted self-consistently in that model. Bound-state wave functions were obtained using the Skyrme–Hartree–Fock model based upon the interaction designated Z_σ.[218,219] The single-particle energy spectra for each target were shifted to obtain the correct separation energies. For each orbital the final-state interactions were evaluated using ejectile energies based upon ω and the shifted Hartree–Fock separation energies. Note that the results are rather insensitive to the details of

the bound-state wave functions, but are quite sensitive to the choice of optical model. These calculations are compared with the data in Fig. 5.8. We find that the EEI model provides a good description of nuclear transparency, while considerably smaller transparencies are obtained with either the Schwandt or the EDAD1 potentials. These results are consistent with the observation in Section 5.4.4 that the EEI model provides more accurate predictions for proton absorption and neutron total cross sections also. It is clear that the EDAD1 model is too absorptive at these energies, so that spectroscopie factors using it will be artificially large to compensate for excessive attenuation.

Similar calculations have been performed by Ireland *et al.*[232] using the Schwandt potential and they obtained larger transparencies which agree better with the data than do our ostensibly similar calculations with the same potential. However, that analysis suffers from several defects. First, the kinematics were artificially altered so that knockout from every orbital was assigned the same ejectile energy, 180 Me V, despite the wide range of energies covered by the experiment. Thus, they used the Schwandt potential at 180 MeV even though, for the same electron kinematics, protons ejected from less bound orbitals actually emerged with energies beyond the range of that optical model. Second, their calculations used a scattered electron energy that is 30 MeV higher than the center of the experimental acceptance. Third, the DWIA cross section was computed using the NR2 current operator, but the distorted momentum distribution was obtained by dividing the cross section by σ_{cc1}, the cross section for the cc l current operator. (These current operators are compared in Section 5.5.) The inconsistency between the numerator and the denominator in their application of Eq. (5.9) leads to a spurious enhancement of the transparency above unity for a plane-wave calculation. However, none of these defects appears to be sufficient to explain the discrepancy between the two calculations. Nevertheless, we consider the apparent agreement between the data and the Schwandt calculations of Ref. 232 to be a fortuitous result of an incorrect calculation.

Alternatively, Pandharipande and Pieper[233] studied nuclear transparency using a correlated Glauber model in which

$$\mathcal{T} = \frac{1}{Z} \int d^3r' \, \rho_p(\mathbf{r}') P_T(\mathbf{r}') \tag{5.42a}$$

$$P_T(\mathbf{r}') = \exp\left\{ -\int_{z'}^{\infty} dz'' \left[g_{pn}(\mathbf{r}', \mathbf{r}'') \tilde{\sigma}_{pn}(q, \rho(\mathbf{r}'')) \rho_n(\mathbf{r}'') \right.\right.$$
$$\left.\left. + g_{pp}(\mathbf{r}', \mathbf{r}'') \tilde{\sigma}_{pp}(q, \rho(\mathbf{r}'')) \rho_p(\mathbf{r}'') \right] \right\} \tag{5.42b}$$

where $P_T(\mathbf{r}')$ represents the probability that a proton struck at position $\mathbf{r}'$ will emerge without rescattering, $\tilde{\sigma}_{pN}(q, \rho(\mathbf{r}''))$ represents the effective *pN* cross

section evaluated in local density approximation, and

$$g_{pN}(\mathbf{r}', \mathbf{r}'') \approx g_{pN}(\rho_0, |\mathbf{r}' - \mathbf{r}''|)$$

represents the pair distribution function evaluated at central density. Although the validity of the Glauber approximation is questionable at these energies, it is important to recognize that the EEI model includes essentially the same physics. Recall that the EEI parametrization was originally based upon Brueckner–Hartree–Fock calculations of the effective interaction in nuclear matter which include both short-range correlations and Pauli blocking, but that the parameters were adjusted to improve the fit to experimental data. The Glauber model includes Pauli blocking in its effective cross section, while the EEI model includes it as a density-dependent damping of its imaginary central interaction. Similarly, the anticorrelation between identical nucleons is represented by the pair distribution function in the correlated Glauber model or by the density-dependent short-ranged repulsion in the real central EEI interaction. Pandharipande and Pieper find that Pauli blocking, effective mass, and correlation effects all play important roles in their transparency calculations.

Phenomenological optical models, nonrelativistic or relativistic, which are fitted only to elastic scattering data may fit that data well but still fail to predict nuclear transparency correctly because such analyses are not sensitive to the interior wave function. The EEI model is much more sensitive to the interior wave function because in fitting inelastic scattering data it requires consistency between distorted waves and inelastic transition amplitudes. Therefore, the EEI model provides a more accurate prediction of nuclear transparency and should also provide more accurate spectroscopie factors. Clearly it will be of interest to obtain transparency data for a wider range of energies and such studies are planned for CEBAF. It would also be of interest to obtain comparable data at lower energies where NIKHEF has performed its extensive survey of spectroscopie factors for complex nuclei, but it appears that the lower-energy regime will soon be abandoned.

5.4.8. Ejectile Polarization

In principle, ejectile polarization can provide additional sensitivity to both the reaction mechanism of nucleon knockout and to the electromagnetic current in the medium. Although no *(e, e'N̄)* data are presently available for complex targets, we present calculations which illustrate some of the basic characteristics of ejectile polarization observables and their expected sensitivities to various aspects of the optical potential. The sensitivity of these

observables to other aspects of the reaction model will be considered in subsequent sections.

The role of various components of the nucleon optical potential is examined in Fig. 5.9, which shows the ejectile polarization components for $^{16}O(\vec{e}, e'\vec{p})$ in coplanar kinematics with constant $(\omega, q) = (148 \text{ MeV}, 521 \text{ MeV}/c)$ and a beam energy of 500 MeV. The EEI optical potential is used, electron distortion is treated in EMA, and the NR4 current is used. In the absence of distortion, the normal component P_N vanishes while the coplanar polarization transfer coefficients P'_L and P'_S have sizable values determined by the (off-shell) electron–nucleon coupling. Note that the abrupt changes in P'_S at $p_m = 0$ result from inversion of the $\hat{S}$ basis vector as $\mathbf{p}'$ moves from one side of $\mathbf{q}$ to the other and that we have arbitrarily identified positive p_m with $\mathbf{p}'$ on the large-angle side of $\mathbf{q}$ with respect to the beam axis. Also note that when electrons are detected to the left of the beam, our conventions give $\hat{N}$ upward (downward) for negative (positive) missing momenta.

Inclusion of the central potentials has very little effect on P'_L or P'_S, which remain practically indistinguishable from the plane-wave results, nor does the real central component have much effect on P_N for modest p_m, but the imaginary central potential does have an important effect on P_N. In hadronic reactions, such as $(p, 2p)$, the induced polarization due to the correlation between absorption and spin is known as the Newns polarization[234,235] or Maris effect.[236] The same effect is also present in $(e, e'\dot{N})$ (or any reaction involving an outgoing nucleon). Suppose that the proton is detected on the large-angle side of $\mathbf{q}$. For initial momenta directed toward the large-angle side of q, spin-up protons correspond to $j = l - 1/2$ on the near side or to $j = l + 1/2$ on the far side. Since nucleons originating from the near side of the nucleus will be attenuated less than those from the far side, we should expect $P_N < 0$ for $j - / - 1/2$ and $P_N > 0$ for $j = l + 1/2$. (Remember that $\hat{N}$ points down here.) Furthermore, since the net polarization summed over subshells would vanish for a closed-shell nucleus if the subshell momentum distributions were identical, we expect the Newns polarization to be approximately twice as large for $1p_{1/2}$ as for $1p_{3/2}$ and opposite in sign. These expectations are realized in the P_N curves in Fig. 5.9 obtained by elimination of the spin–orbit optical potentials, for which much of the induced polarization is then due to the absorptive potential. Finally, we note that the difference between the phase shifts accumulated by nucleons originating from the near versus far sides of the real central potential also contributes to the Newns polarization, but that this effect is relatively small for modest initial momenta.

The real part of the spin–orbit potential also has a large effect upon the ejectile polarization, including both normal and coplanar components. How-
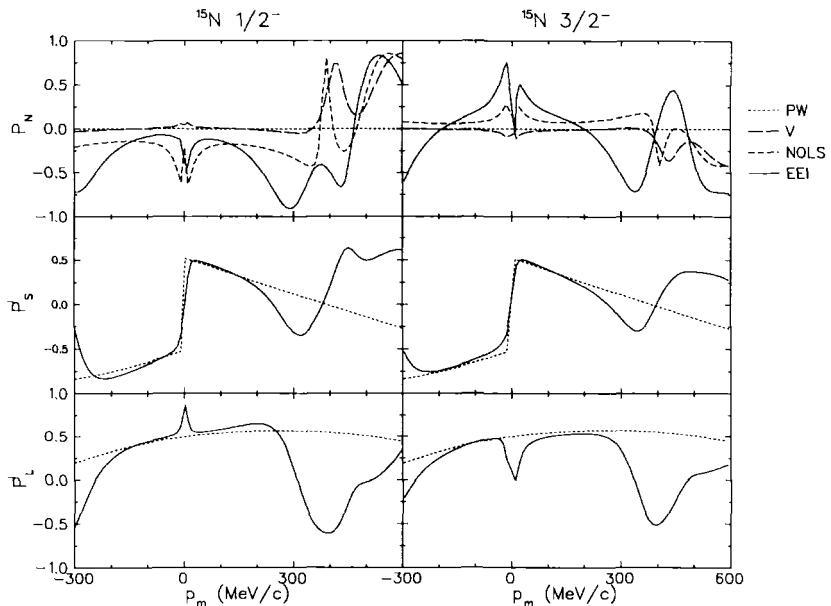
Fig. 5.9. Contributions of various components of the nucleon optical potential to ejectile polarization for $^{16}O(\vec{e}, e'\vec{p})$ **for** $(\omega, q) = $ **(148 MeV, 521 MeV/c) and** $\varepsilon_i = $ **500 MeV.** Plane-wave calculations (PW) are shown as dotted curves, inclusion of the real central potential (V) as long dashes, inclusion of both real and imaginary central potentials (NOLS) as short dashes, and the full potential (EEI) as solid curves. The V and NOLS curves for P'_S and P'_L are practically indistinguishable from PW and are omitted.

ever, the imaginary spin–orbit potential appears to be too small to measurably affect these polarization observables. In the absence of spin–orbit distortion, the polarization transfer coefficients P'_L and P'_S are practically indistinguishable from the plane-wave results; hence, those curves are omitted from Fig. 5.9. We also note that the contribution of spin–orbit distortion to the polarization transfer coefficients is very similar for both spin–orbit partners, $1p_{1/2}$ and $1p_{3/2}$.

It is also of interest to investigate the sensitivity of ejectile polarization to differences between optical models. Several models are compared in Fig. 5.10 for $^{16}O(\vec{e}, e'\vec{N})$, where $\vec{N}$ indicates a polarized nucleon, with proton knockout shown in the left and neutron knockout in the right half of the figure. The induced polarization P_N is very similar for both neutrons and protons because it is determined by distortion effects which are similar for both, while the polarization transfer coefficients are quite dif-

ferent because they are determined by the electron–nucleon coupling. The differences between various optical models are larger for P_N, which vanishes in the absence of final-state interactions, than for P'_L or P'_S, which are finite and appreciable even without FSI. However, the sensitivity of nucleon knockout to details of the optical model is relatively small for modest initial momenta, $p_m < 300$ MeV/c. Although P_N for large missing momenta appears to be sensitive to the optical model, more complicated reaction mechanisms can also be important. Channel coupling within the final-state interactions has been shown to strongly affect the ejectile polarization for large p_m[237] and will be discussed in more detail in Section 7.5. Two-body currents, discussed in Section 7.4, are also expected to be important. Furthermore, the single-particle momentum densities may not be adequately described by mean-field wave functions of the type used here. We note that the rapid variations for p_m near 400 MeV/c are associated with nodes in the Woods–Saxon $\phi(p_m)$ for which there is as yet no experimental evidence and which might be masked by short-range correlations. Therefore, measurements of ejectile polarization do not appear to offer much sensitivity to the optical potential but are expected to be sensitive to other aspects of the reaction mechanism, such as two-body currents.

5.4.9. State Dependence of the Optical Potential

Several other unresolved issues in the proper treatment of optical model distortion merit mention. First, most $(e, e'p)$ experiments have been performed upon even-even targets leaving the residual odd-even nucleus with spin in its ground state. However, optical potentials are usually fitted to elastic scattering data for the even-even target rather than for the odd-even residual nucleus since data for such targets are scarce. Furthermore, for spins greater than 1/2 the optical potential should contain terms beyond the standard central and spin–orbit potentials. Although the effect of such terms on elastic scattering of intermediate-energy nucleons has not been thoroughly delimited, it is expected to be small for the cross section and analyzing power. Larger effects could be expected for depolarization or spin-transfer coefficients. Similarly, for knockout reactions we might expect effects upon the nucleon polarization response functions.[237] Second, the optical potential should in principle depend upon the state of the residual nucleus and such state dependence could be important for deep-hole states. Perhaps one could estimate the importance of differences between optical potentials for various hole states using a folding model in which the effective interaction is folded with a density for the residual nucleus that is constructed by subtracting the contribution
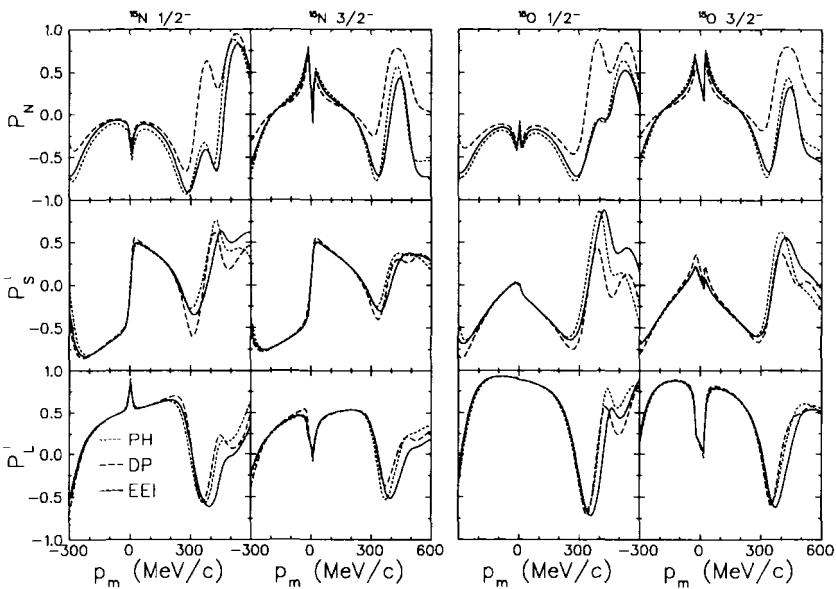
Fig. 5.10. Sensitivity of ejectile polarization for $^{16}O(\vec{e}, e'\vec{N})$ to differences between optical models. Calculations with the PH (dotted), DP (dashed), and EEI (solid) models are shown for $(\omega, q) = (148$ MeV, 521 MeV/c$)$ and $\varepsilon_i = 500$ MeV. Proton (neutron) knockout is shown in the left (right) half.

of the relevant hole, represented by a Hartree–Fock orbital, from the target density. However, a more rigorous theory would be required to include the ground-state correlations.

5.5.   Nonrelativistic Models of the Nuclear Current

In principle the electromagnetic current for a many-body system is represented by an extremely complicated operator, such that practical calculations require rather drastic approximations. Most distorted-wave calculations for finite nuclei employ nonrelativistic wave functions for the target nucleus and hence it becomes necessary to reduce the nuclear current to a nonrelativistic form. The most common procedure is based upon the Foldy–Wouthuysen transformation,[238] which provides an expansion in powers of q/M. Alternatively, the effective momentum approximation can be used to evaluate a current operator based upon an appropriate off-shell extrapolation of the free current. In this section we compare these techniques and discuss their inherent ambiguities.

5.5.1. Nonrelativistic Reduction of the One-Body Current

The nonrelativistic reduction of the nucleon current was carried to second order in the nucleon recoil velocity q/M by McVoy and van Hove[239] and applied to $^{12}C(e, e'p)$ by Boffi, Giusti, and Pacati.[240] The procedure was then extended to fourth order by Giusti and Pacati.[241] Formulas for the half off-shell electron–nucleon cross sections appropriate to these forms of the current operator may be found in Ref. 1. These nonrelativistic current operators may be designated NRn where $n = 1$–4.

The intrinsic accuracy of the nonrelativistic reduction can be assessed by comparison with the relativistic formulas for electron scattering from a free nucleon. Although there are only two independent Lorentz scalars for elastic scattering, for the present purposes it is more convenient to express the results in terms of the virtuality, Q^2, and the beam energy, E_0, for electron scattering from a nucleon initially at rest. The $N(e,e')N$ observables for kinematics typical of extant $A(e,e'p)B$ experiments are shown in Figs. 5.11 and 5.12. Note that GK3 form factors[37] were used. Figure 5.11 compares nonrelativistic approximations to the exact calculations for constant $Q^2 = 0.2$ (GeV/c)^2 as a function of beam energy. For energies above 400 MeV the second-order nonrelativistic formula gives results for σ_{ep} that are accurate to a few percent for protons or about 5% for neutrons, but the accuracy deteriorates rapidly for lower energies and can be recovered below 300 MeV only by carrying the expansion through third or higher order. At $Q^2 = 0.2$ (GeV/c)^2 the polarization converges quite quickly, already by second order, but as Q^2 increases the convergence with respect to order becomes less rapid, particularly for cross sections. This behavior is illustrated in Fig. 5.12, which shows similar calculations as functions of Q^2 for constant beam energies of $E_0 = 0.5$ GeV (left half) and $E_0 = 1.0$ GeV (right half). Note that when measurements of missing momentum distributions are made in parallel kinematics with constant E_0, Q^2 is small for large positive p_m and increases as p_m becomes increasingly negative. Thus, Fig. 5.12 demonstrates that for parallel kinematics the nonrelativistic expansion converges quite slowly for negative p_m and that the commonly used second-order formula may not be sufficiently accurate. Furthermore, although the cross section converges to within a few percent of the correct result by fourth order, significant differences remain for polarizations at large Q^2.

5.5.2. Off-Shell Kinematics

The elementary cross section for knockout reactions is off-shell because the apparent or effective mass of the constituent is not equal to its invariant
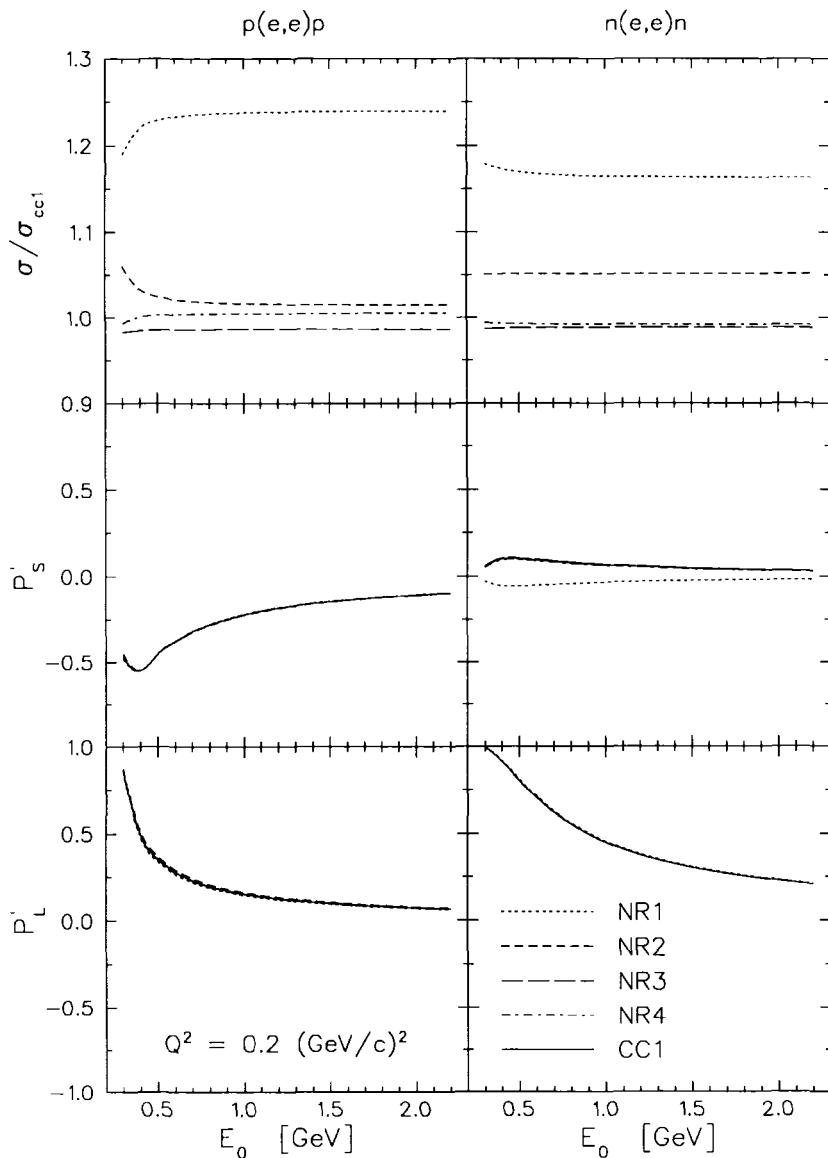
Fig. 5.11. $N(e, e')N$ observables at constant $Q^2 = 0.2$ (GeV/c)^2 as functions of the beam energy E_0 for nonrelativistic expansion of the current operator through fourth order (NR1–NR4) are compared with the relativistic formula (CC1).
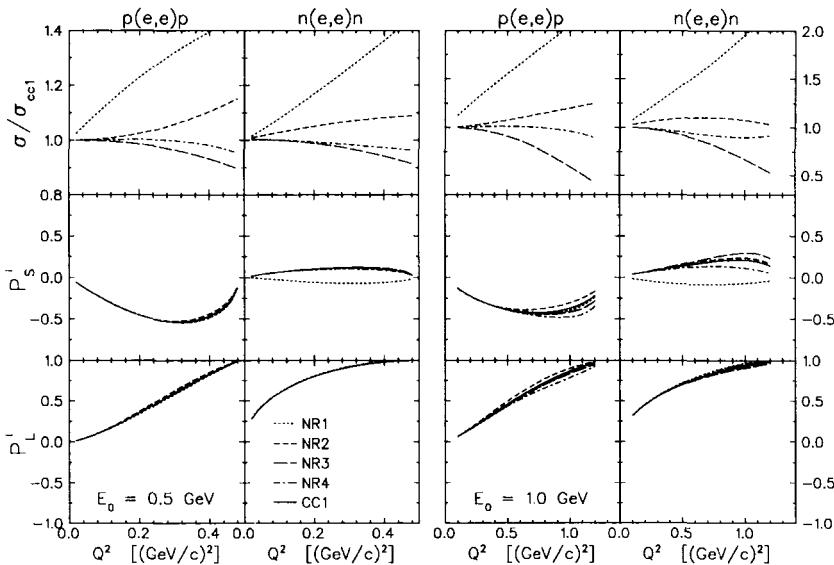
Fig. 5.12. $N(e, e')N$ observables at constant beam energy as functions of Q^2 for nonrelativistic expansion of the current operator through fourth order (NR1–NR4) are compared with the relativistic formula (CC1). The left half shows calculations for $E_0 = 0.5$ GeV and the right $E_0 = 1.0$ GeV as functions of Q^2.

rest mass due to its Fermi motion and the separation energy with respect to the residual nucleus. Let W represent the effective mass of the off-shell constituent and E represent the on-shell energy for a particle of mass m_x and momentum **p,** such that

$$W^2 = (\varepsilon_x - \omega)^2 - (\mathbf{p}_x - \mathbf{q})^2$$
$$\bar{E}^2 = E^2 + m_x^2 - W^2$$

A useful measure of the distance off shell is provided by the quantity

$$\Delta\omega = \omega - \bar{\omega} = \bar{E} - E \qquad (5.43)$$

where

$$\bar{\omega} = \varepsilon_x - \bar{E} = \varepsilon_x - (\mathbf{p}^2 + m_x^2)^{1/2} \qquad (5.44)$$

would have been the energy transfer on shell. Alternatively, we define the mass defect as

$$\Delta m = m_x - W \qquad (5.45)$$

and note that the ratio

$$\frac{\Delta m}{\Delta \omega} = \frac{E + \bar{E}}{m_x + W}$$

is close to unity. Upon substitution for E we find

$$\Delta \omega = \bar{E} + \varepsilon_B - m_A \qquad (5.46)$$

Hence, since $\bar{E} \geq m_x$ and $\varepsilon_B \geq m_B,$ we find that

$$\Delta \omega \geq E_m \geq 0$$

for stable states of the target. Therefore, the initial energy and effective mass for a bound constituent are always less than their on-shell values. Furthermore, the greater the initial momentum or the larger the separation energy, the further off-shell is the PWIA vertex.

For modest momenta and heavy targets, we may approximate $\Delta \omega$ and Δm by

$$\Delta \omega \approx \Delta m \approx \frac{\mathbf{p}^2}{2m_x} + E_m \qquad (5.47)$$

and interpret the first term as the initial kinetic energy and the second as the average potential energy.* Hence, for knockout from a valence orbital at the peak of its momentum distribution with $p_m \approx 100$ MeV/c and $E_m \approx 15$ Me V, we find $\Delta \omega \approx 20$ MeV. Thus, off-shell ambiguities will probably not be too important for such cases. By contrast, for a high-momentum component $p_m \approx 2k_F$ with binding energy $E_m \approx 50$ MeV, we find $\Delta \omega \approx 200$ MeV and might expect the details of off-shell extrapolation to become more critical.

The analysis above is based upon asymptotic kinematics for the projectile and ejectiles. However, interaction of these particles with the mean field of the nucleus alters these kinematics. The influence of the attractive Coulomb interaction with the electron can be described by an effective local momentum transfer that is greater than the asymptotic momentum transfer. Similarly, the ejected nucleon experiences a net attraction which increases its momentum in the interaction region. A quantitative description of these effects requires a distorted-wave analysis, including both nucleon and electron distortions, but for nonrelativistic models we may describe the effects qualitatively as an averaging over a relatively narrow range of momenta and a shift of the

---

*Note that for light targets we must retain the kinetic energy of the residual nucleus also, such that

$$\Delta \omega \approx \Delta m \approx E_m + \frac{\mathbf{p}^2}{2m_x} \frac{m_A}{m_B}$$

kinematics from asymptotic to local values. The shift should be averaged over the nuclear volume using a local-energy prescription, but the net effect is to move the photon–nucleon vertex even further off-shell. These effects are much more important for relativistic models in which the strong Dirac scalar and vector potentials alter the effective mass and distort the spinors in the nuclear medium.

5.5.3. Off-Shell Extrapolation of the Nucleon Current

The ambiguities inherent in applying to knockout reactions free nucleon cross sections, which at best are only known on shell, become evident upon consideration of the three kinematic invariants which may be conveniently chosen as $s = p \cdot k$, $t = Q^2$, and $u = p' \cdot k'$, where k and k' are initial and final electron four-momenta while p and p' are initial and final nucleon four-momenta. For elastic scattering the mass-shell constraint requires $s = u$, but for quasielastic scattering this relationship no longer pertains. Hence, the free current can be described in terms of two independent invariants but the current for bound nucleons requires three. In the absence of a dynamical model, the reduction of the number of invariants can only be made on the basis of more or less *ad hoc* assumptions concerning the γN vertex.

A variety of off-shell extrapolations has been made by altering one of the kinematic invariants within otherwise free forms of the nucleon current operator. Since the ejectile kinematics are not observed prior to knockout, it is customary to modify the s invariant. Initial-state prescriptions are obtained from the replacement $s \to \bar{p} \cdot k$ where $\bar{p} = (\bar{E}, \mathbf{p})$ with $\bar{p}^2 = m^2$ chosen so mat the nucleon is on-shell for its modified energy. Final-state prescriptions are obtained from the replacement $s \to u$. Intermediate prescriptions are obtained by the replacement $s \to (\bar{p} \cdot k + p' \cdot k')/2$. Alternatively, effective mass prescriptions can be obtained by replacing the Dirac spinor for the initial nucleon with the spinor appropriate to a Dirac particle with effective mass W while maintaining the original F_1 and F_2 form factors.[242] A similar effective mass prescription has also been proposed by Mulders.[4] Within each of these strategies several different variations can be constructed depending upon which form of the nucleon current is employed and whether the continuity equation is enforced.

The ambiguities among the aforementioned prescriptions have been reviewed by de Forest[18] and by Frullani and Mougey.[1] It is found that the initial- and final-state prescriptions produce off-shell cross sections which are considerably different both from the on-shell results and from each other, while the intermediate and effective mass prescriptions produce smaller off-

shell variations and agree with each other to within a few percent for quasielas-
tic kinematics in the kinematic regime relevant to experimental studies of the
spectral function. However, these prescriptions give divergent results in the
vicinity of the photon point because current conservation is not enforced prop-
erly.

Several prescriptions which enforce current conservation at the one-body
level were proposed by de Forest[18] and are denoted by cc1 or cc2. These
prescriptions are based upon representations of the free current operator, Eq.
(2.71) for the cc1 or Eq. (2.70) for the cc2 prescription, which are equivalent
on-shell by virtue of the Gordon identity. A third variation, also Gordon-
equivalent on shell, was suggested by Chinn and Picklesimer.[243] Thus, each
of the following vertex operators

$$\Gamma_1^\mu = \gamma^\mu G_M(Q^2) - \frac{P^\mu}{2M}\kappa F_2(Q^2) \tag{5.48a}$$

$$\Gamma_2^\mu = \gamma^\mu F_1(Q^2) + i\sigma^{\mu\nu}\frac{q_\nu}{2M}\kappa F_2(Q^2) \tag{5.48b}$$

$$\Gamma_3^\mu = \frac{P^\mu}{2M}F_1(Q^2) + i\sigma^{\mu\nu}\frac{q_\nu}{2M}G_M(Q^2) \tag{5.48c}$$

gives identical results for elastic scattering from a moving but free nucleon.
The de Forest prescription for extrapolation of these operators off-shell etn-
ploys free spinors for momentum p and mass m, but replaces the energy
E used within the vertex function by the value E it would have had if the
nucleon were on-shell in the initial state. Thus, the off-shell extrapolation is
obtained by replacing the energy transfer and the momenta by

$$q = (\omega, \mathbf{q}) \longrightarrow \bar{q} = (\bar{\omega}, \mathbf{q})$$
$$P = p' + p \longrightarrow \bar{P} = (E' + \bar{E}, \mathbf{p}' + \mathbf{p})$$

in the nucleon current operator. However, the form factors are still evaluated
at the asymptotic momentum transfer, Q^2 rather than $\bar{Q}^2$. Therefore, we
obtain the alternative prescriptions

$$\bar{\Gamma}_1^\mu = \gamma^\mu G_M(Q^2) - \frac{\bar{P}^\mu}{2M}\kappa F_2(Q^2) \tag{5.49a}$$

$$\bar{\Gamma}_2^\mu = \gamma^\mu F_1(Q^2) + i\sigma^{\mu\nu}\frac{\bar{q}_\nu}{2M}\kappa F_2(Q^2) \tag{5.49b}$$

$$\bar{\Gamma}_3^\mu = \frac{\bar{P}^\mu}{2M}F_1(Q^2) + i\sigma^{\mu\nu}\frac{\bar{q}_\nu}{2M}G_M(Q^2) \tag{5.49c}$$

Finally, since none of these models explicitly conserves the electromagnetic
current, current conservation is restored in an *ad hoc* marmer by eliminating

the longitudinal current in favor of the charge using the Siegert theorem

$$J_q \longrightarrow \frac{\omega}{q}\rho$$

Thus, the cc1, cc2, and cc3 current operators are obtained from the $\bar{\Gamma}_1$, $\bar{\Gamma}_2$, and $\bar{\Gamma}_3$ vertex functions by elimination of their longitudinal parts.

It is instructive to examine the in-plane response functions produced by these vertex functions. Since both cc1 and cc2 give virtually identical results within the relevant range of kinematics, and because its formulas are simpler, the cc1 prescription has become the most commonly used for the analysis of experimental data. Thus, it suffices to consider the cc1 prescription in which the unpolarized in-plane response functions from Eq. (2.72) now become[18]

$$R_L = \frac{(\bar{E}+E')^2}{4m^2}\bar{W}_1 - \frac{\mathbf{q}^2}{4m^2}W_2 \tag{5 50a}$$

$$R_T = 2\bar{\tau}W_2 + \frac{\mathbf{p}_f^2 \sin^2\theta_{pq}}{m^2}\bar{W}_1 \tag{5.50b}$$

$$R_{LT} = -\frac{(\bar{E}+E')p'\sin\theta_{pq}}{m^2}\bar{W}_1 \tag{5.50c}$$

$$R_{TT} = \frac{p'^2 \sin^2\theta_{pq}}{m^2}\bar{W}_1 \tag{5.50d}$$

when the initial energy is placed on-shell. These expressions involve modified forms of the basic nucleon response functions

$$\bar{W}_1 = F_1^2 + \bar{\tau}(\kappa F_2)^2 \quad \text{and} \quad W_2 = (F_1 + \kappa F_2)^2$$

where

$$\bar{\tau} = \frac{\bar{Q}^2}{4m^2}$$

is evaluated with modified kinematics. We can express $\bar{W}_1$ and W_2 in terms of the on-shell Sachs form factors

$$\bar{W}_1 = \frac{G_E^2 + \tau G_M^2}{1+\tau} + (\bar{\tau}-\tau)\left(\frac{G_M - G_E}{1+\tau}\right)^2 \quad \text{and} \quad W_2 = G_M^2$$

where the difference between on- and off-shell response functions is isolated in the contribution to $\bar{W}_1$ that is proportional to the difference between on- and off-shell values of τ. This term evidently represent a convection current associated with the initial velocity of the struck particle. Therefore, we can

separate σ_{eN}^{cc1} into a part σ_{eN} due to an on-shell nucleon and a part $\Delta\sigma_{eN}^{cc1}$ due to the off-shell kinematics as follows:

$$\sigma_{eN}^{cc1} = \sigma_{eN} + \Delta\sigma_{eN}^{cc1}$$

$$\sigma_{eN} = \sigma_M \frac{m^2}{2\bar{E}E'}\left[V_1\bar{W}_1 + \bar{V}_2 W_2\right]$$

$$\Delta\sigma_{eN} = \sigma_M \frac{m^2}{2\bar{E}E'}\left[V_1\Delta W_1 + W_2\Delta V_2\right]$$

$$W_1 = \frac{G_E^2 + \tau G_M^2}{1 + \tau}$$

$$\Delta W_1 = (\bar{\tau} - \tau)(\kappa F_2)^2$$

$$\bar{V}_2 = \frac{\bar{Q}^2}{m^2}\tan^2\frac{\theta}{2}$$

$$\Delta V_2 = 2(\bar{\tau} - \tau)\frac{Q^2}{\mathbf{q}^2}$$

5.5.4. Comparison between Nonrelativistic and Relativistic Current Operators

To assess the sensitivity of nucleon knockout calculations to differences between relativistic and nonrelativistic models of the current operator, the elementary electron–nucleon cross sections, σ_{eN}, and response functions, R_α^{eN}, can be compared using the kinematics of quasifree knockout. Elementary cross sections are compared using the kinematics of $^{40}Ca(e,e'N)2s_{1/2}^{-1}$ with $\varepsilon_i = 500$ MeV and $T_N = 135$ MeV in Fig. 5.13. For quasiperpendicular kinematics, $(\omega, q) \approx (145\text{ MeV}, 521\text{ MeV}/c)$ with $-28° < \theta_{qN} < 28°$ for $-250 < p_m < 250$ MeV/c, while for parallel kinematics $584 > Q^2 > 49$ $(\text{MeV}/c)^2$ over the same range of initial momenta. The nonrelativistic expansion, designated NRn with $n = 1$–4, is compared with the de Forest cc 1 prescription. Note that the longitudinal current was eliminated in favor of the charge for the NRn calculations also. First-order calculations (NR1) are obviously inadequate, but by second order NR2 differs from cc1 by less than 5% for small initial momenta. For parallel kinematics with p_m near -250 MeV/c, where Q^2 is relatively large, deviations approach 15% in second order, but are reduced to about 5% by fourth order. However, for neutron knockout significant differences between the relativistic and nonrelativistic models are also observed in parallel kinematics for large positive initial momenta where Q^2 is small. For proton knockout in quasiperpendicular kinematics, the fourth-order formula gives good agreement with cc1 over this range of angles, but for neutron knockout residual differences of up to 8% remain.
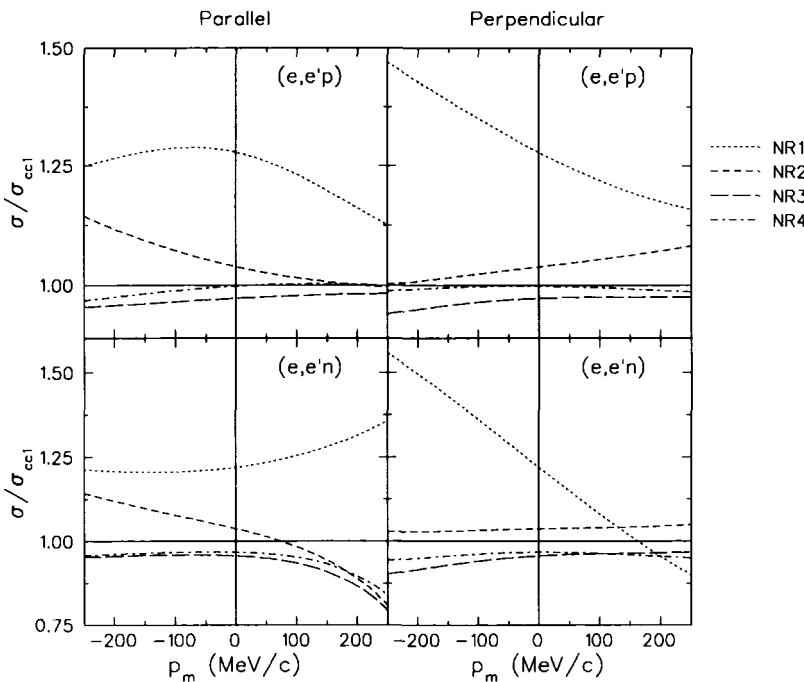
Fig. 5.13. Comparison between σ_{eN} from nonrelativistic expansion of the current operator through fourth order (NR4) with the de Forest ccl prescription using kinematics for $^{40}Ca(e, e'N)2s_{1/2}^{-1}$ with $\varepsilon_i = 500$ MeV and $T_N = 135$ MeV.

Response functions for parallel kinematics are compared in Fig. 5.14. Good agreement is obtained for $(e, e'p)$, although R_L/R_T is slightly larger for NR4 than for ccl. Larger differences are obtained for $(e, e'n)$, where R_T for NR4 is appreciably smaller, particularly for small Q^2. A similar discrepancy is obtained for $(e, e'p)$, but there R_L is slightly larger so that the two models give practically the same cross sections. However, for $(e, e'n)R_L$ is also substantially smaller for NR4 than for ccl and would be too small to compensate the cross section anyway.

Response functions for quasiperpendicular kinematics are compared in Fig. 5.15. (Note the suppressed zeros for R_L and R_T.) The relationship between the two models of R_L and R_T for these conditions is essentially the same as for parallel kinematics with $p_m = 0$. For R_{LT} we find that the second order NR calculations are already in good agreement with ccl, but for R_{TT} it is necessary to go to at least third order to obtain good agreement for $(e, e'n)$.
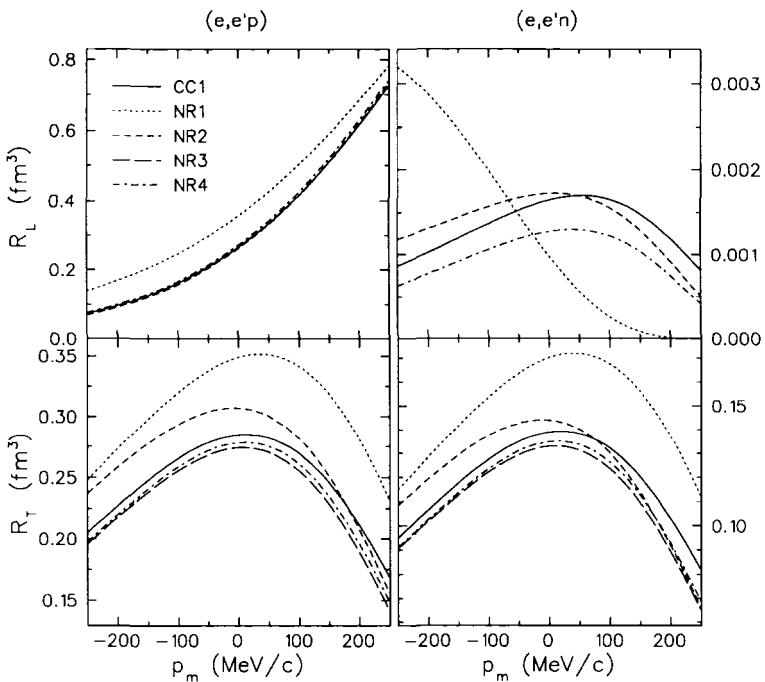
Fig. 5.14. Comparison between the elementary response functions, R_α^{eN}, from nonrelativistic expansion of the current operator through fourth order (NR4) with the de Forest cc1 prescription using parallel kinematics for $^{40}\text{Ca}(e, e'N)2s_{1/2}^{-1}$ with $\varepsilon_i = 500$ MeV and $T_N = 135$ MeV.

Similar comparisons between cc1 and cc2 are shown in Fig. 5.16. We note that the two models are identical for R_L and R_T in parallel kinematics, but for R_T in quasiperpendicular kinematics there is a small difference which increases with opening angle. Substantial differences between cc1 and cc2 are obtained for R_{TT}, but cc 1 remains close to NR4.

The sensitivity of unpolarized coplanar response functions for $^{16}\text{O}(e, e'N)$ to differences between relativistic and nonrelativistic vertex functions is examined in Fig. 5.17. Calculations comparing the fourth-order nonrelativistic operator (NR4) with the cc1, cc2, and cc3 prescriptions are shown for constant $(\omega, q) = (148 \text{ MeV}, 521 \text{ MeV}/c)$ and a beam energy of 500 MeV. The EEI optical potential is used and electron distortion is treated in EMA. The relativistic models give the same results for R_L and R_T and very nearly the same results for R_{LT}, but differences begin to become apparent for R_{TT}. Although these models are identical for a moving but free nucleon, off-shell
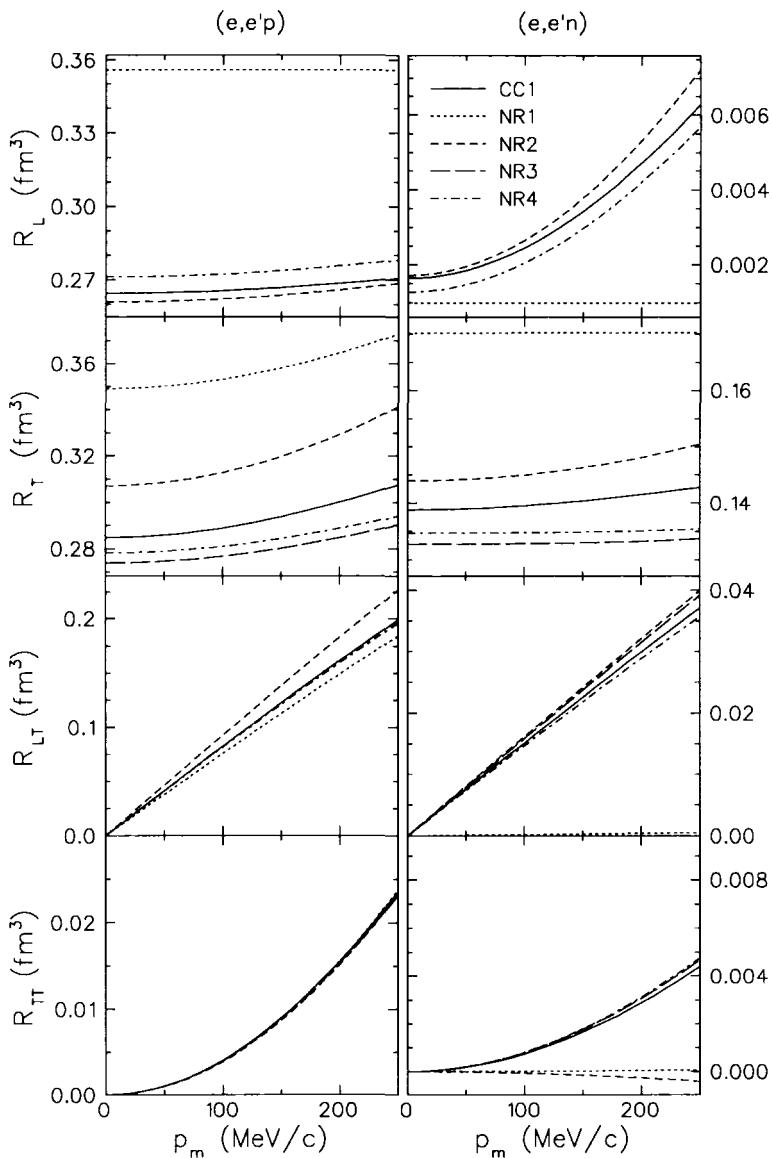
Fig. 5.15. Comparison between elementary response functions, R_α^{eN}, from nonrelativistic expansion of the current operator through fourth order (NR4) with the de Forest cc1 prescription using quasiperpendicular kinematics for $^{40}Ca(e, e'N)2s_{1/2}^{-1}$ with $\epsilon_i = 500$ MeV and $T_N = 135$ MeV.
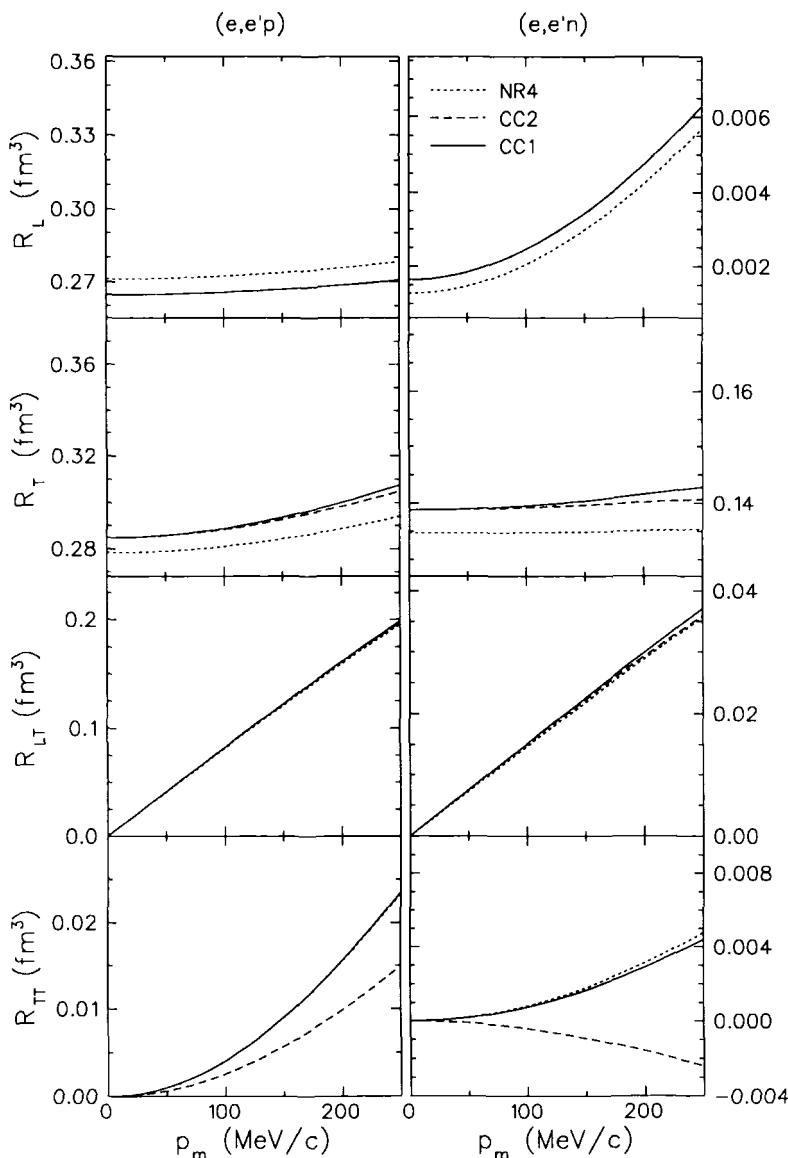
Fig. 5.16. Comparison between elementary response functions, R_α^{eN}, for the de Forest cc1 (solid) and cc2 (dashed) prescriptions using quasiperpendicular kinematics for $^{40}Ca(e, e'N)2s_{1/2}^{-1}$ with $\varepsilon_i = 500$ MeV and $T_N = 135$ MeV. The NR4 model (dotted) is also included for comparison.
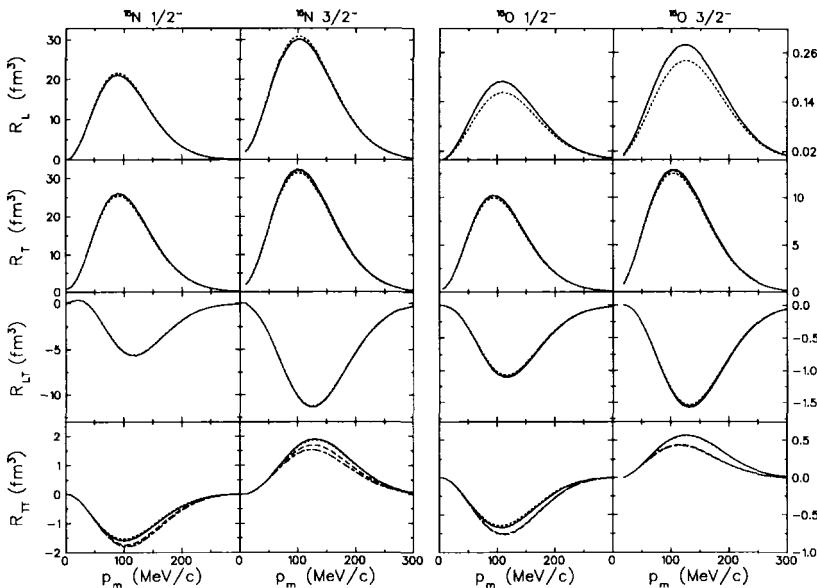
Fig. 5.17. Sensitivity of unpolarized coplanar response functions for $^{16}O(e, e'N)$ to variations of the current operator. Calculations are shown for $(\omega, q) = (148 \text{ MeV}, 521 \text{ MeV}/c)$ and $\varepsilon_i = 500$ MeV. Proton (neutron) knockout is shown in the left (right) half. The fourth-order nonrelativistic operator NR4 is shown by dotted lines, cc1 by solid lines, cc2 by dashed lines, and cc3 by dash–dotted lines.

differences in their spin–orbit couplings produce opposite effects in R_{TT} for the two spin–orbit partners. These effects are similar for both neutron and proton knockout, but will be very difficult to observe for either reaction. Thus, the differences between the elementary response functions seen in Fig. 5.16 are muted when embedded in a nucleus. Similarly, the differences in R_{TT} between NR4 and these relativistic models also involve spin–orbit coupling but are relatively small. The NR4 model for neutron knockout gives significantly smaller R_L, but that effect will be masked by charge exchange contributions in the final state. Finally we note that ejectile polarizations measurable in coplanar kinematics with modest missing momenta do not distinguish between these models either.

Chinn and Picklesimei[243] also investigated the sensitivity of RDWIA calculations to the choice of current operator, comparing Γ_2, Γ_3, and $\bar{\Gamma}_1$. Although the standard restoration of current conservation was employed, their implementation differed from the de Forest prescription in that the spinors were distorted in the medium. For inclusive quasielastic scattering, rather

large variations were obtained for both the longitudinal and transverse response functions, although there was relatively little change in the Coulomb sum rule. For $(e, e'p)$, Γ_2 and $\bar{\Gamma}_1$ gave similar results for most response functions, but Γ_3 was often quite different. The variations were generally smaller for $(e, e'p)$ than for quasielastic (e,e'), but remain considerably larger than obtained in comparable nonrelativistic calculations. Due to the largeness of the Dirac scalar and vector potentials, relativistic calculations are usually more sensitive to ambiguities of the DWIA model than similar nonrelativistic calculations.

5.5.5. *The Off-Shell Vertex*

The apparent agreement between various off-shell prescriptions at the level of a few percent in cross section does not ensure that ambiguities in the current operator have been brought under control — we must consider the choice of vertex function more carefully. The most general covariant form of the electromagnetic vertex operator,

$$
\begin{aligned}
\Gamma^\mu(p', p) = {} & \Lambda_+(p') \left[F_1^{++}\gamma^\mu + F_2^{++}\Sigma^\mu + F_3^{++}q^\mu \right] \Lambda_+(p) \\
& + \Lambda_+(p') \left[F_1^{+-}\gamma^\mu + F_2^{+-}\Sigma^\mu + F_3^{+-}q^\mu \right] \Lambda_-(p) \\
& + \Lambda_-(p') \left[F_1^{-+}\gamma^\mu + F_2^{-+}\Sigma^\mu + F_3^{-+}q^\mu \right] \Lambda_+(p) \\
& + \Lambda_-(p') \left[F_1^{--}\gamma^\mu + F_2^{--}\Sigma^\mu + F_3^{--}q^\mu \right] \Lambda_-(p) \quad (5.51)
\end{aligned}
$$

where

$$
\Sigma^\mu = i\sigma^{\mu\nu}\frac{q_\nu}{2M} \quad \text{and} \quad \Lambda_\pm(p) = \frac{W \pm \not{p}}{2W}
$$

can be expressed in terms of 12 linearly independent functions, $F_i^{\pm,\pm}(Q^2, W, W')$, of the photon virtuality, Q^2, and the off-shell invariant masses in the initial and final states, W and W', respectively. Although the Ward–Takahashi identity, representing gauge invariance, imposes several constraints among the form factors, Naus *et al.*[244] demonstrated that the half off-shell vertex function still contains six operators with four independent form factors, each of which depends upon two Lorentz scalars. Therefore, limitation of the vertex function to only two form factors depending upon only a single kinematic variable represents a rather severe truncation which can only be justified on the basis of a theory of the underlying dynamics of the off-shell γN vertex.

In the absence of definitive contrary information, most calculations assume that $F_i^{++} = F_i^{+-} = F_i^{-+} = F_i^{--}$ and omit the $F_3^{\pm\pm}$ terms. Unfortunately, there does not yet exist a calculable microscopic model of nucleon structure which predicts the general off-shell behavior of the form factors and which

fits the free nucleon data. Naus *et al.* used a simple one-pion loop model to estimate the relative importance of off-shell ambiguities by rescaling the nucleon form factors according to the ratio of model form factors off-shell versus on-shell. The results indicate that substantial ambiguities could exist, but more realistic models are needed. The one-meson loop model was extended by Song *et al.*[245] to include kaons and an expansion of the form factors in terms of the relative deviation of the effective mass W from the free mass was developed. The expansion was expressed in terms of Dirac scalar and vector potentials and the model was applied to inclusive quasielastic scattering. Substantial off-shell effects were predicted by the model, but limited improvement of the agreement with experiment was achieved.

Using vector meson dominance (VMD) models, Tiemeijer and Tjon[246] find much smaller ambiguities in the relevant kinematical regime. However their applications were to the deuteron, where distortion of the spinors is relatively mild. In a large system, the Dirac scalar and vector potentials produce strong medium modifications of the spinors which strongly affect matrix elements of the current operator (see Section 5.7). Therefore, calculations for the deuteron probably understate the off-shell ambiguities that would be encountered in larger systems.

5.5.6. Current Conservation

There is little *a priori* justification for eliminating J_q rather than ρ. If current were conserved by the impulse approximation, then either procedure would give the same results. In fact, there is no fundamental justification for enforcing current conservation in the impulse approximation on the level of the one-body current alone. Current conservation must include many-body currents. For example, with the $\bar{\Gamma}_2$ form of the vertex function, the violation of the continuity equation becomes[244]

$$q \cdot J = F_1(Q^2)(\bar{\omega} - \omega)\bar{u}_f \gamma_0 u_i \qquad (5.52)$$

and hence by itself the one-body current fails to satisfy current conservation by an amount that is proportional to the off-shell energy difference. The remainder is contributed by many-body currents associated with the interactions which establish the mean field and the binding energy and which are responsible for the difference between the effective mass and the rest mass of the struck particle. The mean field restores energy conservation but is subverted by the de Forest prescription.

To assess the ambiguities associated with various prescriptions for restoring current conservation, Fig. 5.18 compares cross sections for $^{16}O(e, e'N)$

$1p_{1/2}^{-1}$ at $T_p = 135$ MeV obtained without enforcing current conservation (dashed), elimination of J_0 (dotted), with the standard cc1 prescription for elimination of J_q (solid). The $\bar{\Gamma}_1$ current operator was used in the effective momentum approximation. NRDWIA calculations based upon the EEI potential were performed without electron distortion; a similar analysis for RDWIA calculations of $(e, e'p)$ in quasiperpendicular kinematics has been presented by Picklesimer et al.[9] For parallel kinematics we find that variations of R_L for $(e, e'p)$ can produce substantial ambiguities for large positive p_m, which correspond to forward electron scattering angles emphasizing R_L and to small momentum transfers emphasizing orthogonality defects. Elimination of J_0 instead of J_q reduces the cross section under these conditions by as much as 50%, while failure to enforce current conservation at all enhances the cross section by about 25% for the same kinematics. The effects upon $(e, e'n)$ for parallel kinematics are much smaller because R_L is almost negligible. For quasiperpendicular kinematics, elimination of J_0 instead of J_q again leads to a substantial reduction of the $(e, e'p)$ cross section with a much smaller difference between the standard cc1 prescription and omission of current conservation. However, elimination of J_0 instead of J_q produces dramatic changes in R_{LT} and hence in the cross section for $(e, e'n)$. Note that for each of these reactions, the variations in recoil polarization are non-negligible but less dramatic.

5.6. Electron Distortion

The dominant effects of Coulomb distortion upon the electron wave functions are most simply described using the local momentum or q-effective approximation.[247] In this approximation, the asymptotic momenta k are replaced by local momenta $\bar{k}$ accelerated by the mean electrostatic potential, such that

$$\bar{\mathbf{k}} = \mathbf{k} + f_Z \frac{\alpha Z}{R_Z} \hat{\mathbf{k}} \tag{5.53}$$

where $f_Z = 1.5$ corresponds to the electrostatic potential at the center of a uniformly charged sphere of radius R_Z. The local or effective momentum transfer

$$\bar{\mathbf{q}} = \bar{\mathbf{k}}_i - \bar{\mathbf{k}}_f = \mathbf{q} + \frac{f_Z}{E_i}(\mathbf{q} - \omega \hat{\mathbf{k}}_f) \tag{5.54}$$

is thus increased in magnitude and altered slightly in direction. The flux is also increased in the interaction zone by the focussing of the electron wave
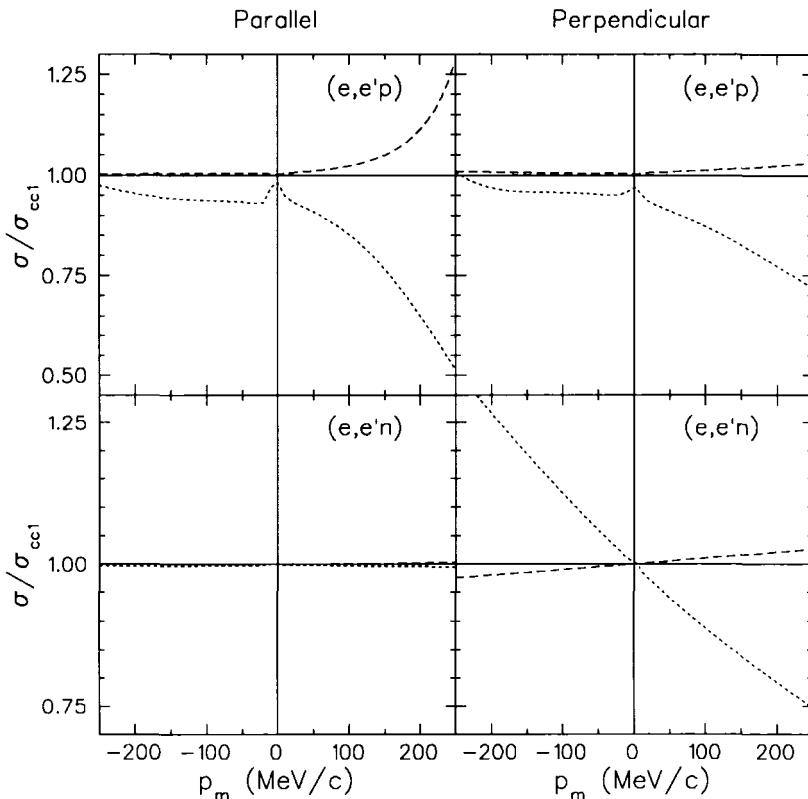
Fig. 5.18. Sensitivity of $^{16}O(e, e'N)1p_{1/2}^{-1}$ to prescriptions for current conservation. Calculations are shown for parallel kinematics with $T_p = 135$ MeV in the left column and for quasiperpendicular kinematics with $(\omega, q) = (148$ MeV, 521 MeV/$c)$ in the right column. The beam energy is $\varepsilon_i = 500$ MeV, but electron distortion is omitted. The $\bar{\Gamma}_1$ current operator is used and the cross sections are compared with the cc1 prescription. Dashed lines do not enforce current conservation, while dotted lines arise from elimination of J_0 instead of J_q.

so that the plane wave becomes

$$e^{i\mathbf{k}\cdot\mathbf{r}} \rightarrow \frac{\bar{k}}{k} e^{i\mathbf{k}\cdot\mathbf{r}} \tag{5.55}$$

In parallel kinematics the term in Eq. (5.54) that is proportional to ω is usually small and we find that Coulomb distortion shifts the apparent momentum distribution toward positive missing momentum p_m by an amount proportional to q. (Note that q decreases in the direction of positive p_m.) In quasiperpendicular kinematics, the term proportional to ω dominates and the Coulomb shift is smaller.

These effects can be described more systematically using a high-energy approximation due Lenz and Rosenfelder.[248] Two expansions are involved, one in powers of $|V/k| \ll 1$ and another in powers of $Z\alpha$. An expansion valid to first order in $Z\alpha$ was derived by Knoll[249] and applied to knockout by Giusti and Pacati.[250] The incoming $(-)$ and outgoing $(+)$ distorted electron waves are approximated by

$$\chi_h^\pm \approx e^{\pm\delta_{1/2}} \frac{\bar{k}}{k} e^{i\mathbf{k}\cdot\mathbf{r}} \left\{ 1 + ar^2(1 + i\bar{\mathbf{k}}\cdot\mathbf{r}) \right.$$
$$\left. \pm ib[(\bar{\mathbf{k}}\otimes\mathbf{r})^2 + 2i\bar{\mathbf{k}}\cdot\mathbf{r} - \boldsymbol{\sigma}\cdot\bar{\mathbf{k}}\otimes\mathbf{r}] \right\} u_h \tag{5.56}$$

where u_h is the Pauli spinor for helicity h and where the parameters are

$$\delta_{1/2} = Z\alpha(\frac{4}{3} - \ln 2kR_Z) + b \tag{5.57a}$$

$$a = -\frac{Z\alpha}{6\bar{k}R_Z^3} \tag{5.57b}$$

$$b = -\frac{3Z\alpha}{4\bar{k}^2 R_Z^2} \tag{5.57c}$$

The dominant focussing effect is found to be due to the term $ib(\bar{\mathbf{k}}\otimes\mathbf{r})^2$, which gives an energy-independent contribution that prevents the DWIA from approaching PWIA even in the high-energy limit.

For lead, $Z\alpha$ is not small and the focussing effect can be quite large. It then becomes necessary to carry the expansion to higher order in $Z\alpha$. However, since the higher-order terms become cumbersome and because the $ib(\bar{\mathbf{k}}\otimes\mathbf{r})^2$ term tends to dominate, Giusti and Pacati[29] investigated the convergence of the eikonal approximation using a schematic expansion of the form

$$\sum_n \frac{(ib)^n}{n!} (\bar{\mathbf{k}}\otimes\mathbf{r})^{2n}$$

to perform sample calculations for knockout of a $3s_{1/2}$ hole from ^{208}Pb using $E_i = 410$ MeV and $T_p = 100$ MeV. In parallel kinematics the Coulomb shift is large and is already well described in first order, while the shift is much smaller in perpendicular kinematics. The focussing effect, however, is more problematical. The first-order effect gives a very large enhancement of the cross section, much of which is then lost in second order. The q-effective approximation without focussing is closer to the second-order result than the first-order calculation, suggesting that the focussing effect is overestimated. This alternating behavior continues to higher order, but since the approximation itself was truncated it is difficult to claim convergence even at this level. The second-order calculation has clearly not converged. Ambiguities in Coulomb distortion are amplified further when attempting to separate the response functions for heavy targets.

Jin et al.[251] have compared the effective momentum approximation with relativistic calculations which treat electron distortion exactly. Using effective kinematical variables and a modified off-shell cross section,

$$\sigma_{EMA}^{cc1} = \left(\frac{\bar{k}_i}{k_i}\right)^2 \sigma_{cc1}(\bar{k}_i, \bar{k}_f, \mathbf{p}', E) \qquad (5.58)$$

where p′ is the asymptotic ejectile momentum and E is the asymptotic missing energy. Note that the nucleon form factors are also evaluated at the effective momentum transfer. The distorted momentum distribution is then

$$\rho^D(\bar{\mathbf{p}}_m, \mathbf{p}') = \frac{\sigma_0}{K\sigma_{EMA}^{cc1}} \qquad (5.59)$$

where $\bar{\mathbf{p}}_m = \mathbf{p}' - \bar{\mathbf{q}}$ is the effective missing momentum. Jin et al.[251] demonstrated that this prescription produces distorted momentum distributions for ^{208}Pb$(e, e'p)$ in parallel kinematics that are very nearly independent of electron energy, at least over the range 300–525 MeV, while omission of electron distortion results in substantial shifts with respect to electron energy. However, there remains a residual shift of approximately $0.6\alpha Z/R_Z$ toward smaller missing momentum when compared with calculations omitting electron distortion due to the aforementioned effects which do not vanish in the high-energy limit.

Unfortunately, the intuitively appealing decomposition of $(\vec{e}, e'\vec{N})$ in terms of 18 response functions for one-photon exchange is no longer valid when electron wave functions are distorted. Nevertheless, it is often useful to extract effective response functions from experimental data or from theoretical calculations using the same procedures that apply to one-photon exchange. For example, one could define an effective R_{LT} response function in terms

of left–right differences between measurements or calculations according to the prescription

$$R_{LT}^{\text{eff}} = \frac{\sigma(\phi = 0) - \sigma(\phi = \pi)}{2KV_{LT}\sigma_M}$$

where $\sigma(\phi)$ describes the azimuthal dependence of the differential cross section for fixed ω, q, and θ_{pq}. In the context of EMA, the angles θ_{pq} and ϕ should be referred to $\mathbf{q}_{\text{eff}}$ (but usually aren't). Although the effective momentum approximation provides an accurate model of Coulomb distortion of the differential cross section, Jin et al.[252] demonstrated that the subtractions needed to form effective response functions amplify errors in the approximation. For example, few percent errors in EMA cross sections for $^{16}O(e, e'p)$ can become $\sim$ 15% errors in R_{LT} with opposite effects for the two 1p-shell spin-orbit partners, reducing R_{LT} for the $1p_{1/2}$ state and enhancing it for the $1p_{3/2}$ state.

5.7. Relativistic Distorted Wave Models

Exact treatment of Coulomb distortion for electron scattering requires a relativistic treatment, which should then be coupled to a relativistic treatment of the ejectile. However, relativistic distorted wave impulse approximation (RDWLA) calculations require much more computation time than NRDWIA models which approximate electron distortion, and hence are not used as often. The first RDWIA calculations were made by McDermott[253] using a helicity-conservation approximation (HCA) to simplify the calculation of electron distortion. For ^{40}Ca he finds that both RDWIA and NRDWIA give very similar results, with the effective momentum approximation being quite accurate, but for $3s_{1/2}$ proton knockout from ^{208}Pb he obtains a spectroscopic factor that is about 30% larger with RDWIA and attributes the difference to a failure of the focussing properties of the second-order eikonal approximation used for the NRDWIA. More complete calculations which eliminate the HCA were then made by Jin et al.,[254] who also concluded that RDWIA leads to substantially larger spectroscopic factors than NRDWIA. However, Jin et al. obtained somewhat different results for $3s_{1/2}$ proton knockout from ^{208}Pb than McDermott even with plane waves. Udías et al.[255] demonstrated that the apparent disagreement between relativistic plane-wave calculations is due to differences between bound-state wave functions and that, when the same bound-state wave functions and distorting models are employed, the smaller residual differences are attributable to the helicity-conservation approximation. However, they also find that even though the cc1 and cc2 current operators give identical results for free spinors, distortion leads to significant differences between those current operators and to substantial ($\sim$ 15%) ambiguities in

the spectroscopic factors for RDWIA. This dependence upon the choice of current operator is much larger for RDWIA than for NRDWIA. Nevertheless, Udias *et al.* also conclude that relativistic models give larger spectroscopic factors than nonrelativistic models.

Therefore, all three of these groups have concluded that relativistic models give larger spectroscopic factors than nonrelativistic models and argue that that is a decisive advantage of RDWIA. They also argue that Dirac phenomenology provides a superior description of proton elastic scattering, especially for spin observables. However, we believe that their conclusion is incorrect. The most important difference between RDWIA and NRDWIA, at least for light- and medium-weight nuclei, is found in the differences between their optical potentials rather than in the differences between the Dirac and Schrödinger equation. When equivalent potentials derived from Dirac phenenomology (DP) are used in NRDWIA calculations, larger spectroscopic factors are obtained as well simply because the potentials are more absorptive that most nonrelativistic potentials. However, as shown in Section 5.4.7, $(e, e´p)$ data for nuclear transparency demonstrate that the DP potentials are too absorptive. The EEI model, on the other hand, reproduces the transparency data, provides more accurate predictions for proton reaction and neutron total cross sections, achieves equally good elastic scattering results, including spin observables, and is designed to fit inelastic scattering data which are sensitive to the interior wave functions needed for knockout reactions. Optical potentials fitted to elastic scattering alone are subject to similar ambiguities whether within a Dirac or Schrödinger formalism — minimization of such ambiguities requires consistent analysis of data for reactions which are sensitive to the interior wave function. Therefore, we argue that the EEI spectroscopic factors are more reliable and those of Dirac phenomenology are too large. Unfortunately, empirical effective interactions are not yet available for $T_p \leq 100$ MeV where many of the $(e, e´p)$ data are, but it is clear that DP potentials remain too absorptive at those energies. The primary advantage of RDWIA is that it permits accurate evaluation of electron distortion for heavy nuclei, but in the future, the fitting procedures used to produce its optical potentials should include inelastic data also.

The dynamical differences between Dirac and Schrödinger models of nucleon knockout have been explicated by Hedayati-Poor *et al.*,[256] who find that when potentials are included in the Pauli reduction of the current operator for distorted Dirac spinors, the series converges to the fully relativistic result. For simplicity, electron distortion was omitted. In their calculations both Dirac and Schrödinger models employ equivalent bound-state wave functions and distorted waves, with the differences between the models being isolated in the current operators. Due to the strength of the Dirac scalar and vector

potentials, spinors in the nuclear medium are substantially altered and these distortions affect the Pauli reduction of the current operators. However, if these potentials are included, the expansion in powers of $(E + m)^{-1}$ appears to converge already in second order even for relatively large missing momenta such that both approaches give nearly identical results even for the induced polarization, which is particularly sensitive to differences between the models. Therefore, Hedayati-Poor *et al.* conclude that the most important dynamical differences between relativistic and nonrelativistic models appear in the current operator rather than in the wave functions. Such differences can only be exacerbated by those matrix elements of the current operator which are permitted to exist off-shell but which are usually omitted because they vanish on-shell and are essentially unknown.

It would be of considerable interest to investigate $(e, e'N)$ for discrete final states using higher ejectile energies. Furnstahl, Wallace, and Kelly have constructed effective interactions based upon the relativistic IA2 model which incorporates spinor distortion and Pauli blocking. These interactions have been shown to give accurate predictions for elastic and inelastic nucleon scattering when $T_N > 300$ MeV,[205] and Figs. 5.4 and 5.5 show that accurate predictions are also obtained for proton absorption and neutron total cross sections. The model is somewhat more transparent than most of the optical potentials from Dirac phenomenology and will be tested further in transparency measurements $T_N > 300$ MeV planned at CEBAF. Thus, it should be possible to perform RDW1A $(e, e'N)$ calculations using folding-model optical potentials which provide a consistent description of nucleon scattering and hence have more confidence in the distortion of spinors in the medium and the resulting medium modifications of the current operator. Since the IA2 model is ultimately based upon a boson-exchange potential, it may also be possible to derive the electromagnetic current operator directly from the hamiltonian. We expect this to be the most promising direction for further development of relativistic distorted wave models.

5.8. Summary

We have made a critical review of the nonrelativistic distorted wave approximation, examining possible variations due to ambiguities in the off-shell current operator. Although these ambiguities appear to be relatively small for the kinematical conditions usually employed for measurements of missing momentum distributions, substantial variations are possible for separated response functions and polarization observables. Measurements of these quantities should be made for both neutron and proton knockout, which often display different sensitivities to variations of the current operator.

The sensitivity of spectroscopic factors for knockout to variations of the optical potential has been examined and it is found that for many states variations up to $\pm 15\%$ are possible among commonly used optical potentials fitted to proton elastic scattering data. These variations are correlated with their absorptive properties and the resulting interior wave functions, but optical potentials fitted to elastic scattering data alone are insensitive to the interior wave function. For energies above about 120 MeV, empirical effective interactions (EEI) fitted to both elastic and inelastic scattering data simultaneously are sensitive to the interior wave function and should provide more accurate spectroscopic factors. Our analysis of nuclear transparency data for $(e, e'p)$ at $T_p \sim 200$ MeV demonstrates that the commonly used global optical potentials are too absorptive at that energy, but that the EEI potentials reproduce the transparency data and also provide more accurate predictions for proton total and neutron absorption cross sections. Clearly it is desirable to measure missing momentum distributions using higher ejectile energies where the EEI approach is applicable. Nuclear transparency measurements for higher proton energies are also planned for CEBAF.

Relativistic distorted wave calculations provide more accurate treatments of Coulomb distortion, which is important for $A \gtrsim 40$, but the potentials presently available from Dirac phenomenology appear to be too absorptive, at least for $100 \leq T_p \leq 200$ MeV. Furthermore, the relativistic approach is more sensitive to ambiguities in the current operator due to the distortion of Dirac spinors by the strong scalar and vector potentials. On the other hand, consistent treatments of the distorting potentials and the current operator are only possible within a relativistic framework. Future developments of the relativistic approach should emphasize microscopic treatments of the effective interaction rather than rely on Dirac phenomenology.

6. SPECTRAL FUNCTIONS FROM (e, e′p) ON COMPLEX NUCLEI

The plane-wave impulse approximation for the single nucleon knockout reaction $A(e, e'p)B$,

$$\text{PWIA} \Longrightarrow \frac{d\sigma}{d\varepsilon_f d\Omega_e d\varepsilon_p d\Omega_p} = K\sigma_{ep}S(\mathbf{p}_m, E_m)$$

provides a physically appealing picture in which a nucleon with initial momentum $\mathbf{p}_m = \mathbf{p}' - \mathbf{q}$ absorbs a virtual photon $(\omega, \mathbf{q})$, and emerges with final momentum $(E', \mathbf{p}')$. The cross section for this process is represented by the product of an elementary cross section, σ_{ep}, and the probability, $S(\mathbf{p}_m, E_m)$, that removal of a nucleon with momentum $\mathbf{p}_m$ will result in a final state of the residual system with missing energy $E_m = m_p + m_B - m_A$. Thus,

to the extent that this simple picture applies, the knockout cross section is proportional to the single-nucleon spectral function for the target, which then forms the bridge between the experiment and the theory of nuclear structure. However, the spectral function is not itself an experimental observable, but rather must be deduced from cross-section measurements using a suitable reaction model. Therefore, to cross this bridge we must refine the picture to account for electron distortion, final state interactions, and modifications of the electromagnetic vertex function.

The distorted wave approximation was reviewed in Section 5 and tests of the reaction model will be reviewed in Section 7. In this section we review the spectroscopic information that has been deduced from $(e, e'p)$ reactions on complex nuclei, by which we mean $A > 4$. We focus here on recent high-resolution measurements and refer the reader to the review by Frullani and Mougey[1] for earlier work and for comparisons with other single-nucleon knockout reactions. In Section 6.1 we provide an introduction to the basic concepts of the spectral function and the quasiparticle approximation. In Section 6.2 we discuss dispersive optical models which seek to connect quasiparticle properties to a mean field that applies to both bound states and continuum states, and in Section 6.3 we discuss a related quasiparticle hamiltonian model by Ma and Wambach. We define the distorted spectral function in Section 6.4 and discuss its relationship to experimental quantities in Section 6.5. In Section 6.6 we review the existing data for missing momentum distributions for quasihole states and in Section 6.7 we present tests of the independence of the spectroscopic information from the kinematics of the reaction. In Section 6.8 we review the data for occupation probabilities and quasiparticle strengths. Finally, in Section 6.9 discuss measurements for large missing momenta.

6.1. Definition of the Spectral Function

In this section we introduce the basic concepts of the spectral function and the quasiparticle approximation, drawing heavily upon the treatise of Mahaux and Sartor[257] to which the reader is referred for further details, greater depth, and more complete references.

6.1.1. Nuclear Matter

The spectral function is intimately related to the single-particle propagator or time-ordered Green's function

$$G(\mathbf{r}, t; \mathbf{r}', t') = G_p(\mathbf{r}, t; \mathbf{r}', t') + G_h(\mathbf{r}, t; \mathbf{r}', t') \qquad (6.1)$$

whose particle and hole contributions are defined by

$$G_p(\mathbf{r},t;\mathbf{r}',t') = -i\Theta(t-t')\langle\Psi_0|a(\mathbf{r},t)a^\dagger(\mathbf{r}',t')|\Psi_0\rangle \qquad (6.2a)$$

$$G_h(\mathbf{r},t;\mathbf{r}',t') = +i\Theta(t'-t)\langle\Psi_0|a^\dagger(\mathbf{r}',t')a(\mathbf{r},t)|\Psi_0\rangle \qquad (6.2b)$$

In infinite nuclear matter, the propagators depend only on the separation $s = |\mathbf{r}-\mathbf{r}'|$ and hence their spatial Fourier transforms reduce to

$$G_p(k,t) = -i\Theta(t)\langle\Psi_0|a(k,t)a^\dagger(k,0)|\Psi_0\rangle \qquad (6.3a)$$

$$G_h(k,t) = i\Theta(-t)\langle\Psi_0|a^\dagger(k,0)a(k,t)|\Psi_0\rangle \qquad (6.3b)$$

Similarly, the spatio-temporal Fourier transforms become

$$G_p(k,\omega) = \langle\Psi_0|a(k)\frac{1}{\omega^+ + E_0 - H}a^\dagger(k)|\Psi_0\rangle \qquad (6.4a)$$

$$G_h(k,\omega) = \langle\Psi_0|a^\dagger(k)\frac{1}{\omega^- - E_0 + H}a(k)|\Psi_0\rangle \qquad (6.4b)$$

where H is the hamiltonian, E_0 is the ground-state energy, and where $\omega^\pm = \omega \pm i\delta$ includes an imaginary infinitesimal $\delta \to 0^+$. Finally, the Lehmann representation

$$G_h(k,\omega) = \int_{-\infty}^{E_F} d\omega' \frac{S_h(k,\omega')}{\omega^- - \omega'} \qquad (6.5a)$$

$$G_p(k,\omega) = \int_{E_F}^{\infty} d\omega' \frac{S_p(k,\omega')}{\omega^+ - \omega'} \qquad (6.5b)$$

relates the propagators to the spectral functions

$$S_p(k,\omega) = \langle\Psi_0|a(k)\delta(\omega + E_0 - H)a^\dagger(k)|\Psi_0\rangle \qquad (6.6a)$$

$$S_h(k,\omega) = \langle\Psi_0|a^\dagger(k)\delta(\omega - E_0 + H)a(k)|\Psi_0\rangle \qquad (6.6b)$$

The mass operator or proper self-energy $\mathcal{N}(k,\omega)$ is defined through the relation

$$G(k,\omega) = \left[\omega - \frac{k^2}{2m} - \mathcal{N}(k,\omega)\right]^{-1} \qquad (6.7)$$

Both G and $\mathcal{N}$ have the same analytic structure in the complex ω plane, namely, branch cuts to the left (right) of E_F above (below) the real axis. It is more convenient to introduce the retarded Green's function G^R and mean field $\mathcal{U}$, which are defined by

$$G^R(k,\omega) = \int_{-\infty}^{\infty} d\omega' \frac{S(k,\omega')}{\omega^+ - \omega'} = \left[\omega - \frac{k^2}{2m} - \mathcal{U}(k,\omega)\right]^{-1} \qquad (6.8)$$

and which are both analytic in the upper half plane and have branch cuts below the real axis. For infinite nuclear matter these branch cuts run the entire length of the real axis, but for finite systems there is a gap between the highest hole and lowest particle states (with specific values for lj) within which no cut is required. Thus, the spectral function can be obtained from the imaginary part of the retarded Green's function for real $\omega = E$ or, equivalently, from the branch-cut discontinuity using

$$S(k, E) = -\frac{1}{\pi} \operatorname{Im} G^R(k, E) = -\frac{1}{2\pi i} \left[G^R(k, E + i\delta) - G^R(k, E - i\delta) \right]$$
(6.9)

Finally, the retarded Green's function for real ω is related to the particle and hole propagators by

$$G^R(k, \omega) = G_p(k, \omega) + G_h(k, \omega)\Theta(\omega - E_F) + G_h^*(k, \omega)\Theta(E_F - \omega)$$
(6.10)

The mean field

$$\mathcal{U}(k, \omega) = \mathcal{V}(k, \omega) + i\mathcal{W}(k, \omega)$$
(6.11)

can be interpreted as the single-particle potential for a nucleon with momentum k and energy ω. For bound states, its real part determines the energy and its imaginary part the spreading width for quasiparticle excitations. For continuum states, the mean field is interpreted as the optical potential.

6.1.2.   Quasiparticle Approximation

Suppose that a hole with momentum k is created in nuclear matter at time $t = 0$ not far below the Fermi energy. The quasiparticle approximation stipulates that such an excitation will evolve according to

$$G_h(k; t) \approx G_h^{QP}(k; t) = iZ_h(k)e^{-iE(k)t}e^{-t/2\tau}$$
(6.12)

where

$$E(k) = \frac{k^2}{2m} + V(k)$$
(6.13a)

$$\tau = [-2W(k)]^{-1} = [\Gamma(k)]^{-1}$$
(6.13b)

are the energy and lifetime and $Z_h(k)$ is the quasiparticle strength. Thus, near the quasiparticle pole, the spectral function can then be expressed in the form

$$S(k, \omega) = S^{QP}(k, \omega) + S^{BG}(k, \omega)$$
(6.14)

where

$$S^{QP}(k,\omega) = \frac{1}{2\pi} \frac{\mathcal{Z}_h(k)\Gamma(k)}{[\omega - E(k)]^2 + [\Gamma(k)/2]^2} \tag{6.15}$$

is the quasiparticle contribution and where $S^{BG}(k,\omega)$ is a smooth background contribution which represents the contribution of more complicated states involving multinucleon emission.

The quasiparticle strength at the Fermi surface is related to the discontinuity in the occupation probability at the Fermi surface by the Migdal–Luttinger theorem,[258,259] which states

$$\mathcal{Z}(k_F) = n(k_F - 0) - n(k_F + 0) \tag{6.16}$$

On the other hand, the background contribution to the occupation probability is continuous and nonvanishing at the Fermi surface.[260] It arises from ground-state correlations which populate otherwise empty orbitals. For example, removal of a nucleon from a $2p2h$ configuration where both particle states are nominally empty leads to a $1p2h$ contribution to the continuum.

Near a quasiparticle pole, we assume that the Green's function can be approximated by

$$G^{QP}(k,\omega) = \frac{\mathcal{Z}(k)}{\omega - \mathcal{E}(k)} \tag{6.17}$$

where

$$\mathcal{E}(k) = \frac{k^2}{2m} + \mathcal{U}(k, \mathcal{E}(k)) \tag{6.18}$$

is the complex energy defining the location of the pole and

$$\mathcal{Z}(k) = \left[1 - \frac{\partial \mathcal{U}(k,\omega)}{\partial \omega}\right]^{-1}_{\omega = \mathcal{E}} \tag{6.19}$$

is the residue of the pole with momentum k. Providing that $\mathcal{W}$ is small, the quasiparticle energy is identified with the approximate solution

$$E(k) = \frac{k^2}{2m} + \mathcal{V}(k, E(k)) \tag{6.20}$$

for the real part of the pole position. The imaginary part of

$$\mathcal{E}(k) \approx E(k) - i\frac{\Gamma(k)}{2} \tag{6.21}$$

is then obtained by Taylor expansion, whereby

$$\frac{\Gamma(k)}{2} = -\frac{\mathcal{W}(k, E(k))}{[1 - \partial\mathcal{V}(k,\omega)/\partial\omega]_{\omega=E(k)}} \tag{6.22}$$

Thus, it is convenient to define the on-shell potentials

$$V(k) = \mathcal{V}(k, E(k)) \quad \text{and} \quad W(k) = \mathcal{W}(k, E(k)) \tag{6.23}$$

and the quasiparticle strength

$$Z(k) = \left[1 - \frac{\partial\mathcal{V}(k,\omega)}{\partial\omega}\right]_{\omega=E(k)}^{-1} \tag{6.24}$$

such that

$$S^{QP}(k,\omega) = \frac{1}{2\pi} \frac{Z(k)\Gamma(k)}{[\omega - E(k)]^2 + [\Gamma(k)/2]^2} \tag{6.25}$$

where

$$\frac{\Gamma(k)}{2} = -Z(k)W(k) \tag{6.26}$$

Note that we assume $\partial W/\partial\omega \ll 1$.

Baldo *et al.*[261] have provided a simple and convenient parametrization of $n(k, k_F)$ for nuclear matter based upon a calculation performed using a separable representation of the Paris interaction to evaluate the Brueckner–Hartree–Fock approximation through second order, with some third order contributions included also. The result for $k_f = 1.36$ fm^{-1} is shown in Fig. 6.1; note that the kink at $k/k_F = 2$ is merely an artifact of the parametrization. It is customary to characterize the depletion of the Fermi sphere in terms of the wound, κ, defined as $\kappa = 1 - n(\bar{k})$ for the mean momentum $\bar{k} = 0.75k_F$. Baldo *et al.* obtained a depletion of $\kappa = 0.24$ and a quasiparticle strength of $\mathcal{Z}(k_F) = 0.44$ from this calculation. Short-range and tensor correlations deplete the Fermi sphere and populate the tail which extends to very high momenta. The occupation of high momenta is dominated by high-energy regions of the spectral function, with appreciable contributions reaching to excitation energies of several hundred MeV.[262] These results are characteristic of all nuclear matter calculations for realistic interactions, with small variations in κ and $\mathcal{Z}(k_F)$ which depend upon the details of the interaction.
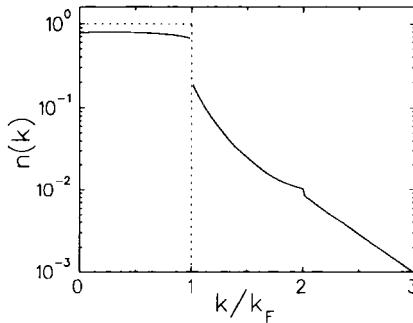
Fig. 6.1. Occupation probability for nuclear matter, as parametrized by Baldo *et al.*[261] The Fermi gas limit is indicated by dotted lines.

A simple parametrization of the spreading width for quasiparticle excitations near the Fermi surface has been proposed by Brown and Rho,[263] for which

$$\Gamma^{BR}(E) = 2\beta \frac{(E - E_F)^2}{(E - E_F)^2 + \rho^2} \tag{6.27}$$

where E_F is the Fermi energy. Typical quasihole and quasiparticle spectral functions are plotted in Fig. 6.2. The spectral function is required to vanish at the Fermi energy. The independent particle model is represented by spikes at the unperturbed peak positions; note that the peaks experience small shifts due to the energy dependence of the width. The energies were chosen to be $E_F \pm 8\,\mathrm{MeV}$, for which the full width at half maximum is approximately 2.7 MeV. Approximately 7% of the quasihole strength is then found above the Fermi energy and represents the depletion of the hole strength. Similarly, about 7% of the quasiparticle strength is found below the Fermi energy and represents population of normally vacant orbits by ground-state correlations. The range of excitation energy accessible to single-nucleon knockout experiments, typically 20 MeV at NIKHEF, is represented by the hatched region — approximately 10% of the hole strength lies deeper.

6.1.3. Finite Nuclei

Single-nucleon removal reactions are described by the partial-wave hole spectral functions

$$S_\alpha^{(-)}(p, E) = \sum_n |\langle \Psi_n^{(A-1)} | a_\alpha(p) | \Psi_0^{(A)} \rangle|^2$$

$$\times \delta(E + E_n^{(A-1)} - E_0^{(A)}) \Theta(E_F - E) \tag{6.28}$$
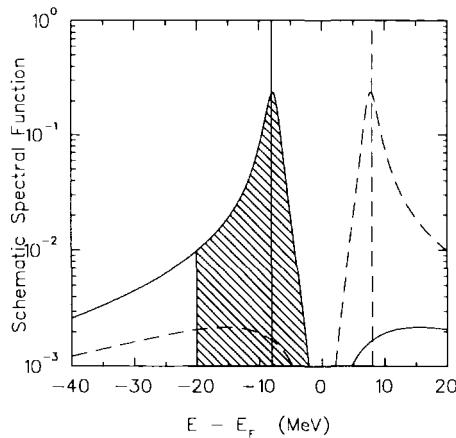
Fig. 6.2. Schematic representation of the spectral function for quasihole (solid) and quasiparticle (dashed) excitations at $E = E_F \pm 8$ MeV, based on the Brown–Rho parametrization with $\beta = 12$ MeV and $\rho^2 = 500$ MeV^2. The independent particle model is represented by spikes. The hatched area represents the range accessible with knockout experiments.

which gives the probability that removal of a nucleon with momentum p in an orbital α from the ground state $\Psi_0^{(A)}$ of an A-nucleon system will leave the residual $(A - 1)$-nucleon system in a state with energy E. Similarly, the single-particle spectral function

$$S_\alpha^{(+)}(p, E) = \sum_n |\langle \Psi_n^{(A+1)} | a_\alpha^\dagger(p) | \Psi_0^{(A)} \rangle|^2$$

$$\times \delta(E - E_n^{(A+1)} + E_0^{(A)}) \Theta(E - E_F) \qquad (6.29)$$

gives the probability that a final $(A + 1)$-nucleon state can be obtained by adding a nucleon of momentum p in orbital a to the A-nucleon ground state. For closed-shell nuclei A, the Fermi energy $E_F = (E_F^- + E_F^+)/2$ may be conveniently defined in terms of the average of the separation energies $-E_F^-$ and $-E_F^+$ for the A and $(A + 1)$ nucleon systems. The complete spectral function is then

$$S_\alpha(p, E) = S_\alpha^{(-)}(p, E) + S_\alpha^{(+)}(p, E) \qquad (6.30)$$

It is also useful to define a spectral strength function, $S_\alpha(E)$, for orbital α by integrating the spectral function over momentum, such that

$$S_\alpha(E) = \frac{1}{2\pi^2} \int_0^\infty dp\, p^2\, S_\alpha(p, E) \qquad (6.31)$$

Whenever clarity of context permits, the superscripts (–) for removal (pickup) or (+) for addition (stripping) reactions will be omitted from the relevant spectral function. The orbital α is specified by its orbital angular momentum l_α, total angular momentum j_α, and nucleon type. Additional quantum numbers, such as the principal and magnetic quantum numbers, usually remain implicit. Most theoretical calculations employ a normalization in which the integrated spectral strength would be unity, as is appropriate when α specifies a complete set of quantum numbers. On the other hand, experimental analyses usually employ a normalization in which the integrated spectral strength would be $(2j_\alpha+1)$, as is appropriate when magnetic substates are summed. Hence, it is useful to introduce g_α as the degeneracy appropriate to the context, such that

$$\int_{-\infty}^{\infty} dE\ S_\alpha(p, E) = g_\alpha \tag{6.32}$$

The hole spectral function is related by closure to the subshell momentum density, $n_\alpha(p)$, by

$$n_\alpha(p) = \int_{-\infty}^{E_F} dE\ S_\alpha(p, E) = \langle \Psi_0^{(A)} | a_\alpha^\dagger(p) a_\alpha(p) | \Psi_0^{(A)} \rangle \tag{6.33}$$

Thus, the occupancy of orbital α is then

$$n_\alpha = \frac{1}{2\pi^2} \int_0^\infty dp\ p^2\ n_\alpha(p) \tag{6.34}$$

and the total momentum density and particle number are, respectively,

$$n(p) = \sum_\alpha g_\alpha n_\alpha(p) \tag{6.35a}$$

$$N = \frac{1}{2\pi^2} \int_0^\infty dp\ p^2\ n(p) = \sum_\alpha g_\alpha n_\alpha \tag{6.35b}$$

where N refers to either the neutron or proton number of the target, as appropriate, and where g_α accounts for the degeneracy of the orbital. Thus, the spectral functions satisfy the sum rules

$$g_\alpha^{-1} \int_{-\infty}^{E_F} dE\ S_\alpha(p, E) = n_\alpha(p) \tag{6.36a}$$

$$g_\alpha^{-1} \int_{E_F}^{\infty} dE\ S_\alpha(p, E) = 1 - n_\alpha(p) \tag{6.36b}$$

$$g_\alpha^{-1} \int_{-\infty}^{\infty} dE\ S_\alpha(p, E) = 1 \tag{6.36c}$$

where the first line refers to the hole, the second to the particle, and the third to the total spectral function. Furthermore, in the independent particle shell model (IPSM), the spectral strength function reduces to

$$S_\alpha(E) \longrightarrow g_\alpha n_\alpha \delta(E - E_\alpha) \qquad (6.37a)$$

$$S(\mathbf{p}, E) \longrightarrow \sum_\alpha g_\alpha n_\alpha(\mathbf{p}) \delta(E - E_\alpha) \qquad (6.37b)$$

where

$$n_\alpha(\mathbf{p}) = |\phi_\alpha(\mathbf{p})|^2 \qquad (6.38)$$

is the momentum distribution and n_α is the occupancy for orbital α.

The quasiparticle approximation to the spectral strength function for orbital α in a finite system can now be expressed in the form

$$S_\alpha(E) = g_\alpha \left[S_\alpha^{QP}(E) + S_\alpha^{BG}(E) \right] \qquad (6.39a)$$

$$S_\alpha^{QP}(E) = \frac{1}{2\pi} \frac{Z_\alpha \Gamma_\alpha(E)}{(E - E_\alpha)^2 + [\Gamma_\alpha(E)/2]^2} \qquad (6.39b)$$

where E_α is the quasiparticle energy and Z_α is its strength. For excitations not far below the Fermi energy, the width is small enough that the energy dependence of the width function obtained from the imaginary part of the mean field may be neglected, such that $\Gamma_\alpha \approx \Gamma_\alpha(E_\alpha)$, and then Z_α is the integral of a Lorentzian quasiparticle peak. Thus, Z_α represents the fraction of the sum rule within the quasiparticle peak and is interpreted as the spectroscopic factor for removal of a nucleon from orbital α. The occupation n_α is somewhat larger due to the background strength found outside the quasiparticle peak.

As the quasiparticle energy approaches the Fermi surface, the spreading width approaches zero. However, since the states below the particle emission threshold are discrete, the spreading width in finite systems loses its meaning near the Fermi surface. Furthermore, the gap in the single-particle excitation spectrum reduces the availability of background configurations and hence reduces the spreading width for finite systems. Under those circumstances the quasiparticle strength for nominally closed-shell nuclei is strongly concentrated in a single discrete state with some minor fragmentation due to coupling to low-lying surface modes, often described as long-range correlations. This fragmentation is more pronounced for open-shell nuclei. These finite-size effects can be evaluated using the random phase approximation (RPA). By this means, Brand et al.[264] obtained a fairly good qualitative description of the fragmentation of hole strength observed for (e,e'p) reactions on [48]Ca and [90]Zr.

6.1.4. Overlap Functions

The hole spectral function can be related to the overlap integral

$$\Phi_{fi}(\mathbf{p}) = \int d^3r \, e^{-i\mathbf{p}\cdot\mathbf{r}} \langle \Psi_f^{(A-1)}|a(\mathbf{r})|\Psi_0^{(A)}\rangle = \int d^3r \, e^{-i\mathbf{p}\cdot\mathbf{r}}\Phi_{fi}(\mathbf{r}) \tag{6.40}$$

obtained by removing a nucleon from position r leaving the residual nucleus in state f. The hole spectral function then becomes

$$S(\mathbf{p}, E) = \sum_f |\Phi_{fi}(\mathbf{p})|^2 \delta(E - E_{fi}) \tag{6.41}$$

where $E_{fi} = E_0^{(A)} - E_f^{(A-1)}$ is the missing energy for population of state f in the $(A-1)$ system by removal of a single nucleon from the ground state of the parent nucleus. Expanding

$$\Phi_{fi} = \sum_\alpha c_{f\alpha}\phi_\alpha$$

in a complete orthonormal set of single-particle orbitals $\{\phi_{nlj}\}$ we find

$$S(\mathbf{p}, E) = \sum_{f\alpha\beta} c_{f\alpha}^* c_{f\beta} \phi_\alpha^*(\mathbf{p})\phi_\beta(\mathbf{p})\delta(E - E_{fi}) = \sum_{\alpha\beta} S_{\alpha\beta}(E)\phi_\alpha^*(\mathbf{p})\phi_\beta(\mathbf{p}) \tag{6.42}$$

where

$$\tilde{\phi}_{nlj}(\mathbf{p}) = \int d^3r \, e^{-i\mathbf{p}\cdot\mathbf{r}}\phi_{nlj}(\mathbf{r}) \tag{6.43}$$

can be interpreted as a single-particle momentum wave function. If we assume that an optimal set of orbitals $\{\phi_\alpha\}$ exists for which a single term dominates each Φ_{fi}, then

$$S_{\alpha\beta}(E) = \sum_f c_{f\alpha}^* c_{f\beta} \delta(E - E_{fi}) \approx S_\alpha(E)\delta_{\alpha\beta} \tag{6.44}$$

is nearly diagonal. It is reasonable to suppose that this set is similar to the set of Hartree–Fock orbitals for the ground state of the target. With these assumptions, the spectral function factorizes, such that

$$S(\mathbf{p}, E) \approx \sum_\alpha S_\alpha(E)|\phi_\alpha(\mathbf{p})|^2 \tag{6.45}$$

where $S_\alpha(E)$ is the spectral strength of the hole state α. Thus, to the extent that the factorization approximation is valid, the Fourier transform of the overlap function is measured in the knockout reaction and is often referred to as the bound-state wave function (BSWF).

6.2. Dispersive Optical Models

The dispersion model of the nuclear mean field has been developed by Mahaux and collaborators[183,225,265–271] and has been reviewed by Mahaux and Sartor.[257] Here we merely summarize some of the salient features.

The mean field for nuclear matter satisfies a subtracted dispersion relation of the form[272]

$$\mathcal{V}(k, E) = \mathcal{V}(k, E_F)$$
$$+ \frac{\mathcal{P}}{\pi} \int_{-\infty}^{\infty} dE' \, \mathcal{W}(k, E') \left(\frac{1}{E' - E} - \frac{1}{E' - E_F} \right) \quad (6.46)$$

where the first term is basically a Hartree–Fock contribution that depends slowly on energy and the term second is a dispersive correction $\Delta \mathcal{V}$ that depends upon the dynamics of the system. Note that $\mathcal{P}$ indicates that a Cauchy principal value is to be taken for the integrals. Thus, the mean field provides a unified description of both bound states at energies below the Fermi energy E_F and scattering states at $E > E_F$.

Similarly, we assume that the equivalent local potential for a finite nucleus can be separated into Hartree–Fock and dispersive contributions, such that

$$V(r, E) = V_{HF}(r, E) + \Delta V(r, E) \quad (6.47)$$

The Hartree–Fock potential

$$V_{HF}(r, E) = V_{HF}(E) f(x_{HF}) \quad (6.48)$$

is assumed to have an energy-independent shape

$$f(x) = [1 + e^x]^{-1} \quad (6.49a)$$
$$x_i = (r - R_i)/a_i \quad (6.49b)$$

and a depth

$$V_{HF}(E) = V_{HF}(E_F) + \left(1 - \frac{m^*_{HF}}{m} \right) (E - E_F) \quad (6.50)$$

that depends slowly on energy. This energy dependence arises from the replacement of a nonlocal energy-independent potential by an equivalent local potential. The dispersive contribution is obtained from the absorptive potential by means of a subtracted dispersion relation

$$\Delta V(r, E) = \frac{\mathcal{P}}{\pi} \int_{-\infty}^{\infty} dE' \, W(r, E') \left(\frac{1}{E' - E} - \frac{1}{E' - E_F} \right) \quad (6.51)$$

This energy-dependent contribution is surface-peaked and is repulsive below and attractive above the Fermi energy. The imaginary potential is also parametrized in Woods-Saxon form, containing both volume and surface terms, such that

$$W(r, E) = W_v(E)f(x_W) + W_s(E)g(x_W) \tag{6.52a}$$

$$g(x) = -4a\frac{df}{dr} \tag{6.52b}$$

It is assumed that the imaginary potential is symmetric with respect to E_F and the depths are usually parametrized using some variation of the following forms:

$$W_v(E) = -\gamma_v\frac{(E - E_F)^4}{(E - E_F)^4 + \mu_v^4} \tag{6.53a}$$

$$W_s(E) = -\beta_s\left[\frac{(E - E_F)^2}{(E - E_F)^2 + \rho_s^2} - \frac{(E - E_F)^4}{(E - E_F)^4 + \mu_v^4}\right] \tag{6.53b}$$

Note that these parametrizations are generalizations of Γ^{BR}, Eq. (6.27).

The effective mass in a finite system,

$$\frac{m^*(r, E)}{m} = 1 - \frac{dV(r, E)}{dE} \tag{6.54}$$

is now defined in terms of the energy dependence of the local mean field. Generalizing our analysis of the effective mass for uniform systems, Eqs. (5.31)–(5.34), it useful to separate the local effective mass into a k-mass, $m_k(r, E)$, which represents the spatial nonlocality and an E-mass, $m_E(r, E)$, which represents the temporal nonlocality of the mean field. Hence, the k-mass is determined by the energy dependence of the Hartree–Fock contribution and the E-mass includes the effect of the dispersive contribution to the net effective mass, such that

$$\frac{m_k(r, E)}{m} = 1 - \frac{dV_{HF}(r, E)}{dE} \tag{6.55a}$$

$$\frac{m_E(r, E)}{m} = \frac{m^*(r, E)}{m_k(r, E)} \tag{6.55b}$$

Thus, within this model the k-mass has the same radial dependence as the Hartree–Fock potential while the .E-mass includes a characteristic surface enhancement originating in coupling to low-lying surface excitations.

Quasiparticle energies, E_α, and wave functions, $\phi_\alpha(\mathbf{r})$, are obtained from solutions of a local Schrödinger equation

$$\left[-\frac{\hbar^2}{2m}\nabla^2 + V(r, E_\alpha)\right]\varphi_\alpha(\mathbf{r}) = E_\alpha\varphi_\alpha(\mathbf{r}) \tag{6.56}$$

upon application of the locality correction

$$\phi_\alpha(\mathbf{r}) \propto \left[\frac{m_k(r, E)}{m}\right]^{1/2} \varphi_\alpha(\mathbf{r}) \tag{6.57}$$

and renormalization to unit norm. Effective masses for particular orbitals are then defined by expectation values of the effective mass operators, such that

$$m_\alpha^* = \langle\alpha|m^*|\alpha\rangle \tag{6.58a}$$

$$m_{k\alpha} = \langle\alpha|m_k|\alpha\rangle \tag{6.58b}$$

$$m_{E\alpha} = \langle\alpha|m_E|\alpha\rangle \tag{6.58c}$$

where $\langle r|\alpha\rangle = \phi_\alpha(r)$. Note that

$$\frac{m_\alpha^*}{m} \approx \frac{m_{k\alpha}}{m}\frac{m_{E\alpha}}{m} \tag{6.59}$$

Similarly, the quasiparticle strength and spreading potential become

$$Z_\alpha = \langle\alpha|\frac{m}{m_E}|\alpha\rangle \tag{6.60a}$$

$$W_\alpha(E) = \langle\alpha|W(r, E)|\alpha\rangle \tag{6.60b}$$

Hence, the quasiparticle spreading width becomes

$$\Gamma_\alpha(E, \Delta) = 2\frac{m}{m_\alpha^*}\left[\frac{m_{k\alpha}}{m}\Delta - W_\alpha\right] \longrightarrow$$

$$\Gamma_\alpha = -2\frac{m}{m_{E\alpha}}W_\alpha\bigg|_{E\to E_\alpha, \Delta\to 0} \tag{6.61}$$

where Δ is an averaging width, usually taken to be about 0.5 MeV. Finally, the occupancy of an orbital α with $E_\alpha < E_F$ is determined from the dispersive dynamics according to

$$n_\alpha = \langle\alpha|n_\alpha(r, E)|\alpha\rangle \tag{6.62a}$$

$$n_\alpha(r, E) = 1 + \pi^{-1}\frac{m}{m_k(r, E)}\frac{d}{dE}\int_{E_F}^\infty dE' \frac{W(r, E')}{E' - E} \tag{6.62b}$$

These relationships suffice to completely determine the spectral strength function for this model. Furthermore, the model also supplies both the quasiparticle momentum distributions and the ejectile distorting potential. Therefore, one could obtain not only the spectral function, $S(p, E)$, but also the distorted spectral function, $S^D(E_m, \mathbf{p}_m, \mathbf{p}')$, for $(e, e'N)$ from the same internally consistent model. On the other hand, the assumption of factorization

between the strength function and the momentum distribution limits the model to relatively low-lying quasiparticle excitations because it cannot describe the enhancement at high momentum expected for large excitation energies. Although spectral strength functions deduced from dispersive optical model analyses of nucleon elastic scattering have been compared with the spectral information deduced from various single-nucleon removal reactions, to our knowledge no one has applied the dispersive optical model to analyze such reactions directly. The consistency between bound and continuum wave functions afforded by the dispersive optical model has not yet been fully exploited.

There are two basic strategies for determining the parameters of the model.

6.2.1. Variational Moment Approach

The variational moment approach[270] is based upon the observation that while optical model parameters may vary considerably due to correlations among their parameters, the moments

$$[r^q]_h(E) = \frac{4\pi}{A} \int dr \, r^q h(r, E) \qquad (6.63)$$

where $h(r, E)$ is either $V(r, E)$ or $W(r, E)$, are relatively well determined for $0.5 \leq q \leq 4$. Therefore, phenomenological optical model analyses can be employed to optimize the dispersive model using the following procedure. First, the shape parameters R_W and a_W are chosen based on averages for phenomenological optical model analyses. Second, the parameters of $W_v(E)$ and $W_s(E)$ are fitted to the $q = 0.8$ and $q = 2$ moments of phenomenological optical potentials subject to the constraint that the net volume integral

$$[r^2]_W = [r^2]_{W_v} + [r^2]_{W_s} = -\beta \frac{(E - E_F)^2}{(E - E_F)^2 + \rho^2} \qquad (6.64)$$

has the Brown–Rho form with appropriate β and ρ parameters. Third, $\Delta V(r, E)$ is computed using the dispersion relation. Fourth, a_{HF} is chosen to be an average phenomenological value and a trial value of R_{HF} is chosen. The value of $V_{HF}(E_F)$ is then chosen to reproduce E_F and m^*_{HF} is fitted to the $q = 0.8$ moments of V for phenomenological optical potentials. Fifth, R_{HF} is varied to reproduce the $q = 2$ moments of V. Finally, steps four and five are iterated until self-consistency is achieved. This procedure is perhaps more accurately called the iterative moment approach (IMA).

6.2.2. Dispersive Optical Model Approach

Dispersive optical-model analysis (DOMA)[269,273] is similar to IMA except that the energy dependence of the strengths of the imaginary components
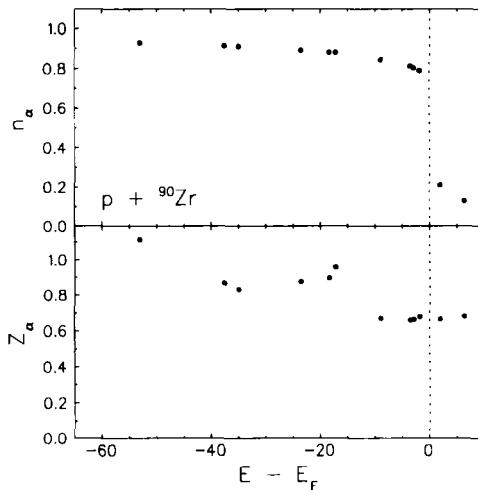
Fig. 6.3. Typical DOMA results for protons in ^{90}Zr.[274]

are fitted to scattering data rather than to moments of fitted potentials from independent analyses. First, shape parameters are chosen; most analyses constrain $R_W = R_{HF}$ and $a_W = a_{HF}$ to reduce the number of parameters. Second, standard energy-dependent optical model fits are made to the available elastic scattering data, where the strengths are given simple analytic forms, using linear forms for the real and forms similar to Eq. (6.53) for the imaginary central potential. Third, $\Delta V(r, E)$ is computed using the dispersion relation. Fourth, the value of $V_{HF}(E_F)$ is chosen to reproduce E_F and m^*_{HF} is fitted to the energy dependence of $V_{HF}(E) = V(E) - \Delta V_v(E)$ where ΔV_v is the volume part of the dispersive contribution to the real potential.

A typical DOMA result is shown in Fig. 6.3 for protons in ^{90}Zr.[274] By using smooth curves to extrapolate to the Fermi surface from both below and above, Wang *et al.* deduce a quasiparticle strength of $\mathcal{Z}(k_F) = 0.53$, which is in good agreement with theoretical expectations. For valence holes not far below the Fermi surface, spectroscopic factors of 0.65–0.70 are calculated from the dispersive optical model.

6.3.   Quasiparticle Hamiltonian Model

Ma and Wambach[275,276] have proposed a phenomenological quasiparticle hamiltonian model which seeks to incorporate effects beyond the Hartree–Fock level and thereby reproduce experimental single-particle properties near

the Fermi surface. Based upon the Skyrme–Hartree–Fock model, the quasiparticle hamiltonian density is represented as

$$\mathcal{H}(r) = -\nabla \cdot \frac{1}{2m^*(r)} \nabla + U(r) \tag{6.65}$$

where

$$U(r) \approx \frac{m}{m^*(r)} \Sigma(r, k_F(r), E_F) \tag{6.66}$$

is the quasiparticle potential determined by the proper self-energy at the Fermi surface. (Note that a complicated but small correction term has been neglected.) They parametrize the self-energy

$$\Sigma(r, k_F(r), E_F) = \mathcal{V}_C(r) + \frac{2}{r}\frac{d}{dr}\mathcal{V}_{LS}(r)\mathbf{L}\cdot\boldsymbol{\sigma} + \mathcal{V}_Z(r) \tag{6.67}$$

in Woods–Saxon form, where

$$\mathcal{V}_C(r) = \frac{V_C}{1 + \exp[(r - R_C)/a_C]} \tag{6.68a}$$

$$\mathcal{V}_{LS}(r) = \frac{V_{LS}}{1 + \exp[(r - R_{LS})/a_{LS}]} \tag{6.68b}$$

are central and spin–orbit potentials and for protons $\mathcal{V}_Z$ is the Coulomb potential. They parametrize the effective mass as

$$\frac{m_k(r)}{m} = 1 - \alpha g(r)$$
$$\frac{m_E(r)}{m} = 1 + \beta_v g(r) + \beta_s \frac{dg(r)}{dr}$$
$$g(r) = \mathcal{V}_C(r, k_F(r), E_F)/\mathcal{V}_C(0, k_F(0), E_F)$$

where α is the parameter which governs the spatial nonlocality represented by the k-mass, β_s and β_v are surface and volume contributions to the temporal nonlocality represented by the E-mass, and $g(r)$ is a radial form factor obtained from the central part of the self-energy. The model is constrained to produce $m^*/m = 0.7$ in the interior based upon the Perey–Buck analysis. The geometry of the mean field is adjusted to fit the experimental charge density. The empirical particle–hole gap and spin–orbit splittings are reproduced mainly by adjustment of β_s. Finally, the quasiparticle strength for the deepest hole observed in ^{208}Pb$(e, e'p)$ by Quint et al.[277] is fitted.

An important difference between this model and the dispersive optical model is that Ma and Wambach associate the overlap function with

$$\phi_\alpha(\mathbf{r}) \propto \left[\frac{m^*(r,E)}{m}\right]^{1/2} \varphi_\alpha(\mathbf{r}) \tag{6.69}$$

where the nonlocality correction involves m^* instead of m_k [cf. Eq. (6.57)]. The additional factor of $\sqrt{m_E(r,E)/m}$ carries a relatively narrow surface peak whose Fourier transform enhances $\tilde{\phi}_\alpha(p_m)$ for $p_m > k_F$. Note that this factor is equivalent to the local quasiparticle amplitude of the dispersive optical model,

$$\sqrt{Z(r,E)} = \sqrt{m/m_E(r,E)} \tag{6.70}$$

such that the difference between the models can be interpreted as a local treatment of the quasiparticle strength by Mahaux *et al.* versus a global spectroscopic amplitude for the model by Ma and Wambach. These models are compared with large-p_m data for ^{208}Pb$(e, e'p)$ in Section 6.9.

6.4. Distorted Momentum Distribution

Suppose that a knockout reaction initiated upon a target of spin $I_0 m_0$ populates channel a in a final-state partition $a + A$ consisting of an ejectile with spin $I_a m_a$ and a residual nucleus with spin $I_A m_A$. The channel wave function may be expanded as

$$\Psi_\alpha = \sum_\beta \chi_{\alpha\beta}(\mathbf{p}',\mathbf{r})\psi_\beta \tag{6.71}$$

where ψ_β represents the internal state of the residual nucleus and $\chi_{\alpha\beta}$ represents the distorted wave containing a plane wave in channel α and spherical waves in each channel β. The overlap between ψ_β and the ground state Ψ_0 may be expanded as

$$\langle \psi_\beta | \Psi_0 \rangle = \sum_\gamma c_{\beta\gamma} \phi_{\beta\gamma}(\mathbf{r}) \tag{6.72}$$

where $c_{\beta\gamma}$ is a coefficient of fractional parentage and where

$$\phi_{\beta\gamma}(\mathbf{r}) = R_{\beta\gamma}(r) \sum_{\nu m} \left\langle \begin{array}{cc} l_\gamma & I_a \\ \nu & m_a \end{array} \middle| \begin{array}{c} j_\gamma \\ m \end{array} \right\rangle \left\langle \begin{array}{cc} j_\gamma & I_A \\ m & m_A \end{array} \middle| \begin{array}{c} I_0 \\ m_0 \end{array} \right\rangle Y_{l,\nu}(\hat{\mathbf{r}}) \tag{6.73}$$

is a normalized wave function based upon a radial function $R_{\beta\gamma}(r)$ which presumably resembles a bound-state wave function within the mean field of

the residual nucleus. For simplicity we assume that $\{R_{\beta\gamma}\}$ form a complete orthonormal basis set.

It is useful to define the distorted momentum amplitude as

$$\tilde{\Phi}_\alpha(\mathbf{p},\mathbf{q}) = \int d^3r\, e^{i\mathbf{q}\cdot\mathbf{r}} \langle \Psi_\alpha^{(-)}(\mathbf{p}',\mathbf{r})|\Psi_0\rangle \tag{6.74}$$

where q is the effective momentum transfer, $\mathbf{p}'$ is the ejectile momentum, and $\mathbf{p} = \mathbf{p}' - \mathbf{q}$ is the initial undistorted momentum of the struck particle. The distorted wave amplitude can then be expressed in the form

$$\tilde{\Phi}_\alpha(\mathbf{p},\mathbf{q}) = \sum_{\beta\gamma} c_{\beta\gamma}\tilde{\phi}_{\alpha\beta\gamma}(\mathbf{p},\mathbf{q}) \tag{6.75a}$$

$$\tilde{\phi}_{\alpha\beta\gamma}(\mathbf{p},\mathbf{q}) = \int d^3r\, e^{i\mathbf{q}\cdot\mathbf{r}} \chi_{\alpha\beta}^{(-)*}(\mathbf{p}',\mathbf{r})\phi_{\beta\gamma}(\mathbf{r}) \tag{6.75b}$$

Thus, the distorted momentum distribution for channel α becomes

$$\rho_\alpha^D(\mathbf{p},\mathbf{p}') = \left[(2\pi)^3(2I_0+1)\right]^{-1} \sum_{m_0 m_a m_A} |\tilde{\Phi}_\alpha(\mathbf{p},\mathbf{q})|^2 \tag{6.76}$$

In the plane-wave limit,

$$\chi_{\alpha\beta}(\mathbf{p}',\mathbf{r}) \longrightarrow e^{i\mathbf{p}'\cdot\mathbf{r}}\delta_{\alpha\beta} \tag{6.77a}$$

$$\tilde{\phi}_{\alpha\beta\gamma}(\mathbf{p},\mathbf{q}) \longrightarrow \int d^3r\, e^{-i\mathbf{p}\cdot\mathbf{r}}\phi_{\alpha\gamma}(\mathbf{r})\delta_{\alpha\beta} \tag{6.77b}$$

we find that

$$\rho_\alpha^D(\mathbf{p},\mathbf{p}') \longrightarrow \rho_\alpha(p) = \frac{1}{2\pi^2}\sum_{\gamma\gamma'} c_{\alpha\gamma}c_{\alpha\gamma'}^* \tilde{\phi}_{\alpha\gamma}(p)\tilde{\phi}_{\alpha\gamma'}^*(p)\delta_{l_\gamma l_{\gamma'}}\delta_{j_\gamma j_{\gamma'}} \tag{6.78}$$

is incoherent with respect to $l_\gamma j_\gamma$. The normalization of ρ_α is then

$$4\pi \int dp\, p^2\, \rho_\alpha(p) = \sum_{\gamma\gamma'} c_{\alpha\gamma}c_{\alpha\gamma'}^*\delta_{l_\gamma l_{\gamma'}}\delta_{j_\gamma j_{\gamma'}} \int dr\, r^2\, R_{\alpha\gamma}(r)R_{\alpha\gamma'}^*(r) \tag{6.79}$$

which reduces to

$$4\pi \int dp\, p^2\, \rho_\alpha(p) = \sum_\gamma |c_{\alpha\gamma}|^2 = \sum_\gamma S_{\alpha\gamma} \tag{6.80}$$

provided that the basis set of overlap functions is orthonormal, as stipulated.

The factorization approximation to the knockout cross section for a discrete final state stipulates that

$$\frac{d\sigma}{d\varepsilon_f d\Omega_e d\Omega_p} \approx K\sigma_{ep}\rho^D(\mathbf{p}_m, \mathbf{p}') \tag{6.81}$$

where K is a kinematic factor and σ_{ep} is the off-shell electron-proton cross section for the appropriate kinematic conditions. Boffi *et al.*[170] have shown that the factorization approximation is fairly accurate for parallel kinematics under the conditions usually employed for measurements of missing momentum distributions, but that significant errors are incurred for quasiperpendicular kinematics even though distortion appears to be reduced. More generally, the *reduced* cross section for an unfactorized calculation is defined by analogy to be

$$\sigma_{\text{red}} = \frac{1}{K\sigma_{ep}}\frac{d\sigma}{d\varepsilon_f d\Omega_e d\Omega_p} \tag{6.82}$$

and is then compared with the experimental distorted momentum distribution that is extracted from data using a relationship based upon the factorization hypothesis, as described below. Most authors do not distinguish between σ_{red} and ρ^D, using the terms interchangeably. Note that even though experimental analyses usually employ the de Forest σ_{ep}^{cc1} prescription, consistency requires calculations of σ_{red} to employ the σ_{ep} that is appropriate to the current operator used in the DWIA calculation.

6.5. Experimental Definition of Distorted Momentum Distributions

The distorted spectral function is obtained experimentally by dividing the differential cross section by the off-shell electron-proton cross section according to the ansatz

$$\frac{d\sigma}{d\varepsilon_f d\Omega_e d\varepsilon_p d\Omega_p} = K\sigma_{ep}S^D(E_m, \mathbf{p}_m, \mathbf{p}') \tag{6.83}$$

Final-state interactions between the ejectile and the residual nucleus make the distorted spectral function $S^D(E_m, \mathbf{p}_m, \mathbf{p}')$ depend upon the ejectile momentum $\mathbf{p}'$, and on the angle between the initial and final nucleon momenta, while the (undistorted) spectral function would depend only on E_m and p_m. Thus, the distorted spectral function depends upon the kinematical conditions and is different for parallel and perpendicular kinematics, for example. Furthermore, the dependence of S^D upon the electron energy that arises from

Coulomb distortion has been left implicit. Therefore, the hole spectral function can be deduced only within the context of a model which allows the effects of Coulomb distortion and final-state interactions to be evaluated for particular experimental conditions. It then becomes important to perform measurements for a variety of conditions designed to test the reliability of the reaction model.

Since the experimental distorted momentum distribution is obtained by dividing the differential cross section by $K\sigma_{ep}$, according to Eq. (6.83), as if factorization were valid, the theoretical momentum distribution must be obtained from an unfactorized calculation according to the same prescription. Although the experimental S^D is generally based upon the de Forest cc1 prescription for σ_{ep}, consistency requires that calculations of S^D should divide out the σ_{ep} that corresponds to the model used for the off-shell current operator.

It is convenient to divide the distorted spectral function into two regions

$$
\begin{aligned}
S^D(E, \mathbf{p}, \mathbf{p}') = \sum_{\alpha} \Bigg[\sum_i S_{\alpha i} \delta(E - E_i) + S_\alpha(E)\Theta(E - E_{2N}) \Bigg] \\
\times \varrho_\alpha^D(\mathbf{p}, \mathbf{p}')
\end{aligned}
\tag{6.84}
$$

where $\varrho_\alpha^D(\mathbf{p}, \mathbf{p}')$ is the distorted momentum distribution for orbital α normalized to full occupancy. In this expression, the low-lying discrete states i with spectroscopic factors $S_{\alpha i}$ are distinguished from the continuum that starts at the two-nucleon emission threshold E_{2N}. Hence the occupancies are

$$
n_\alpha = \sum_i S_{\alpha i} + \int_{E_{2N}}^\infty dE\, S_\alpha(E)
\tag{6.85}
$$

Note that this experimental representation of the spectral function is implicitly based upon a set of orbitals $\{\phi_\alpha\}$ for which $S_{\alpha\beta}$ is diagonal. When this approximation fails or when more than a single j-transfer is permitted for the transition, it becomes necessary to employ a more general representation based on Eq. (6.42) which permits interference between two or more single-particle contributions. Furthermore, analyses of continuum data are usually based upon an incoherent sum of single-particle momentum distributions and often permit, without firm justification, those distributions to vary with separation energy.

Since the hole state α is not a true eigenstate of the residual nucleus, it is useful to characterize the location and spreading of the hole strength by the

mean excitation energy $\bar{E}_\alpha$ and its dispersion σ_α defined by the moments

$$\bar{E}_\alpha = \int dE\, S_\alpha(E) E \tag{6.86a}$$

$$\sigma_\alpha^2 = \int dE\, S_\alpha(E)(E - \bar{E}_\alpha)^2 \tag{6.86b}$$

Assuming that $S_\alpha(E)$ is approximately gaussian, the spreading width

$$\Gamma_\alpha = 2\sigma_\alpha (2\ln 2)^{1/2} \tag{6.87}$$

is the full width at half maximum (FWHM) of the $S_\alpha(E)$ distribution.

For a discrete state or an energy bin E it is convenient to define $\rho_\alpha^D = S_\alpha(E)\varrho_\alpha^D$ for partial occupancy by including the spectroscopic strength. Note that the dependence of the distorted momentum distribution upon missing energy remains implicit. Thus the experimental definition of the distorted momentum distribution for a particular bin of missing energy becomes

$$\rho^D(E_m, \mathbf{p}_m, \mathbf{p}') = \frac{1}{K\sigma_{ep}} \frac{d\sigma}{d\varepsilon_f d\Omega_e d\varepsilon_p d\Omega_p} \tag{6.88}$$

This quantity is more properly referred to as the reduced cross section σ_{red}, but most authors identify it as ρ^D based upon the appealing physical interpretation of the factorization approximation.

A typical multipole decomposition of the spectral strength is shown in Fig. 6.4 for $^{16}\text{O}(e,e'p)$. The data[278] were acquired in parallel kinematics with $T_p \approx 96$ MeV. The missing momentum distributions for each 1 MeV bin of missing energy were fitted using a sum of three contributions with $l \leq 2$ according to Eq. (6.84). The rms radii for each l were determined from independent analyses of the discrete states and were assumed to be independent of E_m. The analysis is insensitive to the difference between spin–orbit partners, but for $l = 0$ a $2s_{1/2}$ orbital was used for $E_m < 20$ MeV while a $1s_{1/2}$ orbital was used for $E_m > 20$ MeV. Approximately 60% of the $1p$ IPSM strength is concentrated in two low-lying states with an additional 12% being distributed among smaller fragments with $E_m < 40$ MeV. Similarly, most of the $1d$ strength for $E_m < 40$ MeV is found in a single state. The $l = 0$ strength is distributed more broadly, with only about 45% being found within $E_m < 40$ MeV, and is clearly not saturated within the accessible range of missing energy.

6.6. Distorted Momentum Distributions for Valence Orbitals

In this section we review some of the specific results of high-resolution $(c,e'p)$ experiments for nuclei with $A > 4$. Most of these data were acquired
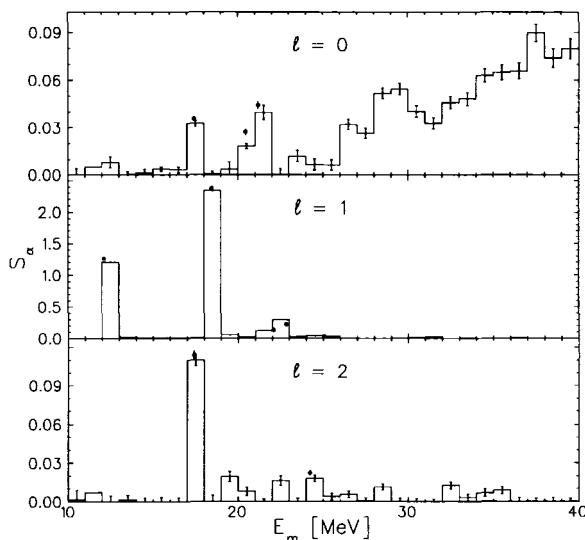
Fig. 6.4. Multipole decomposition of the spectral strength function for $^{16}O(e, e'p)$. The solid circles represent independent analyses for discrete states.

using the MEA facility at NIKHEF, where the resolution in missing energy is often 100 keV or better. A typical spectrum for $^{16}O(e, e'p)$ is shown in Fig. 6.5[278] for $p_m \approx 120$ MeV/c. The spectrum is dominated by two strong peaks corresponding to knockout from the $1p_{1/2}$ and $1p_{3/2}$ orbitals, with two much weaker $1p_{3/2}$ fragments appearing at higher excitation energy. The resolution is adequate to observe clearly the positive-parity doublet at an excitation energy of 5.3 MeV in ^{15}N.

A brief summary of the high-resolution $(e, e'p)$ data obtained by NIKHEF is given in Table 6.1. The column labelled observables lists the quantities of primary interest for each experiment, where $\rho(p_m)$ indicates the distorted momentum distribution, R_i with $i = L, T, LT$ indicates separated response functions, S indicates spectroscopic factors or shell-model occupancy, and R_G indicates the ratio between transverse and longitudinal response functions described in Section 7.1.3. The third column lists the orbitals for which data were obtained. Although $(e, e'p)$ has no specific sensitivity to the single-particle total angular momentum j, in some cases spectral information was used to differentiate between spin–orbit partners. The range of excitation energy E^* is given in the fourth column, where extended ranges indicate that a multipole analysis of the continuum was performed. The range of missing momenta is given in the fifth column. Most experiments are performed
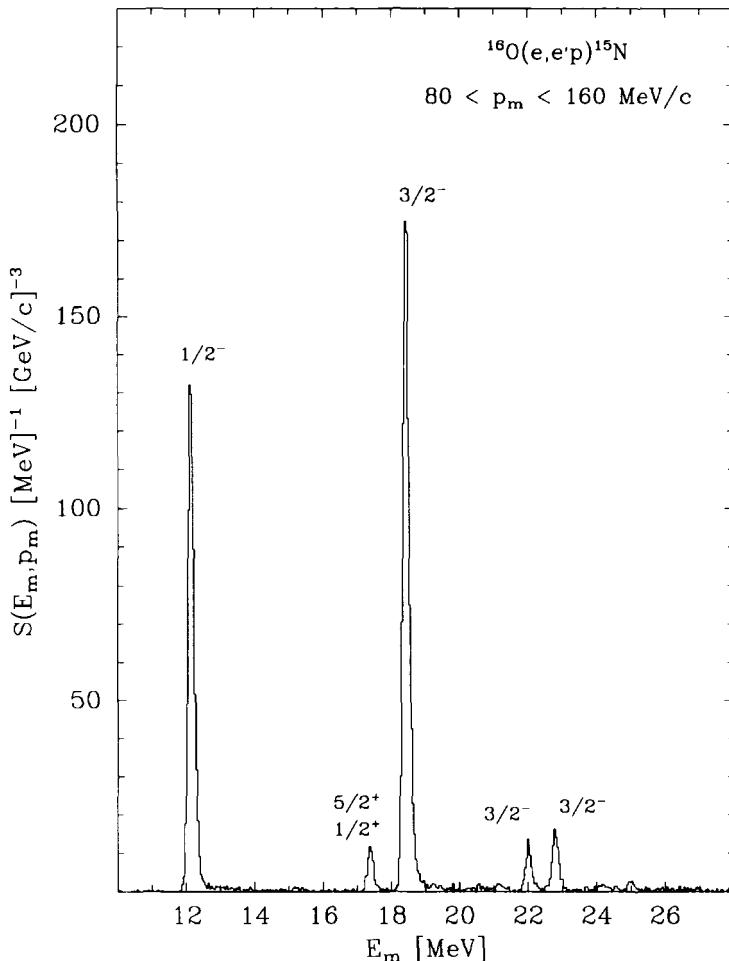
Fig. 6.5. Typical spectrum for $^{16}O(e, e'p)$.

with approximately constant kinetic energy in the residual system to minimize variations of the distortion corrections; T_p then indicates the equivalent laboratory kinetic energy for proton scattering by the residual nucleus. Parallel kinematics are indicated by $\parallel$ and quasiperpendicular kinematics by $\perp$ in the seventh column.

NIKHEF data are usually analyzed using the nonrelativistic distorted wave code DWEEPY developed by the Pavia group. [298] The second-order nonrelativistic reduction of the nucleon current is employed. Overlap functions are represented by bound-state wave functions in a Woods–Saxon well whose depth is constrained to reproduce the experimental separation energy and whose geometry is fitted to the shape of the momentum distribution. Nucleon distorted waves are usually based upon phenomenological optical potentials obtained either from global parametrizations, usually the Schwandt potential for $A \geq 16$ or Comfort and Karp for $A \sim 12$, or by fitting elastic scattering for particular targets and energies. Perey nonlocality factors are usually applied to both bound and scattering wave functions. Electron distortion is usually treated in either the effective momentum approximation or the method of Giusti and Pacati.[250] Each of these assumptions is critically reviewed in Section 5. However, a truly systematic evaluation of the data based upon a consistent model or consistent choices of parameters is not yet available.

Typical fits to distorted momentum distributions for valence orbitals are shown in Fig. 6.6.[299,300] For each target, data are shown for the two highest occupied orbitals. The data for ^{16}O,[278] ^{40}Ca,[220,290] and ^{208}Pb[277] were obtained with $T_p \approx 100$ MeV, while the data for ^{90}Zr[217,292] used $T_p = 70$ MeV. We observe that the simple model described above suffices to accurately describe the data for a wide range of targets and orbitals in the range of missing momenta $|p_m| < 300$ MeV/c that has been accessible to date. The shapes are reproduced using radial overlap functions whose rms radii are close to those predicted by Skyrme–Hartree–Fock calculations. The spectroscopic strength for each transition is then equal to the scale factor required to fit the distorted momentum distribution to the data for single-particle knockout. The uncertainties quoted for $S_\alpha(E_m)$ usually include an estimate of the range of variation consistent with uncertainties in the optical potential. However, usually only conventional Woods–Saxon optical potentials are considered. Nor are ambiguities in the nonlocality corrections considered. Since microscopic optical potentials often have more complicated shapes and may differ in absorption, this procedure underestimates the uncertainty in the spectroscopic amplitude. It is important in this regard to verify that the optical model reproduces reaction and total cross-section data, when available. A consistent description of elastic and inelastic scattering also tests the accuracy of the interior wave functions.

TABLE 6.1

Summary of High-Resolution $(e, e'p)$ Experiments

Target	Observables	Orbitals	E^*	p_m	T_p	Type	Refs.
^{6}Li	$\rho(p_m)$	cluster model	(0, 25)	(−100, 200)	65	$\parallel$	279, 280
	$\rho(p_m), R_G$	$1s, 1p$	(0, 25)				281
^{10}B	$\rho(p_m)$	$1p, 1s$	(0, 25)	(−160, 180)	78	$\parallel$	282
^{10}B	$\rho(p_m)$	$1p, 1s$	(0, 25)	(−160, 250)	139	$\parallel$	282
^{12}C	R_G	$1p_{3/2}$	0.0	(−90, 100)	70	$\parallel$	283
^{12}C	$\rho(p_m)$	$1p_{3/2}$	(0.0, 5.02)	(−170, 210)	70	$\parallel$	284
^{12}C	$\rho(p_m)$	$1s, 2s, 1d, 1f$	(4.4, 12.0)	(−170, 210)	70	$\parallel$	285
^{16}O	R_{LT}	$1p_{3/2}, 1p_{1/2}$	(0, 6.3)	(−200, 200)	160	$\perp$	286
^{16}O	R_L, R_T, R_{LT}	$1p_{3/2}, 1p_{1/2}$	(0, 6.3)	(−200, 200)	84	$\perp$	287
^{16}O	$\rho(p_m)$	$1p_{3/2}, 1p_{1/2}, 1d, 2s$	(0, 28)	(−180, 270)	96	$\parallel$	278
^{16}O	$\rho(p_m)$	$1p_{3/2}, 1p_{1/2}$	(0, 6.3)	(120, 700)	196	$\parallel, \perp$	288
^{30}Si	$\rho(p_m)$	$1d_{5/2}, 2s_{1/2}, 1d_{3/2}, 1p$	(0, 24)	(−40, 240)	90	$\parallel$	289
^{31}P	$\rho(p_m)$	$1d_{5/2}, 2s_{1/2}, 1d_{3/2}, 1p$	(0, 24)	(−40, 240)	90	$\parallel$	289
^{32}S	$\rho(p_m)$	$1d_{5/2}, 2s_{1/2}, 1d_{3/2}, 1p$	(0, 24)	(−40, 240)	90	$\parallel$	289
^{40}Ca	$\rho(p_m)$	$1d_{3/2}, 2s_{1/2}, 1f_{7/2}, 2p_{3/2}$	(0, 3.2)	(0, 270)	100	$\parallel$	220
			(0, 22)	(−220, 270)	100	$\parallel$	290
			(0, 22)	(−190, 340)	100	$\perp$	290
^{40}Ca	$\rho(p_m), R_{LT}$	$1d_{3/2}, 2s_{1/2}, 1f_{7/2}, 2p_{3/2}, 1d_{3/2}$	(0, 6.4)	(−225, 240)	70	$\parallel$	217
				(−200, 250)	70	$\perp$	
				(−180, 250)	135	$\parallel$	
				(−150, 240)	135	$\perp$	

^{40}Ca	R_G	$1d_{3/2}, 2s_{1/2}, 1d_{5/2}$	$(0, 6.4)$	$60, -38, 145$	100	$\parallel$	291
	R_L, R_T, R_{LT}	$1d_{3/2}, 2s_{1/2}, 1d_{5/2}$	$(0, 6.4)$	140	100	$\parallel, \perp$	291
^{48}Ca	$\rho(p_m)$	$1d_{3/2}, 2s_{1/2}, 1d_{5/2}, 1f_{7/2}, 2p$	$(0, 24)$	$(-60, 260)$	100	$\parallel$	290
^{51}V	$\rho(p_m)$	$1d_{3/2}, 2s_{1/2}, 1f_{7/2}, 1p_{5/2}$	$(0, 21)$	$(-20, 160)$	70	$\parallel$	292
				$(70, 280)$	100	$\parallel$	292, 293
^{90}Zr	$\rho(p_m)$	$2p_{1/2}, 1g_{9/2}, 2p_{3/2}, 1f_{5/2}$	$(0, 21)$	$(-20, 160)$	70	$\parallel$	292, 215
				$(70, 280)$	100	$\parallel$	292
^{90}Zr	$\rho(p_m)$	$2p_{1/2}, 1g_{9/2}, 2p_{3/2}, 1f_{5/2}$	$(0, 2)$	$(15, 235)$	70	$\parallel$	217
				$(15, 175)$	100	$\parallel$	
				$(20, 260)$	135	$\parallel$	
^{90}Zr	$\partial\rho(p_m)/\partial Q^2$	$2p_{1/2}, 1g_{9/2}, 2p_{3/2}, 1f_{5/2}$	$(0, 2)$	$120, 140$	$(61, 165)$	$\parallel$	291
^{142}Nd	$\rho(p_m)$	$2d_{5/2}, 1g_{7/2}, 3s_{1/2}, 1h_{11/2}$	$(0, 1)$	$(20, 260)$	100	$\parallel$	294
^{146}Nd	$\rho(p_m)$	$2d_{5/2}, 1g_{7/2}, 3s_{1/2}, 1h_{11/2}$	$(0, 1)$	$(20, 260)$	100	$\parallel$	294
^{205}Tl	$\rho(p_m)$	$3s, 2d, 1g, 1h$	$(0, 20)$	$(-50, 300)$	100	$\parallel$	277
^{206}Pb	S	$3s_{1/2}$	$(0, 5.5)$	$(15, 200)$	100	$\parallel$	295
^{206}Pb	$\rho(p_m)$	$3s, 2d, 1g, 1h$	$(0, 20)$	$(-50, 300)$	100	$\parallel$	277
^{208}Pb	S	$3s_{1/2}$	$(0, 5.5)$	$(15, 200)$	100	$\parallel$	296, 295
^{208}Pb	$\rho(p_m)$	$3s, 2d, 1g, 1h$	$(0, 20)$	$(-50, 300)$	100	$\parallel$	277
^{208}Pb	$\rho(p_m)$	$3s, 2d, 1g, 1h$	$(0, 4)$	$(300, 500)$	100		297
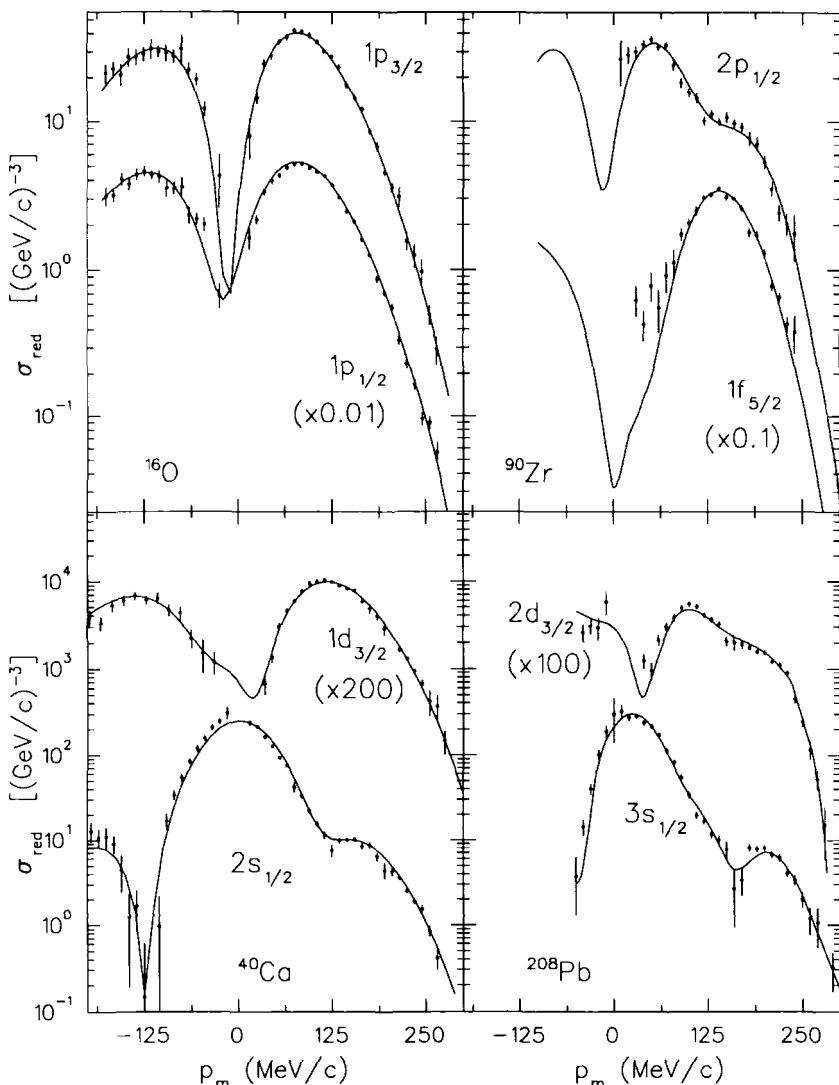
Fig. 6.6. Representative distorted momentum distributions in parallel kinematics. For each target, data for the two highest occupied orbitals are compared with fits made by the NIKHEF group using the DWEEPY code. Data for $T_p \approx 100$ MeV are shown for ^{16}O,[278] ^{40}Ca,[290] and ^{208}Pb,[277] while $T_p \approx 70$ MeV for ^{90}Zr.[217,292] Adapted from Lapikás.[299]

6.7.   Ejectile-Energy Dependence of Missing Momentum Distributions

An important test of the reliability of spectroscopic information deduced from $(e, e'p)$ data is its degree of independence from ejectile energy and kinematical arrangement (e.g., parallel vs. quasiperpendicular). In Fig. 6.7 we display reduced cross-section data for the lowest two states observed with the $^{40}\text{Ca}(e, e'p)^{39}\text{K}$ reaction for both parallel and quasiperpendicular kinematics with $T_p = 70$, 100, and 135 MeV. Some data sets include two beam energies, typically about 480 MeV (circles) and about 300 MeV (triangles), and good agreement between reduced cross sections is obtained where they overlap. The $T_p = 100$ MeV data were obtained using several beam energies, but were scaled to a common energy according to the ratio of distorted-wave calculations. The consistency between the data for different energies and the closeness between the calculations for those energies suggests that little error is introduced by that procedure. For each state, every data set is compared with calculations based upon the same bound-state wave function obtained from a Skyrme–Hartree–Fock calculation. The Schwandt optical potential and standard Perey factors were employed for the ejectile, and electron distortion was treated in EMA. Spectroscopic factors of 2.90 for the $1d_{3/2}$ and 1.35 for the $2s_{1/2}$ holes, obtained "by eye," were applied independent of the kinematical conditions. Thus, we avoid masking reaction model deficiencies by fitting both radii and spectroscopic factors to each set separately, which is the customary practice. We also note that fitted spectroscopic factors and radii are often highly correlated, which can artificially enhance the scatter in the results.

We find that there is good consistency between the missing momentum distributions for both parallel and quasiperpendicular kinematics over this range of ejectile energy. Although it might be possible to obtain slightly better fits to the data by varying the bound-state wave functions or by another choice of optical potential, it is not obvious that such improvements would apply uniformly to each data set. Upon close examination, we also notice that some of the data retain evidence of bunching in which small groups of points originating in successive spectrometer settings are slightly disjointed, suggesting that spectrometer acceptances were not always handled accurately enough. Nevertheless, the general level of consistency is impressive.

Unfortunately, much of the high-resolution data from NIKHEF is limited to $T_p \lesssim 100$ MeV, where accurate empirical effective interactions are not yet available and where optical-model ambiguities are relatively large. The data for $T_p \sim 135$ MeV should be more reliable, especially when analyzed
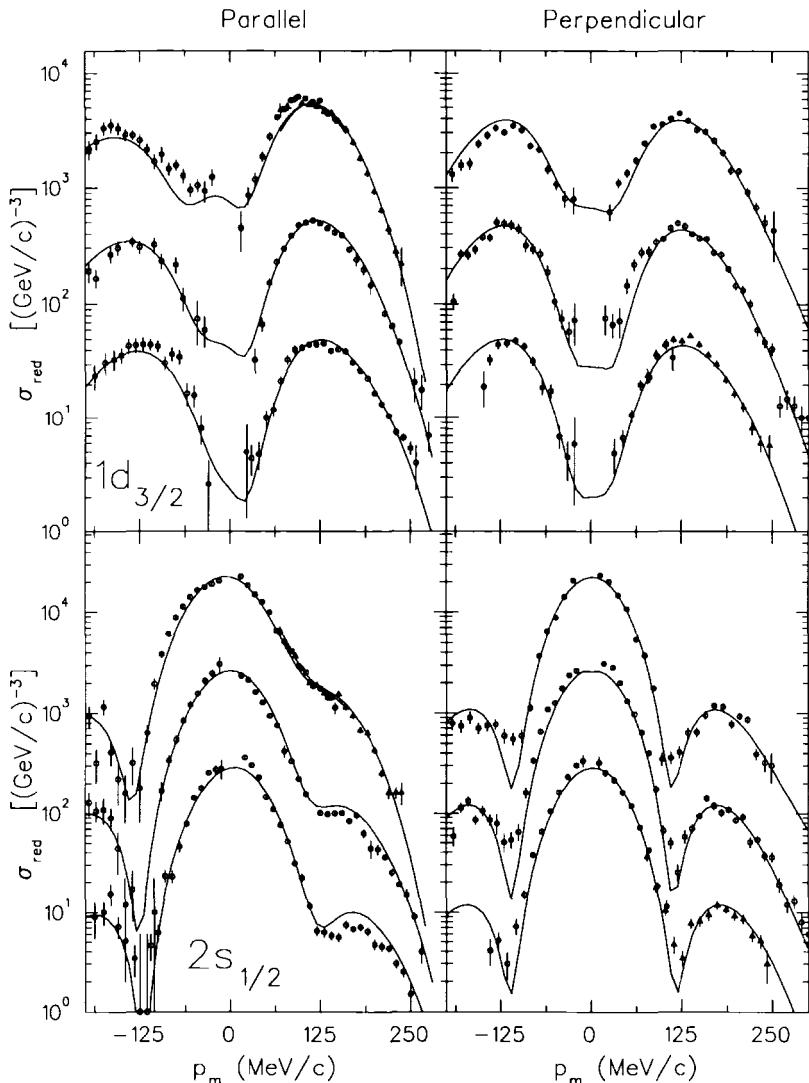
Fig. 6.7. Missing momentum distributions for ^{40}Ca$(e, e'p)$. The left (right) columns were obtained in parallel (quasiperpendicular) kinematics. Data for ejectile energies of 135, 100, and 70 MeV are shown scaled by factors of 1, 10, and 100, respectively. Data sets containing two beam energies are shown with circles (triangles) for the higher (lower) energy and two curves. Spectroscopic factors of 2.90 for the $1d_{3/2}$ and 1.35 for the $2s_{1/2}$ holes were applied independent of the kinematical conditions to wave functions from a Skyrme–Hartree–Fock calculation.

using EEI potentials. On the other hand, although we have criticized some properties of the Schwandt potential and it does break down at higher energies or smaller mass, it produces fairly accurate proton absorption and neutron total cross sections for $70 \lesssim T_N \lesssim 135$ MeV and $A \geq 40$. However, to test these analyses, it is necessary to extend the measurements to ejectile energies of 200 MeV or greater. Measurements at higher ejectile energies will soon be made at CEBAF, but in the meantime measurements with $T_p \sim 200$ MeV can be made at Mainz.

The first such measurements at Mainz were made for ^{16}O by Blomqvist et al.[288] using an electron beam energy of 855 MeV and an ejectile energy of 196 MeV. These data are compared in Fig. 6.8 with NRDWIA calculations based upon the mean-field wave functions fitted to the NIKHEF data of Leuschner et al.[278] The Schwandt potential was used by Blomqvist et al. even though it is clearly not the best choice for ^{16}O. At moderate missing momenta there appears to be a substantial difference between the spectroscopic factors deduced for ejectile energies near 100 and 200 MeV, with the 200 MeV data falling well below the predictions based upon the 100 MeV data. Since the EEI potential is more transparent at 200 MeV, it would produce even larger cross sections and hence would exacerbate the problem. Yet we demonstrated in Section 5.4.7 that near 200 MeV the Schwandt potential is too absorptive, while the EEI potential fits the available transparency data. Data were also taken at Mainz with $T_p = 93$ MeV where agreement with the NIKHEF results was obtained. Therefore, if the normalization of the 200-MeV data is correct, there appears to be a serious problem with the energy dependence of the reaction model used to analyze the proton knockout data for $T_p \sim 200$ MeV. It is important to confirm these data and to perform similar measurements at higher energies and for other targets.

6.8. Occupation Probabilities

Occupation probabilities for ^{208}Pb have been deduced by Quint et al.[277] from $(e, e'p)$ data for parallel kinematics with $T_p \approx 100$ MeV. Occupation numbers were obtained by integrating the experimental spectral function for excitation energies up to 25 MeV, where the continuum was decomposed into multipole contributions. The spectral functions for the more deeply bound orbitals were extrapolated beyond the measured range of excitation energy by fitting their observed portions using a Gaussian parametrization of the quasihole spectral function,

$$S_\alpha^G(E) = \frac{Z_\alpha}{\sqrt{2\pi}\sigma_\alpha} \exp\left[-\frac{(E - E_\alpha)^2}{2\sigma_\alpha^2} \right] \tag{6.89}$$
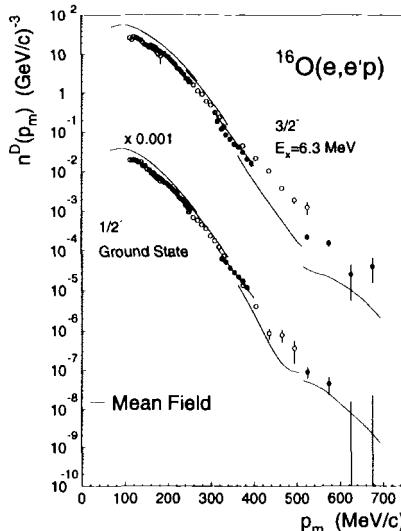
Fig. 6.8. Missing momentum distributions for $^{16}O(e, e'p)$ obtained with $E_0 = 855$ MeV and $T_p = 196$ MeV. Six kinematic settings are distinguished by alternating open and filled circles. The first four sets use parallel kinematics, while the fifth and sixth sets use $\theta_{pq} = 42°$ and $62°$, respectively. The curves for each setting are based upon the Woods–Saxon momentum distributions fitted to the $T_p = 96$ MeV data by Leuschner et al.[278] Figure from Blomqvist et al.[288]

where $\sigma_\alpha = 0.425\Gamma^{BR}(E_\alpha)$. Thus, corrections were applied for the approximately 12% of the total $1g$, $2p$, and $1f$ strengths and 50% of the $2s$ strength that was assumed to lie beyond the measured range of excitation energy.

These results are compared with theoretical calculations due to Pandharipande et al.[301] in Fig. 6.9. Occupation probabilities for nuclear matter, $n_{NM}(k)$, were calculated according to the correlated basis function (CBF) theory of Fantoni et al.[302] using the Urbana v_{14}+TNI interaction.[303] For deeply bound states they obtain an occupancy of about 0.86. For finite nuclei, such as ^{208}Pb, coupling to collective surface modes leads to an additional depletion of states near the Fermi surface. A correction δn_{RPA} for this effect was estimated by Gogny[304] using RPA theory and was added to n_{NM} to produce a prediction for n_{Pb}. Pandharipande et al. argue that double counting of correlations should be minimal because most of the second-order effects in the CBF nuclear matter theory arise from tensor interactions which are absent in Gogny's RPA model, while the latter describes long-range correlations absent in the former. These RPA corrections reduce $n(k_F)$ from about 0.8 to about 0.6 at the Fermi surface. Nevertheless, the $(e, e'p)$ results indicate that
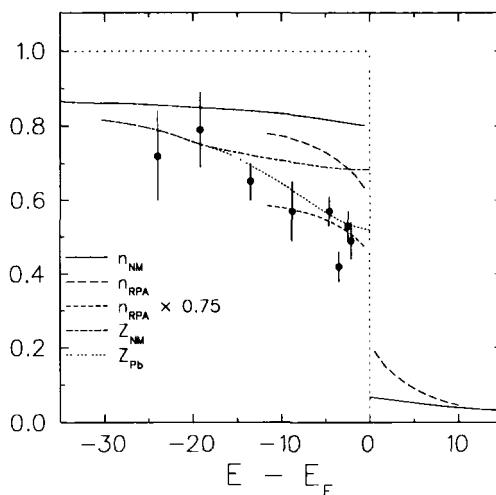
Fig. 6.9. Occupation probability and quasiparticle strength for ^{208}Pb. The solid curve represents the nuclear matter occupation probability of Fantoni *et al.*,[302] the long dashes include an RPA correction estimated by Pandharipande *et al.*,[301] and the medium dashes represent $n \approx 0.75(n_{nm} + \delta n_{RPA})$ fitted to the ^{208}Pb($e, e'p$) data of Quint *et al.*[277] In addition, quasiparticle strengths for nuclear matter (lead) are shown as dash-dotted (short dashed) curves.

even more depletion of the valence orbitals is needed: they can be fitted by $n \approx 0.75(n_{nm} + \delta n_{RPA})$.

To assess the theoretical uncertainty in the nuclear matter calculations, we note that Baldo *et al.*[261] obtained a depletion of deeply bound orbitals that is larger by approximately 0.04 than for the Urbana model, but at the Fermi surface the difference becomes rather sizable with $n(k_F) = 0.62$ for Paris versus 0.79 for Urbana. The corresponding wounds are $\kappa = 0.24$ for the Paris versus 0.16 for the Urbana interactions. The stronger depletion obtained with the Paris interaction probably arises from its stronger tensor component.[261] However, if we were to apply the same RPA correction suggested by Pandharipande to the occupation probability of Baldo, $\mathcal{Z}(k_F)$ would be reduced from 0.44 to about 0.15, which is probably too small.

To assess the experimental uncertainty, we note that more recent analyses of the same data for the $3s_{1/2}$ hole give larger spectroscopic factors,[299] about 0.65, than obtained by Quint,[277] about 0.49. If we assume that similar factors should be applied for other orbitals, then good agreement is obtained with the theoretical predictions shown in Fig. 6.9; in fact the occupancy of the deepest observed holes would be somewhat larger than expected. The differences between these analyses arise from the choices of optical potentials

and various refinements of the NRDWIA calculations, such as improvements in the treatment of electron distortion, but a systematic reevaluation of the data is not yet available.

There remains some ambiguity in whether to compare summed spectroscopic strengths with occupation probabilities, $n(E)$, or with quasiparticle strengths, $Z(E)$. Benhar *et al.*[260] argue that since it is unlikely that the integration of the $(e, e'p)$ data with respect to missing energy included much of the background contribution to the spectral function, which is spread thinly over a wide range of energy, the summed spectroscopic strength should be compared to the quasiparticle strength rather than to the occupation probability. Their CBF calculation of $Z_{NM}(E)$ for nuclear matter is also shown in Fig. 6.9, along with an estimate of the quasiparticle strength for lead, $Z_{Pb}(E)$, obtained by modifying the imaginary part of the CBF mean field to better reproduce experimental spreading widths. This model gives a good account of the spectroscopic data for ^{208}Pb$(e, e'p)$, although once the data are reanalyzed with more accurate Coulomb distortion it is likely that they will fall between the curves shown for Z_{Pb} and Z_{NM}.

Quasiparticle strengths have been calculated by van Neck *et al.*[305] for a wide range of A from an evaluation of the spectral function in finite nuclei using a local-density approximation (LDA). For valence holes they predict $Z \approx 0.74$ with very little dependence upon A. However, since the model does not include surface effects, they estimated the additional depletion due to long-range correlations using the model of Ma and Wambach,[275,276] Eq. (6.69), and obtained $Z_{Pb}(E_F) = 0.50$ for lead, which is somewhat too small. On the other hand, Ma and Wambach[276] obtained quasiparticle strengths slightly greater than the data shown in Fig. 6.9.

The quasiparticle strengths deduced for the orbitals immediately below and above the Fermi level are shown in Fig. 6.10 for $A > 4$. These data were obtained by summing the spectroscopic factors for fragmented strength observed for excitation energies up to about 20 MeV, and were divided by the IPSM values. Thus, approximately 65% of the IPSM strength is found below 20 MeV excitation for orbitals immediately below the Fermi level, while nominally unoccupied orbitals are populated to approximately 7% by ground-state correlations. Little dependence upon mass number is evident. The schematic representation of the quasihole spectral function shown in Fig. 6.2 suggests that about 10% of the quasihole strength for valence orbitals lies at higher excitation energy where unambiguous extraction becomes difficult. We also note that there are significant uncertainties in the fitted spectroscopic factors arising from the reaction model for $T_p \lesssim 100$ MeV. Therefore, we conclude that these results are qualitatively consistent with the quasiparticle strengths predicted by many-body theory or deduced from dispersive optical model analyses.
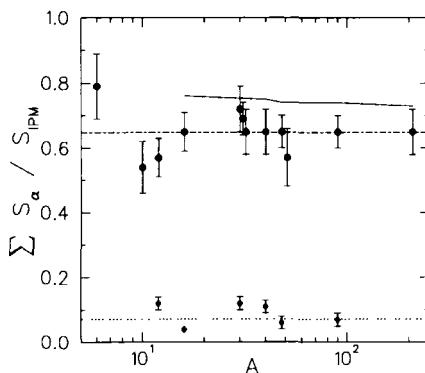
Fig. 6.10. Integrated spectroscopic factors for orbitals just below (circles) and just above (diamonds) the Fermi level compared to IPSM values. Averages for nominally occupied (unoccupied) orbitals are indicated by dash–dot (dotted) lines. The LDA predictions from van Neck *et al.*[305] for closed-shell nuclei are indicated by the solid line.

6.9. High Momentum Components

6.9.1. Continuum Contributions

Short-range and tensor correlations are expected to strongly enhance momentum distributions for $p_m > 300$ MeV/c, especially for the high-energy continuum. In infinite nuclear matter, such correlations deplete the occupation numbers and distribute the hole strength over a broad energy region. These effects are illustrated in Figs. 6.11 and 6.12, which display momentum densities for ^{16}O that were calculated by Müther *et al.*[306,307] from a spectral function, based on a realistic interaction, that was constructed using a self-consistent Green's function approach. Fig. 6.11 shows partial-wave momentum distributions for $l \leq 2$ separated into quasihole and continuum contributions. Müther and Dickhoff[306] showed that the valence wave functions are very close to the Hartree–Fock wave functions. For modest momenta, these quasihole contributions dominate $n(k)$ for occupied orbitals, but beyond 400 MeV/c the continuum contributions become dominant and decrease relatively slowly as k increases. Fig. 6.12 shows the spectral function summed over partial waves with $l \leq 2$ and integrated over several ranges of missing energy, demonstrating that short-range correlations populate high momentum components that are distributed over a very broad energy range up to at least 200 MeV.

Therefore, the short-range and tensor correlations are relatively unimportant for valence quasihole states, but as the excitation energy increases the knockout strength is shifted toward greater momenta. The net effect upon the $1p_{1/2}$ momentum distribution for $p > 400$ MeV/c is predicted to be an enhancement over the mean-field result by about two orders of magnitude that arises from background configurations which contribute only about 4% to the occupancy of that orbital.

The calculation of Müther et al.[307] is also compared in Fig. 6.12 with a nuclear matter result based upon the Reid soft-core potential. Although they used an interaction with a softer core, similar comparisons would be obtained from more modern potentials, such as Paris or Urbana, also. For large k the net momentum density for ^{16}O appears to remain substantially below the nuclear matter result, in part because the average density is lower and in part because partial waves with $l > 2$ have not been included. Recently it has become possible to perform variational Monte Carlo calculations for relatively light complex nuclei, such as ^{16}O, and Pieper et al.[308] find that the high momentum tail is close to that of nuclear matter. Sick et al.[309] showed that very similar results for the momentum density can be obtained from the local-density approximation (LDA) and that, in fact, surprisingly accurate results are obtained even for ^{4}He. Similar results were obtained for heavier nuclei by van Neck et al.[305] using an improved LDA; they also showed that within the LDA the high momentum tail is dominated by continuum contributions extending to very high excitation energy. On the other hand, none of these models includes coupling to the low-lying collective states which are presumably responsible for considerable additional fragmentation of the quasihole strength and which may enhance the distorted momentum distribution at large p_m for valence–hole states.

Several experiments exploiting the new high-duty factor capabilities of the NIKHEF and Mainz laboratories have recently measured proton knockout for missing momenta greater than 300 MeV/c. Missing-energy spectra for high-momentum components in the ^{16}O$(e, e'p)$ reaction are illustrated in Fig. 6.13. [288,310] These spectra were acquired at Mainz using an 855 MeV electron beam. The data are presented in the form of reduced cross sections and have not been subjected to radiative unfolding. Each spectrum spans a broad range of missing momentum, such that the four spectra shown are nearly contiguous. These data demonstrate that the spectral function for small p_m is dominated by the low-lying valence hole transitions, but that for large p_m continuum configurations with much greater missing energy dominate.

A simple interpretation of the high-momentum tail suggests that a large fraction of the continuum strength arises from single-nucleon knockout that breaks a correlated pair with large internal momentum. One member of
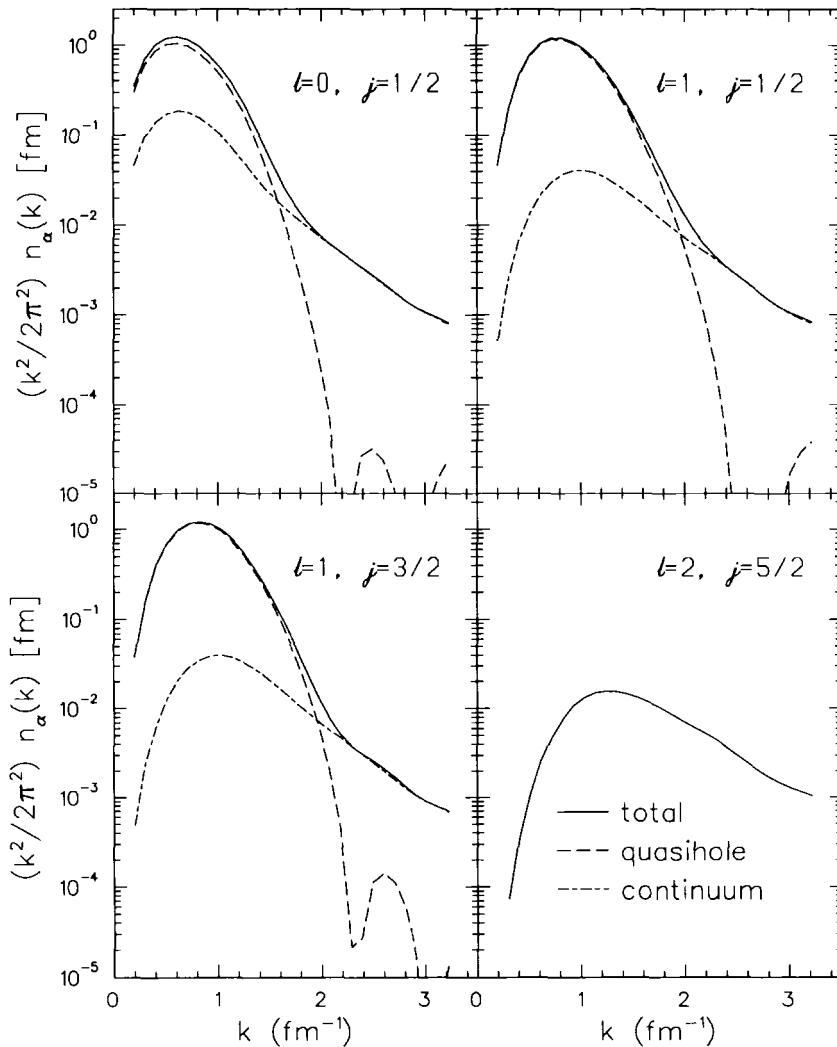
Fig. 6.11. Partial-wave momentum distributions, in the form $k^2 n_\alpha(k)$, for ^{16}O with $l \leq 2$. Dotted curves portray the quasihole and dashed curves the continuum contributions.
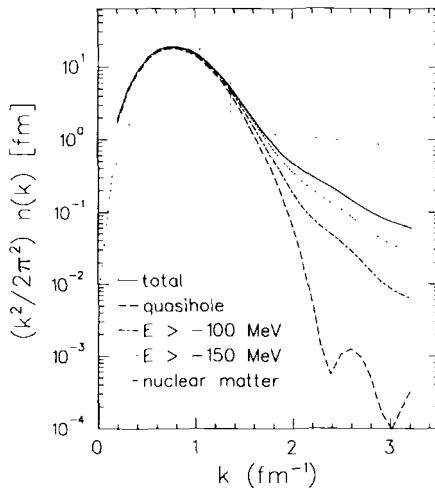
Fig. 6.12. Momentum distribution for ^{16}O in the form $k^2 n(k)$. The long-dashed curve shows the quasihole contribution, the dash–dotted curve is integrated up to 100 MeV excitation, the short-dashed is integrated to 150 MeV excitation, and the solid curve represents the total momentum density for ^{16}O carried by partial waves $l \leq 2$. A nuclear matter result for the Reid soft-core potential is shown for comparison.

the pair is detected in the $(e, e'p)$ experiment while the undetected spectator carries away a large kinetic energy, thereby representing a large excitation energy with respect to the ground state of the $A - 1$ system. Thus, to first order the missing energy and momentum for this process are related by

$$E_m = E_{2N} + \left(\frac{A-2}{A-1}\right) \frac{p_m^2}{2m_p} \tag{6.90}$$

where E_{2N} is the two-nucleon emission threshold. Measurements for ^{3,4}He$(e, e'p)$ performed at Saclay[141,147] have shown that for large momenta there is a prominent peak in the missing-energy distribution whose centroid is consistent with this quasideuteron mechanism and that the momentum distribution for $p_m > 200$ MeV/c is similar to that of the deuteron. The peak is broadened by the momentum distribution of the cluster with respect to the core, but a similar kinematic signature of nucleon knockout from a correlated pair is also seen in preliminary data for ^{16}O$(e, e'p)$ that extend to missing energies of about 200 MeV.[310] These findings are qualitatively consistent with theoretical predictions, such as those of Müther and Dickhoff[306] shown in Figs. 6.11 and 6.12, but to obtain a more complete understanding of the hole spectral function for large E_m it will be necessary to separate the single-
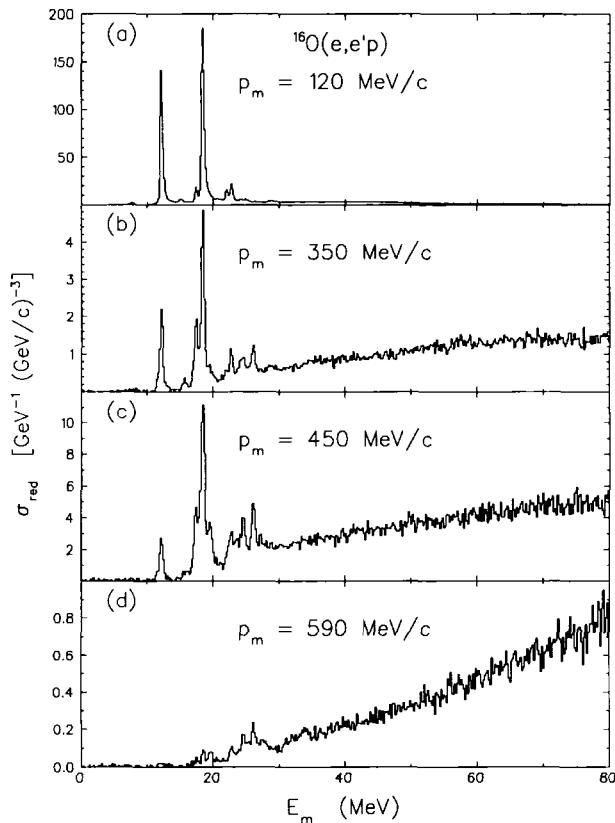
Fig. 6.13. **Missing-energy distributions for $^{16}O(e,e'p)$ are presented as reduced cross sections without radiative unfolding.** The data were acquired at Mainz by Refs. 288, 310 using a beam energy of 855 MeV. The kinematics are: (a) parallel with $T_p = 93$ MeV; (b) parallel with $T_p = 196$ MeV; (c) quasiperpendicular with $(\omega, q) = (247$ Mev, 497 MeV/$c)$; and (d) quasiperpendicular with $(\omega, q) = (252$ Mev, 318 MeV/$c)$.

nucleon mechanism from direct multinucleon mechanisms (see Section 7.6).

One would like to observe both members of a correlated pair directly and to reconstruct the initial momentum of the pair relative to the core. One would also like to observe more complicated configurations in which the excitation energy is shared among more than two energetic nucleons. Observation of such processes should provide insight into the nature of three-nucleon interactions in nuclear matter. Separation of the longitudinal and transverse response functions should greatly assist in the interpretation of the reaction mechanisms involved in multinucleon knockout. Investigations of these phenomena are beginning to be made at the new high duty-factor facilities using large acceptance detectors.

6.9.2. Quasihole Contributions

At NIKHEF, Bobeldijk *et al.*[297] have measured ^{208}Pb$(e, e'p)$ for $300 < p_m < 500$ MeV/c with $(\omega, q) = (110$ Mev, 221 MeV/$c)$ and $T_n = 100$ MeV. The data for several low-lying transitions are shown in Fig. 6.14. For smaller p_m the new results, shown as solid circles, agree well with earlier data from Quint *et al.*,[277] shown as crosses. At large missing momentum the data are enhanced with respect to predictions based upon Woods–Saxon wave functions. To investigate this enhancement, the data are also compared with calculations based upon overlap functions of the form

$$\phi_\alpha(r) \propto G(r)\phi_\alpha^{(WS)}(r) \tag{6.91}$$

where ϕ_α is the normalized quasihole function, $\phi_\alpha^{(WS)}$ is a wave function for a local Woods–Saxon potential, and

$$G(r) = \sqrt{\frac{m^*(r)}{m}} \tag{6.92}$$

is a nonlocality function based upon the local effective mass.

Various models of the nonlocality correction are compared in Fig. 6.15. In models for which the self-energy lacks substantial energy dependence, such as that of Pandharipande,[311] the effective mass is governed by m_k and the nonlocality correction is similar to the Perey–Buck model or to the Skyrme–Hartree–Fock result. Enhancement of m_E near the surface introduces a localized feature at the surface whose Fourier transform contains much stronger high-momentum structure than is found in mean-field wave functions. Hence, the model of Ma and Wambach predicts a much greater enhancement of these high momentum components than does that of Mahaux and Sartor. The data appear to show a slight preference for the intermediate predictions based upon
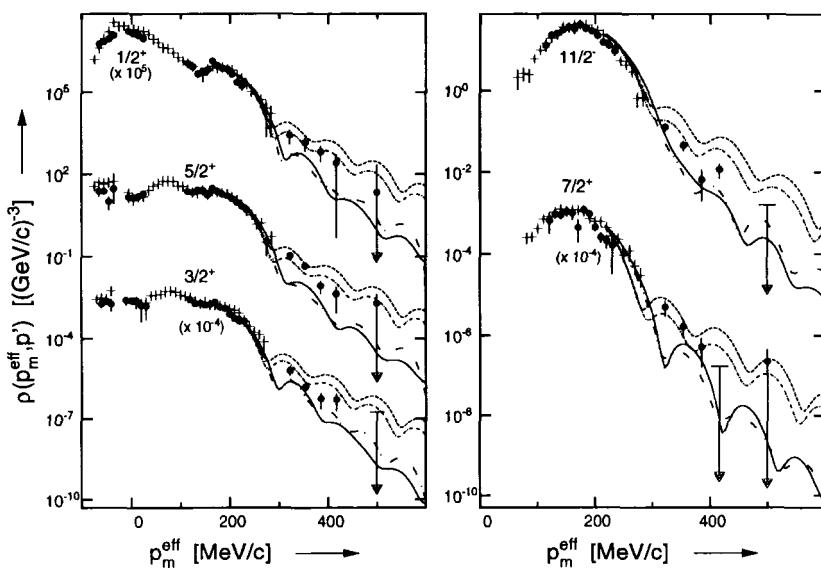
Fig. 6.14. Missing momentum distributions for ^{208}Pb$(e, e'p)$. Solid circles represent new data by Bobeldijk *et al.*[297] for $(\omega, q) = (110$ Mev, 221 MeV/c$)$ and $T_p = 100$ MeV. Solid curves are based upon mean-field wave functions, while dash-dot-dot, dash-dot, and dashed curves include $G(r)$ factors from models due to Pandharipandhe, Mahaux, and Sartor, and Ma and Wambach, respectively.
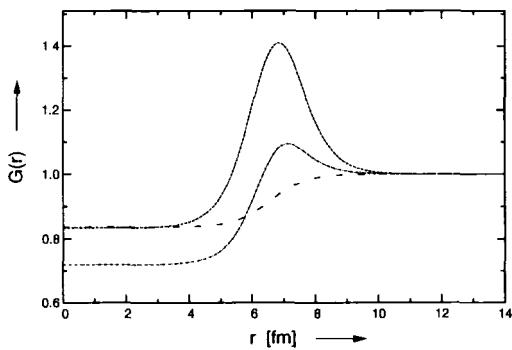
Fig. 6.15. $G(r) = [m^*(r)/m]^{1/2}$ **for protons in ^{208}Pb from Pandharipandhe (dash-dot-dot), Ma and Wambach (dashed), and Mahaux and Sartor (dash-dot).**

the effective mass deduced from the dispersive optical model of Mahaux and Sartor. However, within the context of that model the proper nonlocality factor would have been $[m_k(r)/m]^{1/2}$, which is closer to the Pandharipande model, instead of $[m^*(r)/m]^{1/2}$, as proposed by Ma and Wambach and as applied in Fig. 6.14. As discussed in Section 6.3, these prescriptions differ in their treatment of the quasiparticle strength, with a local treatment given by Mahaux and a global treatment by Ma and Wambach.

The missing-momentum distributions for low-lying transitions in the $^{16}O(e, e'p)$ reaction, displayed in Fig. 6.8, also show a significant enhancement over mean-field predictions for $p_m > 400$ MeV/c, particularly for the state which is more deeply bound. Thus, these results agree qualitatively with the findings for ^{208}Pb and with the expectation that high momentum components become more pronounced with increasing binding energy, but the dominant effect for small E_m and large p_m is probably coupling to surface excitations rather than short-range correlations. However, the failure of calculations based upon wave functions fitted to the data for $T_p \sim 100$ MeV to reproduce these data, with $T_p \sim 200$ MeV, for moderate missing momentum must be understood before definitive conclusions can be drawn.

In Section 7.5 we show that at large missing momentum the reduced cross section for valence–hole states can be substantially enhanced by channel coupling in the final state, particularly for quasiperpendicular kinematics. These effects have not been included in the analysis of the data for ^{208}Pb or for low-lying states in $^{16}O(e, e'p)$. To the extent that the E-mass factor represents the average effect of such couplings, the replacement of m_k by m^* in the nonlocality factor may be an equivalent description, but a more detailed analysis would be needed to evaluate this speculation.

6.10. Summary

The hole spectral function plays a central role in the investigation of single-particle motion in nuclei. A consistent theoretical description of the spectral functions for both nuclear matter and finite nuclei has emerged. For nuclear matter, short-range and tensor correlations deplete the Fermi sphere by approximately 15–20% and populate nominally empty orbitals, thereby producing a long tail on the momentum distribution. The quasihole strength near the Fermi surface is then about 0.5–0.7 and increases with binding energy. In finite nuclei, coupling to low-lying surface modes (long-range correlations) produces additional depletion of the valence hole states, increases the population of nominally empty orbitals, and spreads the quasihole strength over several fragments. These effects probably enhance the missing momentum distributions for quasihole states beyond $p_m > 300$ MeV/c also. The momen-

turn distribution for $p_m < 300$ MeV/c is dominated by low-lying quasihole contributions, but as the missing momentum increases more complicated continuum configurations at high excitation energy dominate. Short-range and tensor correlations spread the high momentum strength over several hundred MeV of excitation energy.

A systematic survey of missing-momentum distributions and spectroscopic factors for quasihole states in complex nuclei has been made at NIKHEF with a missing-energy resolution that is often better than 100 keV. For $p_m < 300$ MeV, the missing-momentum distributions are generally consistent with mean-field calculations, with little dependence upon the kinematical conditions of the experiment. The valence hole strength for $A > 4$ is typically about 65% of independent-particle model expectations, while nominally empty orbitals just above the Fermi level are occupied to typically 5–10%. The quasihole strengths and spreading widths for low-lying excitations are consistent with dispersive optical models which provide a consistent semiphenomenological treatment of the mean field for both positive and negative energies. The results are also qualitatively consistent with many-body theory, although further developments will be needed to incorporate surface effects more consistently.

However, most of the NIKHEF data were acquired with ejectile energies that are lower than optimal and analyzed with optical potentials that are not particularly reliable. Furthermore, the quality of distorted wave calculations has improved significantly during the time the data were acquired, but in most cases the earlier data have not been reanalyzed with the improved techniques. Hence, it is desirable to perform a consistent and uniform analysis of the data within the context of the dispersive optical model, which provides mean-field potentials for both positive and negative energies in a consistent approach. It is also important to perform measurements with higher ejectile energies where empirical effective interactions fitted to both inelastic and elastic scattering data can be applied. Unlike traditional optical potentials fitted to elastic scattering data alone, the consistent use of elastic and inelastic scattering data provides sensitivity to the interior wave function needed for knockout reactions. The resulting potentials provide accurate predictions for proton absorption and neutron total cross sections and for nuclear transparency measured in $(e, e'p)$ experiments for $T_p \sim 200$ MeV. Measurements of nuclear transparency to higher energy protons are planned for CEBAF. Measurements of missing momentum distributions for discrete states should also be made for comparison with the NIKHEF results and to test the reaction models used to extract spectroscopic information from the knockout data. More incisive tests of the reaction mechanism can be made with measurements of interference and polarization response functions.

For quasihole transitions at small excitation energy there is at larger miss-

ing momenta a modest enhancement with respect to mean-field calculations, but for much larger missing momentum preliminary data from Mainz show that the continuum dominates the spectral function. The data from Mainz and Saclay for large momenta and excitation energy are qualitatively consistent with a quasideuteron mechanism in which one member of a correlated pair is detected while an undetected high-momentum partner carries away most of the excitation energy. In the future it will be important to explore the continuum more carefully, defining the momentum and energy dependences of single nucleon and various multinucleon channels separately.

7. STUDIES OF THE REACTION MECHANISM FOR NUCLEON KNOCKOUT

Inclusive quasielastic electron scattering data for $A \geq 4$ exhibit several characteristic deviations with respect to the impulse approximation. Although the nonrelativistic Fermi gas model[312] appeared to provide a satisfactory explanation of the early inclusive (e, e') cross-section data[313,314] for excitation energies below the dip region, Rosenbluth separations[315–321] showed that the longitudinal response function is strongly suppressed in the quasifree region while the transverse response remains closer to the impulse approximation, such that the ratio R_T/R_L is enhanced with respect to the impulse approximation. Furthermore, although there may be experimental difficulties, the Coulomb sum rule for $A \geq 4$ is not saturated within the accessible range of excitation energy. However, some caution must be exercised with respect to these conclusions. Recent measurements of ^{40}Ca(e, e') at MIT-Bates by Yates *et al.*[322] exploit a wider range of electron scattering angles to reduce systematic errors in the separation procedure and obtain substantially larger longitudinal response functions than were obtained at Saclay by Meziani *et al.*[318,319] They now find good agreement between the integrated longitudinal strength and predictions of the relativistic Fermi gas model.[323] Furthermore, they find that the longitudinal response function itself is described fairly well by a relativistic Hartree model[254,324] and conclude that deviations with respect to the impulse approximation are not as large as previously believed. Therefore, it is important to verify these findings and, if correct, to remeasure the quasifree longitudinal response functions for other targets.

There have been innumerable attempts to interpret these and other anomalies in the inclusive response functions, but none has been entirely successful. The status of inclusive electron scattering is beyond the scope of the present review, but more information and references can be found in several other recent reviews.[3,325] To obtain further insight into the electronuclear reaction mecha-

nism and to distinguish between various possible mechanisms, it is necessary to decompose the inclusive process into its constituent exclusive channels and to study the electromagnetic response functions for each. In this manner one hopes to disentangle the roles of correlations, meson-exchange currents, isobar excitation, medium modifications of the electromagnetic properties of the nucleon, many-body currents, final-state interactions, relativistic corrections, et cetera, et cetera, et cetera. Since each of these mechanisms may affect the spin structure of the nuclear current differently, it is important to measure interference response functions and recoil polarization observables in both coplanar and noncoplanar kinematics. Furthermore, nucleon knockout from discrete orbitals with differing spatial localization and average density can be used to probe the density dependence of nucleon form factors.

In this section we consider studies designed to elucidate various aspects of the electronuclear reaction mechanism as manifested by nucleon knockout reactions. Although the exclusive data for one- and two-nucleon knockout that are presently available cover a very limited fraction of the phase space for inclusive electron scattering, the results obtained thus far have already provided much insight and suggest that the more complete and more accurate experiments that will become possible with new high duty-factor accelerators and large acceptance detectors should be most enlightening.

7.1. Enhancement of R_T/R_L

Inclusive quasielastic electron scattering data for $A \geq 4$ exhibit several characteristic deviations with respect to the impulse approximation. For the purposes of this section it is sufficient to note that near the quasielastic peak the transverse response R_T is generally near the impulse approximation but that a substantial suppression is observed in the longitudinal response R_L,[316,326] while in the dip region much more transverse yield is observed than can be accounted for by meson-exchange currents and pion production.[327,328] Hence, in both regions the ratio R_T/R_L is larger for nuclear matter than for the free proton.

7.1.1. y-Scaling

In the simplest version of the impulse approximation for quasielastic scattering, the inclusive cross section

$$\frac{d^3\sigma}{d\omega d\Omega_e} \propto (Z\sigma_{ep} + N\sigma_{en}) f(y) \tag{7.1a}$$

$$f(y) = 2\pi \int_{|y|}^{\infty} dk\, k\, n(k) \tag{7.1b}$$

factors into an elementary electron–nucleon cross section for a moving nucleon times a structure function $f(y)$ which depends upon the nucleon momentum distribution parallel to $\vec{q}$. The variable y is defined to be the minimum value of the initial nucleon momentum consistent with energy conservation, and thus is determined from the relationship

$$\omega + m_A = \sqrt{m_N^2 + (y+q)^2} + \sqrt{m_B^2 + y^2} \tag{7.2}$$

where m_A, m_B, and m_N are the masses of the target, residual system, and ejected nucleon. If we neglect the nuclear binding energy and assume that $m_A = m_B + m_N$, then

$$y = -\frac{q}{2} + \frac{m_N \omega}{q} \sqrt{\frac{\vec{q} \cdot \vec{q}}{Q^2} \left(1 + \frac{Q^2}{4m_N^2}\right)}$$

depends only upon q and ω. Thus, the inclusive cross section is said to exhibit y-scaling behavior to the extent that its dependence upon q and ω can be reduced to a dependence upon the single kinematical variable, $y = y(q, \omega)$.

In the nonrelativistic limit, the scaling variable reduces to

$$y_{nr} = \frac{m_N \omega}{q} - \frac{q}{2}$$

In the same limit, the quasielastic peak is defined by

$$\omega = \frac{\vec{q} \cdot \vec{q}}{2m_M} + \frac{\vec{p} \cdot \vec{q}}{m_N}$$

and hence occupies a region with width

$$\Delta\omega = \pm q k_F / m \Rightarrow \Delta y \approx \pm 0.3 m_N$$

Thus, large negative y, defined to be $y/m_N < -0.3$, corresponds to high momentum components antiparallel to $\vec{q}$ which populate the low-ω side of the quasielastic peak. Conversely, $y/m_N \approx 0.3$ corresponds to the dip region and large positive y to large-ω processes that permit pion production and excitation of baryon resonances.

Since the derivation of y-scaling neglects nonnucleonic degrees of freedom, it is expected to apply primarily to the negative-y side of the quasielastic peak and under those conditions one might hope to extract the nucleon momentum distribution from the scaling function,

$$n(k) = -\frac{1}{2\pi y} \frac{df}{dy}\bigg|_{y=-k} \tag{7.3}$$
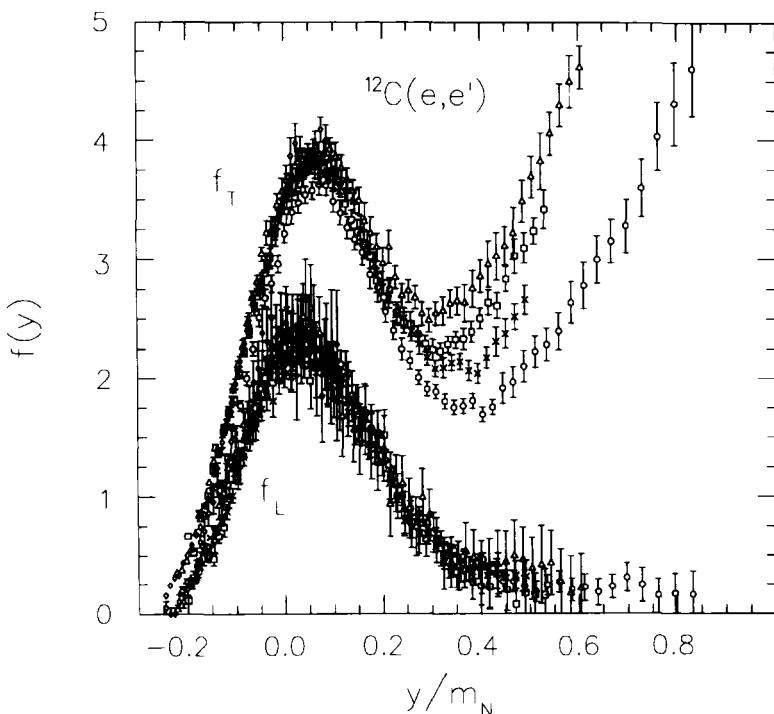
Fig. 7.1. Scaling analysis of separated data for $^{12}C(e, e')$. Circles, crosses, squares, triangles, and diamonds correspond to $q = 400, 450, 500, 550,$ and 600 MeV/c, respectively.

Scaling violations due to binding corrections have been analyzed by degli Atti et al.[329] The data acquired at SLAC[330] for $0.5 < q < 2.2$ GeV/c do exhibit y-scaling for negative y.

    Similarly, the impulse approximation permits separated response functions to be factored into elementary nucleon response functions times structure functions, such as

$$R_{L(T)} = \left[Z R^p_{L(T)} + N R^n_{L(T)} \right] f_{L(T)}(y) \qquad (7.4)$$

where the naive impulse approximation would require that there be a common scaling function, $f_L(y) = f_T(y) = f(y)$. The results of a scaling analysis[326] of separated data[316] for $^{12}C(e, e')$ are shown in Fig. 7.1. Although q is not very large, both of the separated response functions for the quasielastic peak, $|y/m_N| < 0.3$, individually appear to exhibit y-scaling with convergence being evident as q increases. However, the data clearly show that the transverse

response is enhanced with respect to the longitudinal response by a factor of about 1.7. (The strong transverse response in the dip and delta regions, $|y/m_N| > 0.3$, is not relevant to the present discussion.) This enhancement is characteristic of nuclei with $A \geq 4$, but is absent for $A = 3$.

7.1.2. Longitudinal and Transverse Response Functions for $^{12}C(e, e'p)$

Several semiexclusive $^{12}C(e, e'p)$ experiments have been performed at MIT–Bates in an effort to elucidate various aspects of the electronuclear reaction mechanism. The kinematics of those experiments are summarized in Table 7.1. Note that, unlike the definition used in most of this paper, the MIT group defines the missing energy to be $E_m = \omega - T_p$, where the recoil energy of the residual system is not subtracted. Since the difference between these definitions is usually small, all figures based upon the data listed in Table 7.1 employ the MIT convention despite the small inconsistency with figures employing the other convention. As indicated by the column labelled $\max(E_m)$, most of these experiments span a wide range of missing energy. Each bin of missing energy integrates a fairly wide range of missing momenta. Typical ranges for the p-shell and s-shell are indicated. The MIT experiments did not have the resolution to obtain missing momentum distributions like those obtained by NIKHEF, but cover a much broader range of missing energy and Q^2, and hence the former provide reaction mechanism information complementary to the structure information of the latter.

The longitudinal and transverse response functions for $^{12}C(e, e'p)$ in the quasielastic region were separated by Ulmer *et al.*[332] using parallel kinematics with $q \approx 400$ MeV/c and $\omega \approx 120$ MeV, which is approximately 30 MeV above the center of the quasielastic peak. These separated response functions and the difference between the corresponding transverse and longitudinal spectral functions are illustrated in Fig. 7.2. The bins of missing energy are wide enough to compress the peak corresponding to $1p$-shell knockout into a single bin at about 17 MeV which includes recoil momenta in the range between about 30 and 110 MeV/c. The broad peak centered near 40 MeV corresponds to the $1s$-shell. The R_L and R_T spectra appear similar for $E_m < 50$ MeV, but substantial excess strength persists in the transverse response up to the highest missing energy observed. The difference $(S_T - S_L)$ between the transverse and longitudinal spectral functions is consistent with zero for the bound $1p$-shell region, becomes positive near the threshold for two-nucleon emission $(E_m = 28$ MeV), grows across the $1s$ peak, and appears to reach a substantial plateau for $E_m > 50$ MeV.

Thus, the Rosenbluth separations performed at MIT–Bates for quasifree

TABLE 7.1

Summary of MIT–Bates $^{12}C(e, e'p)$ Experiments

q MeV/c	ω MeV	$\Delta\omega$ MeV	E_0 MeV	θ_e deg	Q^2 (GeV/c)^2	y/m_N MeV	$\max(E_m)$	p-shell p_m MeV/c	s-shell p_m MeV/c	Refs.
400	200	52	459	60	0.120	0.29	155	163: 262	129: 232	331
397	122	33	288	120	0.143	0.10	65	6: 108	−38: 71	332
397	122	64	443	60	0.143	0.10	65	−26: 140	−73: 105	
401	275	37	460	60	0.085	0.47	225	312: 367	283: 340	333
473	382	53	647	39.5	0.078	0.56	320	405: 455	380: 431	
585	210	59	505	90	0.298	0.05	155	−23: 113	−56: 84	216
775	355	69	698	90	0.475	0.05	290	23: 155	−3: 130	
827	325	72	686	100	0.578	−0.05	135	−84: 68	−111: 43	
990	475	58	796	118.1	0.754	−0.05	400	−17: 102	−40: 79	334
970	330	66	696	129.7	0.832	−0.18	270	−221: −66	−248: −91	
913	235	76	781	85.1	0.778	−0.23	200	−325:−154	−356:−181	335
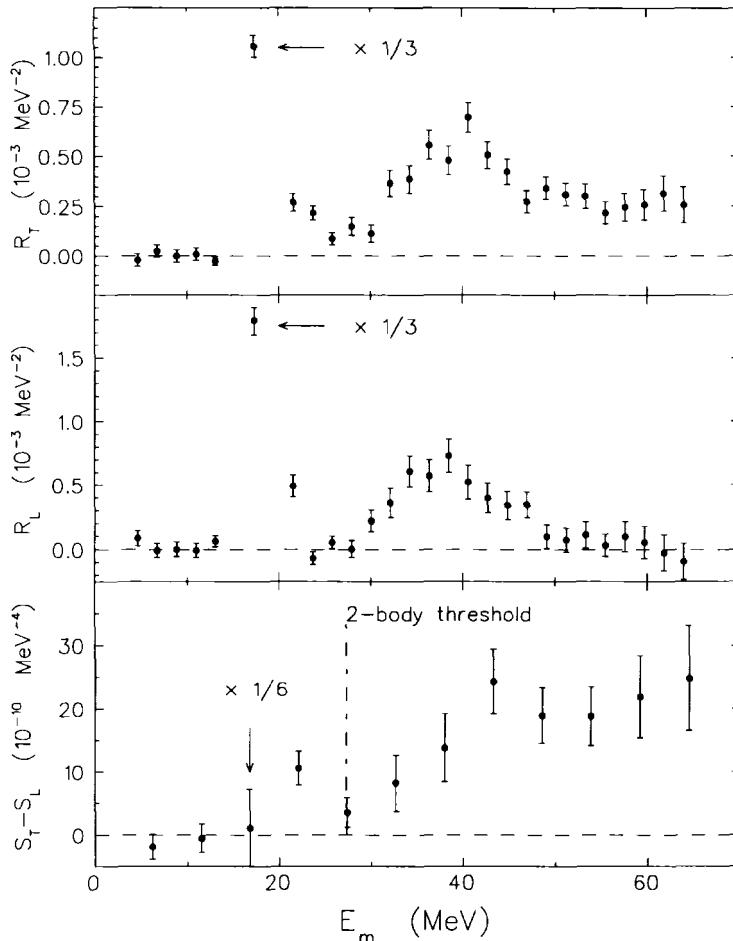
Fig. 7.2. Separated $^{12}C(e, e'p)$ transverse and longitudinal response functions for parallel kinematics near the quasielastic peak with $q = 400$ MeV/c and $\omega = 120$ MeV. The difference between the corresponding transverse and longitudinal spectral functions is shown in the bottom panel. Radiative corrections have been applied.

knockout demonstrate that the transverse/longitudinal coupling, R_T/R_L, for the lp-shell of ^{12}C is essentially the same as for the free proton, but that the transverse response function is enhanced in the continuum. The situation for the ls-shell is somewhat ambiguous because it is difficult to separate the broad peak for single-nucleon knockout from the underlying continuum that begins at the nearby threshold for two-nucleon emission. Hence, it would be of interest to determine explicitly the R_T/R_L ratio for two-nucleon emission. The contrast between consistency for bound final states and enhancement of R_T/R_L for the continuum suggests that the enhancement of f_T/f_L for inclusive quasielastic scattering arises primarily from multinucleon processes.

7.1.3. Enhancement of R_T/R_L from Momentum Distributions in Parallel Kinematics

The electromagnetic properties of bound nucleons have also been studied at NIKHEF-K using higher resolution but lower momentum transfer. Possible variations of the ratio between transverse and longitudinal coupling can be monitored by the quantity

$$R_G(Q^2) = \left[\frac{4m_p^2}{Q^2} \frac{W_T(Q^2)}{W_L(Q^2)} \right]^{1/2} \tag{7.5}$$

obtained as a ratio between the transverse and longitudinal response functions integrated over a quasiparticle peak. In the plane-wave impulse approximation this quantity would simply be

$$R_G^{PWIA}(Q^2) = \frac{G_M(Q^2)}{G_E(Q^2)} \approx \mu_p \tag{7.6}$$

but distortion alters $R_G(Q^2)$. The effect of distortion can be removed by evaluating the ratio

$$\eta = \frac{R_G^{\text{expt}}}{R_G^{DWIA}} \tag{7.7}$$

between experimental and DWIA values of R_G. Two methods have been used to obtain R_G or η from measurements in parallel kinematics.

First, the ratio between reduced cross sections for backward versus forward electron scattering angles can be determined for the same values of Q^2 and p_m. This method is equivalent to Rosenbluth separation, except that to first order the ratio is independent of the missing momentum distribution. Measurements of R_G have been made for ^{6}Li,[336,281] ^{12}C,[283] and ^{40}Ca[337]

using this method. Although the data suggest an enhancement with respect to the impulse approximation, most of the apparent enhancement for low-lying states is accounted for simply by spin–orbit proton distortion[338,339] and, particularly for heavier targets, electron distortion.[29] Effects due to relativistic dynamics[340] and meson exchange and isobar currents[339] have also been estimated and found to be consistent with the observations. For missing energies above the two-nucleon emission threshold, there remains a significant enhancement with respect to DWIA that is best presented in terms of η as below.

Second, recognizing that for the same magnitude of p_m antiparallel kinematics requires a larger electron scattering angle than parallel kinematics, the asymmetry between missing momentum distributions for antiparallel versus parallel kinematics can be correlated with the ratio η between the transverse and longitudinal coupling of the virtual photon to the bound proton. Since Q^2 changes with p_m for parallel kinematics, analyses of this type generally assume that η may depend upon E_m but is independent of Q^2 or p_m. Measurements of $\eta(E_m)$ using this method have been made for ^{6}Li,[281] ^{12}C,[284,285] and ^{10}B[282] and are illustrated in Fig. 7.3. These data, which are qualitatively consistent with those of Ulmer et al.,[332] show that the transverse/longitudinal ratio below the threshold for two-nucleon emission is consistent with unity, but that the ratio is enhanced for larger missing energy. By exploiting differences between the spatial localization of various orbitals, there also have been attempts to correlate the apparent transverse/longitudinal anomaly observed in knockout for light nuclei with average density,[336,283] but no compelling evidence for density dependence of this effect has been found.

Several objections can be raised to the above analyses. The enhancement of the transverse/longitudinal ratio appears to be most prominent where the least is known about final-state interactions. The analyses employ optical potentials which are independent of target excitation, but the validity of that assumption is very difficult to evaluate. Although the differences between distorting potentials for valence versus deep-hole knockout have not been investigated, it seems plausible to suppose that such differences will be greatest for small nuclei and their effects most important at low energy. Yet most of the data were acquired for light targets and small ejectile energies (about 70 MeV for ^{6}Li and ^{12}C or 139 MeV for ^{10}B) where the final-state interactions are expected to depend most strongly upon differences between the structures of the A and $A - 1$ systems. Moreover, in most cases the optical potentials were based upon proton scattering for the target rather than for the residual nucleus, were assumed to be spherical, and were parametrized using simple Woods–Saxon shapes which, as discussed in Section 5.4.3, are not realistic for small tar-
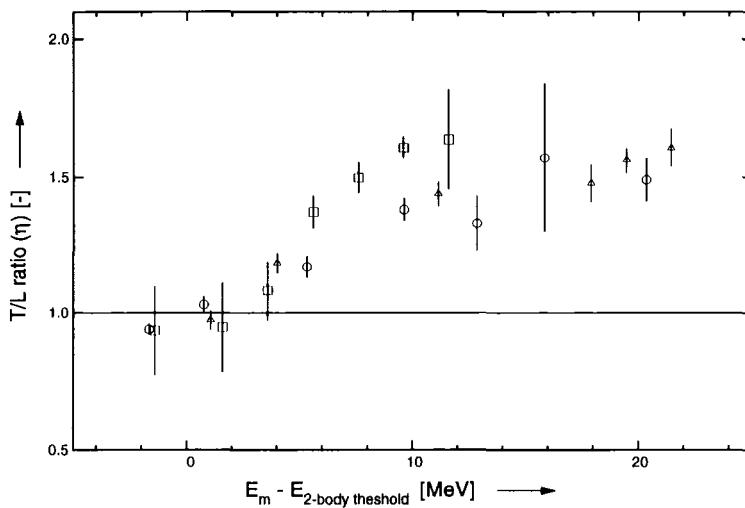
Fig. 7.3. The dependence of the transverse enhancement factor η for $(e, e'p)$ upon the missing energy above the two-body emission threshold based upon measurements on ^{12}C (squares), ^{6}Li (triangles), and ^{10}B (circles).

gets. It has also been demonstrated[284] that inelastic scattering within the final-state interaction can appreciably alter the extracted value of η. Additional effects due to charge exchange may also be important but have not been evaluated systematically. Finally, it has been shown that the asymmetry between parallel and antiparallel kinematics is sensitive to the imaginary part of the spin–orbit optical potential,[341] but that term is difficult to determine from proton elastic scattering data and is absent from many of the potentials used to extract R_G . Hence, we conclude that uncertainties due to final-state interactions have surely been underestimated. Nevertheless, the consistency between the NIKHEF measurements of η and the MIT measurements of $S_T - S_L$ does support an enhancement of R_T/R_L above the two-nucleon emission threshold.

Therefore, the available data suggest that the ratio R_T/R_L is consistent with the free nucleon response functions for small missing energies but is enhanced above the threshold for two-nucleon emission. Although it is possible that both $G_E(Q^2)$ and $G_M(Q^2)$ could change in the nuclear medium with their ratio remaining unaffected, the observation that $R_T \gg R_L$ for $E_m > 50$ MeV suggests that a new transverse current is involved rather than a modification of the single-nucleon current. Additional evidence for multinucleon absorption of the virtual pho-

ton is reviewed in Section 7.6, but the various reaction channels have not been isolated nor have longitudinal/transverse separations been performed. Hence, given the scarcity of separated response function data for large E_m and the uncertainties in final-state interactions for light targets and low ejectile energies, the present data can hardly be considered conclusive. To obtain more definitive results, more systematic data for separated response functions are required for heavy targets and high ejectile energies. It is also highly desirable to characterize each of the reaction channels that contribute to the continuum.

7.2. The Swollen Nucleon Hypothesis

There has been much speculation about the role that possible medium modifications of the electromagnetic properties of nucleons in nuclear matter might play in explaining the EMC effect or the suppression of the inclusive longitudinal response function for quasifree electron scattering. Among these is the hypothesis that the nucleon size increases with nuclear density[342–344] This effect could manifest itself in a Q^2 dependence of spectroscopic factors deduced using free nucleon form factors.

The spectroscopic factors for $1p$ and $1s$ knockout from ^{12}C has been deduced from the MIT data for $0.10 \leq Q^2 \leq 0.75$ (GeV/c)^2. These data, illustrated in Fig. 7.4, include estimates of the uncertainties due to final-state interactions. Note that for this purpose we consider only the data closest to the quasielastic peak, namely, $|y/m_N| < 0.15$. Despite their relatively large uncertainties, these data clearly suggest that the spectroscopic factors decrease as Q^2 increases. The data for both shells are fitted well by the same relative slope

$$\frac{1}{S_\alpha(0)} \frac{dS_\alpha(Q^2)}{dQ^2} = -0.5 \pm 0.2 \text{ (GeV/}c)^{-2} \tag{7.8}$$

suggesting that the effect is attributable to the bound nucleon form factors. However, each of these experiments integrated over different ranges of missing momenta without obtaining p_m distributions, and some of the data for large negative y give different results at similar Q^2, so that it is difficult to assess the accuracy of the models used to extract the spectroscopic factors. Therefore, although these results are qualitatively consistent with a 5% swelling of the nucleon, higher precision data with complete missing momentum distributions for a wide range of Q^2 are needed for several targets before a definitive conclusion can be drawn.
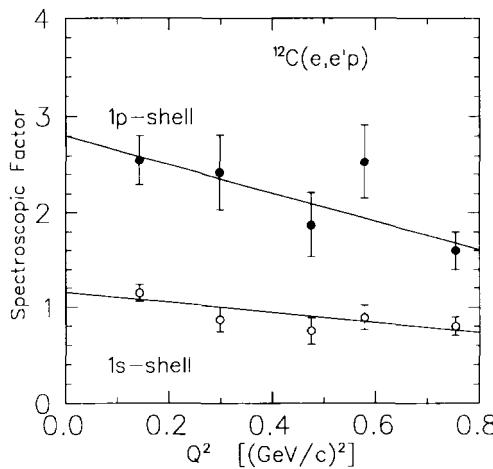
Fig. 7.4. Spectroscopic factors for ^{12}C$(e, e'p)$ deduced from data for parallel kinematics near the quasielastic peak. The data are restricted to $|y/m_N| < 0.15$.

7.3. Interference Response Functions for Complex Nuclei

Only a few measurements of interference response functions have been reported for complex nuclei.

7.3.1. R_{LT} Measurements

The longitudinal–transverse interference response function R_{LT} for ^{16}O$(e, e'p)$ has been measured for the lowest $1p_{1/2}$ and $1p_{3/2}$ hole states by Chinitz *et al.*[286] for $T_p = 160$ MeV and by Spaltro *et al.*[287] for $T_p = 84$ MeV, which correspond to $Q^2 = 0.30$ and 0.20 (GeV/c)^2, respectively. These data are compared in Fig. 7.5 with standard nonrelativistic DWIA calculations which use overlap parameters fitted to the data[278] for parallel kinematics. Although the Schwandt optical potential is not the best choice for ^{16}O, we used it because the data for all three experiments,[278,286,287] were originally compared with calculations based upon that potential and R_{LT} is relatively insensitive to variations of the optical potential. With this model we find that the reduced cross sections for parallel kinematics are fitted by spectroscopic factors of 1.40 and 2.35 for the lowest $(1p_{1/2})^{-1}$ and $(1p_{3/2})^{-1}$ states, respectively.* The calculations of R_{LT}

---

*Leuschner *et al.*[278] obtained spectroscopic factors of 1.22 and 2.13 from the same model. Also note that contrary to their description, the microscopic optical potential was obtained from the Paris–Hamburg interaction and was not calibrated against proton inelastic scattering data.
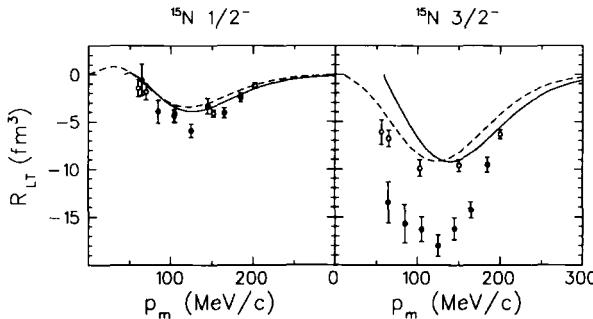
Fig. 7.5. Longitudinal–transverse interference response function for $^{16}O(e, e'p)$ are compared with standard nonrelativistic DWIA calculations based on fits to data for the distorted momentum distribution in parallel kinematics.[278] Solid circles[287] and solid lines are for $T_p = 84$ MeV; open circles[286] and dashed lines are for $T_p = 160$ MeV.

shown in Fig. 7.5 are based upon the same model and use the same spectroscopic factors. The fit to the data for the ground-state transition could be improved by an enhancement factor, but that factor is not as large as the factor of 1.5 suggested by Spaltro *et al.* However, for the $1p_{3/2}$ hole state it is necessary to increase the calculations by a factor of about 2.0 at $T_p = 84$ MeV while the corresponding factor is much smaller at $T_p = 160$ MeV. Spaltro *et al.* point out that the discrepancy for the $1p_{3/2}$ hole state between the two energies is actually larger than this estimate because the data of Chinitz *et al.* include an unresolved contribution, estimated to be about 10%, from a $1d2s$ doublet. Therefore, there appears to be a deficiency in the DWIA model of the R_{LT} response function which depends strongly upon nuclear structure and which appears to decrease with either increasing Q^2 or with increasing T_p. This observation requires further experimental confirmation and theoretical investigation.

7.3.2. R'_{LT} Measurements

The first measurements of the so-called fifth response function, R'_{LT}, were made at MIT-Bates by Mandeville *et al.*[345] for $^{12}C(\vec{e}, e'p)$ using the OOPS (out-of-plane spectrometer) positioned at azimuthal angle $\phi = 90°$ above the scattering plane to detect protons with about 50 MeV kinetic energy. The beam analyzing power, A, is proportional to R'_{LT}. The data for A are compared in Fig. 7.6 with NRDWIA calculations based upon a Schrödinger-equivalent optical potential for $p + {}^{12}C$ from Dirac phenomenology[180] or the
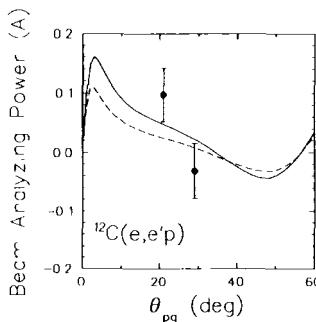
Fig. 7.6. The beam analyzing power data for $^{12}C(\vec{e}, e'p)$ are compared with NRDWIA calculations using a potential from Dirac phenomenology (dashes) or from Comfort and Karp (solid).

optical potential of Comfort and Karp.[177]* The calculations of Boffi and Radici[346] indicate that in this observable there is relatively little sensitivity to MEC+IC.

7.4.   Meson Exchange and Isobar Currents

7.4.1.   Two-Body Current Operators

Two-body and higher-order contributions to the electromagnetic current for a many-body system will most likely become apparent in separated response functions, especially the interference and polarization response functions, because their spin structure can differ from that of the one-body current. Two groups, based at Pavia[346–348] and Gent,[349–351] have made theoretical investigations of the role of meson-exchange currents (MEC) and isobar currents (IC) in the nucleon knockout reactions (γ, N) and $(e, e'N)$. Both consider the same set of diagrams, displayed in Fig. 7.7, but differences between their implementations of the model lead to substantial differences between their predictions.

The momentum-space representation of the meson-exchange current is obtained from a nonrelativistic reduction through order m^{-2} of one-pion exchange diagrams using pseudovector coupling. At this level of approximation, the pair current $\mathbf{J}^p$ vanishes, while the pion-in-flight, $\mathbf{J}^\pi$, and contact

---

*Note that the authors of Ref. 345 also show calculations based upon optical potentials from Schwandt et al.,[174] which applies neither to the target nor the ejectile energy of their experiment, and from Abdul-Jalil and Jackson,[175,176] which produces an imaginary potential with unphysical sign for the relevant energies. Neither is appropriate.
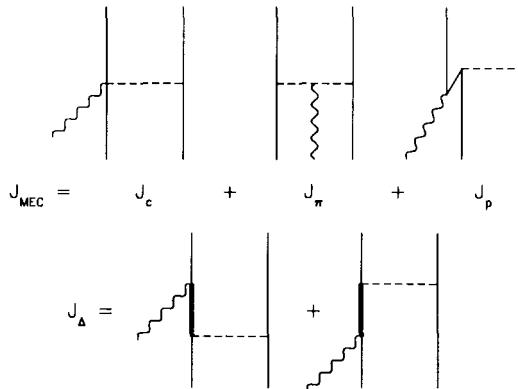
Fig. 7.7. Feynman diagrams for MEC and IC contributions to the two-body current operator. The contact (J_c), pion-in-flight (J_π), and pair (J_p) contributions to the meson exchange current (J_{MEC}) are shown in the top row and the isobar current (J_Δ) is shown in the bottom row.

(or seagull), $\mathbf{J}^c$, diagrams result in currents of the form

$$\mathbf{J}^\pi(\mathbf{k}_1, \mathbf{k}_2) = -i \frac{f_{\pi NN}^2}{m_\pi^2} F_{\gamma\pi\pi}(Q^2)[\tau^{(1)} \otimes \tau^{(2)}]_3$$

$$\times \frac{\sigma^{(1)} \cdot \mathbf{k}_1}{m_\pi^2 + k_1^2} \frac{\sigma^{(2)} \cdot \mathbf{k}_2}{m_\pi^2 + k_2^2} (\mathbf{k}_2 - \mathbf{k}_1) \qquad (7.9a)$$

$$\mathbf{J}^c(\mathbf{k}_1, \mathbf{k}_2) = -i \frac{f_{\pi NN}^2}{m_\pi^2} F_{\gamma N\pi}(Q^2)[\tau^{(1)} \otimes \tau^{(2)}]_3$$

$$\times \left\{ \sigma^{(1)} \frac{\sigma^{(2)} \cdot \mathbf{k}_2}{m_\pi^2 + k_2^2} - \frac{\sigma^{(1)} \cdot \mathbf{k}_1}{m_\pi^2 + k_1^2} \sigma^{(2)} \right\} \qquad (7.9b)$$

where m_π is the pion mass and $f_{\pi NN}^2/4\pi = 0.079$ is the πNN coupling constant. The spin, isospin, and momentum transferred to nucleon i are denoted by $\sigma^{(i)}$, $\tau^{(i)}$, and $\mathbf{k}_i$, respectively. Current conservation at the one-pion level requires all contributions to the meson exchange current to be scaled by the same form factor.[327] Hence, the Pavia group uses $F_{\gamma\pi\pi}(Q^2) = F_{\gamma N\pi}(Q^2) = F_1^V(Q^2)$ where F_1^V is the isovector Dirac form factor for the nucleon. The Gent group, on the other hand, uses the dipole form factor for $F_{\gamma N\pi}$ and a pion form factor $F_{\gamma\pi\pi}$ based upon the vector dominance model.

The two-body current that arises from intermediate excitation of the Δ isobar has the form of a cross product between the momentum transfer $\mathbf{q}$ and a function of the spins and the momenta transferred to the two interacting particles. Since a current of this form is divergenceless, form factors can be

used to regulate both the electromagnetic and strong vertices without disturbing current conservation. Again, the operators employed by the two groups have similar forms but differ in both the form factors and the relative weights assigned to the various terms.

The Pavia group uses a model of the two-body current based upon the chirally invariant lagrangian of Peccei[352,353] in which

$$
\mathbf{J}^\Delta(\mathbf{k}_1, \mathbf{k}_2) = -i\frac{\kappa^* h f_{\pi NN}}{3m_N m_\pi^2} F_{\gamma N\Delta}(Q^2)\mathbf{q}
$$

$$
\otimes \left\{ 2M_1 \left[\tau_3^{(1)} \mathbf{k}_1 \frac{\boldsymbol{\sigma}^{(1)} \cdot \mathbf{k}_1}{m_\pi^2 + k_1^2} + \tau_3^{(2)} \mathbf{k}_2 \frac{\boldsymbol{\sigma}^{(2)} \cdot \mathbf{k}_2}{m_\pi^2 + k_2^2} \right] \right.
$$

$$
+ M_2 \left[\boldsymbol{\tau}^{(1)} \otimes \boldsymbol{\tau}^{(2)} \right]_3
$$

$$
\left. \times \left[\left(\mathbf{k}_2 \otimes \boldsymbol{\sigma}^{(1)} \right) \frac{\boldsymbol{\sigma}^{(2)} \cdot \mathbf{k}_2}{m_\pi^2 + k_2^2} - \frac{\boldsymbol{\sigma}^{(1)} \cdot \mathbf{k}_1}{m_\pi^2 + k_1^2} \left(\mathbf{k}_1 \otimes \boldsymbol{\sigma}^{(2)} \right) \right] \right\}
$$

where

$$
M_1 = \frac{2m_\Delta + 3m_N}{m_\Delta^2 - m_N^2} \quad \text{and} \quad M_2 = \frac{2m_\Delta + m_N}{m_\Delta^2 - m_N^2}
$$

Here $h^2 = 0.290$ and $\kappa^* = 5.0$ represent the $\pi N\Delta$ and $\gamma N\Delta$ coupling constants in the Peccei lagrangian, respectively.[352,353] The electromagnetic form factor of the isobar is assumed to have the dipole form

$$
F_{\gamma N\Delta}(Q^2) = \left(1 + \frac{Q^2}{\Lambda_\Delta^2} \right)^{-2} \tag{7.10}
$$

with $\Lambda_\Delta = 855$ MeV/c based upon the static quark model. However, with these choices of coupling constants, the strength of J^Δ is approximately 50% stronger than predicted by the static quark model.[348]

The Gent group uses

$$
\mathbf{J}^\Delta(\mathbf{k}_1, \mathbf{k}_2) = -i\frac{2f_{\gamma N\Delta} f_{\pi N\Delta} f_{\pi NN}}{9m_\pi^3 (m_\Delta - m_N - \omega - i\Gamma_\Delta(\omega)/2)}
$$

$$
\times F_{\gamma N\Delta}(Q^2) F_{\pi N\Delta}(Q^2) F_{\pi NN}(Q^2)\mathbf{q}
$$

$$
\otimes \left\{ 4 \left[\tau_3^{(1)} \mathbf{k}_1 \frac{\boldsymbol{\sigma}^{(1)} \cdot \mathbf{k}_1}{m_\pi^2 + k_1^2} + \tau_3^{(2)} \mathbf{k}_2 \frac{\boldsymbol{\sigma}^{(2)} \cdot \mathbf{k}_2}{m_\pi^2 + k_2^2} \right] + \left[\boldsymbol{\tau}^{(1)} \otimes \boldsymbol{\tau}^{(2)} \right]_3 \right.
$$

$$
\left. \times \left[\left(\mathbf{k}_2 \otimes \boldsymbol{\sigma}^{(1)} \right) \frac{\boldsymbol{\sigma}^{(2)} \cdot \mathbf{k}_2}{m_\pi^2 + k_2^2} - \frac{\boldsymbol{\sigma}^{(1)} \cdot \mathbf{k}_1}{m_\pi^2 + k_1^2} \left(\mathbf{k}_1 \otimes \boldsymbol{\sigma}^{(2)} \right) \right] \right\}
$$

where $f_{\pi N\Delta}^2/4\pi = 0.37$ and $f_{\gamma N\Delta}^2 = 0.014$. The energy-dependent width of the delta resonance, $\Gamma_\Delta(\omega)$, is taken from the parametrization of Oset,

Toki, and Weise.[354] They assume for simplicity that $F_{\gamma N\Delta} = F_{\gamma N\pi}$ and apply monopole form factors $(\Lambda_\pi^2 - m_\pi^2)/(\Lambda_\pi^2 - \mathbf{k}^2)$ at both πNN and $\pi N\Delta$ vertices. The pion cut-off mass Λ_π is believed to lie between about 650 and 1200 MeV, and various papers used different values with some sensitivity to Λ_π being evident.[351]

Note that this nonrelativistic approximation to the two-body current is static – it contains only spatial parts. Since the longitudinal part is eliminated according to Siegert's theorem, only the transverse part of the two-body current remains. Thus, at this level of approximation, only the transverse components of the current operator are affected by two-body currents. Also note that at this level the MEC with pseudovector coupling agrees with the model of Ref. 355 using pseudoscalar coupling.

7.4.2. *Pavia Implementation of MEC and IC Contributions*

A complete evaluation of matrix elements of the two-body current requires the evaluation of six-fold integrals. To estimate the importance of such contributions, the Pavia group has developed an approximate method in which an effective one-body current is constructed by integration over the coordinates of the unobserved nucleon, assuming that it remains bound and that the momentum distribution $n(\mathbf{k})$ can be approximated by the Fermi gas model. This averaging then takes the schematic form[348]

$$
\mathbf{J} = \int d^3p\, d^3p'\, \delta(\mathbf{p}' - \mathbf{p} - \mathbf{q}) \chi_{E\alpha}^{(-)*}(\mathbf{p}')
$$

$$
\times \left[\mathbf{J}^{(1)}(\mathbf{p}, \mathbf{p}') - \int d^3k\, \mathbf{J}^{(2)}(\mathbf{p}' - \mathbf{k}, \mathbf{k} - \mathbf{p}) n(\mathbf{k}) \right] \phi_{E\alpha}(\mathbf{p}) [S_\alpha(E)]^{1/2}
$$

where $\mathbf{J}^{(2)}$ denotes the full two-body current. Note that this procedure limits the hole contributions to the two-body current to terms which are diagonal except for isospin and is insensitive to nuclear structure. On the other hand, since the the spin structure of the effective one-body current due to MEC and IC differs substantially from that of the bare one-body current, the current is not only renormalized but the response functions are altered significantly.

The MEC and IC effects upon selected $(e, e'p)$ response functions are illustrated in Fig. 7.8 for a $1p_{1/2}$ hole in ^{16}O.[346] Quasiperpendicular kinematics with $Q^2 = 2m\omega = 0.16$ (GeV/c)^2 were employed; θ_{pq} is the opening angle between the momentum transfer $\mathbf{q}$ and the ejectile momentum $\mathbf{p}'$. Standard DWIA calculations based upon the bound-state and optical potentials of Giannini and Ricco[356] are shown as dashed curves. Dotted curves include MEC contributions and solid curves include both MEC and IC. The effect of
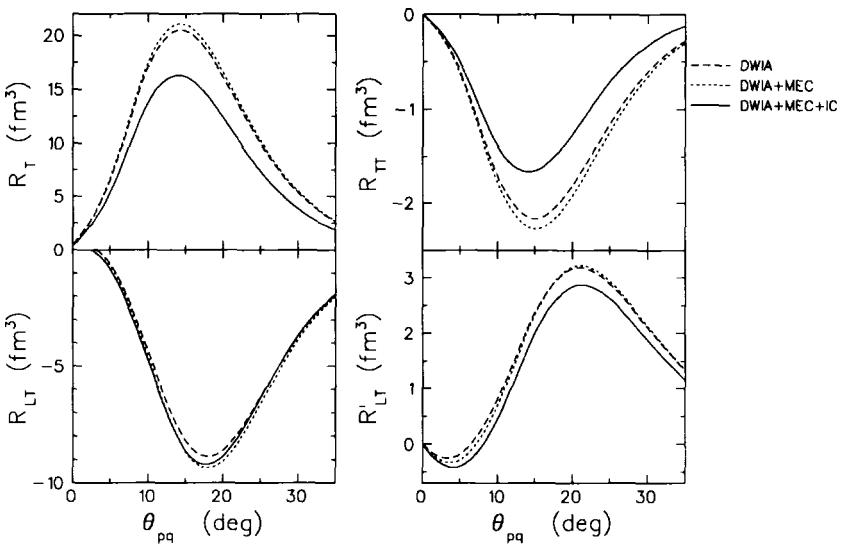
Fig. 7.8. Effect of MEC and IC upon selected response functions for $^{16}O(e, e'p)$ to a $1p_{1/2}$ hole state. Quasiperpendicular kinematics are employed with $Q^2 = 0.16$ (GeV/c)^2. Dashed lines portray DWIA, dotted lines include MEC, and solid lines include IC also. These response functions are normalized to full occupancy of the orbital.

MEC is to increase the transverse response function and cross section, but the effect in quasielastic kinematics is rather small. The effect of IC, on the other hand, is a destructive interference with the one-body contribution that reduces the transverse response function by about 25% at $Q^2 = 0.16$ (GeV/c)^2. Thus the ratio R_T/R_L is predicted to be reduced by the intermediate isobar current and this effect is expected to increase with Q^2.[346] Although most of the experimental evidence suggests that R_T/R_L is enhanced with respect to the impulse approximation, inclusive electron scattering suggests that R_L may be reduced by correlations more than R_T is enhanced by IC.[3,357] Similarly, MEC is predicted to enhance and IC to reduce R_{LT}, but these effects are not sufficiently strong to account for the observed enhancement of R_{LT} (see Fig. 7.5). Furthermore, the effects calculated for the $(1p_{1/2})^{-1}$ state are somewhat larger than for the $(1p_{3/2})^{-1}$ state, which is contrary to experimental findings. Finally, the IC effects predicted for the helicity-independent transverse–transverse and helicity-dependent longitudinal–transverse interference response functions are also appreciable.

The effects of two-body currents upon distorted momentum distributions are illustrated in Fig. 7.9 in which calculations[348] for $^{40}Ca(e, e'p)$ to the
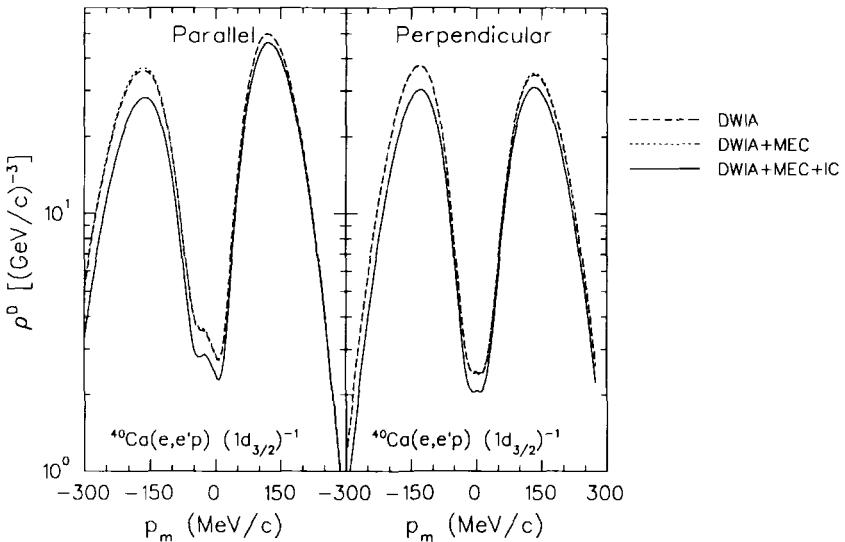
Fig. 7.9. The effects of MEC and IC upon $^{40}Ca(e, e'p)$ to the $\frac{3}{2}^+$ ground state of ^{39}K are shown for $T_p = 100$ MeV. Parallel kinematics are used on the left side, with $p_m > 0$ for $q < p'$. Quasiperpendicular kinematics are shown on the right side, with $p_m > 0$ for $\theta_p > \theta_q$. Dashed lines portray DWIA, dotted lines include MEC, and solid lines include IC also.

$\frac{3}{2}^+$ ground state of ^{39}K are shown for both parallel and quasiperpendicular kinematics with $T_p = 100$ MeV. The dashed curves portray standard DWIA calculations based upon a one-body current operator. Electron distortion is omitted for simplicity. The dotted curves, which are practically indistinguishable from the DWIA curves, were obtained by including the MEC contributions. The solid curves include both MEC and IC contributions. Note that in parallel kinematics the momentum transfer increases with decreasing p_m for constant p', so that the smallest Q^2 corresponds to large positive p_m and the largest to large negative p_m. Also note that more negative p_m corresponds to larger electron scattering angles which emphasize the transverse response. Since both the MEC and IC contributions to the transverse response function increase approximately linearly with Q^2 and interfere destructively with the one-body current, the two-body currents are predicted to suppress the cross section for negative p_m in parallel kinematics. A net suppression is also predicted for quasiperpendicular kinematics, with the left-right asymmetry reduced.

Similar effects can be expected for both proton and neutron knockout except that the IC effect should be more important for neutron knockout. In

that case the absence of a static charge means that the longitudinal response and the convection current are both very small. Hence, the dominance of the spin-magnetic contribution to the transverse response emphasizes the IC effect, which has a similar structure.[357] Furthermore, the absence of an appreciable longitudinal response implies that the transverse response can be isolated without the necessity of a Rosenbluth separation, thereby minimizing systematic errors.

This effect is illustrated in Fig. 7.10 for which the cross section and response functions for $^{17}O(e, e'n)$ to the ^{16}O ground state are shown in coplanar kinematics for which the neutron energy and angle are held constant at $T_{n'} = 135$ MeV and $\theta_n = 37°$, respectively. Both parallel and quasiperpendicular kinematics are shown. These calculations[357] use an optical potential based upon the empirical effective interaction (EEI) fitted to $^{16}O(p, p')$ at the same energy.[201] The cross section is almost entirely due to the transverse response function, which is slightly enhanced by MEC but strongly reduced by IC. Since the effect upon the LT interference is expected to be smaller, the ratio of cross sections σ_{LT}/σ_T is enhanced by the IC contribution, especially for large negative missing momenta. This ratio should be insensitive to ambiguities in the nuclear structure and hence should provide a sensitive test of this model. Measurement of these quantities is expected to become practical with high duty-factor machines and a proposal has been submitted to MIT–Bates. As shown in Ref. 357, the unpolarized response functions are rather insensitive to ambiguities in the optical model, with variations much smaller than the IC effect shown here. Calculations of selected recoil polarization observables for the same coplanar quasiperpendicular kinematics are shown in Fig. 7.11, where the left column examines the sensitivity to two-body currents and the right column to variations of the optical model. We observe that the sideways component of the neutron polarization is predicted to be quite sensitive to IC effects and relatively insensitive to FSI ambiguities, while the reverse is expected for the normal component. In general we find that those observables which survive without FSI tend to be more sensitive to two-body currents than to FSI ambiguities, while the reverse applies to observables which vanish without FSI.

7.4.3. *Gent Implementation of MEC and IC Contributions*

The Gent group employs an approach in which the bound and continuum single-particle states are eigenfunctions of the same Hartree–Fock (HF) mean field obtained from a Skyrme interaction (SKE2).[358] Thus, orthogonality between bound and continuum states is maintained. The one-body current operator is obtained from the HF hamiltonian and hence preserves gauge invariance.[359]
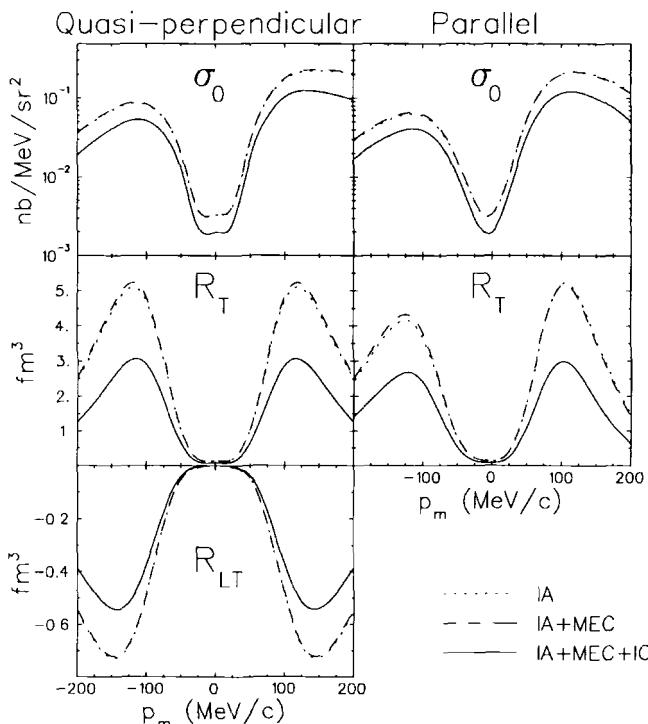
Fig. 7.10. The influence of MEC+IC upon the unpolarized cross section σ_0 and the coplanar response functions for $^{17}O(e, e'n)$ is examined in quasiperpendicular (left) and parallel (right) kinematics for which the neutron energy and angle are kept fixed at $T_n = 135$ MeV and $\theta_n = 37°$. Here quasiperpendicular kinematics with $p_m > 0$ corresponds to $\theta_p < \theta_q$ (or $\phi = 0$). Dotted curves show IA results, dashed curves include MEC, and solid curves include the full two-body current (IA+MEC+IC).

The wave function for the ejectile and the residual nucleus is obtained from a random phase approximation (RPA) formalism that includes particle–hole and hole–particle excitations of a correlated ground state.[360] Thus, the treatment of final-state interactions includes distortion by the HF mean field, which is real, and represents absorption through coupling to all open single-nucleon emission channels. However, unlike approaches based upon complex optical models, flux loss to more complicated configurations is not included. Finally, the Gent approach includes essentially exact evaluation of the matrix elements of the two-body current operator between pairs of orbitals occupied in the initial state and particle–hole configurations in the final state. By avoiding the Pavia reduction of the two-body
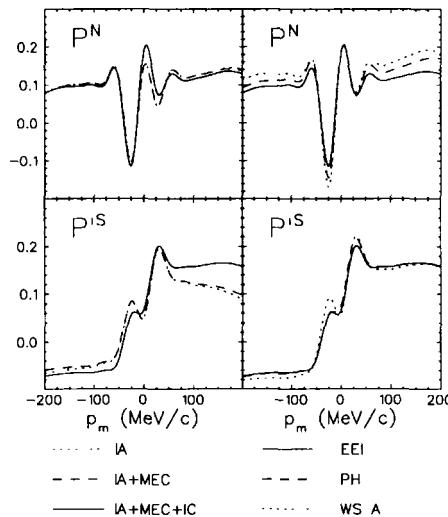
Fig. 7.11. The sensitivities of selected recoil polarization observables for $^{17}O(e, e'n)$ to *two-body currents (left) and optical-model ambiguities (right) are examined in coplanar quasiperpendicular kinematics for which the neutron energy and angle are kept fixed at* $T_n = 135$ **MeV** and $\theta_n = 37°$. For the left column, dotted curves show IA results, dashed curves include MEC, and solid curves include the full two-body current (IA+MEC+IC). For the right column, dotted curves use a Woods–Saxon optical potential, dashed curves use a folded potential based on the PH interaction, and solid curves use an empirical effective interaction (EEI).

operator, the nuclear structure is presumably treated much better.

Calculations* of R_{LT} for $^{16}O(e, e'p)$ are compared with the available data in Fig. 7.12, where dashed curves correspond to DWIA, dotted curves include MEC, and solid curves include both MEC and IC contributions. Unlike the Pavia model, the predictions of the Gent model are quite different for the $1p_{1/2}$ and $1p_{3/2}$ hole states, indicating strong sensitivity to nuclear structure. For the $(1p_{3/2})^{-1}$ state, meson-exchange currents greatly increase R_{LT} with most of the effect being attributable to the contact term. Similar enhancement of R_{LT} for the $(1p_{1/2})^{-1}$ state is obtained also. However, the isobar current has opposite effects upon R_{LT} for these spin–orbit partners, enhancing R_{LT} for the $(1p_{3/2})^{-1}$ and suppressing it for the $(1p_{1/2})^{-1}$ state. The net effect is substantially larger for the $(1p_{3/2})^{-1}$ than for the $(1p_{1/2})^{-1}$ state, but is still not sufficient to reproduce the observed enhancement at $Q^2 = 0.3$ $(GeV/c)^2$.

---

*The calculations were obtained from Ref. 351 but have been corrected for differences between the normalization conventions employed for those calculations and conventions used to analyze the data; these nontrivial differences were originally overlooked.[361] The unfortunate proliferation of conventions in the literature tends to promote such errors.
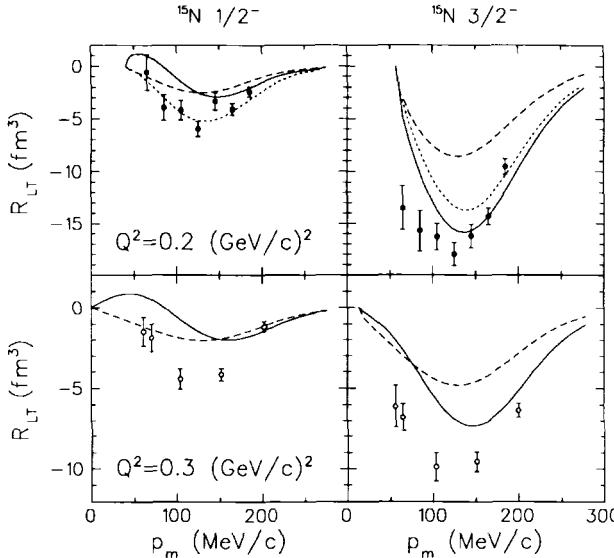
Fig. 7.12. Longitudinal–transverse interference response function for $^{16}O(e, e'p)$**.** Solid circles (top row) are for $T_p = 84$ MeV[287] and open circles (bottom row) are for $T_p = 160$ MeV.[286] Dashed lines are DWIA calculations, dotted lines (top row) include MEC contributions, and solid lines include both MEC and IC contributions within the Gent model.[351]

It is also important to recognize that the Q^2 dependence of the one-body contribution produced by this model differs from the standard DWIA calculations shown in Fig. 7.5 in that the peak strength of R_{LT} decreases more rapidly with increasing Q^2. We also note that the spectroscopic factors used in Ref. 351 are smaller by a factor of 0.8 at the higher ejectile energy than at the lower and that even at the lower energy they are smaller by a factor of about 0.85 than fitted to distorted momentum distributions using standard optical models. These findings suggest that treatment of the HF-RPA treatment of final-state interactions does not adequately represent the energy dependence of absorptive processes. On the other hand, the relative contributions of one- and two-body currents is probably not overly sensitive to the final-state interactions.

Similarly, the R_T and R'_{LT} response functions for $^{16}O(e, e'p)$ in quasiperpendicular kinematics with $Q^2 = 0.2$ (GeV/c)^2 are shown in Fig. 7.13. The spectroscopic factors were fitted to cross-section data and applied to each response function. The R_T data for $T_p = 84$ MeV are from Ref. 287. Although the scatter in these and the corresponding R_L data is relatively large, probably because of experimental difficulties for Rosenbluth separations, it appears that the ratio R_T/R_L predicted by the Gent model is significantly larger than needed to
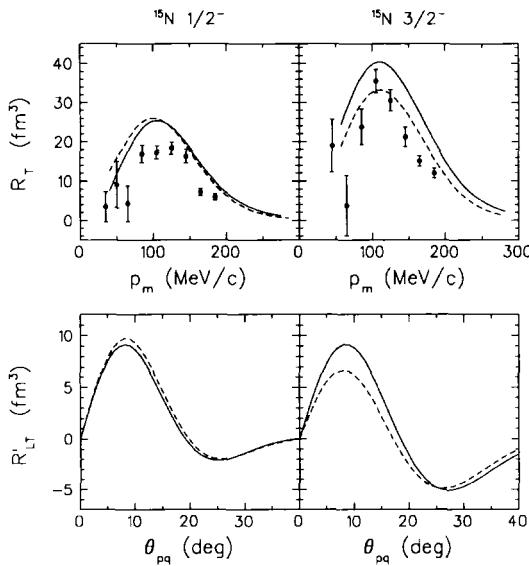
Fig. 7.13. R_T and R'_{LT} response functions for $^{16}O(e, e'p)$ in quasiperpendicular kinematics with $Q^2 = 0.2$ (GeV/c)^2. The R_T data for $T_p = 84$ MeV are from Ref. 287. Dashed lines are DWIA calculations and solid lines include both MEC and IC contributions within the Gent model.[351].

describe these data. On the other hand, there is considerable evidence (see Section 7.1) that this ratio is enhanced with respect to the impulse approximation. Until the data are improved, it is sufficient for our present purposes to note that in the Gent model two-body currents are predicted to enhance R_T and R'_{LT} for the $(1p_{3/2})^{-1}$ state and that the effects upon the $(1p_{1/2})^{-1}$ state are predicted to be much smaller. Thus, the contributions due to two-body currents depend fairly strongly upon nuclear structure.

7.4.4. Comparison of the Pavia and Gent Models

The preceding sections have shown that both the Pavia and Gent models predict that meson-exchange currents and intermediate isobar excitation play important roles in quasielastic knockout reactions. However, both models involve different but rather severe approximations that lead to important qualitative differences between their predictions. The Gent model predicts that meson-exchange currents substantially enhance the transverse current, but the corresponding effect predicted by the Pavia model is much smaller. The Pavia model predicts that intermediate isobar excitation substantially reduces the transverse

current, with effects that are not strongly dependent upon nuclear structure and which are similar for all response functions that depend upon the transverse current, while the corresponding effects produced within the Gent model depend strongly upon nuclear structure, sometimes reducing and sometimes enhancing the response functions that depend upon the transverse current.

Unfortunately, it is difficult to determine which differences between the models are most responsible for the differences between their predictions. The two models employ different one-body current operators, but a systematic comparison is not available. The Pavia group uses phenomenological optical potentials (though often not the best available), while the Gent group treats final-state interactions with a HF-RPA approach which has not been tested against nucleon scattering. Both groups employ static models of the two-body currents based upon nonrelativistic reductions truncated at second order in q/m, but use different form factors and, for the isobar current, different coupling constants; systematic comparisons are again lacking. The Pavia group evaluates the contribution of two-body currents using a relatively simple Fermi averaging procedure, while the Gent group evaluates matrix elements of the two-body current within the same nuclear structure model used for the one-body current; however, neither group has employed the other's current operator in an attempt to determine whether the differences between their results are due primarily to the structure of the operators or to the approximations made in evaluating their matrix elements. Neither group considers the role of heavy mesons or N^* excitation.

Therefore, it appears that two-body currents, particularly those due to intermediate isobar excitation, play an important role in single-nucleon knockout. Since these currents have spin structures which are considerably different from that of the one-body current, systematic study of separated response functions, especially those which would survive even in the absence of final-state interactions, should provide relatively unambiguous tests of models. Although the two models presently available provide some theoretical guidance, their detailed predictions are quite different for reasons that are not yet entirely clear. This reviewer is not prepared to decide these issues, but strongly urges the two groups to clarify their differences. Nevertheless, although further theoretical work is obviously needed to improve the present models, the results thus far do suggest several fruitful avenues for experimental studies using the new facilities that are just now becoming available. Such studies should include recoil polarization and interference response functions for both proton and neutron knockout.

7.5. Channel Coupling in $(e, e'N)$ Reactions

Although standard DWIA calculations based upon optical potentials fitted to proton elastic scattering data provide a good description of $(e, e'p)$ data for

relatively strong transitions corresponding to knockout from a valence orbital, the excitation of weak transitions corresponding to knockout from orbitals above the Fermi level can receive substantial contributions from two-step processes of the type $(e, e'p)(p, p')$ or $(e, e'n)(n, p)$. Inelastic scattering in the outgoing channel would presumably affect the longitudinal and transverse response functions in similar fashion, but since the coupling to the neutron is primarily transverse, charge exchange could affect various response functions quite differently.

The first estimates of two-step contributions to weak transitions were made by Blok and van der Steenhoven[362] using a relatively simple method based upon the observation that the knockout process, described by a distorted momentum distribution of the form

$$\rho_\alpha^D(\mathbf{p}_m, \mathbf{p}') = \left| \int d^3r \, \chi^{(-)*}(\mathbf{r}) \exp\left(i\frac{A-1}{A}\mathbf{q} \cdot \mathbf{r}\right) \phi_\alpha(\mathbf{r}) \right|^2 \quad (7.11)$$

is similar to the pickup reaction in which a fictitious particle with a plane wave function carries away a proton. Thus, they adapted a code for transfer reactions, namely CHUCK,[363] to this model. The mass and energy of the light particle and the Q-value of the pickup reaction are chosen to simulate the kinematics of the knockout reaction. This approach was shown to reproduce direct calculations with standard DWIA codes for $(e, e'p)$. Channel coupling is then incorporated by replacing the distorted wave χ with a coupled-channels wave function.

We have developed a somewhat more sophisticated coupled-channels model for $A(e, e'N)B$ reactions which includes both inelastic excitation and charge exchange in the final state interactions (FSI). The code is based upon the nucléon scattering code LEA[364] and uses an extension of the model recently used to analyze coupled-channel effects upon the distorted momentum distributions for the $^{10}B(e, e'p)^9Be$ and $^{10}B(\gamma, p)^9Be$ reactions.[365]

Matrix elements of the nuclear current $\mathcal{J}_\alpha^\mu$ for final state α can be represented in the form

$$\mathcal{J}_\alpha^\mu(\mathbf{p}', \mathbf{p}_m) = \int d^3r \, \exp\left(i\tilde{\mathbf{q}}_{\text{eff}} \cdot \mathbf{r}\right) \langle \Psi_\alpha^{(-)} | \Gamma^\mu | \Psi_0 \rangle \quad (7.12)$$

where Ψ_0 represents the ground state of the target, $\Psi_\alpha^{(-)}$ represents the wave function for the final state of the ejectile and the residual nucleus, Γ^μ is the vertex operator for the nucleon current, and $\tilde{\mathbf{q}}_{\text{eff}} = \mathbf{q}_{\text{eff}} m_B/m_A$ is the effective momentum transfer scaled to the frame of the residual nucleus. For simplicity, we evaluate the current for asymptotic kinematics represented by the ejectile momentum, $\mathbf{p}'$, and the missing momentum, $\mathbf{p}_m = \mathbf{p}' - \mathbf{q}$. We use the fourth-order expansion of the nonrelativistic current operator developed by Giusti and

Pacati,[241] based upon the model of McVoy and van Hove.[239] Furthermore, we assume that Coulomb distortion for light nuclei can be evaluated in the effective momentum approximation.

Channel coupling is included by expanding the wave function for the residual nucleon–nucleus system as

$$\Psi_\alpha = \sum_\beta \chi_{\alpha\beta} \psi_\beta \qquad (7.13)$$

where ψ_β represents the internal state of the $(A - 1)$ system and $\chi_{\alpha\beta}$ represents the coupled-channels wave function containing an incoming plane wave in channel α and outgoing spherical waves in each channel β, The overlap between the initial A-body state Ψ_0 for the target and the $(A - 1)$-body state of the residual nucleus is expanded in the form

$$\langle \psi_\beta | \Psi_0 \rangle = \sum_\gamma c_{\beta\gamma} \phi_{\beta\gamma}(\mathbf{r}) \qquad (7.14)$$

where $c_{\beta\gamma}$ is a parentage coefficient (or pickup amplitude) and $\phi_{\beta\gamma}(\mathbf{r})$ resembles a bound-state wave function in the potential generated by the residual nucleus with single-particle quantum numbers labelled by γ. Therefore, the nuclear current matrix elements can be expanded in the form

$$\mathcal{J}_\alpha^\mu(\mathbf{p}', \mathbf{p}_m) = \sum_{\beta\gamma} c_{\beta\gamma} \int d^3r \, \exp\left(i\tilde{\mathbf{q}}_{\text{eff}} \cdot \mathbf{r}\right)$$
$$\times \chi_{\alpha\beta}^{(-)*}(\mathbf{r}) \Gamma^\mu(\mathbf{p}', \mathbf{p}' - \mathbf{q}_{\text{eff}}) \phi_{\beta\gamma}(\mathbf{r}) \qquad (7.15)$$

and can be analyzed further by standard partial-wave and recoupling techniques.

7.5.1. Weak Transitions in $^{12}\text{C}(e, e'p)$

The dominance of the direct reaction mechanism has been demonstrated by the extremely small cross sections for $^{12}\text{C}(e, e'p)^{11}\text{B}$ to the $\frac{5}{2}^-$ state at 4.45 MeV or the $\frac{7}{2}^-$ state at 6.74 MeV.[285,366] Direct knockout from the $1f$ orbitals is expected to be very small because those orbitals lie far above the Fermi level. These states are based upon dominant configurations of the type $2^+ \otimes (1p_{3/2})^{-1}$, which cannot be reached in a single step. Until recently, only upper limits below the estimated two-step level[362] were available for these transitions. The $\frac{5}{2}^-$ transition was recently observed[367] at $p_m = 170$ and 200 MeV/c using nonparallel kinematics for which the momentum transfer

was chosen equal to the outgoing momentum of the ejectile with $T_p = 70$ MeV, conditions which previously had been shown to emphasize the two-step mechanism.[362] These data are compared in Fig. 7.14 with improved calculations based upon the same direct and coupling amplitudes used by van der Steenhoven et al.[285,366] Both parallel and quasiperpendicular kinematics are shown. The dotted curves represent direct excitation where optical-model distortion is the only final-state interaction. The dashed curves represent pure two-step calculations based upon population of the ^{11}B ground state via $1p_{3/2}$ knockout followed by 2^+ excitation via a collective-model coupling potential. Finally, the solid curves represent coupled-channels calculations which include both direct and indirect excitation. Although the two-step mechanism is dominant, interference with the direct mechanism remains important in most cases. For the $\frac{5}{2}^-$ state in quasiperpendicular kinematics, interference is relatively unimportant and both two-step and coupled-channels calculations reproduce the available data. It would be of some interest to acquire more complete data with which to test the coupled channels calculations, which can easily be extended to include more complete coupling schemes.

7.5.2. Charge Exchange in $^{16}O(e, e'N)$ Reactions

To evaluate the role of charge exchange and channel coupling in neutron knockout, we consider the $^{16}O(e, e'N)$ reaction at $T_p = 135$ MeV. We consider two states in each residual nucleus formed as pure holes. The overlap functions for ^{15}N were obtained from the $^{16}O(e, e'p)$ measurements of Leuschner et al.[278] For ^{15}O we used the same potential shapes and adjusted the central well depths to reproduce the separation energies for the two states. The coupling potentials which connect these states with each other were computed by folding a density-dependent effective interaction with transition densities based upon these independent-particle shell model wave functions. All possible couplings and all relevant terms of the effective interaction, except tensor exchange, were included. We verified that charge exchange cross sections for $^{15}N(p, n)$ computed from the coupled-channels wave function accurately reproduce those obtained in a standard DWIA calculation. The small differences between these calculations are attributed to the neglect of tensor exchange and are expected to have a negligible effect upon $^{16}O(e, e'N)$. Our calculations for $^{15}N(p, n)$ at $T_p = 135$ MeV agree well with the calculations of Watson et al.[368] and agree with the data for the $\frac{1}{2}^-$ ground state, but are approximately twice as strong as the data for the lowest $\frac{3}{2}^-$ state of ^{15}O. Thus, this model may overestimate the effect of coupling between the $\frac{1}{2}^-$ and $\frac{3}{2}^-$ states. On the other hand, the model probably represents the net effect of coupling between distributions of $(1p_{1/2})^{-1}$
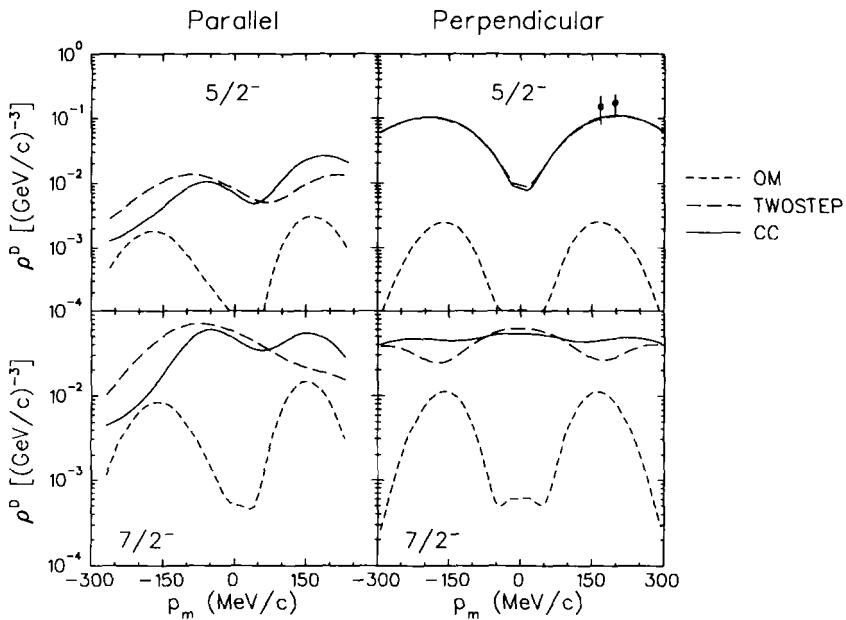
Fig. 7.14. Coupled-channels calculations are compared with data for weak transitions in $^{12}C(e, e'p)$ **at** $T_p = 70$ **MeV.** Direct optical-model calculations are shown as dotted curves, pure two-step calculations as dashed curves, and coupled-channels calculations as solid curves.

and $(1p_{3/2})^{-1}$ hole states.

Calculations for parallel kinematics are shown in Figs. 7.15–7.17 and for quasiperpendicular kinematics in Figs. 7.18–7.20. These calculations were performed for a fixed electron energy of 500 MeV and the invariant mass of the recoil system was held constant, equivalent to a proton with kinetic energy $T_p = 135$ MeV incident upon the ground state of ^{15}N. Five sets of calculations are shown. The dotted curves represent the direct knockout mechanism using only spherical optical potentials. The short-dashed curves include the nonspherical (reorientation) potentials for elastic scattering but omit coupling to other channels. The long-dashed curves include charge exchange between analog states. Thus, the two $(1p_{1/2})^{-1}$ states, for example, are coupled by the isospin-changing interactions but are not connected to either of the $(1p_{3/2})^{-1}$ states. The dot-dash curves include all possible isospin-changing interactions, but do not include inelastic scattering. Finally, the solid curves represent full coupled-channels calculations which include both charge exchange and inelastic scattering.
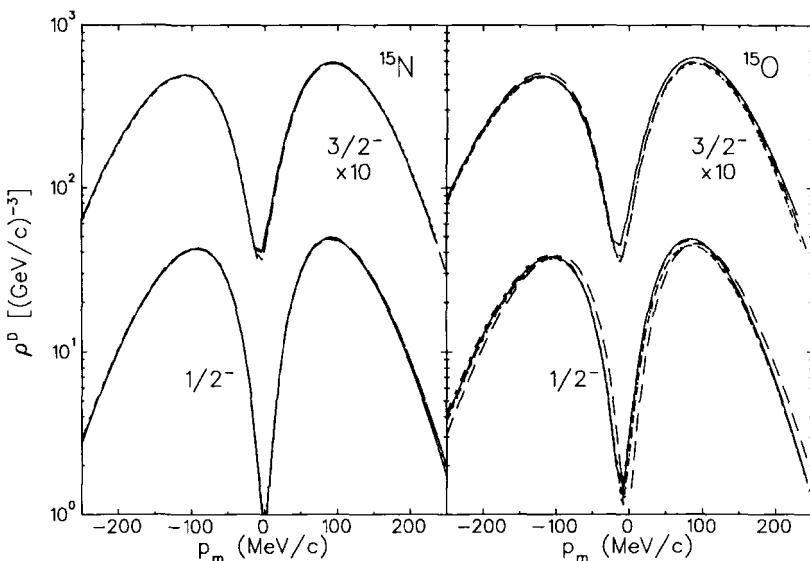
Fig. 7.15. Distorted momentum densities for $^{16}O(e, e'N)$ in parallel kinematics with $\epsilon_i = 500$ MeV and $T_N = 135$ MeV. The top set of curves has been multiplied by 10 and is for $1p_{3/2}$ knockout, while the bottom set is for $1p_{1/2}$ knockout. Dotted curves portray direct knockout with spherical optical potentials, short-dashed curves include elastic reorientation potentials, long-dashed curves include charge exchange between analog states, dot-dash curves include all possible isospin-changing interactions, and solid curves represent full coupled-channels calculations which include both charge exchange and inelastic scattering.

For quasiperpendicular kinematics we find that channel coupling can significantly enhance the cross sections to valence quasihole states for $p_m \gtrsim 300$ MeV/c. Significant enhancements are found for $(e, e'p)$ as well as for $(e, e'n)$. The enhancements tend to be larger for nonparallel than for parallel kinematics because the coupling potentials with $L > 0$ usually dominate. Note that significantly larger effects were predicte[365] at large p_m in quasiperpendicular kinematics for $^{10}B(e, e'p)^9Be$ because quadrupole coupling within the rotational band is quite strong. Thus, the magnitude of these effects depends upon nuclear structure. Therefore, investigations which use $(e, e'p)$ to study short-range correlations in nuclear wave functions must carefully consider the enhancements of single-nucleon knockout at large p_m produced by channel coupling within final-state interactions.

For $(e, e'n)$ response functions we generally find the strongest channel coupling effects for L- and LT-type response functions. The most important couplings are usually those that change both spin and isospin and are driven by the
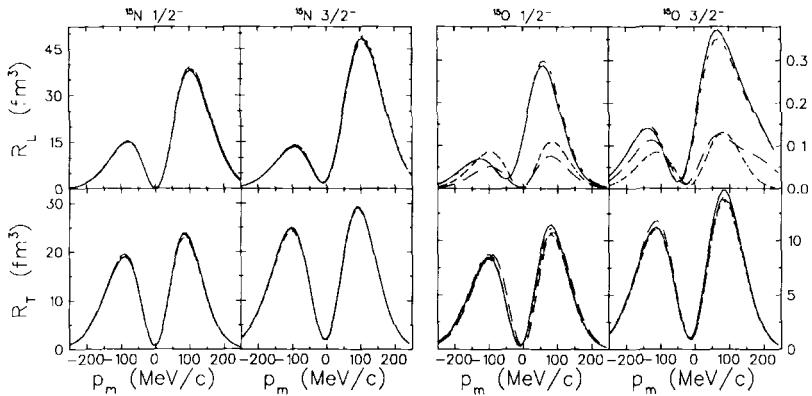
Fig. 7.16. Response functions for $^{16}O(e, e'N)$ **in parallel kinematics with** $\varepsilon_i = 500$ **MeV and** $T_N = 135$ **MeV.** Proton (neutron) knockout from the $1p$-shell is portrayed in the left (right) half. See Fig. 7.15 for legend.
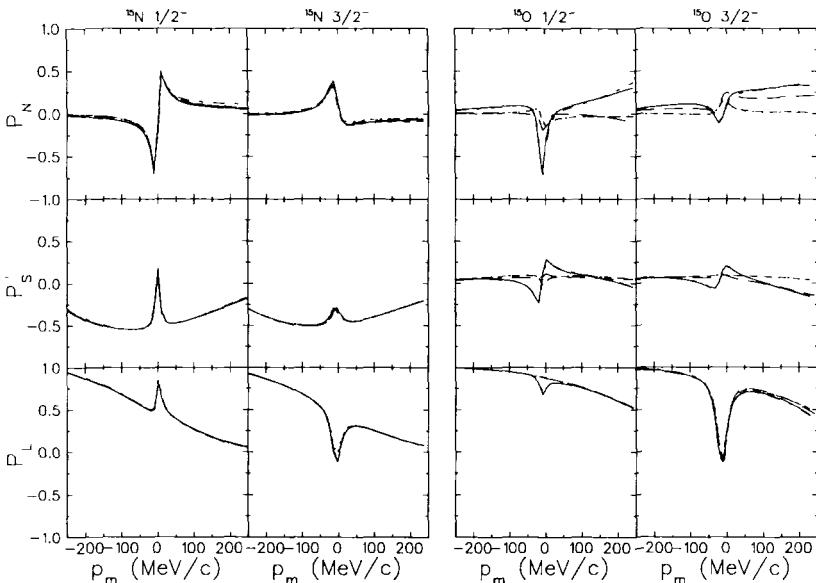
Fig. 7.17. Recoil polarization for $^{16}O(e, e'N)$ **in parallel kinematics with** $\varepsilon_i = 500$ **MeV and** $T_N = 135$ **MeV.** Proton (neutron) knockout from the $1p$-shell is portrayed in the left (right) half. See Fig. 7.15 for legend.
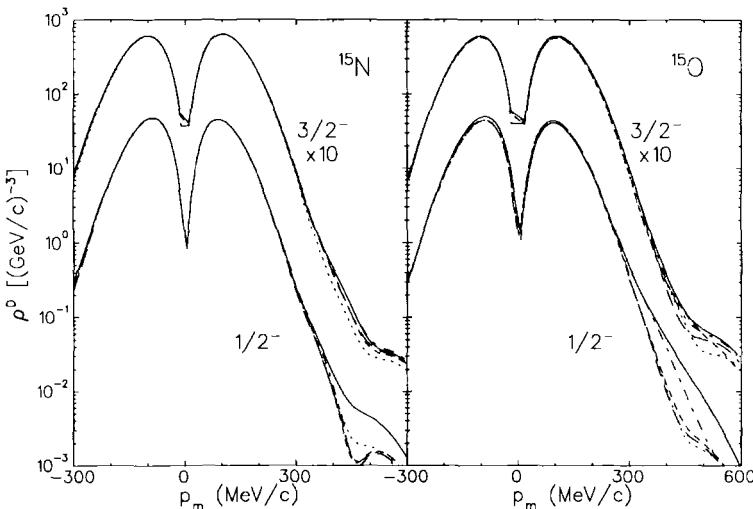
Fig. 7.18. Distorted momentum densities for $^{16}O(e, e'N)$ in quasiperpendicular kinematics with $\varepsilon_i = 500$ MeV and $T_N = 135$ MeV. The top set of curves has been multiplied by 10 and is for $1p_{3/2}$ knockout, while the bottom set is for $1p_{1/2}$ knockout. Dotted curves portray direct knockout with spherical optical potentials, short-dashed curves include elastic reorientation potentials, long-dashed curves include charge exchange between analog states, dot-dash curves include all possible isospin-changing interactions, and solid curves represent full coupled-channels calculations which include both charge exchange and inelastic scattering.

$t_{\sigma\tau}$ component of the two-nucleon effective interaction, which is the dominant isospin-changing interaction for these ejectile energies. Note that this term does not contribute to the Lane model potentials used in earlier calculations of charge-exchange between analog states.[13,369] The largest effects occur for response functions which would vanish in the absence of final-state interactions (FSI), but significant effects on those which survive without FSI are sometimes found also. Similarly, for $(e, e\,p)$ nonnegligible effects are found most often in those response functions which would vanish without FSI.

The longitudinal response functions for $^{16}O(e, e'n)$ in parallel kinematics are quite sensitive to both charge exchange and inelastic scattering and the effects are quite different for the $(1p_{1/2})^{-1}$ and $(1p_{3/2})^{-1}$ states, but the contribution of the longitudinal response to the cross section for neutron knockout is quite small. The effects upon the transverse response, which dominates the cross section, are relatively small, but a 10% enhancement of $1p_{1/2}$ neutron knockout for positive p_m is predicted. For parallel kinematics, these effects are much smaller than those predicted for isobar currents. The effects for $^{16}O(e, e'p)$ are
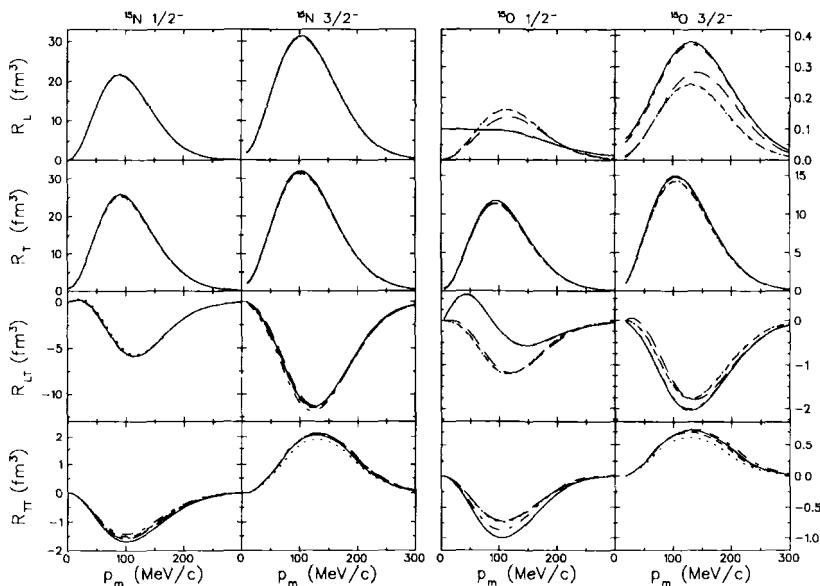
Fig. 7.19. Response functions for $^{16}O(e, e'N)$ in quasiperpendicular kinematics with $\varepsilon_i =$ 500 MeV and $T_N = 135$ MeV. Proton (neutron) knockout from the $1p$-shell is portrayed in the left (right) half. See Fig. 7.18 for legend.

relatively small and need not be discussed further here.

Our calculations for $(e, e'n)$ at modest p_m disagree sharply with those of van der Steenhoven *et al.*[369] who have published calculations for $^{12}C(e, e'n)$ which suggest very large charge exchange effects, amounting to as much as an order of magnitude enhancement of the missing momentum distribution for parallel kinematics. On the other hand, Giusti and Pacati[13] have published calculations based upon an ostensibly similar model which predict very small effects. We have performed calculations for both sets of kinematics using our model and also find quite small effects, qualitatively similar to those of Giusti and Pacati and to the present results for $^{16}O(e, e'N)$ but quite different than those of van der Steenhoven *et al.* Since both of the earlier calculations used central spin-independent Lane potentials based upon global optical models to represent charge exchange, while we include spin-dependent and noncentral components also, we repeated the calculations using Lane potentials and obtained qualitatively similar results, demonstrating that the choice of coupling potential is not the primary origin of this disagreement. Therefore, we believe that the calculations of van der Steenhoven *et al.* are incorrect.
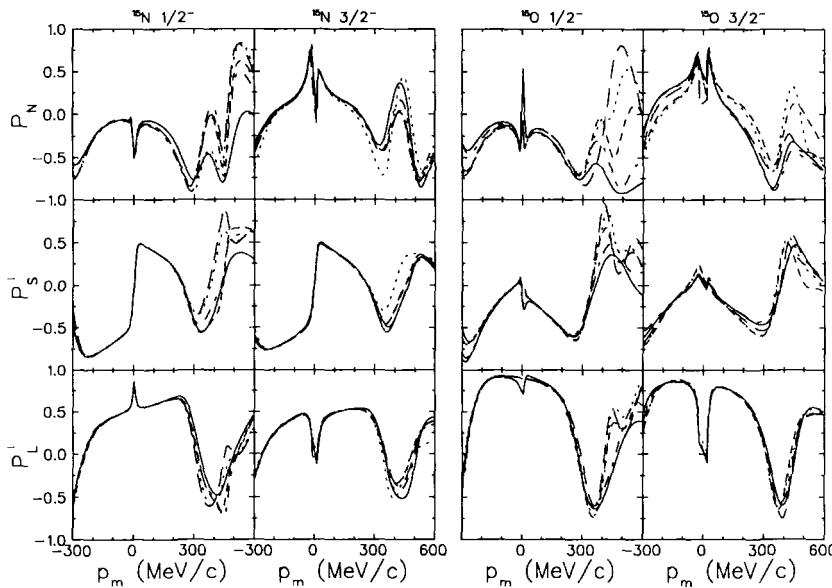
Fig. 7.20. Recoil polarization for $^{16}O(e, e'N)$ in coplanar quasiperpendicular kinematics with $\varepsilon_i = 500$ MeV and $T_N = 135$ MeV. Proton (neutron) knockout from the $1p$-shell is portrayed in the left (right) half. See Fig. 7.18 for legend.

Similar conclusions have been reached by Jeschonnek *et al.*[370] using a continuum RPA model with phenomenological optical potentials and either *t*-matrix or *G*-matrix nucleon–nucleon interactions in the final state. They also find that the calculations of Ref. 369 exaggerate the enhancement of $(e, e'n)$ cross sections and that $t_{\sigma\tau}$ interactions play an important role in charge exchange.

For quasiperpendicular kinematics, we find that the R_{LT} response function for $^{16}O(e, e'n)$ may be affected significantly, with the coupling between spin-orbit partners being very important. These effects are largest for the $\frac{1}{2}^-$ state, for which the R_{LT} response function is suppressed and even changes sign for small p_m when coupling between spin–orbit partners is included. For the $\frac{3}{2}^-$ state, channel coupling is predicted to enhance the cross section by a nearly uniform $8 - 10\%$ arising primarily from R_T. Although the effects of charge exchange appear to be comparable in magnitude to those of two-body currents, we note that the effects upon the two states are predicted to be quite different for charge exchange but similar for isobar currents, at least in the Pavia model. Thus, we may be able to distinguish between these mechanisms using measurements of both response functions. We also note that if two-body currents do substantially

reduce the transverse response for $(e, e'n)$, the relative importance of channel coupling in the final-state interaction may be enhanced. Therefore, we expect that channel coupling in the final state produces effects upon R_{LT} for $(e, e'n)$ which are comparable in magnitude to those predicted by models of meson exchange and isobar currents, but the channel coupling effects for $(e, e'p)$ do not appear to be strong enough to explain the problems in R_{LT} for ^{16}O.

Although the effects of charge exchange and inelastic scattering on the cross sections for $(e, e'n)$ are relatively modest, at least for $p_m < 300$MeV/c, the effects on polarization observables can be appreciable. Calculations of the recoil polarization for ^{16}O$(\vec{e}, e'\vec{N})$ are shown in Fig. 7.17 for parallel kinematics and in Fig. 7.20 for quasiperpendicular kinematics. The normal polarization P_N for parallel kinematics predicted for direct knockout of a neutron is quite small, but charge exchange can significantly enhance this polarization, particularly for the $1p_{3/2}$ hole and for positive p_m. Channel coupling effects are much smaller for P_S' and P_L'. Note that P_N arises from the imaginary part of an interference between longitudinal and transverse currents, and hence vanishes in the absence of final-state interactions, while P_S' and P_L' arise from real parts which do not require FSI to be nonzero. Hence, P_N is more sensitive to the details of the final-state interactions such as, in this case, charge exchange. Also note that in parallel kinematics the recoil polarization for proton knockout appears to be rather insensitive to channel coupling.

Similarly, P_N for neutron knockout in quasiperpendicular kinematics is also sensitive to channel coupling, while the polarization transfer components are relatively insensitive to channel coupling. Larger effects are predicted for the $1p_{3/2}$ hole, with a significant asymmetry with respect to $\phi = 0, \pi$. However, unlike parallel kinematics, P_N for the $1p_{1/2}$ proton hole is also predicted to be sensitive to channel coupling, where the dominant contribution appears to come from inelastic scattering.

The effects of channel coupling upon the observables for nucleon knockout clearly depend upon the details of both nuclear structure and the properties of the nucleon–nucleon interaction. Therefore, studies of the contributions of two-body currents to separated response functions must include the effects of both inelastic scattering and charge exchange in a microscopic model of the final state interaction.

7.6. Evidence for Multinucleon Knockout

7.6.1. Continuum Yields at Large Missing Energy for $(e, e'p)$

The separated response functions near the ^{12}C$(e, e'p)$ quasielastic peak show that a substantial continuum at large missing energies is populated pri-
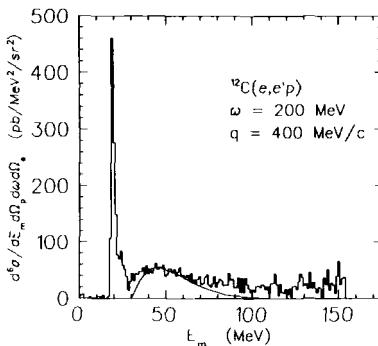
Fig. 7.21. Missing energy spectrum for $^{12}C(e, e'p)$ **in the dip region with** $q = 400$ MeV/c **and** $\omega = 200$ MeV. Radiative corrections have been applied. The area above the dotted line is attributed to the $1s_{1/2}$ shell. The solid line shows a quasideuteron calculation.

marily by the transverse response. Furthermore, the spectrum shown in Fig. 7.21 that was obtained by Lourie et al.[331] for the predominantly transverse dip region ($\omega = 200$ MeV for $q = 400$ MeV/c) also shows that the transverse continuum persists to missing energies at least as large as 150 MeV. In that figure the area above the dotted line is attributed to $1s$ knockout, based upon the spectroscopic factor obtained by Mougey et al.[242] from measurements at forward electron scattering angles made on the low-ω side of the quasielastic peak, conditions which suppress both the transverse response and the continuum yield. The similarity between the dotted line and the continuum level suggests that the multinucleon mechanism rises quickly from the two-nucleon emission threshold to reach a nearly uniform continuum level. The solid curve arises from a quasideuteron calculation by Laget,[371] which shows that the quasideuteron mechanism can contribute to the continuum near 50 MeV but cannot account for the substantial excess strength beyond about 80 MeV.

Similarly, Weinstein et al.[216] measured missing-energy spectra for $^{12}C(e, e'p)$ in parallel kinematics for $q = 585$, 775, and 827 MeV/c with $\omega = 210$, 355, and 325 MeV, which with $|y/m_N| = 0.05$ all lie near the top of the quasielastic peak. These data, shown in Fig. 7.22, demonstrate that the continuum yield at large missing energies increases with momentum transfer and represents a large fraction of the total cross section. On the other hand, despite the large energy transfer that is available, the spectrum for $Q^2 = 0.47$ (GeV/c)^2 shows no evidence of appreciable pion production for $E_m > 160$ MeV; apparently pion production is not very important near the center of the quasielastic peak (small $|y|$). If we define the integrated yield for an interval
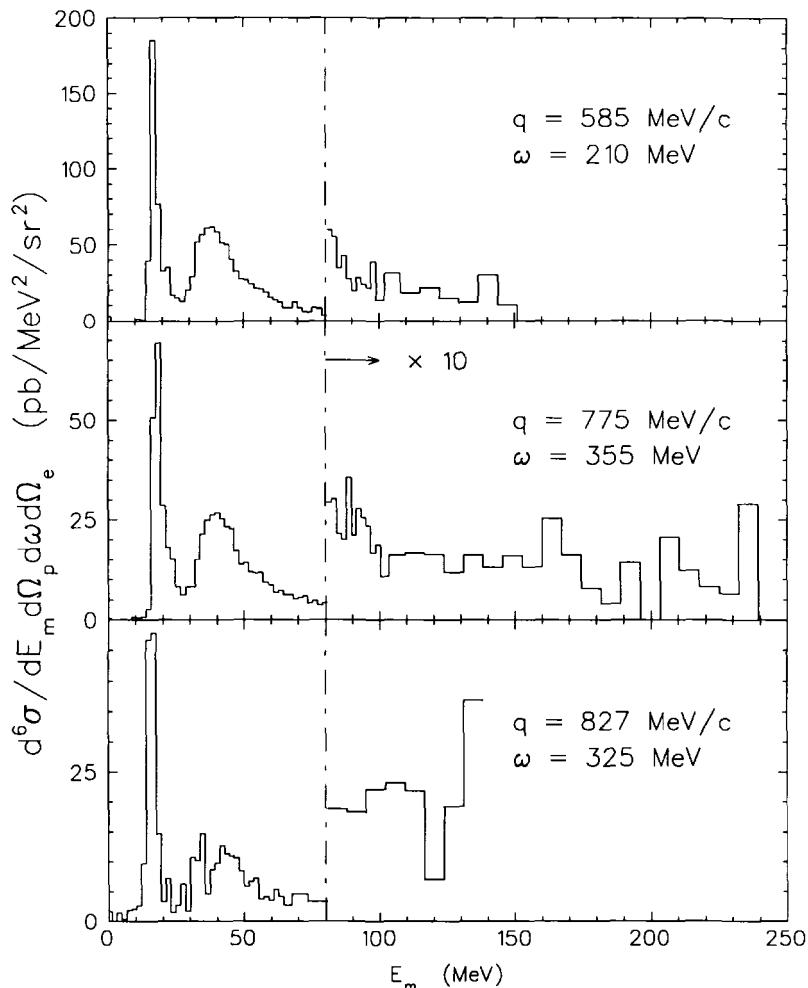
Fig. 7.22.   **Missing energy spectra for** $^{12}C(e, e'p)$ **for parallel kinematics near the quasielastic peak.** Radiative corrections have been applied. Data beyond 80 MeV have been scaled by a factor of 10.
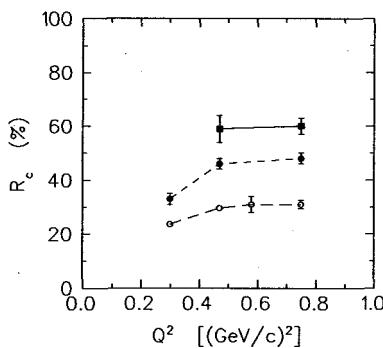
Fig. 7.23. Ratio between continuum and quasifree yields for ^{12}C$(e, e'p)$ in parallel kinematics near the quasielastic peak. Open circles correspond to $E_c = 80$ MeV, solid circles to $E_c = 150$ MeV, solid squares to $E_c = 250$ MeV. Lines are drawn merely to guide the eye. Note that a similar figure appears in Ref. 372 but is inaccurate due to mishandling of variable bin sizes.
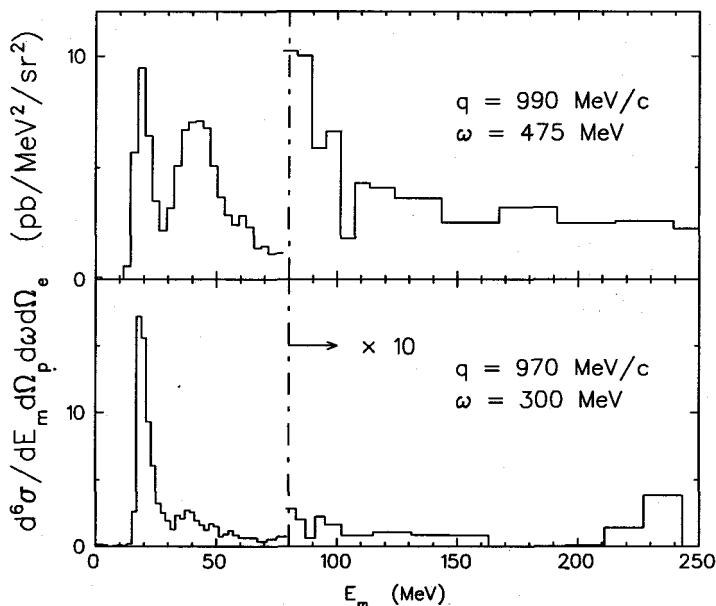
Fig. 7.24. Missing energy spectra for ^{12}C$(e, e'p)$ for parallel kinematics with $q \approx 980$ MeV/c. Radiative corrections have been applied. Data beyond 80 MeV have been scaled by a factor of 10.

of missing energy to be

$$Y(E_1, E_2) = \int_{E_1}^{E_2} dE_m \frac{d^6\sigma}{dE_m d\Omega_p d\omega d\Omega_e} \qquad (7.16)$$

the ratio between the continuum and quasifree yields

$$R_c(Q^2) = \frac{Y_c}{Y_{qf}} = \frac{Y(50, E_c)}{Y(12, 50)} \qquad (7.17)$$

can be assessed by somewhat arbitrarily defining the quasifree region to be the interval $12 < E_m < 50$ MeV, and the "continuum" region to be the interval $50 < E_m < E_c$. Note that the dependence of R_c upon kinematic variables other than Q^2 and the cut-off energy E_c has been suppressed. The MIT-Bates results for the quasielastic peak are summarized in Fig. 7.23. We find that the continuum fractions appear to be relatively constant for $0.4 \leq Q^2 \leq 0.8$ (GeV/c)^2 and not to have been saturated even at $E_c = 250$ MeV. Thus, more than 40% of the yield for these kinematics is found in the continuum with $E_m > 50$ MeV.

The data for negative-y shown in Fig. 7.24 demonstrate that for (nearly) constant q the relative continuum yield decreases rapidly as ω decreases on the low-ω side of the quasielastic peak.[334] In this case, for $E_c = 150$ MeV we find $R_c \approx 48\%$ for $y = -0.05$ and $R_c \approx 21\%$ for $y = -0.18$ at $q \approx 980$ MeV/c. Presumably the reduced phase space for multinucleon emission accounts for this behavior.

Several attempts to interpret these data in terms of proton rescattering have been made. Takaki[373] studied the role of small-angle inelastic scattering using a model calibrated with respect to (p, p') data and found that rescattering following single-nucleon knockout could only account for roughly 8% of the yield observed in the dip region for $E_m > 50$ MeV and is negligible for $E_m > 100$ MeV. He concludes that two-body or more complicated photoabsorption mechanisms are required. Phase-space considerations favor the dominance of three-body absorption for large missing energies. Using a cascade calculation, Weinstein *et al.*[216] find that at $q = 585$ MeV/c rescattering accounts for only 10% of the continuum yield for $50 < E_m < 100$ MeV and 20% for $100 < E_m < 160$ MeV. However, rescattering accounts for less than 5% of the yield for $E_m > 50$ MeV for $q = 775$ and 827 MeV/c. They further argue that two-nucleon correlations do not provide appreciable continuum yield for $E_m > 80$ MeV, and hence attribute most of the high-energy continuum to multinucleon absorption in which the virtual photon is absorbed by a cluster of three or more nucleons.

It is also important to recognize that even though a fairly wide range of missing energies was included in the measurements listed in Table 7.1,

only a very small fraction of the inclusive (e, e') phase space has been covered. Extrapolation from (e, e') to $(e, e'p)$ typically requires factors of 30–250, while extrapolation of multinucleon mechanisms requires factors of 100–1500.[374] However, despite the large extrapolation, single nucleon knockout amounts to only 40–60% of the inclusive quasielastic yield, and less in the dip, with the remainder presumably attributable to various multinucleon emission channels.[374] Characterizing these mechanisms will require measurements with large acceptance devices.

Finally, Baghaei *et al.*[333] measured the two missing-energy spectra in parallel kinematics shown in Fig. 7.25. Kinematics I corresponds to a point approximately halfway between the dip and the peak in the inclusive spectrum for excitation of the Δ, while kinematics II corresponds to the top of the Δ peak. In both spectra a quasifree Δ peak is observed astride a broader continuum. The spectra are qualitatively similar to the (γ, p) data obtained by Homma *et al.*[375,376] with tagged photons. The latter were fitted with two Gaussians and the peak at lower missing energy was attributed to quasideuteron absorption based upon its kinematic behavior. The $(e, e'p)$ results are qualitatively consistent with those of (γ, p), but cannot distinguish between two-body and multinucleon absorption mechanisms because the continuum yield is also compatible with three-body phase space. However, multinucleon absorption was favored on the basis of the foregoing estimates which do not produce adequate yield from two-body mechanisms under these kinematic conditions. The possibility of a substantial multinucleon continuum complicates the extraction of the Δ peak.

The absence of appreciable longitudinal strength for $E_m > 50$ MeV suggests that the single-nucleon mechanism does not contribute much to the continuum yield at large missing energy. The failure of rescattering mechanisms to account for a large fraction of the continuum yield suggests the multinucleon absorption must play a dominant role in the transverse response for large missing energy. These observations are consistent with the expectation that the transverse/longitudinal ratio is determined primarily by the absorption mechanism for the virtual photon and is not substantially altered by final-state interactions. Multinucleon mechanisms involving meson-exchange currents, isobar excitation, or pion production and reabsorption are all predominantly transverse in character. At larger missing momenta, short-range correlations may also contribute to the longitudinal response in the continuum, but Rosenbluth separations are not yet available for the appropriate kinematics.

An obvious consequence of these results is that multipole decompositions of the continuum which seek to extract the single-particle properties of deep-hole orbitals may be contaminated by multinucleon contributions. Since these processes are primarily transverse, it would be useful to obtain separated
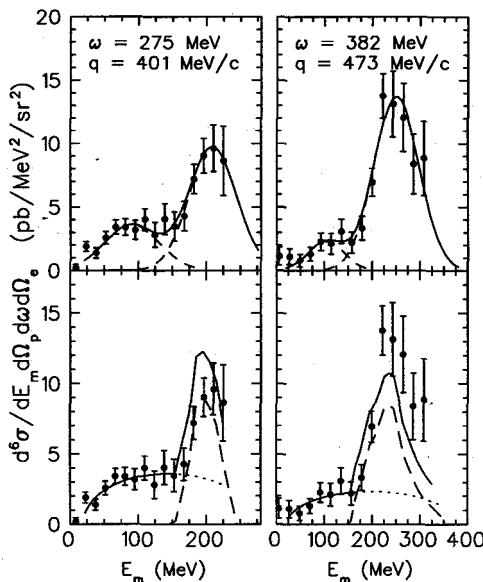
Fig. 7.25. Missing energy spectrum for $^{12}C(e, e'p)$ in the delta region. Kinematics I (left) correspond to about midway between the dip and the Δ peak, while kinematics II (right) are at the Δ peak. Radiative corrections have not been applied. In the top row the data are fitted by two Gaussians. In the bottom row the same data are fitted (solid curves) with three-body phase space (dotted) and quasifree (dashed) contributions.

response functions for the deep-hole region of the spectral function ($E_x \lesssim 50$ MeV). It is also of vital importance to observe short-range correlations directly through experiments which detect two or more nucleons in coincidence with the scattered electron. Separated response functions should be measured for each of the possible isospin channels.

7.6.2. Contribution of Two-Nucleon Knockout to $(e, e'p)$

The $(e, e'pp)$ and $(e, e'pn)$ contributions to $^{12}C(e, e'p)$ in the dip and Δ regions have been studied by Ryckebusch et al.[377] using the Gent model described in Section 7.4.3 Assuming that removal of the first nucleon does not affect removal of a second, the two-hole spectral function was represented by a convolution of single-hole spectral functions[350]

$$S_{hh'}(E) = \int_0^E dE' \, S_h(E') S_{h'}(E - E') \tag{7.18}$$

where $S_h(E)$ is parametrized using a quasihole form.[378] After integration with respect to the undetected nucleon, the two-nucleon contribution to single-nucleón knockout is found to peak at about 80 MeV of missing energy for $\theta_{pq} = 0°$ and to broaden and shift toward larger E_m as θ_{pq} increases. The $(e, e'pn)$ contribution is much stronger and has a wider E_m distribution than the $(e, e'pp)$ contribution, but is not sufficient to explain the continuum yield at large E_m for parallel kinematics. These findings are qualitatively consistent with the phase-space model of Takaki.

Data for $^{12}C(e, e'p)$ have been acquired by Kester $et\ al.$[379] for $E_m < 180$ MeV in the dip region, $(\omega, q) = (212\ \text{MeV}, 270\ \text{MeV}/c)$, in the angular ranges $20° \leq \theta_{pq} \leq 80°$ and $100° \leq -\theta_{pq} \leq 170°$ corresponding to $250 < p_m < 750\ \text{MeV}/c$. The Gent MEC+IC describes the data fairly well for $\theta_{pq} > 70°$, but does not produce enough strength for smaller angles where the emission of correlated nucleón pairs is likely to be important[377,379] Part of the difficulties for large E_m and small θ_{pq} in the dip region may also be due to neglect of real pion production processes.

7.6.3. $(e, e'NN)$ and (γ, NN) Measurements

There is presently much interest in studies of $(e, e'NN)$ reactions, and several pioneering experiments have been performed, but since few results are available it is premature to review that subject here. On the other hand, much high-quality work has been performed for (γ, NN) reactions; a recent review of the available data has been made by MacGregor.[380] For energies much below the Δ resonance, the (γ, pn) contribution dominates the two-nucleon mechanism through its electric dipole moment, while the absence of electric dipole absorption limits the (γ, pp) and (γ, nn) channels to a few percent of the (γ, pn) contribution. Near the Δ resonance the three channels are closer in magnitude and angular dependence. Furthermore, it has become clear that absorption on nucleon pairs makes a large contribution to (γ, N) cross sections, especially to (γ, n). For example, the exclusive $^{16}O(\gamma, n)$ for $150 \leq E_\gamma \leq 250\ \text{MeV}$ of Beise $et\ al.$[381] can be reproduced within the Gent model[350] where it is found that the MEC contribution is dominant for $E_\gamma < 200\ \text{MeV}$ with the IC contribution becoming important for larger E_γ. However, the model[350] still underestimates $^{12}C(\gamma, p)$ cross sections, particularly for forward proton angles, and the $^{16}O(\gamma, pN)$ data for $E_\gamma = 281$ MeV and $\theta_p = 52°$[382] at low proton energies.

Boffi $et\ al.$[383] argue that short-range correlations tend to enhance the contributions to (γ, pn) made by the one-body current and to reduce the two-body current. Thus the photon asymmetry becomes a valuable probe of the reaction mechanism. Uncertainties due to optical-model ambiguities tend

to divide out in the asymmetry, but dynamical effects which alter the spin structure of the reaction are emphasized. Of course similar sensitivities are expected for $(e, e'NN)$ reactions, possibly including beam and/or ejectile polarization, in which the polarization of the virtual photon can be manipulated with greater flexibility.

It is often argued that suppression of transverse two-body currents for the $(e, e'pp)$ channel offers the best view of short-range dynamical correlations of central spin- and isospin-independent character. Pairs of identical nucleons are expected to be found preferentially in $^1S_0$ states which have no magnetic dipole moment and to which charged meson-exchange currents do not contribute. Similarly the $p\Delta^+ \longrightarrow pp$ contributions are suppressed because coupling to the pp channel requires $L = 2$. Thus, one expects $(e, e'pp)$ to have a strong longitudinal response, while $(e, e'pn)$ is predominantly transverse. For example, Giusti and Pacati[384] conclude that the nature of the two-nucleon correlation function plays a dominant role in determining the magnitude of the $(e, e'pp)$ cross section for symmetric coplanar kinematics, while ambiguities in final-state interactions are relatively unimportant.

7.6.4. Multinucleon Pion Absorption

Related evidence for true multinucleon pion absorption, beyond what is associated with initial- or final-state interactions, is available from recent pion absorption measurements.[385–389] For pion energies as low as 65 MeV, three- and four-nucleon emission accounts for about a third of the total π^+ absorption cross section on ^{16}O.[385] The ratio between $3p$ and $2p$ cross sections grows sharply with increasing pion energy up to about 200 MeV and then tends to flatten out for higher energies,[388] which is qualitatively consistent with a prediction of Oset et al.[390] for the energy dependence of the fraction of the total absorption cross section which results in direct emission of more than two nucléons. The three-body and more complex emission channels also tend to populate large missing energy. Although a complete theoretical interpretation of these data is not yet available, it is likely that real and virtual photon absorption with comparable energy transfer will also populate multinucleon emission channels through similar mechanisms at similar relative rates.

7.7. Summary

Separated response functions and polarization observables can be used to make very incisive tests of the electronuclear reaction mechanism. The ratio between the transverse and longitudinal response functions for inclusive quasielastic scattering is larger than predicted by the best available the-

oretical calculations. Measurements for quasielastic $^{12}C(e, e'p)$ show that $R_T/R_L \sim 1$ for small excitation energy, but that the ratio increases beyond the two-nucleon emission threshold. The longitudinal response becomes small beyond the region dominated by single-nucleon knockout, but the transverse response features a nearly uniform continuum extending to much larger excitations energies. Although strong multinucleon contributions to the continuum are expected for large missing momenta, the transverse continuum for modest momenta appears to be surprisingly large. However, only a tiny fraction of the phase space has been examined thus far and separated response functions have been obtained for even less. Further insight into the nature of multinucleon currents requires measurement of separated response functions in which single-nucleon, two-nucleon, and multinucleon contributions to the continuum are distinguished.

Theoretical calculations suggest that R_{LT} is especially sensitive to two-body currents, but the two models presently available disagree sharply over the relative importance of meson-exchange and isobar currents and over the sensitivity to nuclear structure. Several pioneering measurements have been made, but are not described well by the existing models. Since the spin structure of various contributions to the two-body electromagnetic current differ from each other and are different for neutron versus proton knockout, measurements of interference and polarization response functions for both ejectile types should provide discriminating tests of the models. Since it is expected that neutron knockout will be particularly sensitive to the isobar current, we have developed a coupled channels model which describes both inelastic scattering and charge exchange in the final state using density-dependent effective interactions.

Channel coupling in the final state can appreciably enhance the cross sections for low-lying states reached by proton knockout with $p_m \gtrsim 300$ MeV/c. These effects depend upon details of nuclear structure and appear to be strongest for deformed residual nuclei. Therefore, the analysis of experiments designed to investigate short-range correlations in nuclear wave functions using knockout reactions with large missing momenta must carefully consider channel coupling in the final state using microscopic models of the coupling potentials. Unfortunately, channel coupling effects appear to be most important for nonparallel kinematics where, for practical reasons, most of the experiments have been done or are planned. It is unlikely that unambiguous information about short-range correlations can be obtained from single-nucleon knockout.

Therefore, although much has been learned from the existing data, there remain several outstanding issues. Fortunately, it soon will be possible to perform much more extensive investigations of the electromagnetic response of

nuclear matter using the vastly expanded kinematic range made available by the continuous duty-cycle, high intensity, polarized beams of at least 4 GeV electrons deliverable at CEBAF to three halls which feature complementary detection capabilities, including a pair of high-resolution spectrometers and a recoil polarimeter in Hall A, a large acceptance spectrometer in Hall B, and a flexible mix of instruments in Hall C. These facilities will make it possible to perform detailed studies of the electronuclear reaction mechanism involving the detection of two or more ejectiles in coincidence with the scattered electron.

8.   CONCLUSIONS

We have reviewed the current status of nucleon knockout by electron scattering. Over the last decade or so, technological progress has broadened the range of phenomena accessible to experimental investigation considerably, but the capabilities of new facilities, principally at Mainz and CEBAF, augur an even brighter future.

The availability of polarized beams, polarized targets, and recoil polarimetry for both protons and neutrons now makes it possible to measure nucleon electromagnetic form factors with much greater precision. Rather than rely on delicate Rosenbluth separations of the cross section, which is dominated at high Q^2 by the magnetic form factor, recoil polarization allows the ratio between the electric and magnetic form factors to be obtained with much less systematic error. The feasibility of this technique has been demonstrated, for both neutrons and protons, and it will soon be applied over a wider range of Q^2 with better statistical precision at the new continuous-beam facilities. Furthermore, polarized $^3\vec{\mathrm{He}}$ targets are now available and can be used to obtain similar information. Several inclusive $^3\vec{\mathrm{He}}(\vec{e}, e')$ experiments have been performed, but greater Q^2 is needed to reduce the proton contributions to a level that permits extraction of neutron form factors. Alternatively, detection of the recoil neutron in the $^3\vec{\mathrm{He}}(\vec{e}, e'n)$ suppresses the proton contribution and also provides a sensitive probe of the neutron form factors; feasibility has been demonstrated and systematic measurements are expected. Other techniques, such as $\vec{d}(\vec{e}, e'N)$ reactions using deuterated ammonia targets, are under development also. Clearly, by requiring consistency between form factors extracted from measurements of several reactions, it should be possible to limit uncertainties due to nuclear structure and reaction mechanisms and thereby to obtain accurate knowledge of these fundamental quantities.

Away from the quasielastic ridge, nucleon knockout reactions on few-nucleon systems can be used to test models of three-nucleon interactions,

two-body currents, and off-shell properties of the electromagnetic vertex. Several measurements of the unpolarized longitudinal–transverse interference response function have been made for $\mathbf{d}(e, e'p)$, but the systematic errors remain uncomfortably large — better precision is expected for new measurements proposed for Mainz and CEBAF. Furthermore, the wider range of separated response functions and polarization observables accessible at the new facilities will permit much more incisive tests of these models to be made.

A systematic survey of the low-lying quasihole states in complex nuclei has been made at NIKHEF with a missing-energy resolution that is often better than 100 keV. For $p_m \lesssim 300$ MeV/c, the quasihole momentum distributions are generally consistent with simple Skyrme–Hartree–Fock calculations, with little spurious dependence upon the kinematical conditions of the experiment. The valence hole strength is typically about 65% of the independent particle model, almost independent of A. The spreading widths for deeper hole states are qualitatively consistent with dispersive optical models of the mean field and the quasiparticle strength tends to increase for deeper hole states, although some extrapolation is needed to account for strength outside the accessible range of missing energy. The excellent resolution has also permitted observation of knockout from nominally empty orbitals, which, immediately above the Fermi level, are found to be occupied to typically about 5–10%. These findings are in good qualitative agreement with both many-body theory and dispersive optical models of nucleon scattering. For larger missing momenta (above 300 MeV/c), recent measurements for low-lying states show evidence of a modest enhancement with respect to mean-field wave functions. However, coupled-channels effects in the final state can produce similar enhancements without invoking short-range correlations. It is unlikely that high-momentum components in nuclear wave functions can be extracted unambiguously from single-nucleon knockout measurements for low-lying quasihole states.

Unfortunately, most of the $(e, e'p)$ data for complex nuclei were acquired with ejectile energies that are lower than optimal and were analyzed with optical models that are not very reliable. Optical potentials fitted to elastic scattering data alone offer no direct sensitivity to the interior wave function needed for knockout calculations. Our analysis of the nuclear transparency data for 180–200 MeV protons demonstrates that the commonly used global optical potentials, both relativistic and nonrelativistic, are too absorptive at that energy. For energies above about 120 MeV, empirical effective interactions fitted to both inelastic and elastic scattering data simultaneously provide accurate predictions for proton absorption and neutron total cross sections and for nuclear transparency in $(e, e'p)$ reactions. Therefore, some of these measurements should be repeated with higher ejectile energies. Transparency

measurements for 0.4–1.0 GeV protons are planned for CEBAF and will be analyzed using potentials from Dirac phenomenology and from empirical effective interactions. Missing momentum distributions for discrete states in several nuclei should also be measured for comparison with the NIKHEF data as a test of the model independence of spectroscopic information.

Measurements of interference and polarization response functions provide more detailed tests of the electronuclear reaction mechanism. Several measurements of the longitudinal–transverse response function for $(e, e'p)$ have been made, but are not yet understood. Theoretical calculations suggest that R_{LT} should be sensitive to two-body currents, but the two models presently available disagree sharply about the relative importance of meson-exchange and isobar currents and about the dependence of these effects upon nuclear structure. Since the spin structures of various two-body currents differ from each other and from the one-body current, measurements of other separated response functions and polarization observables, especially those quantities which would survive even in the absence of final-state interactions, should provide much insight into the roles of meson-exchange and isobar currents. Furthermore, neutron knockout is expected to be especially sensitive to the isobar current. These experiments will also become possible with the new facilities.

Preliminary data from large-acceptance measurements at Mainz suggest that the momentum components below about 300 MeV/c are dominated by low-lying quasihole configurations but that the tail of the momentum distribution is dominated by a continuum distribution at large excitation energy. Saclay measurements of the high-momentum continuum for light nuclei display a kinematic signature of knockout from a correlated pair in which an undetected high-momentum partner carries away most of the excitation energy for the $A - 1$ system. Hence these data are qualitatively consistent with theoretical calculations that predict that the high-momentum strength produced by short-range and tensor correlations is spread over several hundred MeV of excitation energy. Clearly it is desirable to separate the single-nucleon continuum from more complicated multinucleon channels and to characterize each channel more completely. Measurements of separated response functions should provide much insight into the reaction mechanisms that contribute to multinucleon knockout. Indirect evidence for multinucleon knockout has been obtained from $^{12}C(e, e'p)$ measurements at MIT–Bates that at modest missing momenta feature a nearly uniform, predominantly transverse continuum extending to large missing energy that cannot be ascribed to single-nucleon processes. However, only a minuscule fraction of the available phase space has been examined thus far. The CEBAF large-acceptance spectrometer should prove invaluable to these investigations.

Therefore, although much has been learned since the last review of nucleon knockout reactions by electron scattering appeared in this series, the subject is certainly not closed. By the time the next review is performed, we can expect to have precise measurements of the nucleon electromagnetic form factors, the spectral functions of light and complex nuclei, and to understand much better the electromagnetic current in many-body systems. Parity-violating asymmetries should also provide information about strangeness in nucleons and nuclei. Although not discussed here, electroproduction of baryon resonances and their propagation in nuclear matter will also be an exciting field made accessible by the emerging experimental capabilities at new facilities.

ACKNOWLEDGMENTS

REFERENCES

1. S. Frullani and J. Mougey, in *Advances in Nuclear Physics,* edited by J. W. Negele and E. W. Vogt, volume 14, Plenum Press, New York (1984).
2. A. E. L. Dieperink and P. K. A. de Witt Huberts, *Ann. Rev. Nucl. Part. Sci.* **40**, 239 (1990),
3. S. Boffi, C. Giusti, and F. D. Pacati, *Phys. Rep.* **226**, 1 (1993).
4. P. J. Mulders, *Phys. Rep.* **185,** 83 (1990).
5. M. J. Musolf, T. W. Donnelly, J. Dubach, *et al., Phys. Rep.* **239**, 1 (1994).
6. B. Frois and I. Sick, editors, *Modern Topics in Electron Scattering,* World Scientific, Singapore (1991).
7. T. W. Donnelly, in: *Proceedings of the Workshop on Perspectives in Nuclear Physics at Intermediate Energies,* edited by S. Boffi, C. C. degli Atti, and M. Giannini, World Scientific, Trieste (1984).
8. T. W. Donnelly, *Progress in Particle and Nuclear Physics ,* 183 (1985).
9. A. Picklesimer, J. W. van Orden, and S. J. Wallace, *Phys. Rev.* **C32,** 1312 (1985).

10. T. W. Donnelly and A. S. Raskin, *Ann. Phys. (N.Y.)* **169**, 247 (1986).
11. A. Picklesimer and J. W. van Orden, *Phys. Rev.* **C35,** 266 (1987).
12. S. Boffi, C. Giusti, and F. D. Pacati, *Nucl. Phys.* **A476**, 617 (1988).
13. C. Giusti and F. D. Pacati, *Nucl. Phys.* **A504**, 685 (1989).
14. A. S. Raskin and T. W. Donnelly, *Ann. Phys. (N.Y.)* **191**, 78 (1989).
15. A. Picklesimer and J. W. van Orden, *Phys. Rev.* **C40**, 290 (1989).
16. J. D. Bjorken and S. D. Drell, *Relativistic Quantum Mechanics,* McGraw-Hill, New York (1964).
17. V. Devanathan, *Annals of Physics* **43**, 74 (1967).
18. T. de Forest, *Nucl. Phys.* **A392**, 232 (1983).
19. T. de Forest, *Annals of Physics* **45**, 365 (1967).
20. N. Dombey, *Rev. Mod. Phys.* **41**, 236 (1969).
21. S. Boffi, C. Giusti, and F. D. Pacati, *Nucl. Phys.* **A435**, 697 (1985).
22. S. Nozawa, B. Blankleider, and T. S. H. Lee, *Nucl. Phys.* **A513**, 459 (1990).
23. S. Nozawa, B. Blankleider, and T. S. H. Lee, *Nucl. Phys.* **A513**, 511 (1990).
24. S. Nozawa, B. Blankleider, and T. S. H. Lee, *Nucl. Phys.* **A513**, 543 (1990).
25. D, Drechsel and L. Tiator, *J. Phys. G* **18**, 449 (1992).
26. K. M. Watson, *Phys. Rev.* **95,** 228 (1954).
27. G. G. Ohlsen, *Rep. Prog. Phys.* **35**, 717 (1972).
28. M. Simonius, *Lecture Notes in Physics,* volume 30, pp. 38–87, Springer Verlag, Berlin (1974).
29. C. Giusti and F. D. Pacati, *Nucl. Phys.* **A485**, 461 (1988).
30. U. Fano, Technical Report 1214, National Bureau of Standards (1951).
31. V. Dmitrasinovic and F. Gross, *Phys. Rev.* **C40**, 2479 (1989).
32. H. Arenhövel, W. Leidemann, and E. L. Tomusiak, *Few-Body Systems* **15**, 109 (1993).
33. M. Bernheim, A. Bussiére, J. Mougey, *et al., Nucl. Phys.* **A375**, 381 (1982).
34. L. Frankfurt and M. Strikman, *Phys. Rep. 150,* 235 (1988).
35. W. Gordon, *Z. Phys.* **50**, 630 (1928).
36. M. F. Gari and W. Krümpelmann, *Phys. Lett.* **B274**, 159 (1992).
37. M. F. Gari and W. Krümpelmann, *Phys. Lett.* **B282**, 483 (1992).
38. R. Schiavilla and D. O. Riska, *Phys. Rev.* **C43**, 437 (1991).
39. R. G. Sachs, *Phys. Rev.* **126**, 2256 (1962).
40. M. N. Rosenbluth, *Phys. Rev.* **79**, 615 (1950).
41. R. G. Arnold, C. E. Carlson, and F. Gross, *Phys. Rev.* **C23**, 363 (1981).
42. S. Galster, H. Klein, J. Moritz, *et at., Nucl. Phys.* **B32**, 221 (1971).
43. J. Sakurai, *Ann. Phys. (N.Y.)* **11**, 1 (1960).
44. F. Iachello and A. D. Jackson, *Phys. Lett.* **43B**, 191 (1973).
45. G. G. Simon, C. Schmitt, F. Borkowski, and V. H. Walther, *Nucl. Phys.* **A333**, 381 (1980).
46. G. Höhler, E. Pietarinen, I. Sabba-Stefanescu, *et al., Nucl Phys.* **B114**, 505 (1976).
47. S. J. Brodsky and G. Farrar, *Phys. Rev. Lett.* **31**, 1153 (1973).
48. S. J. Brodsky and G. Farrar, *Phys. Rev.* **D11**, 1309 (1975).
49. G. P. Lepage and S. J. Brodsky, *Phys. Rev. Lett.* **43***,* 545 (1979).
50. G. P. Lepage and S. J. Brodsky, *Phys. Rev. Lett.* **43**, 1625 (1979).
51. M. F. Gari and W. Krümpelmann, *Zeit. Phys.* **A322**, 689 (1985).
52. M. F. Gari and W. Krümpelmann, *Phys. Lett.* **B173**, 10 (1986).
53. R. Hofstadter, *Rev. Mod. Phys.* **28**, 214 (1956).
54. L. Durand, *Phys. Rev.* **123**, 1393 (1961).
55. F. M. Renard, J. T. T. Van, and M. L. Bellac, *Il Nuovo Cimento* **38**, 553, 1689 (1965).
56. H. Theissen and W. Schiltz, *Zeit. Phys.* **266**, 33 (1974).
57. J. J. Murphy, Y. M. Shin, and D. M. Skopik, *Phys. Rev.* **C9**, 2125 (1974).

58. F. Borkowski, G. G. Simon, V. H. Walther, and R. D. Wendling, *Nucl. Phys.* **B93**, 461 (1975).
59. T. Janssens, R. Hofstadter, E. B. Hughes, and M. R. Yearian, *Phys. Rev.* **142,** 922 (1966).
60. P. E. Bosted, A. T. Katramatou, R. G. Arnold, *et al, Phys. Rev.* **C42**, 38 (1990).
61. C. Berger, V. Burkhert, G. Knop, B. Langenbeck, and K. Rith, *Phys. Lett.* **35B**, 87 (1971).
62. W. Bartel, F.-W. Büsser, W.-R. Dix, *et al, Nucl. Phys.* **B58**, 429 (1973).
63. R. C. Walker, B. W. Filippone, J. Jourdan, *et al., Phys. Lett.* **B224**, 353 (1989).
64. R. C. Walker, B. W. Filippone, J. Jourdan, *et al, Phys. Rev.* **D49**, 5671 (1994).
65. J. Litt, G. Buschhorn, D. H. Coward, *et al., Phys. Lett.* **31B**, 40 (1970).
66. P. E. Bosted, L. Andivahis, A. Lung, *et al, Phys. Rev. Lett.* **68**, 3841 (1992).
67. L. Andivahis, P. E. Bosted, A. Lung, *et al., Phys. Rev.* **D50,** 5491 (1994).
68. R. G. Arnold, P. E. Bosted, C. C. Chang, *et al, Phys. Rev. Lett.* **57**, 174 (1986).
69. A. F. Sill, R. G. Arnold, P. E. Bosted, *et al., Phys. Rev.* **D48,** 29 (1993).
70. F. A. Bumiller, F. R. Buskirk, J. W. Stewart, and E. B. Daly, *Phys. Rev. Lett.* **25**, 1774 (1970).
71. G. G. Simon, C. Schmitt, and V. H. Walther, *Nucl. Phys.* **A364,** 285 (1981).
72. H. Anklin, E. E. W. Bruins, D. Day, *et al, Phys. Lett.* **B336,** 313 (1994).
73. E. E. W. Bruins, T. S. Bauer, H. W. den Bok, *et al.,* Phys. Rev. Lett. **75**, 21 (1995).
74. B. Grossetête, S. Jullian, and P. Lehmann, *Phys. Rev.* **141,** 1435 (1966).
75. P. Markowitz, J. M. Finn, B. D. Anderson, *et al, Phys. Rev.* **C48,** R5 (1993).
76. E. B. Hughes, T. A. Griffey, R. Hofstadter, and M. R. Yearian, *Phys. Rev.* **146**, 973 (1966).
77. P. Stein, M. Binkley, R. McAllister, A. Suri, and W. Woodward, *Phys. Rev. Lett.* **16**, 592 (1966).
78. S. Platchkov, A. Amroun, S. Auffret, *et al., Nucl. Phys.* **A510,** 740 (1990).
79. W. Bartel, F.-W. Büsser, W.-R. Dix, *et al., Phys. Lett.* **30B**, 285 (1969).
80. A. S. Esaulov, A. P. Rekalo, M. P. Rekalo, *et al, Sov. J. Nucl. Phys.* **45**, 258 (1987).
81. E. B. Hughes, T. A. Griffey, M. R. Yearian, and R. Hofstadter, *Phys. Rev.* **139**, B458 (1965).
82. D. Braess, D. Hasselmann, and G. Kramer, *Zeit. Phys.* **198**, 527 (1967).
83. W. Bartel, F.-W. Büsser, W.-R. Dix, *et al., Phys. Lett.* **39B**, 407 (1972).
84. K. M. Hanson, J. R. Dunning, Jr., M. Goitein, *et al, Phys. Rev.* **D8**, 753 (1973).
85. R. G. Arnold, D. Benton, P. Bosted, *et al., Phys. Rev. Lett.* **61,** 806 (1988).
86. A. Lung, L. M. Stuart, P. E. Bosted, *et al., Phys. Rev. Lett.* **70**, 718 (1993).
87. R. J. Budnitz, J. Appel, L. Carrol, *et al, Phys. Rev.* **173**, 1357 (1968).
88. S. Rock, R. G. Arnold, P. Bosted, *et al., Phys. Rev. Lett.* **49**, 1139 (1982).
89. S. J. Brodsky and G. P. Lepage, *Physica Scripta* **23**, 945 (1981).
90. H. Arenhövel, *Phys. Lett.* **B199,** 13 (1987).
91. H. Arenhövel, W. Leidemann, and E. L. Tomusiak, *Zeit. Phys.* **A331**, 123 (1988).
92. F. C. P. Joosse, PhD thesis, Rijksuniversiteit te Utrecht (1993).
93. D. Fritschi, PhD thesis, University of Basel (1993).
94. L. L. Foldy, *Rev. Mod. Phys.* **30**, 471 (1958).
95. V. E. Krohn and G. R. Ringo, *Phys. Rev.* **D8,** 1305 (1973).
96. V. F. Sears, *Phys. Rep.* **141,** 281 (1986).
97. L. Koester, W. Nistler, and W. Waschkowski, *Phys. Rev. Lett.* **36**, 1021 (1976).
98. L. Koester, W. Waschkowski, and J. Meier, *Zeit. Phys.* **A329,** 229 (1988).
99. Y. A. Alexandrov, Sov. *J. Nucl. Phys.* **37,** 149 (1983).
100. H. Leeb and C. Teichtmeister, *Phys. Rev.* **C48,** 1719 (1994).
101. Y. A. Alexandrov, *Phys. Rev.* **C49,** R2297 (1994).
102. Y. A. Alexandrov, J. Vavra, M. Vrana, *et al, Sov. Phys. JETP* **62**, 19 (1985).
103. M. Lacombe, B. Loiseau, J. M. Richard, *et al., Phys. Rev.* **C21**, 861 (1980).
104. M. Lacombe, B. Loiseau, R. Vinh Mau, *et al, Phys. Lett.* **101B,** 139 (1981).

105. R. V. Reid, *Ann. Phys. (N.Y.)* **50**, 411 (1968).
106. R. B. Wiringa, R. A. Smith, and T. L. Ainsworth, *Phys. Rev.* **C29**, 1207 (1984).
107. M. M. Nagels, T. A. Rijken, and J. de Swaart, *Phys. Rev.* **D17**, 769 (1978).
108. S. Platchkov, private communication (1994).
109. T. Eden, R. Madey, W.-M. Zhang, *et al., Phys. Rev. C* **50**, R1749 (1994).
110. A. K. Thompson, A. M. Bernstein, T. E. Chupp, *et al., Phys. Rev. Lett.* **68**, 2901 (1992).
111. C. E. Jones, E. J. Beise, J. E. Belz, *et al., Phys. Rev.* **C47**, 110 (1993).
112. M. Meyerhoff, D. Eyl, A. Frey, *et al., Phys. Lett.* **B327**, 201 (1994).
113. T. Eden, R. Madey, W.-M. Zhang, *et at., Nucl. Instrum. Methods* **A338**, 432 (1994).
114. F. Klein, in: *Proceedings of the Workshop on Perspectives in Nuclear Physics at Inter-mediate Energies,* World Scientific, Trieste (1993).
115. B. Blankleider and R. M. Woloshyn, *Phys. Rev.* **C29**, 538 (1984).
116. J. L. Friar, B. F. Gibson, G. L. Payne, A. M. Bernstein, and T. E. Chupp, *Phys. Rev.* **C42**, 2310 (1990).
117. I. R. Afnan and N. D. Birrell, *Phys. Rev.* **C16,** 823 (1977).
118. C. C. degli Atti, E. Pace, and G. Salmé, *Phys. Rev.* **C46**, R1591 (1992).
119. R.-W. Schulze and P. U. Sauer, *Phys. Rev.* **C48**, 38 (1993).
120. C. C. degli Atti, E. Pace, and G. Salmé, in *Proceedings of the VI Workshop on Perspectives in Nuclear Physics at Intermediate Energies,* World Scientific, Singapore (1993).
121. C. C. degli Atti, E. Pace, and G. Salmé, *Phys. Rev.* **C51**, 1108 (1995).
122. C. E. Woodward, E. J. Beise, J. E. Belz, *et al., Phys. Rev. Lett.* **65,** 698 (1994).
123. H. Gao, J. Arlington, E. J. Beise, *et al., Phys. Rev.* **C50**, R546 (1994).
124. C. E. Jones-Woodward, E. J. Beise, J. E. Belz, *et al., Phys. Rev.* **C44**, R571 (1991).
125. J.-O. Hansen, M. A. Titko, D. DeSchepper, *et al., Phys. Rev. Lett.* **74**, 654 (1995).
126. J. M. Laget, *Phys. Lett.* **B273**, 367 (1991).
127. M. A. Miller, K. Lee, J.-O. Hansen, *et al., Phys. Rev. Lett.* **74**, 502 (1995).
128. J. M. Laget, *Phys. Lett.* **B276**, 398 (1992).
129. D. Day, The Electric Form Factor of the Neutron from the $\vec{d}(\vec{e}, e'n)p$ Reaction, Technical Report Experiment 93-026, CEBAF (1993).
130. M. P. Rekalo, G. I. Gakh, and A. P. Rekalo, *J. Phys. G* **15**, 1223 (1989).
131. T. W. Donnelly, J. Dubach, and I. Sick, *Phys. Rev.* **C37**, 2320 (1988).
132. S. Auffret, J.-M. Cavedon, J.-C. Clemens, *et al., Phys. Rev. Lett.* **55**, 1362 (1985).
133. M. Bernheim, A. Bussiére, J. Mougey, *et al., Nucl. Phys.* **A365**, 349 (1981).
134. S. Turck-Chieze, P. Barreau, M. Bernheim, *et al., Phys. Lett.* **142B**, 145 (1984).
135. M. van der Schaar, H. Arenhövel, T. S. Bauer, *et al., Phys. Rev. Lett.* **66**, 2855 (1991).
136. M. van der Schaar, H. Arenhövel, H. P. Blok, *et al., Phys. Rev. Lett.* **68**, 776 (1992).
137. F. Frommberger, D. Durek, R. Gothe, *et al., Phys. Lett.* **B339**, 12 (1994).
138. J. E. Ducret, M. Bernheim, J. F. Danel, *et al, Phys. Rev.* **C49**, 1783 (1994).
139. E. Jans, M. Bernheim, M. K. Brussel, *et al., Nucl Phys.* **A475**, 687 (1987).
140. P. H. M. Keizer, J. F. J. van den Brand, J. W. A. den Herder, *et al., Phys. Lett.* **B197**, 29 (1987).
141. C. Marchand, M. Bernheim, P. C. Dunn, *et al., Phys. Rev. Lett.* **60**, 1703 (1988).
142. J. F. J. van den Brand, H. P. Blok, R. Ent, *et al., Phys. Rev. Lett.* **60**, 2006 (1988).
143. J. F. J. van den Brand, H. P. Blok, R. Ent, *et al., Phys. Rev. Lett.* **66**, 409 (1991).
144. J. F. J. van den Brand, H. P. Blok, R. Ent, *et al., Nucl. Phys.* **A534**, 637 (1991).
145. A. Magnon, M. Bernheim, M. K. Brussel, *et al., Phys. Lett.* **B222**, 352 (1989).
146. M. B. Epstein, K. A. Aniol, D. J. Margaziotis, *et al., Phys. Rev. Lett.* **70**, 2868 (1993).
147. J. M. L. Goff, M. Bernheim, M. K. Brussel, *et al., Phys. Rev.* **C50**, 2278 (1994).
148. J. L. Friar, in *Modern Topics in Electron Scattering,* edited by B. Frois and I. Sick, pp. 104–135, World Scientific, Singapore (1991).
149. J. Carlson, *Phys. Rev.* **C36**, 2026 (1987).

150. R. Schiavilla, V. R. Pandharipande, and R. B. Wiringa, *Nucl. Phys.* **A449,** 219 (1986).
151. J. M. Laget, *Phys. Lett.* **B151,** 325 (1985).
152. J. M. Laget, *Phys. Lett.* **B199,** 493 (1987).
153. T. Tamae, H. Kawahara, A. Tanaka, *et al., Phys. Rev. Lett.* **59,** 2919 (1987).
154. W. Fabian and H. Arenhövel, *Nucl. Phys.* **A314,** 253 (1979).
155. H. Arenhövel, *Nucl. Phys.* **A384,** 287 (1982).
156. B. Mosconi and P. Ricci, *Nucl. Phys.* **A517,** 483 (1990).
157. G. van der Steenhoven, *Few-Body Systems* **17,** 79 (1994).
158. E. Hummel and J. A. Tjon, *Phys. Rev. Lett.* **63,** 1788 (1989).
159. G. Beck and H. Arenhövel, *Few-Body Systems* **13,** 165 (1992).
160. E. Hummel and J. A. Tjon, *Phys. Rev.* **C42,** 423 (1990).
161. H. Meier-Hajduk, C. Hajduk, P. U. Sauer, and W. Theis, *Nucl. Phys.* **A395,** 332 (1983).
162. E. van Meijgaard and J. A. Tjon, *Phys. Rev.* **C42,** 74 (1990).
163. E. van Meijgaard and J. A. Tjon, *Phys. Rev.* **C42,** 96 (1990).
164. E. van Meijgaard and J. A. Tjon, *Phys. Rev.* **C45,** 1463 (1992).
165. K. Dow, S. Dytman, D. Beck, *et al., Phys. Rev. Lett.* **61,** 1706 (1988).
166. S. Ishikawa, H. Kamada, W. Glöckle, and H. Witala, *Il Nuovo Cimento* **107A,** 305 (1994).
167. J. Golak, H. Kamada, H. Witala, W. Glöckle, and S. Ishikawa, *Phys. Rev.* **C51,** 1638 (1995).
168. M. Buballa, **S. Drożdż,** S. Krewald, and A. Szczurek, *Phys. Rev.* **C44,** 810 (1991).
169. T. Warmann and K. Langanke, *Phys. Lett.* **B273,** 193 (1991).
170. S. Boffi, C. Giusti, F. D. Pacati, and S. Frullani, *Nucl. Phys.* **A319,** 461 (1979).
171. L. R. B. Elton and A. Swift, *Nucl. Phys.* **A94,** 52 (1967).
172. F. Perey and B. Buck, *Nucl. Phys.* **32,** 353 (1962).
173. F. G. Perey, in *Direct Interactions and Nuclear Reaction Mechanisms,* edited by E. Clementel and C. Villi, pp. 125–138, Gordon and Breach, New York (1963).
174. P. Schwandt, H. O. Meyer, W. W. Jacobs, *et al., Phys. Rev.* **C26,** 55 (1982).
175. I. Abdul-Jalil and D. F. Jackson, *J. Phys. G* **5,** 1699 (1979).
176. D. F. Jackson and I. Abdul-Jalil, *J. Phys. G* **6,** 481 (1980).
177. J. R. Comfort and B. C. Karp, *Phys. Rev.* **C21,** 2162 (1980).
178. Y. Jin and D. S. Onley, *Phys. Rev.* **C50,** 377 (1994).
179. S. Hama, B. C. Clark, E. D. Cooper, H. S. Sherif, and R. L. Mercer, *Phys. Rev.* **C41,** 2737 (1993).
180. E. D. Cooper, S. Hama, B. C. Clark, and R. L. Mercer, *Phys. Rev.* **C47,** 297 (1993).
181. J. Hüfner and C. Mahaux, *Ann. Phys.* (*N.Y.*) 73, 525 (1972).
182. J. P. Jeukenne, A. Lejeune, and C. Mahaux, *Phys. Rev.* **C10,** 1391 (1974).
183. J. P. Jeukenne, A. Lejeune, and C. Mahaux, *Phys. Rep.* **25,** 83 (1976).
184. J. P. Jeukenne, A. Lejeune, and C. Mahaux, *Phys. Rev.* **C15,** 10 (1977).
185. J. P. Jeukenne, A. Lejeune, and C. Mahaux, *Phys. Rev.* **C16,** 80 (1977).
186. F. A. Brieva and J. R. Rook, *Nucl. Phys.* **A291,** 299 (1977).
187. F. A. Brieva and J. R. Rook, *Nucl. Phys.* **A291,** 317 (1977).
188. F. A. Brieva and J. R. Rook, *Nucl. Phys.* **A297,** 206 (1978).
189. F. A. Brieva and J. R. Rook, *Nucl. Phys.* **A307,** 493 (1978).
190. H. V. von Geramb, F. A. Brieva, and J. R. Rook, in *Microscopic Optical Potentials,* edited by H. von Geramb, p. 104, Springer-Verlag, Berlin (1979).
191. T. Hamada and I. D. Johnston, *Nucl. Phys.* **34,** 382 (1962).
192. L. Rikus, K. Nakano, and H. V. von Geramb, *Nucl. Phys.* **A414,** 413 (1984).
193. H. V. von Geramb, in *The Interaction Between Medium Energy Nucleons in Nuclei — 1982,* edited by H. Meyer, volume 97 of *AIP Conference Proceeding,* p. 44, AIP, New York (1983).
194. P. J. Siemens, *Nucl. Phys.* **A141,** 225 (1970).

195. N. Yamaguchi, S. Nagata, and J. Michiyama, *Prog. Theor. Phys.* **70**, 459 (1983).
196. N. Yamaguchi, S. Nagata, and J. Michiyama, *Prog. Theor. Phys.* **76**, 1289 (1986).
197. K. Nakayama and W. G. Love, *Phys. Rev.* **C38**, 51 (1988).
198. R. Machleidt, K. Holinde, and C. Elster, *Phys. Rep.* **149**, 1 (1987).
199. L. Ray, *Phys. Rev.* **C41**, 2816 (1990).
200. J. J. Kelly, W. Bertozzi, T. N. Buti, *et al., Phys. Rev.* **C39**, 1222 (1989).
201. J. J. Kelly, *Phys. Rev.* **C39**, 2120 (1989).
202. J. J. Kelly, J. M. Finn, W. Bertozzi, *et al., Phys. Rev.* **C41**, 2504 (1990).
203. Q. Chen, J. J. Kelly, P. P. Singh, *et al, Phys. Rev.* **C41**, 2514 (1990).
204. J. J. Kelly, A. E. Feldman, B. S. Flanders, *et al., Phys. Rev.* C43, 1272 (1991).
205. J. J. Kelly and S. J. Wallace, *Phys. Rev.* **C49**, 1315 (1994).
206. M. A. Franey and W. G. Love, *Phys. Rev.* **C31**, 488 (1985).
207. T. Cheon, K. Takayanagi, and K. Yazaki, *Nucl. Phys.* **A437**, 301 (1985).
208. T. Cheon, K. Takayanagi, and K. Yazaki, *Nucl. Phys.* **A445**, 227 (1985).
209. A. Nadasen, P. Schwandt, P. P. Singh, *et al., Phys. Rev.* **C23**, 1023 (1981).
210. W. Bauhoff, *At. Data Nucl. Data Tables 35,* 429 (1986).
211. R. W. Finlay, W. P. Abfalterer, G. Fink, *et al., Phys. Rev.* **C47**, 237 (1993).
212. R. W. Finlay, G. Fink, W. P. Abfalterer, *et al,* in *Proceedings of the International Conference on Nuclear Data for Science and Technology,* edited by S. M. Qaim, p. 720, Springer-Verlag, Berlin (1992).
213. Y. Jin and R. W. Finlay, *Phys. Rev.* **C47**, 1697 (1993).
214. H. P. Blok, L. R. Kouw, J. W. A. den Herder, L. Lapikás, and P. K. A. de witt Huberts, *Phys. Lett.* **B198**, 4 (1987).
215. J. W. A. den Herder, E. Jans, P. H. M. Keizer, *et al, Phys. Lett.* **B184**, 11 (1987).
216. L. B. Weinstein, H. Baghaei, W. Bertozzi, *et al, Phys. Rev. Lett.* **64**, 1646 (1990).
217. H. B. M. Raben, private communication (1992).
218. J. Friedrich and P.-G. Reinhard, *Phys. Rev.* **C33**, 335 (1986).
219. P.-G. Reinhard, in *Computational Nuclear Physics 1: Nuclear Structure,* edited by K. Langanke, J. A. Maruhn, and S. E. Koonin, pp. 28–50, Springer-Verlag, Berlin (1991).
220. G. J. Kramer, H. P. Blok, J. F. J. van den Brand, *et al., Phys. Lett.* **B227**, 199 (1989).
221. S. Boffi, C. Giusti, and F. D. Pacati, *Il Nuovo Cimento* **98A**, 291 (1987).
222. H. Fiedeldey, R. Lipperheide, G. H. Rawitscher, and S. A. Sofianos, *Phys. Rev.* **C45**, 2885 (1992); G. H. Rawitscher, *Phys. Rev.* **C31**, 1173 (1985).
223. J. W. Negele and K. Yazaki, *Phys. Rev. Lett.* **47**, 71 (1981).
224. J. W. Negele, *Comments on Nuclear and Particle Physics* **12**, 1 (1983).
225. C. Mahaux and R. Sartor, *Nucl. Phys.* **A516**, 285 (1990).
226. M. Jaminon and C. Mahaux, *Phys. Rev.* **C41**, 697 (1990).
227. F. de Jong and R. Malfliet, *Phys. Rev.* **C44**, 998 (1991).
228. M. Jaminon and C. Mahaux, *Phys. Rev.* **C40**, 354 (1989).
229. J. J. Kelly, submitted to *Phys. Rev.* **C** (1994).
230. G. Garino, M. Saber, R. E. Segel, *et al, Phys. Rev.* **C45**, 780 (1992).
231. D. F. Geesaman, R. Gilman, M. C. Green, *et al., Phys. Rev. Lett.* **63**, 734 (1989).
232. D. G. Ireland and G. van der Steenhoven, *Phys. Rev.* **C49**, 2182 (1994).
233. V. R. Pandharipande and S. C. Pieper, *Phys. Rev.* **C45**, 791 (1992).
234. H. C. Newns, *Proc. Phys. Soc. London* **A66**, 477 (1953).
235. H. C. Newns and M. Y. Refai, *Proc. Phys. Soc. London* **A71**, 627 (1958).
236. G. Jacob, T. A. J. Maris, C. Schneider, and M. R. Teodoro, *Nucl. Phys.* **A257**, 517 (1976).
237. J. J. Kelly, submitted to *Phys. Rev.* **C** (1994).
238. L. L. Foldy and S. A. Wouthuysen, *Phys. Rev.* **78**, 29 (1950).
239. K. W. McVoy and L. van Hove, *Phys. Rev.* **125**, 1034 (1962).
240. S. Boffi, C. Giusti, and F. D. Pacati, *Nucl. Phys.* **A336**, 416 (1980).

241. C. Giusti and F. D. Pacati, *Nucl. Phys.* **A336,** 427 (1980).
242. J. Mougey, M. Bernheim, A. Bussière, *et al., Nucl. Phys.* **A262,** 461 (1976).
243. C. R. Chinn and A. Picklesimer, *Il Nuovo Cimento* **105A,** 1149 (1992).
244. H. W. L. Naus, S. J. Pollock, J. H. Koch, and U. Oelfke, *Nucl. Phys.* **A509,** 717 (1990).
245. X. Song, J. P. Chen, P. K. Kabir, and J. S. McCarthy, *J. Phys. G* **17,** L75 (1991).
246. P. C. Tiemeijer and J. A. Tjon, *Phys. Rev.* **C42,** 599 (1990).
247. L. L. Schiff, *Phys. Rev.* **103,** 443 (1956).
248. F. Lenz and R. Rosenfelder, *Nucl. Phys.* **A176,** 513 (1971).
249. J. Knoll, *Nucl. Phys.* **A223,** 462 (1974).
250. C. Giusti and F. D. Pacati, *Nucl. Phys.* **A473,** 717 (1987).
251. Y. Jin, H. P. Blok, and L. Lapikás, *Phys. Rev.* **C48,** R964 (1993).
252. Y. Jin, D. S. Onley, and L. E. Wright, *Phys. Rev.* **C50,** 168 (1994).
253. J. P. McDermott, *Phys. Rev. Lett.* **65,** 1991 (1990).
254. Y. Jin, D. S. Onley, and L. E. Wright, *Phys. Rev.* **C45,** 1311 (1992).
255. J. M. Udías, P. Sarriguren, E. M. de Guerra, E. Garrido, and J. A. Caballero, *Phys. Rev.* **C48,** 2731 (1993); *ibid.* **C51,** 3246 (1995).
256. M. Hedayati-Poor, J. I. Johansson, and H. S. Sherif, *Phys, Rev.* **C51,** 2044 (1995).
257. C. Mahaux and R. Sartor, *Adv. Nucl. Phys.* **20,** 1 (1991).
258. A. B. Migdal, *Sov. Phys. JETP* **5,** 333 (1957).
259. J. M. Luttinger, *Phys. Rev.* **119,** 1153 (1960).
260. O. Benhar, A. Fabrocini, and S. Fantoni, *Phys. Rev.* **C41,** R24 (1990).
261. M. Baldo, I. Bombaci, G. Giansiracusa, *et al., Phys. Rev.* **C41,** 1748 (1990).
262. A. Ramos, A. Polls, and W. H. Dickhoff, *Nucl. Phys.* **A503,** 1 (1989).
263. G. E. Brown and M. Rho, *Nucl. Phys.* **A372,** 397 (1981).
264. M. G. E. Brand, G. A. Rijsdijk, F. A. Muller, and K. Allaart, *Nucl. Phys.* **A531,** 253 (1991).
265. C. Mahaux and H. Ngô, *Nucl. Phys.* **A378,** 205 (1982).
266. C. Mahaux and H. Ngô, *Nucl. Phys.* **A431,** 486 (1984).
267. C. H. Johnson, D. J. Horen, and C. Mahaux, *Phys. Rev.* **C36,** 2252 (1987).
268. J.-P. Jeukenne, C. H. Johnson, and C. Mahaux, *Phys. Rev.* **C38,** 2573 (1988).
269. C. H. Johnson and C. Mahaux, *Phys. Rev.* **C38,** 2589 (1988).
270. C. Mahaux and R. Sartor, *Nucl. Phys.* **A503,** 525 (1989).
271. C. Mahaux and R. Sartor, *Nucl. Phys.* **528,** 253 (1991).
272. A. B. Migdal, *Theory of Finite Fermi Systems,* Wiley, New York (1967).
273. W. Tornow, Z. P. Chen, and J. P. Delaroche, *Phys. Rev.* **C42,** 693 (1990).
274. Y. Wang, C. C. Foster, R. D. Polak, J. Rapaport, and E. J. Stephenson, *Phys. Rev.* **C47,** 2677 (1993).
275. Z. Y. Ma and J. Wambach, *Nucl. Phys.* **A402,** 275 (1983).
276. Z. Y. Ma and J. Wambach, *Phys. Lett.* **B256,** 1 (1991).
277. E. N. M. Quint, PhD thesis, Universiteit van Amsterdam (1988).
278. M. Leuschner, J. R. Calarco, F. W. Hersman, *et at., Phys. Rev.* **C49,** 955 (1994).
279. J. B. J. M. Lanen, A. M. van den Berg, H. P. Blok, *et al., Phys. Rev. Lett.* **62,** 2925 (1989).
280. J. B. J. M. Lanen, R. G. Lovas, A. T. Kruppa, *et al., Phys. Rev. Lett.* **63,** 2793 (1989).
281. J. B. J. M. Lanen, H. P. Blok, E. Jans, *et al., Phys. Rev. Lett.* **64,** 2250 (1990).
282. L. J. de Bever, PhD thesis, Vrije Universiteit te Amsterdam (1993).
283. G. van der Steenhoven, H. P. Blok, J. F. J. van den Brand, *et al., Phys. Rev. Lett.* **57,** 182 (1986).
284. G. van der Steenhoven, H. P. Blok, E. Jans, *et al., Nucl. Phys.* **A480,** 547 (1988).
285. G. van der Steenhoven, H. P. Blok, E. Jans, *et al., Nucl. Phys.* **A484,** 445 (1988).
286. L. Chinitz, M. Bernheim, G. P. Capitani, *et al., Phys. Rev. Lett.* **67,** 568 (1991).

287. C. M. Spaltro, H. P. Blok, E. Jans, *et al., Phys. Rev.* **C48,** 2385 (1993).

288. K. I. Blomqvist, W. U. Boeglin, R. Böhm, *et al., Phys. Lett.* **B344,** 85 (1995).

289. J. P. Wesseling, PhD thesis, Vrije Universiteit te Amsterdam (1992).

290. G. J. Kramer, PhD thesis, Universiteit van Amsterdam (1990).

291. H. J. Bulten, PhD thesis, Rijksuniversiteit te Utrecht (1992).

292. J. W. A. den Herder, H. P. Blok, E. Jans, *et al., Nucl. Phys.* **A490,** 507 (1988).

293. J. W. A. den Herder, J. A. Hendriks, E. Jans, *et al., Phys. Rev. Lett.* **57,** 1841 (1986).

294. J. B. J. M. Lanen, H. P. Blok, H. J. Bulten, *et al., Nucl. Phys.* **A560,** 811 (1993).

295. E. N. M. Quint, B. M. Barnett, A. M. van den Berg, *et al., Phys. Rev. Lett.* **58,** 1088 (1987).

296. E. N. M. Quint, J. F. J. van den Brand, J. W. A. den Herder, *et al., Phys. Rev. Lett.* **57,** 186 (1986).

297. I. Bobeldijk, M. Bouwhuis, D. G. Ireland, *et al., Phys. Rev. Lett.* **73,** 2684 (1994).

298. S. Boffi, C. Giusti, and F. D. Pacati, computer program DWEEPY.

299. L. Lapikás, *Nucl. Phys.* **A553,** 297c (1993).

300. L. Lapikás, private communication (1995).

301. V. R. Pandharipande, C. N. Papanicolas, and J. Wambach, *Phys. Rev. Lett.* **53,** 1133 (1984).

302. S. Fantoni and V. R. Pandaripande, *Nucl. Phys.* **A427,** 473 (1984).

303. I. E. Lagaris and V. R. Pandharipande, *Nucl. Phys.* **A359,** 331 (1981).

304. D. Gogny, in *Nuclear Physics with Electromagnetic Interactions,* Volume 108, pp. 88–98, Springer-Verlag, Berlin (1979).

305. D. van Neck, A. E. L. Dieperink, and E. M. de Guerra, *Phys. Rev.* **C51,** 1800 (1995).

306. H. Müther and W. H. Dickhoff, *Phys. Rev.* **C49,** R17 (1994).

307. H. Müther, A. Polls, and W. H. Dickhoff, *Phys. Rev.* **C51,** 3040 (1995).

308. S. C. Pieper, R. B. Wiringa, and V. R. Pandharipande, *Phys. Rev.* **C46,** 1741 (1992).

309. I. Sick, S. Fantoni, A. Fabrocini, and O. Benhar, *Phys. Lett.* **B323,** 267 (1994).

310. E. A. J. M. Offermann, private communication (1995).

311. V. R. Pandharipande and S. C. Pieper, *Nucl. Phys.* **A507,** 167c (1990).

312. E. J. Moniz, *Phys. Rev.* **184,** 1154 (1969).

313. E. J. Moniz, I. Sick, R. R. Whitney, *et al., Phys. Rev. Lett.* **26,** 445 (1971).

314. R. R. Whitney, I. Sick, J. R. Ficenec, R. D. Kephart, and W. P. Trower, *Phys. Rev.* **C9,** 2230 (1974).

315. R. Altemus, A. Cafolla, D. Day, *et al., Phys. Rev. Lett.* **44,** 965 (1980).

316. P. Barreau, M. Bernheim, J. Duclos, *et al., Nucl. Phys.* **A402,** 515 (1983).

317. A. Hotta, P. J. Ryan, H. Ogino, *et al., Phys. Rev.* **C30,** 87 (1984).

318. Z. E. Meziani, P. Barreau, M. Bernheim, *et al., Phys. Rev. Lett.* **52,** 2130 (1984).

319. Z. E. Meziani, P. Barreau, M. Bernheim, *et al., Phys. Rev. Lett.* **54,** 1233 (1985).

320. M. Deady, C. F. Williamson, P. D. Zimmermann, R. Altemus, and R. R. Whitney, *Phys. Rev.* **C33,** 1897 (1986).

321. C. C. Blatchley, J. J. LeRose, O. E. Pruet, *et al., Phys. Rev.* **C34,** 1243 (1986).

322. T. C. Yates, C. F. Williamson, W. M. Schmitt, *et al., Phys. Lett.* **B312,** 382 (1993).

323. W. M. Alberico, A. Molinari, T. W. Donnelly, E. L. Kronenberg, and J. W. van Orden, *Phys. Rev.* **C38,** 1801 (1988).

324. Y. Jin, D. S. Onley, and L. E. Wright, *Phys. Rev.* **C45,** 1333 (1992).

325. W. Bertozzi, R. W. Lourie, and E. J. Moniz, in *Modern Topics in Electron Scattering,* edited by B. Frois and I. Sick, World Scientific, Singapore (1991).

326. J. M. Finn, R. W. Lourie, and B. H. Cottmann, *Phys. Rev.* **C29,** 2230 (1984).

327. J. W. van Orden and T. W. Donnelly, *Ann. Phys. (N.Y.)* **131,** 451 (1981).

328. W. M. Alberico, T. W. Donnelly, and A. Molinari, *Nucl. Phys.* **A512,** 541 (1990).

329. C. C. degli Atti, E. Pace, and G. Salmé, *Phys. Rev.* **C43,** 1155 (1991).

330. D. B. Day, J. S. McCarthy, T. W. Donnelly, and I. Sick, *Ann. Rev. Nucl. Part. Sci.* **40,** 357 (1990).
331. R. W. Lourie, H. Baghei, W. Bertozzi, *et al., Phys. Rev. Lett.* **56,** 2364 (1986).
332. P. E. Ulmer, H. Baghei, W. Bertozzi, *et al., Phys. Rev. Lett.* **59,** 2259 (1987).
333. H. Baghaei, W. Bertozzi, K. I. Blomqvist, *et al., Phys. Rev.* **C39,** 177 (1989).
334. J. Morrison, PhD thesis, M. I. T. (1993).
335. S. D. Penn, PhD thesis, M. I. T. (1993).
336. G. van der Steenhoven, A. M. van den Berg, H. P. Blok, *et al., Phys. Rev. Lett.* **58,** 1727 (1987).
337. D. Reffay-Pikeroen, M. Bernheim, S. Boffi, *et al., Phys. Rev. Lett.* **60,** 776 (1988).
338. T. Suziki, *Phys. Rev.* **C37,** 549 (1988).
339. M. Kohno, *Phys. Rev.* **C38,** 584 (1988).
340. T. D. Cohen, J. W. van Orden, and A. Picklesimer, *Phys. Rev. Lett.* **59,** 1267 (1987).
341. S. Boffi, C. Giusti, and F. D. Pacati, *Nucl. Phys.* **A336,** 437 (1980).
342. J. Noble, *Phys. Rev. Lett.* **46,** 412 (1981).
343. L. S. Celenza, A. Harindranath, A. Rosenthal, and C. M. Shakin, *Phys. Rev.* **C31,** 946 (1985).
344. P. J. Mulders, *Phys. Rev. Lett.* **54,** 2560 (1985).
345. J. Mandeville, R. Alarcon, R. Beck, *et al., Phys. Rev. Lett.* **72,** 3325 (1994).
346. S. Boffi and M. Radici, *Nucl. Phys.* **A526,** 602 (1991).
347. S. Boffi, C. Giusti, F. D. Pacati, and M. Radici, *Nucl. Phys.* **A518,** 639 (1990).
348. S. Boffi and M. Radici, *Phys. Lett.* **B242,** 151 (1990).
349. J. Ryckebusch, K. Heyde, L. Machenil, *et al., Phys. Rev.* **C46,** R829 (1992).
350. J. Ryckebusch, L. Machenil, M. Vanderhaeghen, V. van der Sluys, and M. Waroquier, *Phys. Rev.* **C49,** 2704 (1994).
351. V. van der Sluys, J. Ryckebusch, and M. Waroquier, *Phys. Rev.* **C49,** 2695 (1994).
352. R. D. Peccei, *Phys. Rev.* **176,** 1812 (1968).
353. R. D. Peccei, *Phys. Rev.* **181,** 1902 (1969).
354. E. Oset, H. Toki, and W. Weise, *Phys. Rep.* **83,** 281 (1982).
355. J. Hockert, D. O. Riska, M. Gari, and A. Huffman, *Nucl. Phys.* **A217,** 14 (1973).
356. M. M. Giannini and G. Ricco, *Ann. Phys. (N.Y.)* **102,** 458 (1976).
357. S. Boffi, M. Radici, J. J. Kelly, and T. M. Payerle, *Nucl. Phys.* **A539,** 597 (1992).
358. M. Waroquier, J. Ryckebusch, J. Moreau, *et al., Phys. Rep.* **148,** 249 (1987).
359. J. Ryckebusch, K. Heyde, D. van Neck, and M. Waroquier, *Nucl. Phys.* **A503,** 694 (1989).
360. J. Ryckebusch, M. Waroquier, K. Heyde, J. Moreau, and D. Ryckbosch, *Nucl. Phys.* **A476,** 237 (1988).
361. V. van der Sluys, private communication (1995).
362. H. P. Blok and G. van der Steenhoven, *Phys. Rev.* **C35,** 2347 (1987).
363. P. Kunz, computer program CHUCK.
364. J. J. Kelly, computer program LEA.
365. L. J. de Bever, H. P. Blok, J. Blouw, *et al., Nucl. Phys.* **A579,** 13 (1994).
366. G. van der Steenhoven, H. P. Blok, J. W. A. den Herder, *et al., Phys. Rev.* **C32,** 1787 (1985).
367. I. Bobeldijk, H. P. Blok, and G. van der Steenhoven, *Phys. Lett.* **B281,** 25 (1992).
368. J. W. Watson, W. Pairsuwan, B. D. Anderson, *et al., Phys. Rev. Lett.* **55,** 1369 (1985).
369. G. van der Steenhoven, H. P. Blok, M. Thies, and P. J. Mulders, *Phys. Lett.* **B191,** 227 (1987).
370. S. Jeschonnek, A. Szczurek, G. Có, and S. Krewald, *Nucl. Phys.* **A570,** 599 (1994).
371. J. M. Laget, *Can. J. Phys.* **62,** 1046 (1984).
372. R. W. Lourie, W. Bertozzi, J. Morrison, and L. B. Weinstein, *Phys. Rev.* **C47,** R444 (1993).

373. T. Takaki, *Phys. Rev.* **C39,** 359 (1989).
374. L. B. Weinstein and G. A. Warren, *Phys. Rev.* **C50,** 350 (1994).
375. S. Homma, M. Kanazawa, K. Maruyama, *et al., Phys. Rev.* **C27,** 31 (1983).
376. M. Kanazawa, S. Homma, M. Koike, *et al., Phys. Rev.* **C35,** 1828 (1987).
377. J. Ryckebusch, V. van der Sluys, M. Waroquier, *et al., Phys. Lett.* **B333,** 310 (1994).
378. J. P. Jeukenne and C. Mahaux, *Nucl. Phys.* **A394,** 445 (1983).
379. L. J. H. M. Kester, W. H. A. Hesselink, N. Kalantar-Nayestanaki, *et al., Phys. Lett.* **B344,** 79 (1995).
380. I. J, D. MacGregor, in *International Conference on Nuclear and Particle Physics, Glasgow, 1993,* pp. 93–111, IOP Publishing, Ltd., Bristol, England (1993).
381. E. J. Beise, G. Dodson, M. Garçon, *et al., Phys. Rev. Lett.* **62,** 2593 (1989).
382. J. Arends, P. Detemple, N. Floss, *et al., Nucl. Phys.* **A526,** 479 (1991).
383. S. Boffi, C. Giusti, F. D. Pacati, and M. Radici, *Nucl. Phys.* **A564,** 473 (1993).
384. C. Giusti and F. D. Pacati, *Nucl. Phys.* **A535,** 573 (1991).
385. T. S. Bauer, R. Hamers, P. Boberg, *et al., Phys. Rev.* **C46,** R20 (1992).
386. R. D. Ransome, C. L. Morris, V. R. Cupps, *et al., Phys. Rev.* **C45,** R509 (1992).
387. R. D. Ransome, C. L. Morris, M. K. Jones, *et al., Phys. Rev.* **C46,** 273 (1992).
388. M. K. Jones, R. D. Ransome, V. R. Cupps, *et al., Phys. Rev.* **C48,** 2800 (1993).
389. T. Alteholz, D. Androi , G. Backenstoss, *et al., Phys. Rev. Lett.* **73,** 1336 (1994).
390. E. Oset, Y. Futami, and H. Toki, *Nucl. Phys.* **A448,** 597 (1986).

INDEX